

Characterisation of Strike-slip Tectonics in Rifts and
Rifted Margins

Athanasia Vasileiou

Submitted in accordance with the requirements
for the degree of Doctor of Philosophy

The University of Leeds
School of Earth and Environment

January 2024

Declaration

The candidate confirms that the work submitted is their own authorship, with the exception of portions from collaborative publications. The contribution of the candidate and the other authors to this work has been indicated below. The candidate confirms that appropriate credit has been given within the thesis where reference has been made to the work of the others.

The work in Chapter 3 contains a published article, subsequently edited and included in the thesis. The status of the manuscript is as follows:

Vasileiou A., Gouiza, M., Mortimer, E., Paton, D., Nanfito, A., & Lewis, D., (2023). New insights into the crustal architecture and tectonics evolution of the Eastern Gulf of Mexico. Basin Research. <https://doi.org/10.1111/BRE.12812>

As lead author, I was responsible for data analysis, interpretation, and figures and manuscript preparation. The contribution of the authors was limited to discussion of the results, and manuscript review and editing.

This copy has been supplied on the understanding that it is copyright material and that no quotation from the thesis may be published without proper acknowledgment.

The right of Athanasia Vasileiou to be identified as Author of this work has been asserted by her in accordance with the Copyright, Designs and Patents Act 1988.

© 2024 The University of Leeds and Athanasia Vasileiou

Acknowledgements

I extend my most honest thanks

to my supervisors, Mohamed Gouiza, Estelle Mortimer, and Richard Collier, for all the support, guidance, technical discussions, and encouragements. I would like to thank them for all their patience and understanding over the past years. Thank you all for making me a better scientist. Moh, thank you for the different roles you have undertaken as a supervisor and a friend, the useful advices and enthusiasm especially during fieldwork, which kept me motivated.

to Douglas Paton for the support in the very early stages of the project. I would not have been here if it were not you, your enthusiasm for structural geology, and your trust towards me since the master's.

to the sponsors of the Basin Structure Group, University of Leeds, which supported the project.

to David Lewis and Aleece Nanfito from Woodside Energy for the discussions during the Master's and the early stages of this project.

to TGS and the Petroleum Commission of Ghana for providing the DeepEast and Ghana surveys, and their permission to publish them.

to journal editor and reviewers for the positive and constructive comments, which greatly improved the manuscript.

to Mike Shotton and Jonathan Hare for tolerating me for three weeks each during the fieldwork. Also, kudos to David Fernandez for the amazing maps you generated for me during the second field season.

to people from the department for the helpful chats and encouragements. I would like to particularly thank Mike Shotton, Ben Craven, Jason Williams, Georgian Manuc, Sam Haynes, and Charlotte Botter.

to Roxana Stanca for not getting tired of all of my questions. Thank you for the many roles you have undertaken during this project, as demonstrator, honorary supervisor, friend, sister. Thank you very much for all the moral support throughout the project, especially during the last two years.

to friends from back home, the UK and beyond for keeping me motivated, distracted when needed, and generally being there in person and virtually. I thank Sawsan Demnati, Paraskevi Fotoglou, Matthew Wade, Ofelia Silio, Horte Riviera, Anthony Ramirez-Salazar, Mofe Wilkey, Anas Sahin, and others for the walks, chats, laughs, games, meals, and cakes.

to the people behind the scenes, geoscientist and no, for the discussions that changed my mindset.

to my family, Lena, Vasilis, Mara, James, and Hermis, for all the love and support. Thank for being there when I needed you, for always accepting and supporting my choices, for doing everything you could so I can achieve my goals. I will not be near anywhere I am without you. Thank you for just being by my side even not knowing how to help. Σας αγαπώ!

Abstract

Traditionally, research on oblique extension has primarily focused on pure strike-slip systems and well-known pull-apart basins, with an emphasis on characterising strike-slip tectonics mainly within contractional tectonic settings. Oblique deformation, induced by the movement of tectonic plates, is a common occurrence at both plate boundaries and intracontinental systems in divergent zones. In recent years, an increasing number of studies have turned their attention to characterising oblique extension to gain a better understanding of rifts and rifted systems that were previously assumed to have orthogonal extension. Recognising the varying degrees of obliquity in divergent systems is crucial for enhancing the reliability of plate tectonic models, resource exploration, and the identification of natural hazards.

This thesis adopts a multi-disciplinary, multi-scale approach, utilising offshore 2D seismic reflection data accompanied by gravity data, and onshore field data. The methodology is applied to various case studies with different degrees of obliquity to investigate the evolution of different divergent systems. The combination of seismic reflection data and field data is chosen for their complementary strengths: seismic reflection data provide insights at the crustal scale, while field data focuses on elements within the basin.

Despite the degree of obliquity in the system, the findings reveal spatial alternation in the stress regimes within the oblique rifts and rifted margins. These stress alternations are reflected in syn-kinematic growth strata, allowing the differentiation between oblique and orthogonal stress regimes. The findings encompass the role of pre-existing structures on the evolution of the oblique systems. Furthermore, oblique systems often exhibit magmatic intrusions through strike-slip, transfer, or continental transform faults, typically located at plate boundaries or the core of the rift system. At the crustal scale, intrusions through transform faults are capable of forming a transitional crust, which disproves the previous notion of the absence of continental-oceanic transitional crust in transform margins.

In conclusion, this study contributes to the refinement of the strike-slip tectonics model, traditionally centred on contractional settings by providing additional insights into divergent strike-slip systems, and displays the implications on the

Pangaea break-up. The findings not only enhance our understanding of these settings but also suggest potential directions for further research in this dynamic field.

Contents

Declaration.....	i
Acknowledgements.....	ii
Abstract.....	iv
Contents.....	vi
List of Figures	ix
List of Tables	xix
List of terminology	xxi
Chapter 1 – Introduction.....	22
1.1 Motivation.....	2
1.1.1 Rifted margins	2
1.1.2 Oblique divergent systems.....	3
1.2 Research questions	8
1.3 Approach – Study localities.....	8
1.4 Thesis structure.....	9
Chapter 2 – Moroccan High Atlas: The case study on strike-slip influenced rifted systems	11
Summary	11
2.1 Introduction	12
2.2 Background	15
2.3 Methodology.....	18
2.4 Results - Key Outcrops	21
2.4.1 Aït Attab	21
2.4.2 Ouaouizaght.....	24
2.4.3 Zawyat-Ahancal.....	28
2.4.4 Agoudal	31
2.4.5 Er-Rich	35
2.4.6 Bou Annane.....	39
2.5 Discussion.....	42
2.5.1 Orthogonal extension	42
2.5.2 Oblique extension	44
2.6 Conclusion.....	54
Chapter 3 - Florida margin, Eastern Gulf of Mexico: Identifying strike-slip activity during rifting	57
Summary	58
3.1 Introduction.....	59
3.2 Geological Background	62
3.3 Data and Approach	65

3.3.1 Data.....	65
3.3.2 Approach.....	66
3.4 Stratigraphic and Crustal Architecture	67
3.4.1 Rift to drift sedimentary sequences.....	67
3.4.2 Structural configuration.....	69
3.4.3 Crustal Types.....	70
3.5 Gravity analysis.....	79
3.5.1 Methodology.....	80
3.5.2 Gravity Modelling Results	82
3.6 Proposed crustal model for the Eastern Gulf of Mexico.....	86
3.7 Discussion.....	90
3.7.1 Structural evolution	90
3.7.2 SDRs.....	91
3.7.3 Magmatic crust	93
3.7.4 Serpentinized subcontinental mantle.....	93
3.7.5 Evolutionary model for the EGOM.....	96
3.7.6 Further discussion	98
3.8 Conclusion.....	99
Chapter 4 – The transform margin of Ghana.....	102
Summary	102
4.1 Introduction	103
4.2 Geological Background	106
4.3 Data and Methodology	110
4.3.1 Data.....	110
4.3.2 Methodology.....	112
4.4 Seismic Analysis	115
4.4.1 Seismo-stratigraphic sequences	115
4.4.2 Faults.....	120
4.4.3 Crustal types.....	121
4.5 Velocity and Gravity Analysis	133
4.5.1 From time-to-depth	133
4.5.2 Gravity analysis	137
4.6 Discussion.....	140
4.6.1 Crustal-tectonic model for the Ghanaian margin	140
4.6.2 Magmatic material.....	145
4.6.3 Comparison with the conjugate Barreirinhas-Ceará.....	147
4.6.4 Structural and crustal evolution	149

4.7 Conclusion.....	156
Chapter 5 – Discussion, future work and conclusions	159
5.1 Introduction	159
5.2 Stress-regime and tectono-stratigraphy	160
5.2.1 Stress regime.....	160
5.2.2 Faults.....	161
5.2.3 Sediment characteristics.....	165
5.3 Crustal types-fault relationships and magmatism	167
5.4 Classic rifted margins vs strike-slip influenced margins.....	169
5.4.1 Rifted margins.....	169
5.4.2 Transform margins	169
5.5 Atlantic opening.....	171
5.6 Comparison with other divergent systems influenced by strike-slip faults.....	173
5.6.1 East Africa Rift and the Main Ethiopian Rift.....	173
5.6.2 Agulhas transform margin – South Africa.....	176
5.6.3 Barents Sea and Norwegian transform margins	177
5.6.4 Gulf of California	179
5.6.5 Bohai, China	181
5.7 Suggested future research	183
5.7.1 Magmatism in oblique rifts	183
5.7.2 Data availability.....	183
5.7.3 Modelling	183
5.8 Conclusions	186
References	189
Appendix	224
<u>A.</u> Appendix for Chapter 2 – High Atlas, Morocco.....	224
<u>B.</u> Appendix for Chapter 3 – Florida, Eastern Gulf of Mexico.....	242
<u>C.</u> Appendix for Chapter 4 – Ghana, Equatorial Atlantic.....	245

List of Figures

<p>Figure 1.1: Indicative cross-sections with the rifted (Aa-b) and transform (B) margins (Doré & Lundin, 2015; Franke, 2013; Lister et al., 1991; Loncke et al., 2020; Mercier de Lépinay et al., 2016; Peron-Pinvidic et al., 2013; Planke & Eldholm, 1994; Sutra & Manatschal, 2012).....</p>	3
<p>Figure 1.2: Schematic sketch of strike-slip faults at the plate boundaries, the cratonic continental and oceanic crusts (after Woodcock, 1986; Mann, 2007).</p>	4
<p>Figure 1.3: Transform margins and onshore strike-slip setting across the world (after Chorowicz, 2005; Mann, 2007; Mercier de Lépinay et al., 2016). Fracture zones from Müller et al. (2008) and Matthews et al. (2011), and Continental-Oceanic Boundary (COB) from Exxon World Mapping Project (1985). High Atlas – discussed in Chapters 2 and 5; Florida margin – discussed in Chapters 3 and 5; and Ghanaian margin – discussed in Chapters 4-5.</p>	6
<p>Figure 2.1: A. Schematic regional geological map of Morocco, NW Africa, which displays the main units and structures, and the outcrop localities in the Central and Eastern High Atlas. SAF: South Atlas Fault; NAF: North Atlas Fault (modified from Hafid <i>et al.</i>, 2006). Geological maps of the Central and Eastern High Atlas with the selected outcrops of key localities 1-4 in B, locality 5 in C, and locality 6 in D and their equivalent cross-sections; bold black transects (I-IV) (after Rolley and Etienne, 1978; Monbaron, 1985; Jenny, 1988; Jossen, 1988; Du Dresnay <i>et al.</i>, 1997; Milhi, 1997; Fadile, 2003; Baidder <i>et al.</i>, 2018). Green transects indicate cross-sections based on fieldwork measurements and geological maps, whilst red transects are only based on geological maps. (F) indicates the studied faults on the cross-sections in figures 2.7 and 2.9.</p>	14
<p>Figure 2.2: A. Main tectonic events during the evolution of the Atlas region, with Pangaea formation (a) and break-up (b), followed by the convergence of Africa and Eurasia (c) (modified from Arthaud and Matte, 1977; Muttoni et al., 2003; Schettino and Turco, 2011; Kroner and Romer, 2013; Ellero et al., 2020). ASZ: Atlas Shear Zone; CIFZ: Canary Islands Fracture Zone. B. Tectonostratigraphic column capturing the main tectonic events in the High Atlas, Morocco (modified from Ellouz et al., 2003; Walker et al., 2018; Escosa et al., 2021).....</p>	17
<p>Figure 2.3: Representative photos and interpretation of Aït Attab region, whose localities are presented in Figure 2.1B. (a) Middle Jurassic fault slay that consists of strike-slip and normal faults, and (b) Riedel structures in the eastern limit of the anticline. (c) Inherited structure reactivated as a strike slip and (d) normal faults with growth strata, form a negative flower structure, south of the Aït Attab region. (e) Lower Jurassic, potentially Toarcian in age and (f) Middle Jurassic Riedel structures at the northern limb of the anticline. (g) Paleostress results. MJ: Middle Jurassic. Field data are presented in appendix Tables A-1 to A-4.....</p>	23

Figure 2.4: Ouaouizaght representative photos whose localities are presented in Figure 2.1B. (a) Early Jurassic faults in the northern NE-SW trending regional scale fault. In the rose diagram, blue indicates faults in locality (a) and green indicates the faults in the southern NE-SW main structure in locality (A.1; Figures 2.1B and A.1 in appendix). (b) Contractional related sinistral strike slip fault and shear structures (c) within the Middle Jurassic sequence; faults - red stereonet and rose diagram; shear structures - black stereonet. (d) Late Middle Jurassic dextral NW-SE regional scale fault and (e) late Middle Jurassic E-W trending transtensional fault. (g) Paleostress analysis. TG: tension gashes. Field data are presented in appendix Tables A-5 to A.8..... 27

Figure 2.5: Zawyat-Ahancal representative photos and interpretations, whose localities are presented in Figure 2.1B. (a) Lower Jurassic to Toarcian units in contact with Triassic evaporites-basalt placed in the background. The dashed lines indicate ENE-WSW trending reactivated structures, on which growth strata are developed. Bedding poles along the green cross-section (indicated in Figure 3.1B). (b) Lower Jurassic sequence with a reactivated positive flower structure. (c) Toarcian ENE-WSW normal faults with growth strata. (d) A conjugate set of tension gashes in Lower Jurassic carbonates and their schematic stress interpretation posterior to the unfolding. (e) Stress interpretation based on the faults and the tension gashes. (f) Paleostress analysis. TG: tension gashes. Field data are presented in appendix Table A-9..... 30

Figure 2.6: Agoudal representative photos and interpretations, whose localities are presented in Figure 2.1B. (a) Lower Jurassic carbonates with two tension gashes generations. (b) N-S and (c) NW-SE perspective of Middle Jurassic carbonates, showing syn-contractional growth strata and an open anticline, respectively. (d) Representative structures identified along the Middle Jurassic carbonates, showing two different phases. (e) Middle Jurassic growth strata with overturned bedding caused by Middle Jurassic – Cretaceous gabbro. (f) Paleostress analysis. TG: tension gashes; MJ: Middle Jurassic; LJ: Lower Jurassic. Field data are presented in appendix Tables A-10 to A-12. 34

Figure 2.7: Er-Rich region cross-sections (a), whose localities are imaged in Figure 2.1C, and their restoration (b). 36

Figure 2.8: Er-Rich region localities presented in Figure 2.1C. (a) Panoramic view of the syncline, and restored bedding poles that show fanning towards the SE. (b) Representative Middle Jurassic shear zone with dominant contractional shear, (c) an older (red) tension gash deformed by younger tension gashes (black). (d) Middle Jurassic antiform with syn-kinematic bedding, and the bedding poles that indicate fanning towards the south. (e) Paleostress analysis in the Middle Jurassic. TG: tension gashes; MJ: Middle Jurassic. Field data are presented in appendix Tables A-13 and A-14. 38

Figure 2.9: (a) Panoramic view of the basement and the rifting sequences of Triassic and Lower Jurassic in Bou Annane. Middle Jurassic in the background towards the N. (b) NE-SW and ~E-W trends of tension gashes within the Lower Jurassic carbonates, which are sub-perpendicular and sub-parallel to the bedding, respectively. (c) Paleostress analysis. d. Cross-sections and schematic cross-section restorations in the Bou Annane region that cover the basement exposure (Figure 2.1D). LJ: Lower Jurassic; TG: tension gashes. Field data are presented in appendix Table A-15. 41

Figure 2.10: Schematic 3D tectonic model of the Atlas rift system during the orthogonal phase in the Late Triassic to late Early Jurassic. Detailed representation of the outcrops where orthogonal extension was observed and their calculated local stress. 1. Aït Attab; the orthogonal extension occurred mostly in the Triassic than Jurassic and produced grabens. 2. Ouaouizaght; the orthogonal extension influenced both Upper Triassic to Lower Jurassic sequences and formed a soft or hard-linked relay ramp. 3. Zawyat – Ahancal; the orthogonal extension occurred during the Late Triassic to Early Jurassic, which reactivated ENE-WSW faults and developed half grabens. 6. Bou Annane; Two distinct orthogonal extensional events occurred during the Late Triassic and Early Jurassic to Middle Jurassic boundary. The stereonet refers to the latest orthogonal event..... 51

Figure 2.11: : Schematic 3D tectonic model of the Atlas rift system during the oblique extensional phase in the late Early Jurassic to Middle Jurassic. Detailed representation of the outcrops where oblique extension was identified, and their calculated local stress. 1. Aït Attab; the oblique extension reactivated the structures and evolved the structures to strike-slip splays and negative flower structure, which involved halokinesis. 2. Ouaouizaght; the oblique extension reactivated the pre-existing structures and developed the core of the hard-linked relay ramp with ENE-WSW extensional oblique-slip faults. Magmatism might have been occurred in the southern fault. 4. Agoudal; gentle oblique transpression associated with evaporites and potential magmatic activity in the ridge. 5. Er-Rich; the oblique extension reactivated the pre-existing normal faults, and developed open folding. 53

Figure 3.1: Bathymetry map (Smith & Sandwell, 1997) in the Florida margin, Eastern Gulf of Mexico, which includes: the transparent orange and white zones that correspond to the geographic range of the inner limit of the oceanic crust (ILOC) and the extinct spreading ridges, respectively, previously interpreted in the EGOM (Bird et al., 2005; Pindell and Kennan, 2009; Kneller and Johnson, 2011; Hudec, et al., 2013; Christeson et al., 2014; Sandwell et al., 2014; Nguyen and Mann, 2016; Pindell et al., 2016; Deighton et al., 2017; Lundin and Doré, 2017; Filina et al., 2020; Minguez et al., 2020; Izquierdo-Llavall et al., 2022; Filina and Beutel, 2022); black dotted/dashed line traces represent formerly proposed NW-SE trending transfer fault (FTZ: Florida Transfer Zone; Pindell, 1985); yellow dashed line traces are the GUMBO refraction lines 3 and 4; seismic lines used in this study are shown in white, with portion of interest displayed in Figures 3.4-3.7 highlighted in orange, and black dashed traces indicating the 2-D gravity models presented in Figure 3.9. The location of the well 224-A #1-C (Babcock, 1970) in the north, and the DSDP Leg 77, site 535 (Schlager, 1984; Buffler et al., 1984) in the south which were used to further analyse the age and nature of volcanism, and the top of syn-rift sequence. Seismic data courtesy of TGS..... 61

Figure 3.2: (a-d) Tectonic evolution of the Gulf of Mexico (modified from Steier and Mann, 2019; Pindell et al., 2020a; Pindell and Heyn, 2022). (a) Initiation of Pangaea’s breakup with North America plate WNW synchronous motion (Müller et al., 2019; red arrow). The first phase of rifting was NW-SE with sinistral slip of the Florida-Bahamas Transfer Zone (FTZ). (b) Middle Jurassic continental extension, formation of Houston Magnetic Anomaly (HMA), Florida Magnetic Anomaly and Campeche Magnetic Anomaly (CMA) (James Pindell et al., 2016) and deposition of Middle Jurassic salt. Green arrows indicate the local orientation of extensional between North America plate and Yucatan Block. (c) Yucatan’s counter-clockwise rotation and oceanic seafloor spreading during the Late Jurassic. (d) End of seafloor spreading in the Early Cretaceous. Green lines indicate the Cretaceous shelf in Florida and Yucatan margins. 64

Figure 3.3: (a) Free Air Gravity Anomaly (FAA; Sandwell et al., 2014); (b) Residual gravity anomaly; (c) Vertical gradient of Residual gravity anomaly with structures trends, and (d) Earth Magnetic Anomaly Grid (EMAG; Meyer et al., 2017) in the Eastern Gulf of Mexico. Seismic data courtesy of TGS. 66

Figure 3.4: High amplitude eroded pre-rift sequence in the shelf domain, which is placed between syn-rift sediments and continental crust. Full seismic line of high resolution is provided in Appendix (Figure B.1). Seismic data courtesy of TGS. 70

Figure 3.5: Representative seismic lines and interpretation of oceanic crust. Oceanic crust characteristics with a smaller (a) and a bigger scale (b) spreading ridge (post-spreading basin), interpreted volcanoes on the top crust and, faults and dykes influence the crust. Full seismic lines of high resolution are provided in Appendix (Figures B.3-B.4). Seismic data courtesy of TGS. 74

- Figure 3.6: (a) Representative seismic line and interpretation of thinned continental crust at the proximal domain and an uncertain crust type II with intra-basement magmatism. (b) Representative seismic line and interpretation image the continental crust and the two different uncertain crustal domains. Uncertain crust type I (right) and uncertain crust type II (left). Full seismic line E of high resolution is provided in Appendix (Figure B.4). Seismic data courtesy of TGS. 76**
- Figure 3.7: (a) Representative seismic line and interpretation of sedimentary sequences and ambiguous continental crust beneath the salt deposits that juxtapose to the oceanic crust, and (b) Possible Seaward Dipping Reflections (SDRs) overlaying by post-SDR volcanoes and surrounded by the uncertain crust type I and continental crust with uncertain depth of Moho. Full seismic lines of high resolution are provided in Appendix (Figures B.2-B.3 & B.5). Seismic data courtesy of TGS. 78**
- Figure 3.8: Crustal domains map based on the seismic characteristics. Yellow and brown traces show the location of the gravity models in Figure 3.9 and Figure 3.10, respectively. Seismic data courtesy of TGS..... 79**
- Figure 3.9: Gravity modelling of the depth converted profiles C and E, whose locations are presented on Figures 3.1 and 3.3c. In the first scenario, high density was applied in the uncertain domain. In the second scenario, different low densities were applied for each section best fit in the model. In section C, dashed line represents the uncertain crust beneath the SDRs. Scenario three, proposes an extra high-density sequence (marked with dashed uncertain domain), which is partly detectable in the seismic reflection data. 85**
- Figure 3.10: Gravity modelling results along the uncertain crustal domain. Line locations are presented in Figure 3.8. The uncertain domains identified in the seismic reflection data are marked with solid black line, while dashed line highlights the misfit of observed and calculated gravity anomaly, which was corrected with the 3.0 g/cm³ high density layer..... 85**
- Figure 3.11: (a) Crustal and tectonic map of the NE Gulf of Mexico. The arrow on the SDRs shows the dip direction. FTZ: Florida-Bahamas Transfer Zone. Seismic data courtesy of TGS. (b) Representative regional scale cross-sections of seismic lines C and E..... 87**

Figure 3.12: Tectonic evolution focusing on the Florida margin, Eastern Gulf of Mexico (modified from Steier and Mann, 2019; Pindell et al., 2021; Pindell and Heyn, 2022). a) Late Triassic-Early Jurassic phase of rifting with NW-SE extension. b) SDR formation in the continental domain of the northern Florida margin during the transition from NW-SE phase to Yucatan’s rotation. Arrow on the SDR indicates the dip direction, parallel to the local extension. Yellow arrow indicates that the rotation pole of North America is further north (see Pindell, Villagómez, et al., 2020). c) Initiation of Yucatan’s rotation in the Middle Jurassic, salt deposition, continuous extension of the continental crust and possible mantle exhumation. d) Late Jurassic post-salt formation of magmatic crust and continental break-up. e) Early Cretaceous cessation of seafloor spreading. FTF: Florida Transfer Fault; HMA: Houston Magnetic Anomaly; FMA: Florida Magnetic Anomaly; CMA: Campeche Magnetic anomaly; NSE: Northern Cretaceous shelf edge; YSE: Yucatan shelf edge. Red arrow indicates the regional WNW-ESE extension from the America and Africa separation. Green arrows indicate the local extension in the conjugate margins of Florida and Yucatan at the Eastern Gulf of Mexico. 98

Figure 4.1: A. Equatorial Atlantic with plotted major fracture zones, spreading ridges, and key areas of the Ghanaian margin (B.), the conjugate basins of Barreirinhas and Ceará, and the Côte d’Ivoire basin (modified from Matthews et al., 2011; Müller et al., 2008). RFZ: Romanche Fracture Zone. B. Onshore topography (Sandwell & Smith, 1997) of the Ghanaian Margin, West Africa, which includes: TGS offshore seismic reflection data in black traces; the location of the onshore exploration wells (Attoh et al., 2004) and offshore wells (Adda, et al., 2015; IHS, 2010); white dashed lines as the oceanic transform faults based on FAA (Sandwell et al., 2014). Seismic data courtesy of TGS.104

Figure 4.2: A. Plate reconstruction of the Equatorial Atlantic opening (modified after Mascle et al., 1988; Antobreh et al., 2009). Arrows indicate the direction of movement for Africa plate. (a) Stage 1: “continental-continental” or “intracontinental rifting”; (b) Stage 2: “active continental-continental” or “continental transform”; (c) Stage 3: “continental-oceanic” or “syn-transform”; (d) Stage 4: “oceanic-oceanic” or “post-transform”. RFZ: Romanche Fracture Zone. B. Three stage model for transform margin formation with key elements of active and passive transform faults, thermal uplift and subsidence, and inner and outer corners during the (a) intra-continental and active continental-continental, (b) continental-oceanic and (c) passive margin stages (after Basile, 2015; Lorenzo, 1997; Mascle & Blarez, 1987).108

Figure 4.3: Seismic-well-tie at the offshore wells Takoradi 11-1 (a) and 13-A7 (b) in depth and time and the correspondent reflections of top syn-rift and top post-rift.111

Figure 4.4: Onshore topography (Smith & Sandwell, 1997) with offshore a) Free Air Anomaly (Sandwell et al., 2014) and b) Earth Magnetic Anomaly Grid (EMAG; Meyer et al., 2017) along the Ghanaian region.112

- Figure 4.5: Key seismic lines illustrating the structural features and seismo-stratigraphic sequences along the margin. RFZ: Romanche Fracture Zone. Seismic data courtesy of TGS.....114**
- Figure 4.6: Representative seismic lines and interpretation of sedimentary sequences, focusing on the post-rift sequence in the proximal (a) and the distal domain (b). (c) Post-rift distribution and thickness map in time (twt). Seismic data courtesy of TGS.....116**
- Figure 4.7: (a-c) Representative seismic lines and interpretation of sedimentary sequences in the western and eastern segments, focusing on the syn-rift sequence. Regional scale (a) extensional fault with growth strata, (b) positive flower structure in the syn-rift sequence in the western segment. (d) Minor syn-rift growth strata in the eastern segment. (e) Syn-rift sequence distribution and thickness map in time (twt) with the major faults influencing the syn-rift sediments. Seismic data courtesy of TGS.....117**
- Figure 4.8: (a-c) Representative seismic lines and interpretation of sedimentary sequences, focusing on the pre-rift sequence. (a) Pre-rift sequence of antiforms, which are related to pre-rift orogeny, and (b) pre-rift salt identified in the western region. (c) Post-rift sequence distribution and thickness map in time (twt). Seismic data courtesy of TGS.....119**
- Figure 4.9: (a) Depth in time (twt) of the interpreted Moho, and (b) isochron map between the top crusts and Moho.....121**
- Figure 4.10: The seismic line A (a) and B (b) illustrate representative seismic characteristics of the different oceanic crustal types, the continental crust, and the uncertain crustal type, and the Romanche Fracture Zone (RFZ) at the eastern segment of the margin. Seismic data courtesy of TGS.....127**
- Figure 4.11: Seismic lines C and D illustrate characteristics of the eastern and central segments of the margin. Seismic line C (a) illustrates representative seismic characteristics of the different continental and oceanic crusts, and the Romanche Fracture Zone (RFZ). Uncertain crustal type is imaged at the continental-oceanic transition. Seismic line D (b,c) illustrates the continental crust's NW-SE trending faults. Seismic data courtesy of TGS.....130**
- Figure 4.12: Seismic lines E and F illustrates the margin's characteristics in the western segment. The continental crust in (a) changes thickness south of the marginal ridge in the Romanche Fracture Zone (RFZ). Seismic line F (b,c) illustrates the transition from continental to oceanic crust, and the oceanic crust's structures along the strike line, with zoom-in (c) on the growth strata. Seismic data courtesy of TGS.....131**
- Figure 4.13: Representative seismic line of the oceanic crust type-2 with the uncertain underlying high amplitude reflection (a) and the magmatic crust (b). (a) Oceanic crust type-2 illustrates seaward-like dipping reflectors on the upper crust. The irregular high amplitude reflection is imaged deeper than the surrounding oceanic Moho. (b) Geometries of potential volcanoes are imaged on the magmatic crust basement, and Moho is not imaged. Seismic data courtesy of TGS.132**

Figure 4.14: Crustal types and displayed uncertainties based on the seismic characteristics. Red traces indicate the gravity models location in Figure 4.17.	133
Figure 4.15: Plots of interval velocity and depth pairs [interval velocity, depth] for each seismo-stratigraphic and crustal unit calculated from the extracted migration velocities using the Dix's formula (Dix, 1955).....	134
Figure 4.16: (a) Depth in km of the interpreted Moho, and (b) thickness between the top crusts and Moho after the depth conversion.	137
Figure 4.17: Gravity modelling of different sections and segments of the margin. (a) Crustal validation and Moho's modification occurred in the central segment line I. (b-c) Gravity models of eastern segment lines B and G, and (d-e) western segment lines H and E.....	139
Figure 4.18: (a) Crustal and tectonic map of the Ghanaian margin, bounded by seismic reflection data polygon. Marked traces indicate the location of the depth converted sections presented in (b). RFZ: Romanche Fracture Zone, marked with a transparent grey polygon.	144
Figure 4.19: Structural and tectonic evolution of the Equatorial Atlantic margins, with a specific focus on the Ghanaian margin. The positions of the African plate and the north arrow are presented in reference to the present day, remaining fixed for orientation. (a) Stage-1 of NNE-SSW orthogonal extension. (b) Stage-2 of dextral transtension in the eastern and central segments of Ghana and Ceará basin, which formed pull-apart basins and sheared structures in the continental crust. Migration of the ENE-WSW orthogonal extension towards the western segment and Barreirinhas basin. Intrusions within the RFZ in the western segment that formed the magmatic crust. Potential formation of oceanic crust type-1 at the end of the transtensional phase and the separation of Africa and South America plates. (c) Stage-3 of dextral transpressional phase caused inversion, oceanic crust type-1 deformation, and oceanic spreading. (d) Stage-4 of post-transform stage with oceanic crust formation cessation, and post-rift intrusions along the RFZ. Gh: Ghana; Br: Barreirinhas; Ce: Ceará; RFZ: Romanche Fracture Zone. Structural framework compilation for the conjugate Barreirinhas and Ceará basins from Andrade et al. (2018), de Castro et al. (2022), Davison et al. (2016), Morais Neto et al. (2003), Pinéo et al. (2020), Tavares et al. (2022) and Vasconcelos et al. (2004). Onshore structures of the Ghanaian margins from Akpaki (1978), Attoh et al. (1997) and Tidjani et al. (1997). Oceanic transform faults based on Free Air Anomaly from Sandwell et al. (2014). Ages are derived by Adda et al. (2015), Antobreh et al. (2009), Attoh et al. (2004), IHS (2010), Mascle & Blarez (1987) Scarselli et al. (2020), Tavares et al. (2020), and the seismic interpretation of this study.....	155
Figure 5.1: Analogue modelling (modified from Corti et al., 2020) of pull-apart basin with different orientations of pre-existing structures – parallel (i-iv) and oblique to the opening (v-viii), and Atlas system opening (ix-x) based on Chapter 2.	163
Figure 5.2: Equatorial Atlantic opening – analogue modelling (i-iii; modified from de Souza Rodrigues et al., 2023), and schematic diagram (iv-v) based on Chapter 4.....	164

Figure 5.3: Orthogonal influenced growth strata. (a) seismic data indicating growth strata in the orthogonal influenced segment of the Ghanaian margin. Seismic data courtesy of TGS. (b) Inverted growth strata from the orthogonal failed rifting of the Atlas system. (c) Analogue modelling cross-section modified from de Souza Rodrigues et al. (2023). Red rectangular corresponds to the seismic and field data observations. ..166	
Figure 5.4: Oblique influenced growth strata. (a) seismic data indicating growth strata in the strike-slip influenced segment of the Ghanaian margin. Seismic data courtesy of TGS. (b) Growth strata occurred in the Atlas system during the transtensional phase. (c) Analogue modelling cross-section modified from de Souza Rodrigues et al. (2023). Red rectangular corresponds to the seismic and field data observations. ..166	
Figure 5.5: A. Updated strike-slip tectonics 3D model capturing both contractional and extensional tectonics (after Woodcock, 1986). Red illustrates the intrusions occur in a pull-apart basin and a continental transform margin. B. Schematic illustration of a pull-apart basin with intrusions (after Dewey et al., 1986).	168
Figure 5.6: Pangaea’s break-up evolution integrating the kinematic characteristics from Chapters 2-4. Kinematic characteristics in North and South Atlantic opening are based on previous studies (Antobreh et al., 2009; Granot & Dymant, 2015; He et al., 2008; Malinverno et al., 2012; Moulin et al., 2010; Scotese, 2016), (model from Scotese, 2016). Tr-Jr Boundary: Triassic-Jurassic Boundary. Jr-Cr Boundary: Jurassic-Cretaceous Boundary.	172
Figure 5.7: A. Seismic profile in the Tanganvika Lake of the East African Rift System (modified from Project PROBE, 1986; Chorowicz, 2005). B. Seismic reflection profile of Lake Malawi (modified from Specht and Rosendahl, 1989; Rosendahl et al., 1992) and inferred lithospheric cross-section of the northern Kenyan rift.	175
Figure 5.8: Crustal distribution in the South African margin with key structural elements and igneous features (modified from Markwick et al., 2022; Paton et al., 2023). FZ: Fracture Zone.	176
Figure 5.9: Regional structural map with structural elements related to different rift phases and crustal transects across the rifted margin of mid Norway (1-6), and the mainly sheared western Barents Sea-Svalbard margin (7-12) (modified from Faleide et al., 2008).	178
Figure 5.10: Structural framework of the Gulf of California and seismic profile in Tiburon basin bounded by strike-slip and oblique slip faults (after Martín-Barajas et al., 2013 and references therein).	180
Figure 5.11: Structural map of the Bohai basin in China illustrating the master dextral strike-slip fault with NE-SW orientation (Qi & Yang, 2010).....	181
Figure A.1: Sub-horizontal normal faults in vertical beds in the southern NE-SW regional scale fault of Ouauizaght.	224
Figure A.2: NW-SE trending fault in the Zawyat-Ahancal region.	225
Figure A.3: Post-Middle Jurassic (blue) and syn-Middle Jurassic (orange) tensional fractures in the Early Jurassic carbonates.....	225

Figure B.1: Seismic line B of the Eastern Gulf of Mexico. Seismic data courtesy of TGS.	242
Figure B.2: Seismic line C of the Eastern Gulf of Mexico. Seismic data courtesy of TGS.	242
Figure B.3: Seismic line D of the Eastern Gulf of Mexico. Seismic data courtesy of TGS.	243
Figure B.4: Seismic line E of the Eastern Gulf of Mexico. Seismic data courtesy of TGS..	243
Figure B.5: Seismic line H of the Eastern Gulf of Mexico. Seismic data courtesy of TGS.	244
Figure C.1: Indicative marginal ridge of the Ghanaian margin. Seismic data courtesy of TGS.....	245
Figure C.2: Indicative migration velocity line. Seismic data courtesy of TGS.....	246

List of Tables

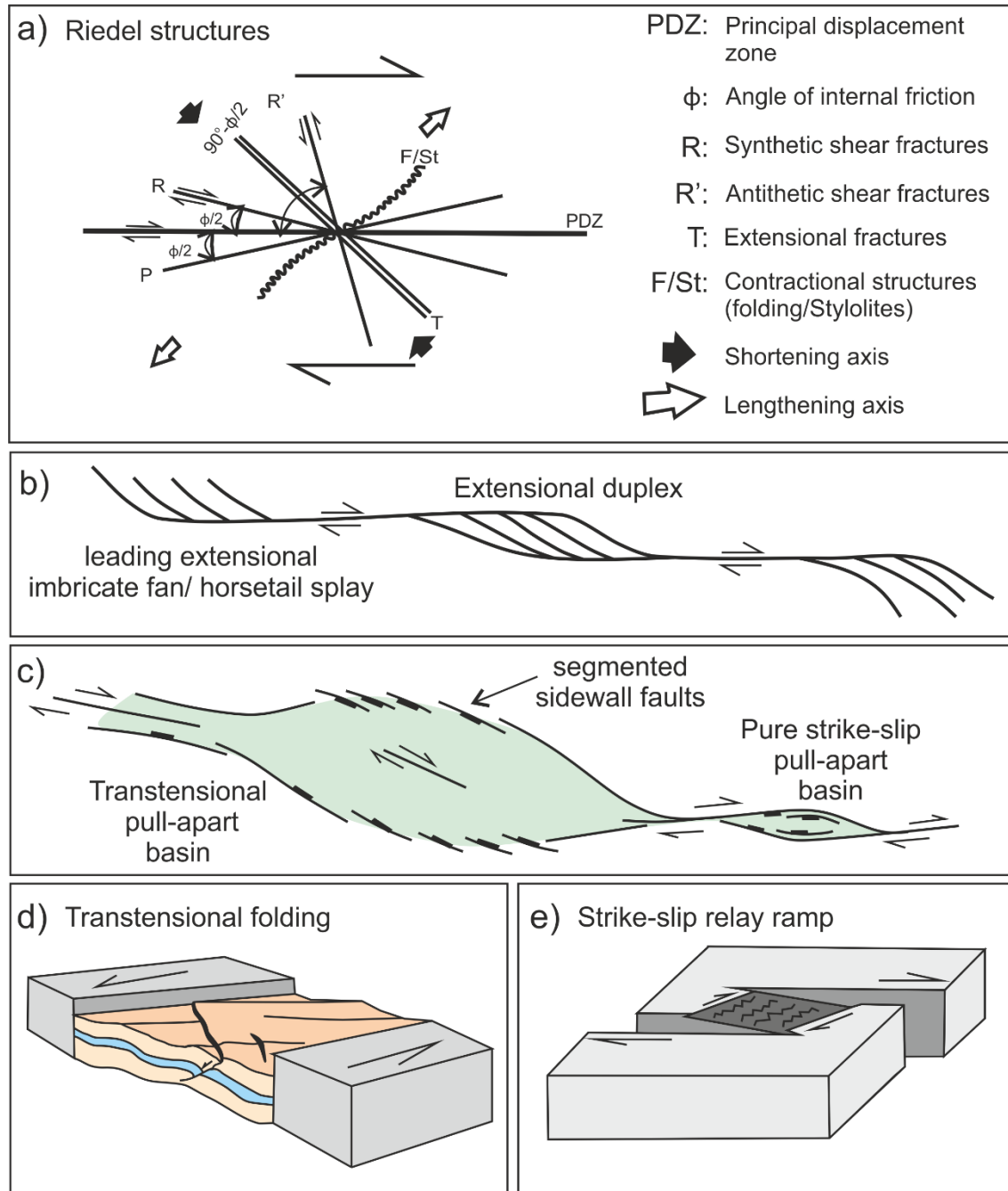
Table 2-1: Differences between dip-slip (normal) and strike-slip faults (Barnett et al., 1987; Diabat et al., 2004; Elliott, 1976; Jackson & McKenzie, 1983; Sylvester, 1988; Walsh & Watterson, 1991; Watterson, 1986; Wu et al., 2009).	20
Table 3-1: Velocity model with the average interval velocities and densities used in this study for the depth conversion and the gravity models, respectively, and the GUMBO lines 3 and 4 velocity models derived by refraction data (Christeson et al., 2014; Eddy et al., 2014).	80
Table 4-1: Sequence's depth based on published wells in the Ghanaian margin (Attoh et al., 2004; IHS, 2010; Adda et al., 2015).	112
Table 4-2: Key seismic facies and reflection relationships for the crustal type "Oceanic crust" (Oc) and "Magmatic crust" (Mc). Highlighted in red indicates the specific reflections of interest. Highlighted in blue indicates the reflections that are not directly linked to the oceanic crustal type. ..125	
Table 4-3: Key seismic facies and reflection relationships for the crustal type "Continental crust" (Cc). Highlighted in red indicates the high amplitude reflections in the crust. Highlighted in grey indicates the low amplitude reflections in the crust.	126
Table 4-4: Summarised table of the different velocities and the applied density values of each unit. The asterisk (*) indicates the units where typical values were applied for the depth conversion and the gravity models. 136	
Table A-1: Field data from the Ait Attab region, locality (a). The shear interpretation corresponds to the overall kinematic and not individually each Riedel structure. 226	
Table A-2: Field data from the Ait Attab region, locality (b). The shear interpretation corresponds to the overall kinematic and not individually each Riedel structure. 226	
Table A-3: Field data from the Ait Attab region, localities (c-d). The shear interpretation corresponds to the overall kinematic and not individually each Riedel structure. 227	
Table A-4: Field data from the Ait Attab region, localities (e-f). The shear interpretation corresponds to the overall kinematic and not individually each Riedel structure. 228	
Table A-5: Field data from the Ouaouizaght region, locality (a).229	
Table A-6: Field data from the Ouaouizaght region, localities (b-c). The shear interpretation corresponds to the overall kinematic and not individually each Riedel structure.229	
Table A-7: Field data from the Ouaouizaght region, localities (d-e).230	
Table A-8: Field data from the Ouaouizaght region, locality (B.1).230	
Table A-9: Field data from the Zawyat-Ahancal region.231	
Table A-10: Field data from the Agoudal region, locality (a).233	
Table A-11: Field data from the Agoudal region, localities (b-d).233	
Table A-12: Field data from the Agoudal region, locality (e).235	
Table A-13: Field data from the Er-Rich region, localities (a-c).237	
Table A-14: Field data from the Er-Rich region, localities (d).240	

Table A-15: Field data from the Bou Annane region.....241

List of terminology

- a) **Riedel structures:** developed under simple shear and simple sheared influenced settings (Riedel, 1929; Sylvester, 1988). These structures include different fractures and structures of antithetic and synthetic fractures, both extensional and contractional structures, developed based on the shortening and lengthening axis and the principal zone of displacement. They can be recognised based on the angle of internal friction (Figure i.a). Observations of these structures span from microscopic to megascopic scales (e.g., Aydin and Page, 1984; Pucci et al., 2007; Rao et al., 2011; Stanca et al., 2022) and are crucial for identifying shear.
- b) **Duplexes:** Duplexes of strike-slip faults, along with the development of pull-apart basins at the realising bends and uplifting push-ups at restraining bends, can be observed in an oblique system (Crowell, 1974; Mann et al., 1983). Lateral involvement of duplexes can lead to the development of imbricate fans (Woodcock and Fischer, 1986) or **horsetail splays/terminations** (Figure i.b).
- c) **Sidewall extensional faults:** Extensional faults appear in a transtensional pull-apart basin (Figure i.c), they appear fragmented, and are linked to the principal displacement zone (e.g., Burchfiel and Stewart, 1966; Crowell, 1974; Mann et al., 1983; Christie-Blick and Biddle, 1985; Woodcock and Fischer, 1986; Sylvester, 1988; Mann, 2007; Wu et al., 2009; Corti et al., 2020; Farangitakis et al., 2020).
- d) **Folding under transtension:** Appears in a transtensional setting, oblique to the shear (Figure i.d), which occurs concurrently with normal faulting (Fossen et al., 2013).
- e) **Relay ramps:** relay ramps can be formed not only under pure shear but also under contractional and oblique extensional or contractional settings (Figure i.e; Peacock and Sanderson, 1995).
- f) **Marginal Ridge:** In transform margins, a marginal ridge may be associated with the transform fault, and underlines a sharp contrast at the oceanic-continental boundary (Basile et al., 1993). Vertical displacements along the transform faults may explain their formation (Basile, 2015). These may have been developed due to transportation of thick continental

crust within the transform fault (Le Pichon & Fox, 1971), or crustal thickening due to transpression (Attoh et al., 2004; Huguen et al., 2001) or due to lateral heat transfer from the oceanic crust to the continental across the transform fault (Basile, 2015).



(a) Riedel structures (after Riedel, 1929; Sylvester, 1988). (b) Duplexes and horsetail splays (after Woodcock and Fischer, 1986). (c) Pure strike-slip pull-apart basin and transtensional pull-apart basin with the identical extensional sidewall faults (after Wu et al., 2009). (d) Oblique folding under a transtensional regime (after Fossen et al., 2013), and (e) relay ramps formed under a strike-slip regime (Peacock & Sanderson, 1995).

Chapter 1 – Introduction

1.1 Motivation

Understanding the tectonic processes related to the continent formation can provide insights on Earth's history. A part of the continents' elements are the rifts and rifted systems, which influence the geomorphology, the climate, the biodiversity, and the economy, and provide insights on the natural hazards, and the processes related to the formation of oceanic basins (e.g., Judd et al., 2002; Minshull, 2002; Donnadieu et al., 2016; Brune, 2016).

Various models have been developed to explain the formation of rifts and oceanic basins (Biari et al., 2021) however, the majority of them assume orthogonal extension with little consideration for the role of obliquity (Brune et al., 2018), even though it is common to many continental and oceanic regions and it is associated with divergent plate boundaries worldwide. Divergent margins can be categorised into two main types: "*rifted*" or "*passive*", and "*transform*" margins (Figure 1.1). Rifted margins are further classified based on magma supply into "*magma-poor*" or "*magma-rich*" categories, each displaying different processes, features, and transitional crusts.

1.1.1 Rifted margins

In magma-rich margins, the magma supply is sufficient to form a magmatic transitional crust, known as Seaward Dipping Reflectors (SDR; e.g., Paton et al., 2017). In contrast, magma-poor margins exhibit different processes. Rifting is slower than in magma-rich margins, allowing for continental hyperextension, possible transitional crust with mantle exhumation, and the development of thinner oceanic crust (Figure 1.1A; e.g., Doré & Lundin, 2015; Franke, 2013; Peron-Pinvidic et al., 2013; Sutra & Manatschal, 2012). While, in transform margins, there is direct contact between the continental and oceanic crusts (Figure 1.1B; e.g., Loncke et al., 2020; Mercier de Lépinay et al., 2016) with an uncertain presence of transitional crusts.

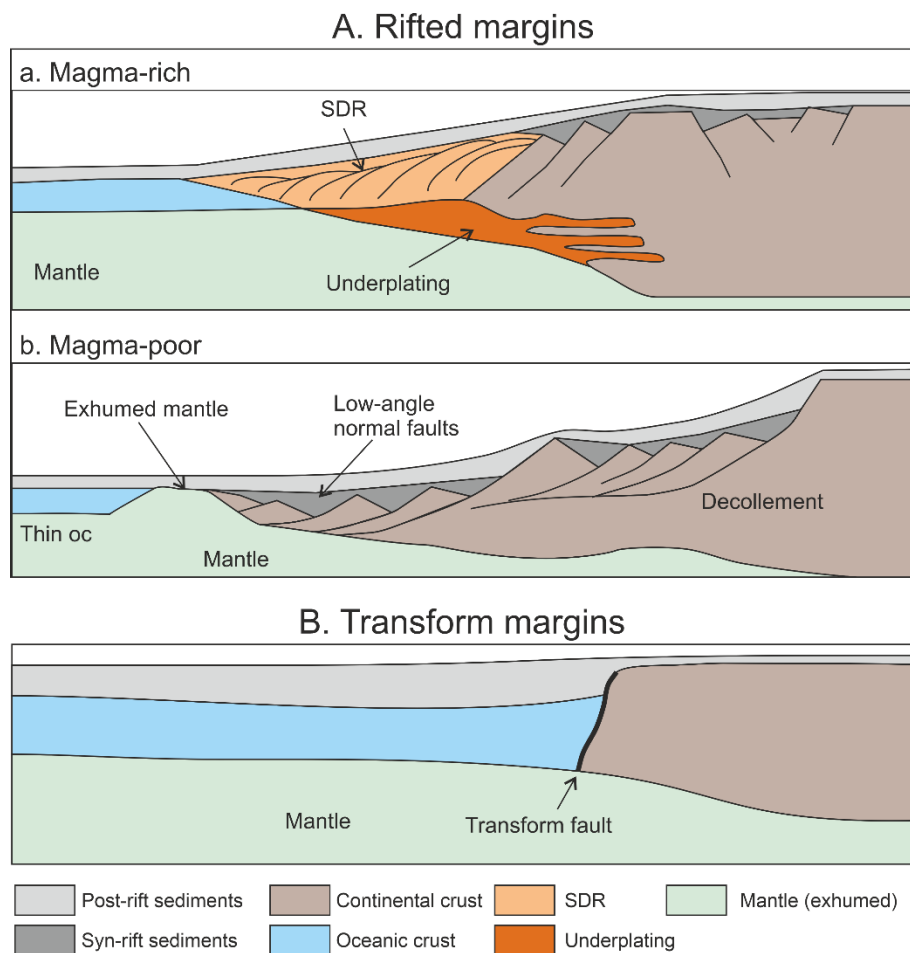


Figure 1.1: Indicative cross-sections with the rifted (Aa-b) and transform (B) margins (Doré & Lundin, 2015; Franke, 2013; Lister et al., 1991; Loncke et al., 2020; Mercier de Lépinay et al., 2016; Peron-Pinvidic et al., 2013; Planke & Eldholm, 1994; Sutra & Manatschal, 2012).

1.1.2 Oblique divergent systems

The initial consideration of strike-slip faults can be tracked back to Wegener's continental drift theory in the 1912, and was introduced as an official term by Reid et al. (1913). Since then a series of various studies focused on the oceanic domain and the oceanic transform faults (Heezen, 1960; Heezen, Bunce, et al., 1964; Heezen, Gerard, et al., 1964; Heezen & Tharp, 1965), as well as the context of sheared margins (Masclé, 1976; Scrutton, 1979; Wilson, 1965).

Masclé (1976) and Scrutton (1979) introduced the term “transform margin” as an alternative to continental margin, as the shear observed did not conform to the established margin distinction of Atlantic (passive continental) and Pacific (active continental-subduction) classifications. These types of margins accommodate at

some point during their evolution strike-slip motion through transform faults at the plate boundaries (Masle, 1976; Scrutton, 1979).

A few approaches to distinguish the strike-slip faults were adopted by Woodcock (1986) and Sylvester (1988). Woodcock's classification of strike-slip faults outlines four distinct categories based on the structures they connect at the plate boundaries (Figure 1.2). Woodcock's classification primarily concentrates on convergent plate boundaries, assuming that strike-slip faults in divergent boundaries are well understood:

1. Ridge transforms: These strike-slip faults link spreading ridges and appear at the boundaries of oceanic-oceanic crusts (e.g., Owen, Romanche, Charlie Gibbs fracture zones), but can also be active during early rifting.
2. Boundary transforms: Occurring at continental-continental, continental-oceanic, and rarely at oceanic-oceanic boundaries, these strike-slip faults form integral components of plate boundaries (e.g., San Andreas, Alpine fault).
3. Trench-linked strike-slip faults: Found within plates at oblique subduction zones, these faults are associated with local arc intrusions and volcanic rocks (e.g., Semanko, Median Tectonic line).
4. Indent-linked strike-slip faults: Similarly to the previous category, these faults emerge within the continental domain and are associated with intra-continental shortening.

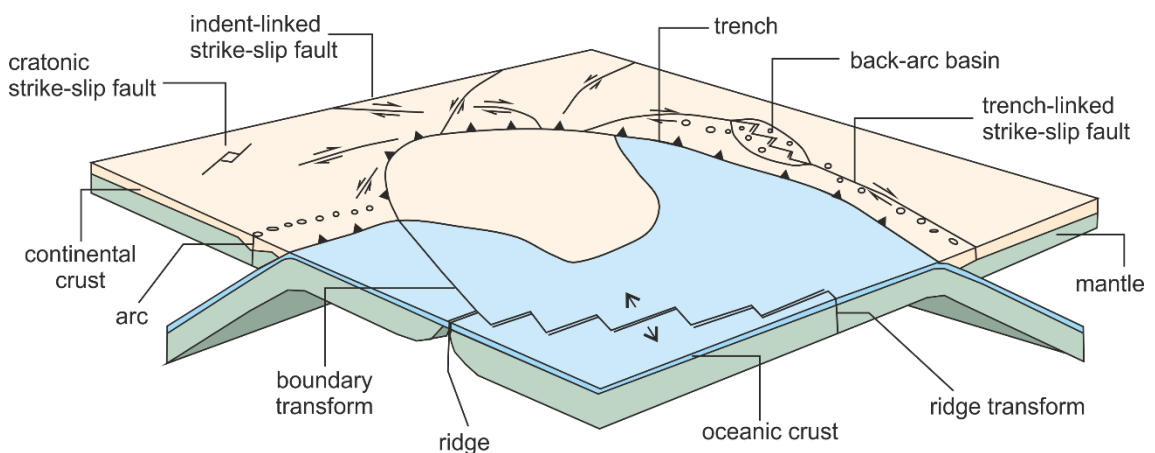


Figure 1.2: Schematic sketch of strike-slip faults at the plate boundaries, the cratonic continental and oceanic crusts (after Woodcock, 1986; Mann, 2007).

In addition to Woodcock's classification, Mann (2007) incorporated cratonic continental strike-slip faults, encompassing pre-existing crustal faults. While, Sylvester (1988) introduced the terms of "transtension" and "transpression", introducing the concept of obliquity into the systems.

Only recently more studies (Basile, 2015; Brune, 2014; de Souza Rodrigues et al., 2023; Farangitakis et al., 2019; Loncke et al., 2020; Markwick et al., 2022; Mercier de Lépinay et al., 2016; Nemčok, Rybár, et al., 2016; Nemčok et al., 2023; Philippon & Corti, 2016; Yassin et al., 2017; Ye et al., 2017; Zwaan et al., 2016) have been focusing on the oblique divergent tectonic settings due to the oilfield discoveries of Ghana and Guyana (Dailly et al., 2017; Maia de Almeida, Alves, Filho, Freire, de Souza, Leopoldino Oliveira, et al., 2020; Maia de Almeida, Alves, Filho, Freire, de Souza, Normando, et al., 2020; Tetteh, 2016). Due to their complexity, strike-slip influenced divergent systems lack of the structures evolution, and their influence on the crusts' under the tectonic regime, in contrast to the convergent systems, where the strike-slip framework development is better studied (Figure 1.2; Woodcock, 1986; McClay and Massimo, 2001; Noda, 2013).

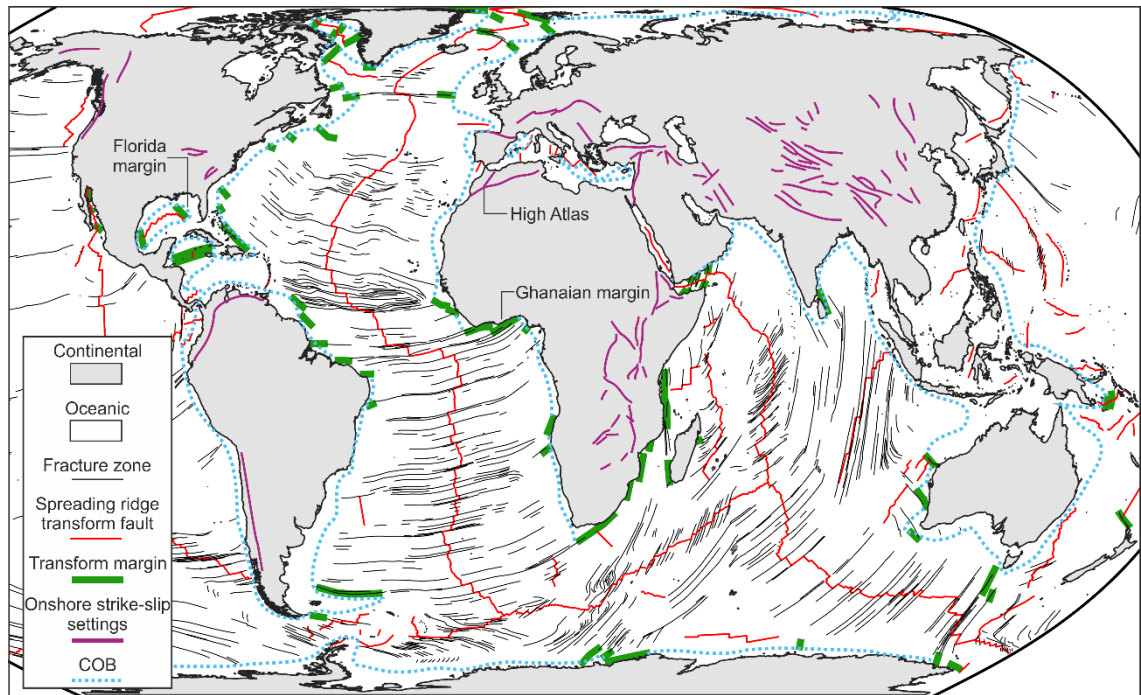


Figure 1.3: Transform margins and onshore strike-slip setting across the world (after Chorowicz, 2005; Mann, 2007; Mercier de Lépinay et al., 2016). Fracture zones from Müller et al. (2008) and Matthews et al. (2011), and Continental-Oceanic Boundary (COB) from Exxon World Mapping Project (1985). High Atlas – discussed in Chapters 2 and 5; Florida margin – discussed in Chapters 3 and 5; and Ghanaian margin – discussed in Chapters 4-5.

Globally (Figure 1.3), one-third of the margins are activated with low obliquity, ranging from 0° to 30° , another third with moderate obliquity (30° to 60°), and 40% of the margins accommodate high obliquity, falling between 60° and 90° (Philippon & Corti, 2016) and 16% of the continental margins are classified as transform margins (Mercier de Lépinay et al., 2016). Jeannot and Buitier (2018) re-evaluated these number and proposed that 26 major conjugate rift systems that they studied worldwide have experienced obliquity, while Brune et al. (2018) proposed that 70% of the rift systems involved obliquity higher than 20° , and the global average in terms of rift obliquity is 34° . Examples of present day oblique active rift systems include the Ethiopian Rift (Corti, 2008) and the Gulf of California (Bennett & Oskin, 2014; Lizarralde et al., 2007). Passive transform margins include the conjugate margins of the Agulhas Bank and Falklands Plateau (Ben-Avraham et al., 1993) in South Atlantic, the Equatorial Atlantic's conjugate margins (Basile, 2015), the East African-Madagascar-Antarctica (Marks & Tikku, 2001), the Antarctica-Australia conjugate margins (Dalziel,

1991), the Gulf of Aden (e.g. Beydoun, 1970) and the Red Sea (Daggett et al., 1986).

While extensive information exists regarding contractional strike-slip settings, the principal objective of this study is to deepen our understanding of strike-slip deformation in divergent settings. This project is a contribution to the current knowledge base of strike-slip extensional settings by focusing on the role of strike-slip faults in rifts and rifted margins, examining their interaction with the various crustal types, and investigating the tectonostratigraphic relationship within oblique systems.

1.2 Research questions

This piece of research aims to address the following questions:

1. How do strike-slip faults influence the tectono-stratigraphy in oblique extensional settings and what are the key differences with orthogonal extension?
2. How does the stress regime vary locally during oblique extension?
3. What is the relationship between magmatism and strike-slip tectonics?
4. How do pre-existing structures influence the evolution of the oblique extensional systems?
5. Do the identified findings encompass generic strike-slip characteristics that can be applied to other divergent oblique settings?
6. What are the differences between rifted and transform margins?
- 7.

1.3 Approach – Study localities

In order to examine the tectono-stratigraphic, crustal and stress variation characteristics that appear in strike-slip extensional settings, the study investigates three localities (Figure 1.3), each using a different approach:

1. High Atlas, Morocco. The field-based case study focuses on the inverted aborted rift system of Atlas in NW Africa, with a specific emphasis on investigating the proposed transtensional tectonic event and the former orthogonal rifting (Ellouz et al., 2003; Escosa et al., 2021; Fernandez, 2019).
2. Florida margin, Eastern Gulf of Mexico. The study area explores the presence of strike-slip fault activity during rifting, previously characterized as a transform margin (Figure 1.3; Pindell and Kennan, 2009; Pindell et al., 2021) by utilising 2D seismic reflection and gravity data.
3. Ghanaian margin, Equatorial Atlantic. Ghanaian margin represents a stereotypical transform margin (Antobreh et al., 2009; Basile et al., 1998; Mascle & Blarez, 1987; Sage et al., 2000). The study utilises 2D seismic reflection and gravity data.

1.4 Thesis structure

The thesis is structured in five chapters. Three of these compromise result chapters, structured as a series of “journal-style” research papers due to the different study areas, approach, and their individual geological backgrounds. Chapter 2 discusses the structural framework, the tectono-stratigraphy and paleostress analysis during the orthogonal extension and subsequent transtensional tectonic events. Lastly, this chapter explores the role of pre-existing structures in the evolution of the rift system. Chapter 3 investigates the presence of strike-slip fault activity during the rifting in the Florida margin. Chapter 4 focuses on discussing the crustal architecture, tectonic framework, and the tectonic processes of the Ghanaian transform margin, which comprises orthogonal, oblique extension and oblique contraction. This analysis is conducted in alignment with the conjugate NE Brazilian margin. Chapter 5 encompasses the thesis discussion and summarises the findings from the three different result chapters. It presents an updated conceptual 3D model of strike-slip tectonics (Figure 1.2), tectono-stratigraphic characteristics that can be found in strike-slip tectonic settings. It describes the differences between rifted and transform margins, and integrates the research areas interpretation on the Pangaea’s break-up. Additionally, it addresses the research questions posed in Section 1.2. Lastly, it suggests future work on strike-slip extensional systems, and it outlines the key finding.

As stated in the declaration, Chapter 3 has been published in the Journal of the Basin Research and subsequently incorporated in the thesis by adding a further discussion.

Chapter 2 – Moroccan High Atlas: The case study on strike-slip influenced rifted systems

Summary

The failed Atlas rift system in NW Africa formed during the Mesozoic Pangaea break-up and experienced inversion during the Cenozoic Alpine orogeny. Despite the well-studied inversion, the Late Triassic-Jurassic rifting remains poorly understood. The rifting, synchronous with the Atlantic and Tethyan opening, reactivated pre-existing Hercynian structures. Reconstruction of the Atlantic-Tethyan triple junction suggests orthogonal extension in the early stages and sinistral transtension in the Middle Jurassic. The well-exposed stratigraphy of the High Atlas, weakly deformed by the Alpine orogeny, offers an ideal opportunity to study extensional systems influenced by strike-slip tectonics.

This study utilised field data focusing on metre-to-kilometre scale outcrops in the Central and Eastern High Atlas, examining structures and sediment-structure relationships across the failed rift. It investigates the degree of obliquity in the Early and Middle Jurassic sequences and analyses the reactivation of pre-existing structures and the development of new ones, along with strain variations along the system.

Results indicate that extension was orthogonal during the Triassic to Early Jurassic, transitioning to oblique extension in the Middle Jurassic, with an uncertain cessation time. Paleostress analyses indicate a consistent stress regime during the orthogonal extension, but lateral stress variation during the oblique extension, leading to localised orthogonal extension, transtension, and strike-slip with contractional features. Lastly, the results unveil the reactivation of Hercynian structures in both phases, the reactivation of normal faults as strike-slip faults, and the development of minor structures during the later extensional phase.

2.1 Introduction

The evolution of divergent margins has traditionally been examined along regional 2D profiles enabling the understanding of margin architecture and fault development during the rifting process (e.g., McKenzie, 1978; White, 1993; Whitmarsh, Manatschal and Minshull, 2001; Ranero and Pérez-Gussinyé, 2010; Peron-Pinvidic, Manatschal and Osmundsen, 2013; Brune *et al.*, 2017; Naliboff *et al.*, 2017). This approach emphasised the role of orthogonal extension at the expense of the oblique component. However, over the last few years, research has stressed the importance of obliquity, which is almost always present in rifts and rifted margins (e.g., Brune *et al.*, 2018), due to the relative oblique motion of tectonic plates and the irregularities in plate boundaries (Díaz-Azpiroz *et al.*, 2016; Philippon & Corti, 2016). Thus, it is essential to recognise the role of obliquity during the different rifting phases, identify the stress pattern laterally, and understand the impact of both pre-existing and newly formed features on the final structural architecture.

Acknowledging the changing view of rift margins with a growing focus on obliquity, this study specifically delves into this aspect. The High Atlas, located in NW Africa, is an intracontinental fold and thrust belt extending from Morocco to Tunisia (Figure 2.1A). It is an aborted Triassic to Jurassic rift that was inverted during the Cenozoic Alpine orogeny (Ellero *et al.*, 2020; Ellouz *et al.*, 2003; Escosa *et al.*, 2021; Frizon de Lamotte *et al.*, 2008, 2009; Leprêtre *et al.*, 2018). The High Atlas presents a unique opportunity to study extensional systems influenced by strike-slip tectonics, as the well-exposed syn-rift basins in this region are still well preserved and have experienced relatively weak deformation during their inversion (Ellouz *et al.*, 2003; Frizon de Lamotte *et al.*, 2008; Laville *et al.*, 2004; Piqué *et al.*, 2002).

The Atlas rifted system formed during the Mesozoic breakup of Pangaea and was subsequently inverted during the Alpine Orogeny (Ellero *et al.*, 2020; Ellouz *et al.*, 2003; Escosa *et al.*, 2021; Frizon de Lamotte *et al.*, 2008; 2009; Leprêtre *et al.*, 2018). While the inversion and the orogeny build-up have been extensively studied (e.g., Frizon de Lamotte *et al.*, 2008, 2009, 2011; Leprêtre *et al.*, 2015, 2018; Fekkak *et al.*, 2018), the Late Triassic to Jurassic rifting, which coincided with the opening of the Atlantic and the Tethys Oceans, remains ambiguous. Previous studies propose that true orthogonal rifting occurred in the Late Triassic

to Early Jurassic, followed by a prolonged phase of oblique extension (Biddle & Christie-Blick, 1985; El Kochri & Chorowicz, 1996; Ellouz et al., 2003; Escosa et al., 2021; Frizon de Lamotte et al., 2008; Laville, 1985; Laville et al., 2004; Laville & Petit, 1984; Mattauer et al., 1977). A few tectonic reconstruction models (e.g., Ellouz et al., 2003; Fernandez, 2019; Escosa et al., 2021) suggest that NE-SW and ENE-WSW Hercynian faults were reactivated under sinistral transtensional tectonics (Laville et al., 2004) driven by the movement between Africa and Iberia in the Middle Jurassic. Despite various analyses and models, little is known (El Kochri & Chorowicz, 1996) about the regional-scale influences on the rift system during this transtensional event.

This study focuses on the Central and Eastern High Atlas of Morocco (Figure 2.1A) and aims to characterise the orthogonal and the oblique extensional phases that shaped the Atlas system during the Mesozoic. To achieve this, the study's objectives are as follows:

1. Evaluate stratigraphic architectures to identify evidence of active rifting and characterize the geometry of structures developed during the Late Triassic to Early Jurassic extensional phase.
2. Investigate the hypothesis of an oblique extensional phase during the Middle Jurassic and explore the kinematics and the geometry of structures active during this phase, while also examining any stress variations along the Atlas system's length.
3. Determine how pre-existing orthogonal rift-related structures influenced Middle Jurassic deformation, by analysing structural, kinematic, and stratigraphic data.
4. Develop an updated tectonic model that incorporates field observations for both orthogonal and oblique extensional phases.

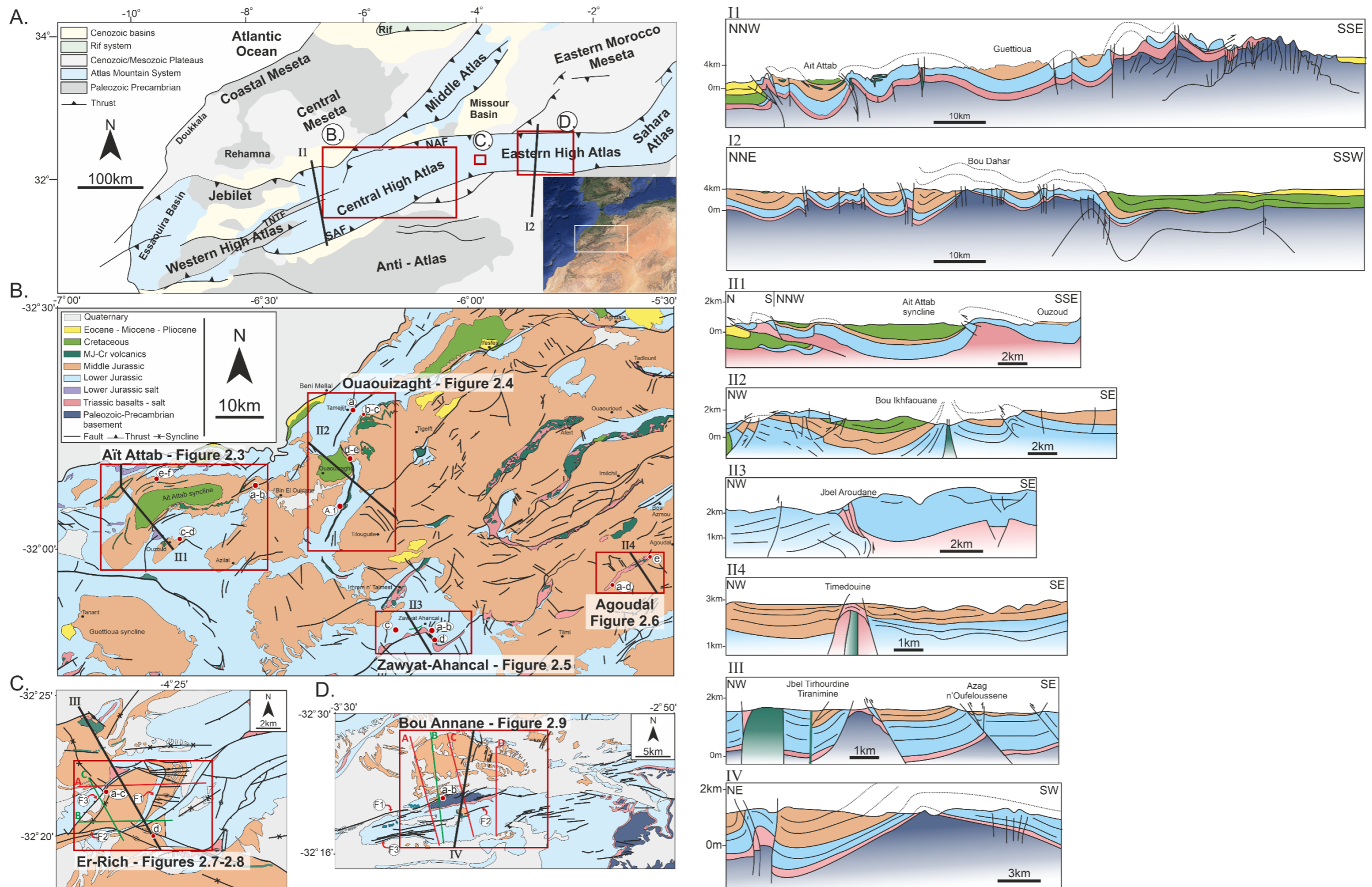


Figure 2.1: A. Schematic regional geological map of Morocco, NW Africa, which displays the main units and structures, and the outcrop localities in the Central and Eastern High Atlas. SAF: South Atlas Fault; NAF: North Atlas Fault (modified from Hafid *et al.*, 2006). Geological maps of the Central and Eastern High Atlas with the selected outcrops of key localities 1-4 in B, locality 5 in C, and locality 6 in D and their equivalent cross-sections; bold black transects (I-IV) (after Rolley and Etienne, 1978; Monbaron, 1985; Jenny, 1988; Jossen, 1988; Du Dresnay *et al.*, 1997; Milhi, 1997; Fadile, 2003; Baidder *et al.*, 2018). Green transects indicate cross-sections based on fieldwork measurements and geological maps, whilst red transects are only based on geological maps. (F) indicates the studied faults on the cross-sections in figures 2.7 and 2.9.

2.2 Background

The High Atlas Mountains have a complex geological history shaped by multiple tectonic phases (Figure 2.2). Three significant tectonic events have marked the region:

(1) The Late Palaeozoic Hercynian orogeny (Figure 2.2A-a), occurred from the Cambrian to the Carboniferous, led to the formation of NE-SW and ENE-WSW trending structures, and formed the structural template for the Atlas rift system (Beauchamp, 1988; Frizon de Lamotte *et al.*, 2015; Laville & Petit, 1984; Laville & Piqué, 1992; Michard *et al.*, 2008; Piqué *et al.*, 2002). During this phase, the lithospheric zone of Atlas (ASZ; Figure 2.2A-a) was developed, which later marked the southern boundary of the Moroccan microplate (Ellero *et al.*, 2020; Kroner & Romer, 2013; Labails *et al.*, 2010; Michard *et al.*, 2010; Muttoni *et al.*, 2003; Schettino & Turco, 2009, 2011).

(2) The Atlas rift system evolved through two main stages. The first stage might have started as early as late Permian to Early Triassic (Figure 2.2B; dotted blue line), but it mainly influenced the region during the Late Triassic – Early Jurassic (Ellouz *et al.*, 2003; Fernandez, 2019; Frizon de Lamotte *et al.*, 2008; Lachkar *et al.*, 2009). This rifting phase was a result of the simultaneous opening of the Central Atlantic and the Tethys, in the west and the north, respectively (Figure 2.2A-b; Laville and Piqué, 1991; Charriere, 1996; Ellouz *et al.*, 2003; Frizon de Lamotte *et al.*, 2008; Fernandez, 2019). This resulted in the reactivation of the pre-existing NE-SW and N-S Hercynian structures (Ellouz *et al.*, 2003; Frizon de Lamotte *et al.*, 2008, 2011, 2015). The co-existence of Tethyan and Central Atlantic rifting makes it challenging to identify the temporal and spatial influences on the Atlas domain (Ellouz *et al.*, 2003; Huon *et al.*, 1993). During the rifting, the Atlas system accumulated interbedded Central Atlantic Magmatic Province (CAMP) sequences with Triassic evaporites and Lower Jurassic carbonates (CAMP, Figure 2.2B; e.g., Marzoli *et al.*, 2019; Escosa *et al.*, 2021).

In the Early Jurassic, despite ongoing Central Atlantic opening, it has been suggested that the Atlas rifting was aborted, and thermal subsidence led to the formation of a carbonate platform during the Toarcian (upper Early Jurassic; e.g., Ellouz *et al.*, 2003; Laville *et al.*, 2004; Hafid *et al.*, 2006; Frizon de Lamotte *et al.*, 2008, 2009, 2011; Moragas *et al.*, 2018). This post-rift phase of the Atlas rift

system was characterised by the continuous separation of Africa from America and the Tethyan opening and Africa's plate movement towards the south, which eventually ceased in the Early Cretaceous (Fernandez, 2019; Laville et al., 2004). This movement triggered a transtensional tectonic regime in the Atlas system, involving sinistral motion along pre-existing NE-SW and ENE-WSW structures (Ait Brahim et al., 2002; El Kochri & Chorowicz, 1996; Ellouz et al., 2003; Laville, 1985; Laville & Piqué, 1991; Laville et al., 2004; Piqué et al., 2002; Schwarz & Wigger, 1988). These sinistral strike-slip faults would have accommodated transtension and contributed to the development of pull-apart basins (Laville, 1988; Laville & Piqué, 1992; Mattauer et al., 1977; Schaer & Rodgers, 1987).

The later event of potential transtension has been associated with Middle Jurassic to Cretaceous magmatism (Calvín et al., 2018; Laville, 1988; Laville et al., 2004), linked to mantle upwelling (Allouban et al., 2021; Bensalah et al., 2013; Essaifi & Zayane, 2018; Moratti et al., 2018) and the formation of lava flows, sills and dykes, and it is considered to have implications on the geodynamic model of the Atlas evolution. The magmatism could either be related to the extensional regime (Bensalah et al., 2013; Laville et al., 1994) or to mantle upwelling (Bensalah et al., 2013; Frizon de Lamotte et al., 2009; Moratti et al., 2018). In addition, they might be related to the reactivation of pre-existing structures (Bensalah et al., 2013), where mantle upwelling formed antiformal ridges (Laville and Piqué, 1991, 1992; Ellouz et al., 2003). The age of the magmatic event is poorly constrained and still debated. Geochemical, structural, and paleomagnetic data suggest a Middle-Late Jurassic age (Armando, 1999; Bensalah et al., 2013; Calvín et al., 2017; Charrière et al., 2005; Essaifi & Zayane, 2018; Hailwood & Mitchell, 1971) or Early Cretaceous in age (Bensalah et al., 2013; Moratti et al., 2018). In the case of the Early Cretaceous activity, the antiformal ridges observed in sediments (Laville and Piqué, 1991, 1992; Ellouz et al., 2003) are likely to be related to either salt tectonics (Calvín et al., 2018; Martín-Martín et al., 2017; Moratti et al., 2018; Saura et al., 2014; Vergés et al., 2017) or the local stress that influenced the NE-SW trending strike-slip faults with step-over geometries (e.g., Laville, 1985; Laville and Piqué, 1992; Piqué et al., 2002; Laville et al., 2004).

(3) The final phase involved the counter-clockwise rotation of the African plate and its collision with the Iberian-European plate (Figure 2.2A-c), resulting in the progressive closure of Tethys and inversion of the Atlas system (e.g., Frizon de

Lamotte *et al.*, 2000, 2009; Teixell *et al.*, 2003). The inversion phase began in the Late Cretaceous and extended into the present. The major shortening events occurred in the Oligocene-Miocene with the Alpine orogenic event, leading to a complex transpressional system with dextral movement in the Atlas region (e.g., Ait Brahim *et al.*, 2002; Ellero *et al.*, 2012, 2020).

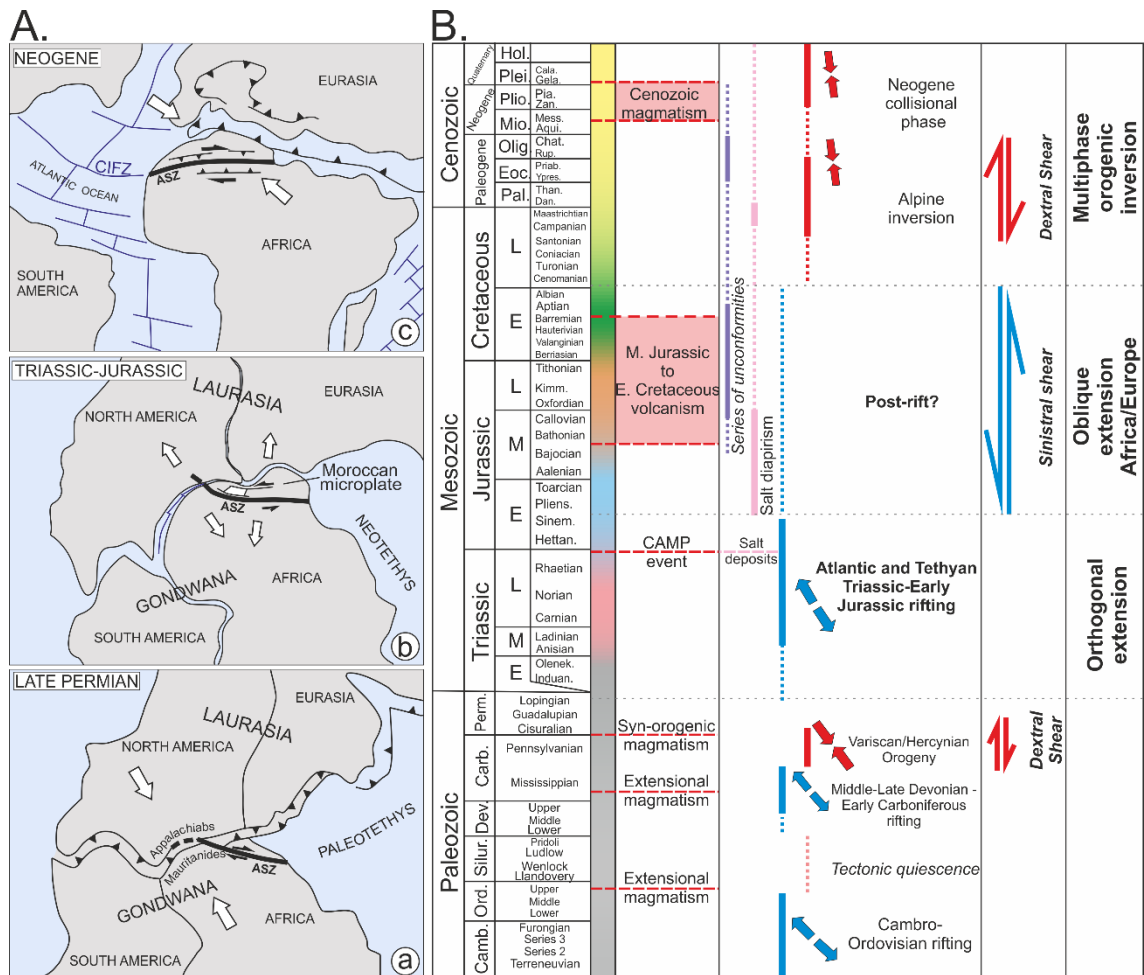


Figure 2.2: A. Main tectonic events during the evolution of the Atlas region, with Pangaea formation (a) and break-up (b), followed by the convergence of Africa and Eurasia (c) (modified from Arthaud and Matte, 1977; Muttoni *et al.*, 2003; Schettino and Turco, 2011; Kroner and Romer, 2013; Ellero *et al.*, 2020). ASZ: Atlas Shear Zone; CIFZ: Canary Islands Fracture Zone. B. Tectonostratigraphic column capturing the main tectonic events in the High Atlas, Morocco (modified from Ellouz *et al.*, 2003; Walker *et al.*, 2018; Escosa *et al.*, 2021).

2.3 Methodology

This study utilises field data, which were collected during two field seasons in 2021 and 2022, and published geological maps of Morocco with map scales ranging from 1/50,000 to 1/200,000 (Figure 2.1B-D; Rolley and Etienne, 1978; Monbaron, 1985; Jenny, 1988; Jossen, 1988; Du Dresnay *et al.*, 1997; Milhi, 1997; Fadile, 2003; Baidder *et al.*, 2018). Most of the outcrop areas have been mapped at the 1/100,000 scale.

Here, detailed field observations from six localities are presented to illustrate their structural configuration, tectonic evolution, and implications for the wider kinematics of the Central and the Eastern High Atlas. These localities are, from west to east (Figure 2.1B-D):

1. the Aït Attab syncline;
2. the Ouaouizaght syncline;
3. the Zawyat - Ahancal region;
4. the Timedouine ridge in the Agoudal region;
5. the Azzag basin, in the Er-Rich region; and
6. the region of Bou Annane.

The studied localities include Triassic and Jurassic sequences which have previously been interpreted as being deposited during the extensional phase (e.g., Ellouz *et al.*, 2003) in the Atlas evolution. They illustrate the relationship between the Lower and the Middle Jurassic, as well as any possible relationship with pre-existing Paleozoic basement structures. In the localities, the upper part of the Lower Jurassic is distinguished, when thermal relaxation is proposed to have occurred (e.g., Ellouz *et al.*, 2003; Laville *et al.*, 2004; Hafid *et al.*, 2006; Frizon de Lamotte *et al.*, 2008, 2009, 2011; Moragas *et al.*, 2018) and different structures have been identified. Outcrops were also selected to assess whether there is an associated magmatic activity in the Central High Atlas during the transtensional event, and aiming to identify any relationship with the strike-slip faults.

For each locality, analysis on the sediment-structure interaction was performed for the Lower and/or Middle Jurassic beds to identify if they got influenced by any orthogonal or oblique extension, identified in growth strata against structures. This occurred on both mesoscopic and megascopic scales, encompassing both

outcrop-level and kilometre-scale perspectives. The Triassic sequence was excluded due to the nature of pillow lavas and altered red lacustrine beds, which did not provide any information. Due to the reactivation of the regional scale faults along with the nature of the beds, in the Central High Atlas, they usually appear as geomorphic valleys, where there is a stratigraphic and structural variability in the opposite flanks of these valleys.

Due to the lack of physical regional scale faults, observations and measurements were mostly focused on mesoscopic scale faults and their kinematic characteristics of fault-slip data and slickensides, Riedel structures identified in bedding, and growth strata. The tectonic measurements were then integrated to distinguish the tectonic regime for each sequence. In addition, paleostress analysis was carried out using Win-Tensor software (Delvaux & Sperner, 2003) and the Angelier (1984) method from multiple waypoints laterally distributed for each locality.

Due to the multi-phase history of the High Atlas, faults were divided based on their characteristics (trends, kinematics), even if not fully consistent due to different deformation along the study area. The differentiation between normal fault, pure strike-slip fault, and strike-slip with dip-slip in the field (Table 2-1) relies on several distinct characteristics. These include kinematic indicators and sediments-structure relationship. Normal faults show typical wedge geometry growth strata, while strike-slip faults show thickness variation on the either side of the fault. Strike-slip faults demonstrate limited formation of the typical growth strata, which appear more sub-horizontal in nature (Wu et al., 2009). Flower structures and splays that feature a central strike-slip fault surrounded by normal sidewall faults (refer to terminology list), and lastly the shear plunge in the fault plane where present. If the faults are lacking the previous characteristics, were interpreted based on the consistency in the interpreted faults. The aforementioned bedding and structures were restored based on an average bedding measurement of the locality's youngest unit, which is usually Cretaceous or Middle Jurassic. Each locality's interpretation is based on the field data, metre-to-kilometre-scale cross-sections and their restored sections, and the interpretation of the laterally distributed structures in space and time. The measurement format presented here is dip direction (azimuth) and dip.

Furthermore, during the interpretation, the structures associated with the orogenic event were ignored, emphasising the presentation of primarily pre-orogenic features. Indicative features are presented in the Ouauizaght region (Figure 2.4b-c). Typically, the orogenic related structures appear undeformed, constituting the most recent generation in cross-cut tension gashes, Riedel structures often indicating dextral movement along NNW-SSE trending structures, aligning with the regional NW-SE trend of contraction (Figure 2.2A-c). A paleostress analysis using Win-Tensor was conducted to clarify the contractional stress regime controlling these structures.

Table 2-1: Differences between dip-slip (normal) and strike-slip faults (Barnett et al., 1987; Diabat et al., 2004; Elliott, 1976; Jackson & McKenzie, 1983; Sylvester, 1988; Walsh & Watterson, 1991; Watterson, 1986; Wu et al., 2009).

	Dip-slip faults	Strike-slip faults
Fault geometry	Upward or listric; dip of 45°-60° or greater	Upward; dip between 65°-90°
Kinematics	Extensional, dip-slip	Extensional/contractional; strike-slip
Growth strata	Maximum displacement in the middle of the fault; against the footwall.	Central depocenter
Subsidiary fractures	-	Riedel shears

Here, it is worth noting the two main uncertainties that arose by following the abovementioned methodology. Firstly, by restoring the sequences based on the youngest unit for each locality. Due to the erosion, some sequences cannot be restored based on the main contractional events that influenced the areas individually. Secondly, the regional scale structures and half-grabens are associated with the Triassic basalts commonly co-exist with the Triassic evaporites. The main structures and the surrounding area may have been influenced by halokinesis, and more attention is required for the interpretation and the paleostress analysis in such regions.

2.4 Results - Key Outcrops

Observations and interpretations for each key kilometre-scale outcrop in the Central and Eastern High Atlas are presented from west to east in Figures 2.3 to 2.9.

2.4.1 Aït Attab

2.4.1.1 Area overview

The Aït Attab syncline (Figure 2.1B) is located in the Central High Atlas. The youngest exposed sequence consists of continental red beds, Cretaceous in age, while, the Middle and Lower Jurassic sequences consist of alternating shallow marine carbonates and marls (Figure 2.1B; Ellouz et al., 2003; Fedan, 1989; Frizon de Lamotte et al., 2008; Ghorbal et al., 2007). An unconformity between the Middle Jurassic and Lower Cretaceous marks the contact between the two sequences, indicating the absence of the Upper Jurassic sequence. The syncline is bounded by main NE-SW and ENE-WSW structures. It is associated with the presence of Middle Jurassic to Lower Cretaceous lava, sills and dykes (Haddoumi et al., 2010; Charrière et al., 2011; Bensalah *et al.*, 2013). The structures' geometries, time activity, and the sediment-structure interaction are identified within Lower Jurassic, Middle Jurassic, and Cretaceous sequences. These will be integrated to calculate the stress regime.

Based on the sediment-structure interaction analysis, the Middle Jurassic sequence is 2km and 2.5km thick towards the NW and SE, respectively. The thickness of Lower Jurassic and Cretaceous strata cannot be calculated due to erosion, and the lack of exposure of the older Triassic sequence, thus, growth strata in these sequences cannot be identified.

2.4.1.2 Field observations

In the Early Jurassic, NE-SW and ENE-WSW regional scale faults were identified as geomorphic valleys. In the Middle Jurassic carbonates and continental beds, NNW-SSE, NW-SE, NE-SW, and E-W (Figures 2.3a and 2.3c-d) faults are present along the Aït Attab region. These faults are 60-85° steep, they lack slickensides, due to the nature of the continental beds, and show thickness variations on either side of the faults (Figure 2.3c-d). In Figure 2.3c, the observed strike-slip fault is possibly associated with a regional scale fault, evident from the

salt diapirism. In both cases of Figures 2.3a and 2.3c-d, the faults are situated metres apart, indicating steep strike-slip (Figure 2.3c) and oblique-slip (Figure 2.3a) faults surrounded by dip-slip faults featuring growth strata (Figures 2.3a & 2.3d). However, the formation of growth strata is primarily attributed to tectonic activity rather than salt deformation, given that growth strata are formed in areas where evaporites are absent (Figures 2.3a & 2.3d).

In the late Lower Jurassic (Figure 2.3e) beds, dominant M and P Riedel structures of NE-SW to ENE-WSW trend and sinistral movement were found, while in the Middle Jurassic various orientations were observed in different localities. In Figure 2.3f tension gashes are mostly oriented NE-SW, and the main (M) and primary (P) structures are NW-SE oriented, while in Figure 2.3b, the main structures are NE-SW oriented. However, in the Middle Jurassic, the most dominant main structures (M, P and R) are NW-SE trending and tension gashes are oriented ENE-WSW, which contradicts the dominant trend of the Early Jurassic Riedel structures. This indicates their formation occurred during a different timing and tectonic event.

The age classification of these structures was determined based on the geological background of the Atlas system (Figure 2.2). Structures consistent with inversion were excluded, while those from the Early and Middle Jurassic periods were grouped according to their overall orientation and their interactions. Age allocation relied on the consistency of the geological history. It is important to note the possibility of deformation during the Late Jurassic, which is not represented in the stratigraphic sequence.

2.4.1.3 Interpretation

In the Early Jurassic, NE-SW and ENE-WSW regional scale faults and Riedel structures are identified. These were possibly reactivated during the Middle Jurassic, based on structures of similar trend identified in the Middle Jurassic sequences, and newly formed NNW-SSE and NW-SE faults were activated with a normal displacement and syn-extensional growth strata (Figures 2.3a and 2.3c-d). The pre-existing and the newly formed structures interacted and formed either negative flower structures (Figure 2.3c-d) at the southern part, or a strike-slip fault splay (Figure 2.3a) in the eastern part of the Aït Attab region, respectively. The

paleostress analysis indicates that σ_3 remained NW-SE during both phases, and σ_1 was sub-vertical during the Middle Jurassic (Figure 2.3g).

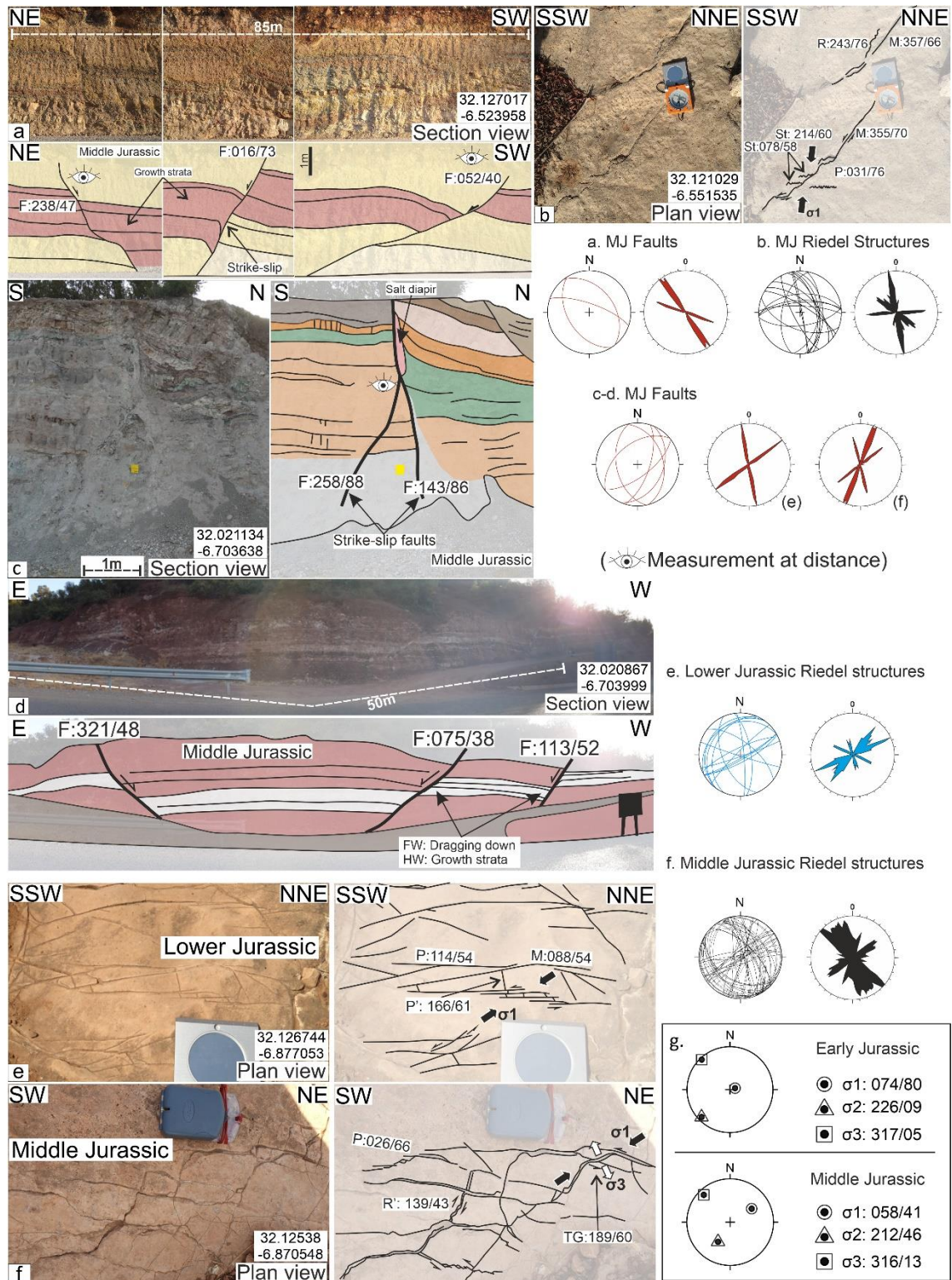


Figure 2.3: Representative photos and interpretation of Ait Attab region, whose localities are presented in Figure 2.1B. (a) Middle Jurassic fault slay that consists of strike-slip and normal faults, and (b) Riedel structures in the eastern limit of the anticline. (c) Inherited structure reactivated as a strike slip and (d) normal faults

with growth strata, form a negative flower structure, south of the Aït Attab region. (e) Lower Jurassic, potentially Toarcian in age and (f) Middle Jurassic Riedel structures at the northern limb of the anticline. (g) Paleostress results. MJ: Middle Jurassic. Field data are presented in appendix Tables A-1 to A-4.

2.4.2 Ouaouizaght

2.4.2.1 Area overview

Ouaouizaght (Figure 2.1B) is situated in the Central High Atlas, a few kilometres to the east of the Aït Attab syncline. The region displays NE-SW and NW-SE regional scale trending faults, and it features Lower Jurassic to Cretaceous stratigraphy. This combination forms an ideal location to investigate the relationship between the Early and Middle Jurassic, and the degree of obliquity in these sequences. Similar to the Aït Attab region, the Cretaceous continental red beds here have a consistent dip (30°S or 30°N) that corresponds with the upper Middle Jurassic continental red beds sequence, despite the regional unconformity between Middle Jurassic and Cretaceous. This uniformity in dip and lithology presents a challenge for field-based differentiation, and corresponds to a stable state depositional environment. The lower Middle Jurassic sequence primarily comprises carbonates, while the Lower Jurassic alternates between carbonates and marls, both of shallow marine environment (Figure 2.1B; Ellouz et al., 2003; Fedan, 1989; Frizon de Lamotte et al., 2008; Ghorbal et al., 2007; Guezal et al., 2014). In Ouaouizaght, the objectives align closely with those of the Aït Attab region. Fieldwork involved conducting a sediment-structure analysis in the Middle Jurassic strata, revealing fanning towards the SE, with some local variations towards the NW. The Middle Jurassic sequence can reach a thickness of nearly 3km. However, the thickness of the Lower Jurassic layer remains uncertain due to erosion in the faults hanging wall, which prevents the identification of growth strata, and therefore, the faults time activity.

2.4.2.2 Field observations

Magmatic rocks and sills (Figure 2.1B) were observed, along the NE-SW and NW-SE regional scale trending faults. Some of these faults show slickensides in different stratigraphic units. Notably, the NE-SW trending regional-scale faults in the region have distinct characteristics, varying between the northern and

southern parts of Ouaouizaght. Both of these structures are bounded by the Lower Jurassic sequence, with the Middle Jurassic nearby. The northern structure encompasses a wide fracture zone with unidentifiable distinct tectonic features of slickensides. However, a few metres to the south, two sets of faults are potentially related to the main structure (Figure 2.4a). One set of NE-SW to ENE-WSW faults displays extensional growth strata, which have been inverted afterwards, while another set consists of NNW-SSE trending normal faults without any growth strata (Figure 2.4a).

The southern regional-scale structure (Figure 2.1B-A.1) is likely linked to magmatic intrusions of uncertain age, spanning from the Middle Jurassic to the Early Cretaceous, as well as to the Triassic evaporites (Jossen et al., 1985). Vertical beds characterize the surrounding stratigraphy, likely influenced by both evaporites and magmatic activity. These beds are faulted by NE-SW trending normal faults (Figures A.1 in appendix, and 2.4a, as indicated by the green trend on the rose diagram). The faults may appear horizontal, but when restored, they exhibit characteristics of normal faults with minor normal displacement, without growth strata. Their trend aligns with that NE-SW trending northern structures, and they could be associated with the same event, despite the halokinesis that caused the vertical beds.

The primary NW-SE trending regional scale structure (Figures 2.1B-d and 2.4d) exhibits dextral slip and is accompanied by ~E-W trending oblique-slip extensional faults (Figure 2.4e) of approximately 70° angle within the youngest Middle Jurassic sequence. These latter oblique-slip faults indicate normal displacement and display growth strata, with thickening in the hanging wall.

Lastly, in the region of Ouaouizaght, well-developed tectonic features are the only structures presented in this chapter that are associated with the orogeny, and they are used as a guidance to withdrawn similar structures from the paleostress analysis. NNW-SSE sinistral strike-slip faults (Figure 2.4b) and the equivalent tension gashes and stylolites (Figure 2.4c) were found in the oldest Middle Jurassic sequence. These structures are undeformed, and indicate a NW-SE orientation for σ_1 and a NE-SW orientation for σ_3 , which reflect to the orogenic event. Similar structures were identified in most of the outcrops, with varying degrees of prominence, though they were not included in the kinematic analysis.

In the Ouaouizaght region, the classification of structures was more straightforward due to the well-developed features related to the orogeny (Figure 2.4b-c) and the absence of complex deformation within the Lower and Middle Jurassic sequences (Figure 2.4d-e), although the approach remains similar to the Aït Attab region.

2.4.2.3 Interpretation

In the Lower Jurassic strata, there are reactivated NE-SW inverted normal faults (Figure 2.4a) and their inversion is related to a later tectonic event. While the NW-SE trending normal faults (Figure 2.4a) and NE-SW (Figure A.1 in appendix) that lack growth strata are more likely to be related to the thermal subsidence, due to minor normal displacement. During the Early Jurassic, the presence of NE-SW and ENE-WSW trending faults and growth strata, suggest NW-SE orientation of σ_3 , and σ_1 had an oblique orientation along the NW-SE axis. In contrast, when examining the Middle Jurassic strata after restoring the beds, stress analysis of tension gashes and faults (Figure 2.4d-e) indicates a shift in the orientation of σ_3 towards the ENE-WSW, with σ_1 being oblique along the NE-SW axis (Figure 2.4f).



Figure 2.4: Ouauizaght representative photos whose localities are presented in Figure 2.1B. (a) Early Jurassic faults in the northern NE-SW trending regional scale fault. In the rose diagram, blue indicates faults in locality (a) and green indicates the faults in the southern NE-SW main structure in locality (A.1; Figures 2.1B and A.1 in appendix). (b) Contractional related sinistral strike slip fault and shear structures (c) within the Middle Jurassic sequence; faults - red stereonet and rose diagram; shear structures - black stereonet. (d) Late Middle Jurassic dextral NW-SE regional scale fault and (e) late Middle Jurassic E-W trending transtensional fault. (g) Paleostress analysis. TG: tension gashes. Field data are presented in appendix Tables A-5 to A.8.

2.4.3 Zawyat-Ahancal

2.4.3.1 Area overview

Zawyat-Ahancal (Figure 2.1B) is located in the Central High Atlas, to the south of the Ouaouizaght region. This area is characterised by the presence of Toarcian carbonates-shales alternation, Lower Jurassic carbonates, and Triassic evaporites. The carbonate sequences in Zawyat-Ahancal alternate from shallow to deeper marine depositional environments (Figure 2.1B; Ellouz et al., 2003; Fedan, 1989; Frizon de Lamotte et al., 2008; Saura et al., 2014) with some local unconformities (e.g., Figure 2.5a). The ENE-WSW and NW-SE trending regional scale faults are linked with evaporite-filled half grabens (Jossen et al., 1990). These regional structures are visible as geomorphic valleys, prompting stratigraphic and tectonic analysis of the surrounding units. Therefore, the primary objective in Zawyat-Ahancal is to uncover the tectonostratigraphic relationship within the Lower Jurassic beds, and recognise the degree of obliquity during the extension.

2.4.3.2 Field observations

Sediment-structure analysis was conducted in proximity to and away from the Triassic evaporites, focusing on the Lower Jurassic (Figures 2.1B and 2.5a) and Toarcian sequences (green trace, Figure 2.1B), respectively. Figure 2.5a presents Triassic basalts with evaporites in the background, which are stratigraphic below the pre-kinematic and syn-kinematic Lower Jurassic sequences in the foreground. These are divided by a ~E-W trending Triassic structure (Figure 2.5a; black dashed line) that reactivated during the orogeny. The results from the stratigraphic analysis in both localities reveal growth strata towards the north or south along ENE-WSW trending faults (Figure 2.5a).

In addition to the regional scale faults, there are NE-SW and NW-SE to NNW-SSE trending faults in the Lower Jurassic sequence, mostly exhibiting an approximately 80° steep angle with mostly dextral slip, with a few exceptions showing sinistral slip. The NNW-SSE faults accommodate extensional growth strata, which were reactivated and formed positive flower structures (Figure 2.5b), however, the reactivation timing is ambiguous. The NW-SE faults show calcite mineralisation on the fault surface (Figure A.2 in appendix), but the lack of hanging wall and erosion prevent the observation of growth strata. Meanwhile,

extensional faults with minor growth strata are found in the Toarcian sequence, including ENE-WSW and NE-SW trending faults (Figure 2.5c).

The Lower Jurassic carbonates are characterised by the presence of well-developed tension gashes. Two sets of trends, NW-SE and ENE-WSW (Figure 2.5d), are observed, with the NW-SE ones (purple; Figure 2.5d) forming conjugate tension gashes, while the second trend (green; Figure 2.5d), locally cross-cuts the previously mentioned set. The conjugate tension gashes, when restored, provide insights into the stress regime. The bedding hosting the tension gashes has been restored according to the dip direction (Figure 2.5e), either NW or NE, with an average dip of 40°.

2.4.3.3 Interpretation

The Zawyat-Ahancal region was affected by one observed extensional phase. Growth strata in the Early Jurassic are primarily associated with the ENE-WSW trending faults (Figure 2.5a; black dash line). Additionally, more faults of NE-SW and NNW-SSE trend (Figures 2.5a-c) show extensional features. The NNW-SSE faults show minor syn-tectonic growth during the Early Jurassic and were inverted at a later stage, likely to be post-Toarcian. While the NE-SW trending faults suggest a Toarcian to post-Toarcian activity. The timing of the conjugate set of tension gashes activity (Figure 2.5d-e) aligns with the previously mentioned Early Jurassic growth strata, with paleostress analysis indicating σ_1 to be vertical, and σ_3 oriented WNW-ESE (Figure 2.5f).

It is important to note that halokinesis might play a crucial role, as previously suggested by Saura et al. (2014) in a neighboring area of Zawyar-Ahancal. However, the tectonic features and observations indicate synchronous tectonic activity, which will be further discussed.

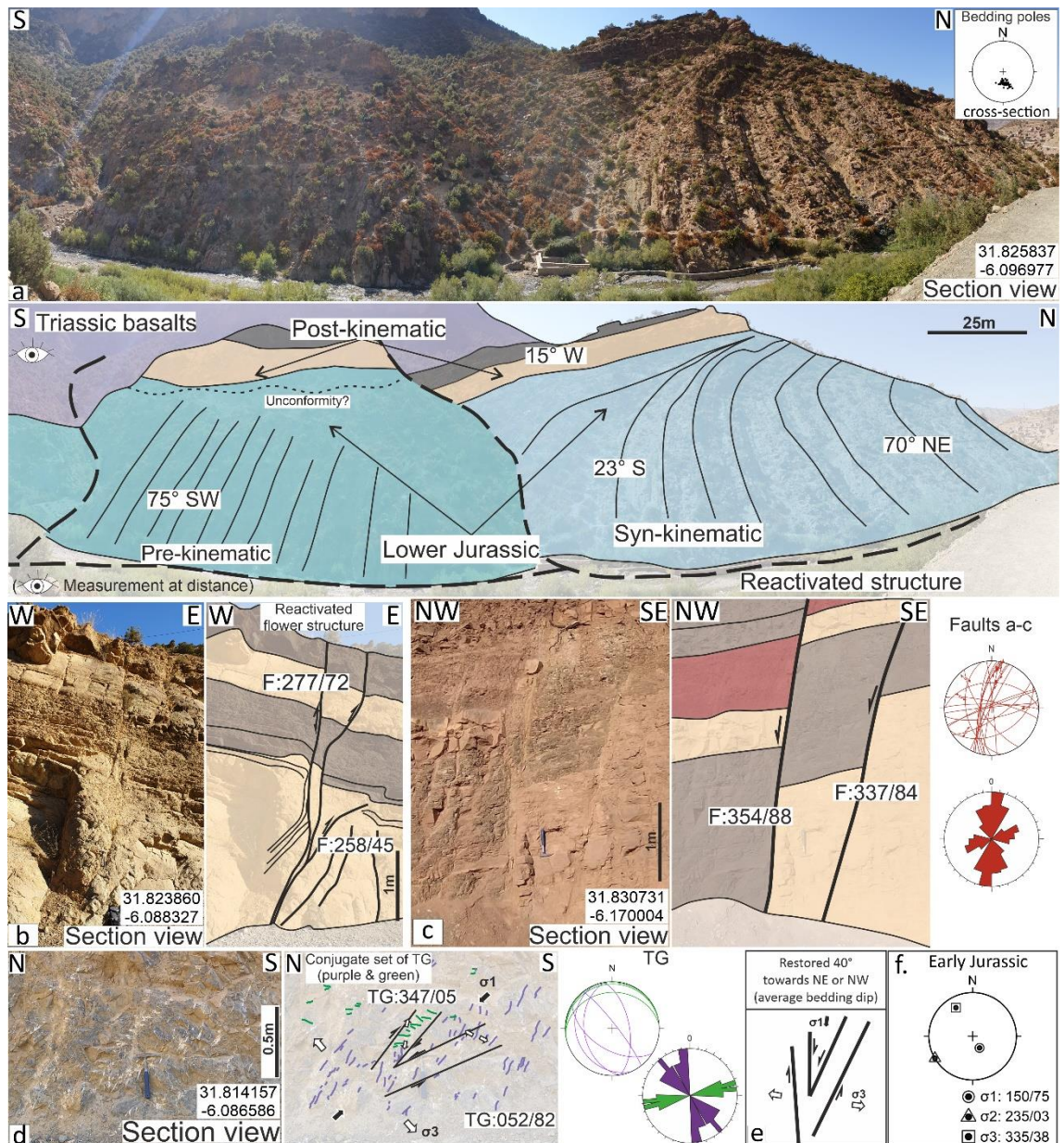


Figure 2.5: Zawayat-Ahancal representative photos and interpretations, whose localities are presented in Figure 2.1B. (a) Lower Jurassic to Toarcian units in contact with Triassic evaporites-basalt placed in the background. The dashed lines indicate ENE-WSW trending reactivated structures, on which growth strata are developed. Bedding poles along the green cross-section (indicated in Figure 3.1B). (b) Lower Jurassic sequence with a reactivated positive flower structure. (c) Toarcian ENE-WSW normal faults with growth strata. (d) A conjugate set of tension gashes in Lower Jurassic carbonates and their schematic stress interpretation posterior to the unfolding. (e) Stress interpretation based on the faults and the tension gashes. (f) Paleostress analysis. TG: tension gashes. Field data are presented in appendix Table A-9.

2.4.4 Agoudal

2.4.4.1 Area overview

In the eastern part of the Central High Atlas, prominent NE-SW to ENE-WSW trending wide ridges (Figure 2.1B) are associated with dykes of Triassic basalts and evaporites, penetrated by Middle Jurassic to Cretaceous magmatic rocks (Milhi, 1997; Fadile, 2003; Charrière *et al.*, 2011). Timedouine ridge, situated to the west of Agoudal (Figure 2.1B), was previously interpreted as a salt wall (e.g., Saura *et al.*, 2014). This ridge is characterised by Triassic red siliciclastic and basalts at its core, overlain by Lower Jurassic carbonates of shallow to deep marine environment (Ellouz *et al.*, 2003; Fedan, 1989; Frizon de Lamotte *et al.*, 2008; Milhi *et al.*, 2002; Pierre *et al.*, 2010). Middle Jurassic to Cretaceous gabbro outcrops can be observed at the north-eastern part of the ridge (Figure 2.6e). The Lower Jurassic unit within the core of the ridge appears highly deformed, while the Middle Jurassic carbonates exhibit gentle fanning away from the ridge (Figures 2.6b and 2.6e). The primary objective in this region is to investigate the potential relationship between the volcanics and the Middle Jurassic sediments, identify structural features, and calculate the paleostress regime within the area.

2.4.4.2 Field observations

Lower Jurassic carbonates are found on the top of the dyke core and at higher elevations, where three extensional structure sets can be identified (Agoudal; Figures 2.1B and 2.6a), i.e., tension gashes and veins. The oldest Early Jurassic extensional structures are marked by sub-vertical NW-SE trending tension gashes (purple; Figure 2.6a), subsequently crosscut by a younger stage of NNE-SSW trending sub-horizontal tension gashes (light blue; Figure 2.6a). Finally, a set of WNW-ESE trending tension gashes and veins can be observed in the Lower Jurassic (orange; Figure 2.6a), are locally highly fragmented and are also cross-cut by the NNE-SSW dilational structures (Figure A.3 in appendix). I classified the tensional structures within the Lower Jurassic sequence by grouping them into syn- and post-Middle Jurassic categories (Figure 2.6a; stereonet). This classification was based on trends and deformation criteria, considering both known patterns of structural evolution and the presence of previously unrecorded ones.

In the Middle Jurassic, comprehensive stratigraphic and structural analyses were conducted at two distinct localities: one situated to the west (Figure 2.6b-c) and the other to the east (Figure 2.6e) of the dyke. In the western locality (Figures 2.6b and 2.6c), Middle Jurassic carbonates are gently folded (Figure 2.6c) along the ridge, with beds fanning towards the southeast (Figure 2.6b), having dips of 65° close to the ridge core and gradually shallowing to 15°. The Middle Jurassic carbonates also exhibit gentle folding, with bedding dipping approximately 05° towards the northwest (Figure 2.6c). In the valley, where the stratigraphic analysis was conducted, various structural features were observed, including NW-SE and NE-SW strike-slip faults, various sets of tension gashes, and NW-SE trending veins and joints. Two trends of tension gashes (Figure 2.6d) indicate two distinct tectonic events. The first set of WNW-ESE tension gashes, concurrent with NE-SW trending stylolites implies an E-W orientation for σ_1 and an approximate N-S orientation for σ_3 . The presence of fault (Figure 2.6d) in conjunction with the aforementioned structural features suggests a stress regime characterised by strike-slip movement. The second set of NE-SW trending tension gashes and veins showing dextral shear intersect the WNW-ESE tension gashes (Figure 2.6d), indicating a post-Middle Jurassic deformation event likely linked to the orogeny.

The eastern locality of the Timedouine ridge (Figure 2.6b) has similar stratigraphic characteristics to the western locality (Figure 2.6b-c), including the presence of Middle Jurassic to Cretaceous gabbro. Here, the magmatic sequence comprises gabbro embedded within the Middle Jurassic. Four E-W trending stratigraphic sections were analysed, revealing growth strata towards the southeast. Similar to the western locality (Figure 2.6b-c), the Middle Jurassic carbonates are gently folded. However, in areas where gabbro intrusions are present, the Middle Jurassic carbonates are tightly folded, forming an overturned anticline with bedding dipping towards the southwest (Figure 2.6e).

2.4.4.3 Interpretation

In summary, the Agoudal region exhibits pronounced deformation in the Lower Jurassic carbonates and gentler deformation in the Middle Jurassic. This variation suggests relatively mild tectonic deformation during the Middle Jurassic period. The deformation of the Middle Jurassic beds varies in proximity to the ridge core. Due to the limited presence of structures within the Middle Jurassic

carbonates and the observation of growth strata in the outcrops, these sequences are interpreted as having been deformed by the Middle Jurassic to Cretaceous magmatic rocks and evaporites. Consequently, I believe that the gabbro upwelling combined with the pre-existing evaporites, triggers the fanning in the Middle Jurassic beds (Figure 2.6) and played a role in gently deforming the bedding in the west, and an abrupt deformation in the east. In this case, the gabbro is determined to be Middle Jurassic in age for this region in the Central High Atlas. Finally, based on the two distinct deformation phases identified in the tension gashes (Figure 2.6a and 2.6d), the stress regime during the Middle Jurassic in the Agoudal region is characterised by σ_1 oriented WNW-ESE and σ_3 oriented NNE-SSW, with a gentle tectonic deformation (syn-MJ; Figure 2.6a and 2.6d) compared to the orogenic events (post-MJ; Figure 2.6a and 2.6d).

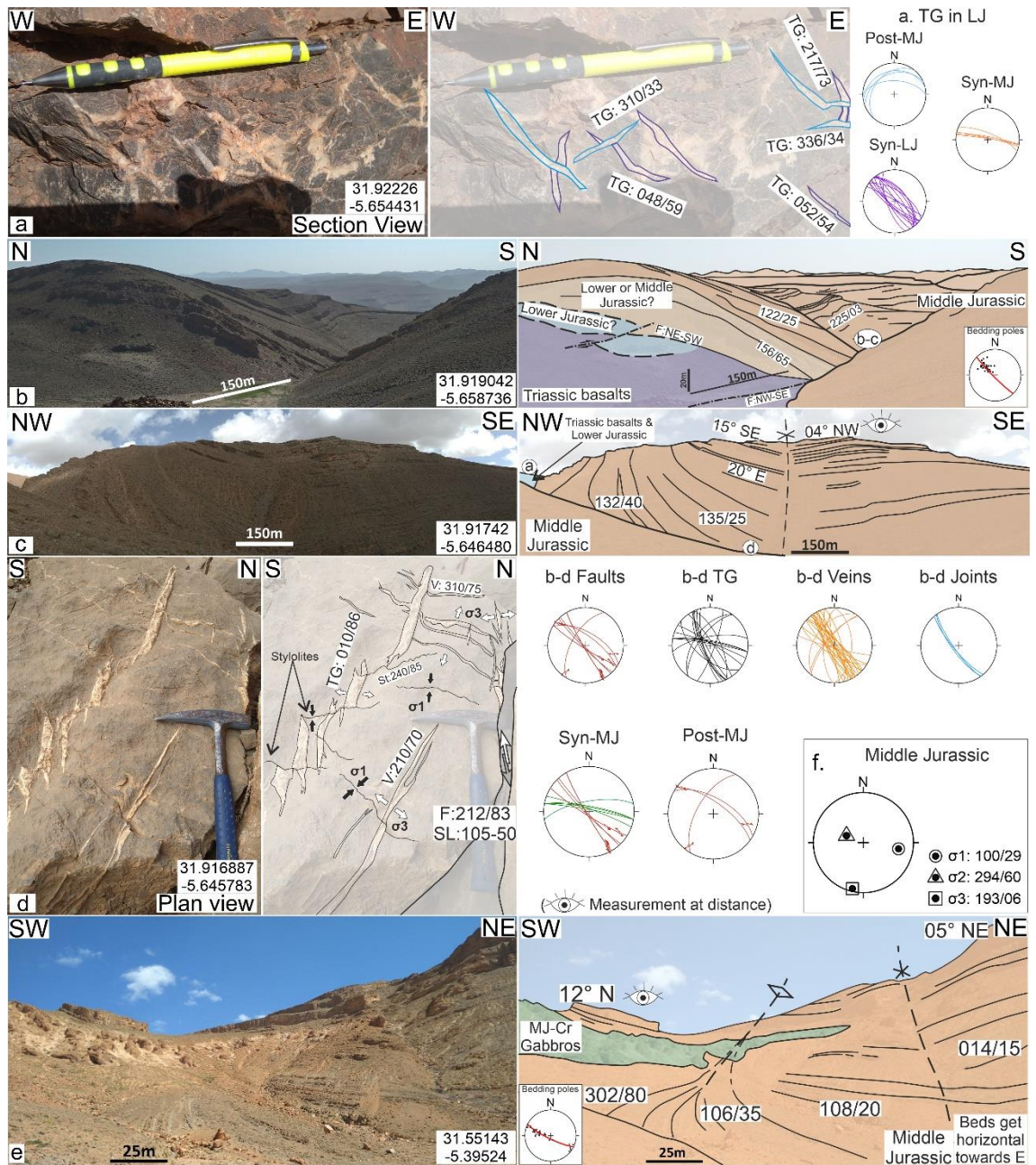


Figure 2.6: Agoudal representative photos and interpretations, whose localities are presented in Figure 2.1B. (a) Lower Jurassic carbonates with two tension gashes generations. (b) N-S and (c) NW-SE perspective of Middle Jurassic carbonates, showing syn-contractual growth strata and an open anticline, respectively. (d) Representative structures identified along the Middle Jurassic carbonates, showing two different phases. (e) Middle Jurassic growth strata with overturned bedding caused by Middle Jurassic – Cretaceous gabbro. (f) Paleostress analysis. TG: tension gashes; MJ: Middle Jurassic; LJ: Lower Jurassic. Field data are presented in appendix Tables A-10 to A-12.

2.4.5 Er-Rich

2.4.5.1 Area overview

In the transitional area between the Central and Eastern High Atlas, we find the Azag mini basin (Figure 2.1C) located in the Er-Rich region. The landscape features an open Middle Jurassic syncline, surrounded by adjacent E-W and NE-SW trending faults. The primary focus was on two key localities within the Er-Rich region: the basin (Figure 2.1C-a) and an antiform (Figure 2.1C-d) located southeast of the basin. The goal was to conduct comprehensive stratigraphic and tectonic analyses within the Middle Jurassic beds, with the objective of understanding the interplay between these structures and determining the paleostress regime. The Middle Jurassic sequences consists mainly of shallow to deep water shales and sandstones (Figure 2.1C; Evans et al., 1974; Teixell et al., 2017; Warme, 1988), which exhibit significant fragmentation.

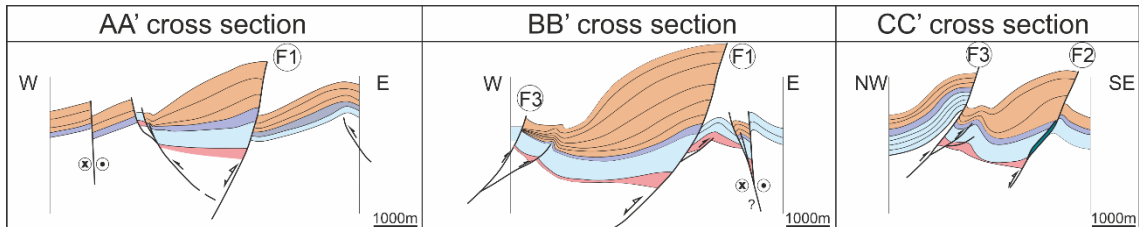
2.4.5.2 Field observations

Within the basin, three cross-sections were built, two of which relied on field measurements (Figure 2.1C and 2.7a; sections BB' and CC'), while one was based solely on the geological map (Figures 2.1C and 2.7a; section AA'). The sections reveal three main N-dipping faults and two dextral strike-slip faults. Both faults F1 and F2 accommodate deformed Triassic to Middle Jurassic beds (Figures 2.1C, 2.7a and 2.8a), with fault F2 also accommodating rocks Middle Jurassic to Cretaceous in age. Faults F1 and F2 are likely to have formed during the early stages of rifting in the Atlas system. Fault F3 indicates a more complex fault forming a splay deforming beds of consistent thickness. The remaining faults in the region are associated with the orogenic event, which is the last deformation imprinted on the maps.

Cross-sections were restored (Figure 2.7b) under the assumption that the youngest Middle Jurassic sequence deposited flat, not considering the oblique movement observed on the map (Figure 2.1C) for simplicity. It is important to acknowledge that uncertainties may arise in the restored sections due to the observed lateral motions. These sections reveal growth strata within the Middle Jurassic (Figure 2.7) and Triassic beds, dipping towards the east and southeast, and juxtaposing against adjacent NE-SW (F1) and ENE-WSW (F2) trending normal faults (Figure 2.1C and 2.7b). It is worth noting that the basin was

previously interpreted as a salt basin (Teixell et al., 2017). Although the influence of evaporites cannot be ruled out, the syn-tectonic growth observed in the field (Figure 2.8a) and illustrated in the cross-sections (Figure 2.7), coupled with the tectonic features identified on-site along the main fracture zones (Figure 2.1C), suggests a fault controlled activity.

a. Er-Rich cross-sections



b. Er-Rich cross-sections restoration

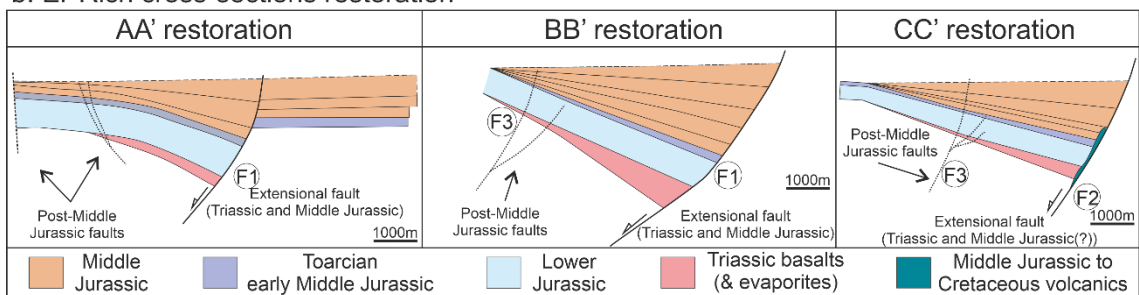


Figure 2.7: Er-Rich region cross-sections (a), whose localities are imaged in Figure 2.1C, and their restoration (b).

A series of tectonic measurements were gathered throughout the Middle Jurassic sequence along the basin. The identified faults exhibit ENE-WSW, NE-SW, NW-SE, and N-S strike-slip orientations. Sinistral slip is more predominant, with some instances of dextral slip (Figure 2.8a-c; Stereonet Syn-MJ faults). Given the lack of slickensides, the majority of the faults' kinematics were inferred and correlated with the associated tension gashes and stylolites. Additionally, two sets of tension gashes from different tectonic events were recognised (Figure 2.8b-c; stereonet). The first generation includes ENE-WSW to NE-SW trending tension gashes (red; Figure 2.8c), later deformed by NW-SE to NNW-SSE trending tension gashes (black; Figure 2.8c). The associated structural features of tension gashes and stylolites in Figure 2.8b, imply an WNW-ESE orientation for σ_1 and an NNE-SSW orientation for σ_3 . After correlating the faults with the associated tension gashes and recognising different generations of the latter dilational structures (Figure 2.8c), I distinguished the faults into generations based on the deformation criteria of both predicted and previously unrecorded structures. An older set of ENE-WSW, NE-SW, and NW-SE trending faults, and a younger set of NNW-SSE to

NW-SE faults were delineated (stereonet; Figure 2.8a-c). The older set is characterised by a dense population of structures exhibiting shear with significant presence of stylolites (Figure 2.8b), indicating a more contractional deformation, akin to the shear structures in the Ouaouizaght region (Figure 2.4b-c). Therefore, the older set was likely active the earliest in the Middle Jurassic, as it was discovered within the Middle Jurassic, while the younger set is likely associated with the later orogenic event.

Southeast of the basin (Figure 2.1C-d and 2.8d), a Middle Jurassic antiform trending NNW-SSE displays syn-contractional growth strata oriented towards the south. This observation is based on three N-S sections, east and west of the anticline's axial plane. While minor structures are present in proximity to the antiform, they have a limited impact on the overall area and align with the previously mentioned youngest strike-slip fault in the basin (Figure 2.8d; Post-MJ faults). It is important to mention that meter-scale veins were identified within the antiform, exhibiting consistent development with the deformed bedding, indicating their synchronous formation (Figure 2.8d; veins).

2.4.5.3 Interpretation

I interpret the Er-Rich region as a reactivated breached relay ramp that originated during the early stages of rifting, based on the Triassic growth strata observed in the cross-sections (Figure 2.8). In the Middle Jurassic, regional scale NE-SW and ENE-WSW trending faults evolved in this complex structural zone. Growth strata formed mainly in relation to the ENE-WSW faults. The coexistence of coeval extensional faults and folding in the Middle Jurassic of the Er-Rich region suggests a likely strike-slip stress regime, with principal stresses σ_1 and σ_3 trending WSW-ENE and NNW-SSE (Figure 2.8e), respectively. Additionally, a later tectonic event activated NNW-SSE strike-slip faults, characterised by a NW-SE σ_1 and a NE-SW σ_3 , based on the faults kinematics, stylolites and tension gashes identified in both basin and antiform (Figure 2.8) and along the main structures (Figure 2.1C). Triassic evaporites in the basin could have played a crucial role in the interaction between faults and sediments; this aspect will be further discussed below.

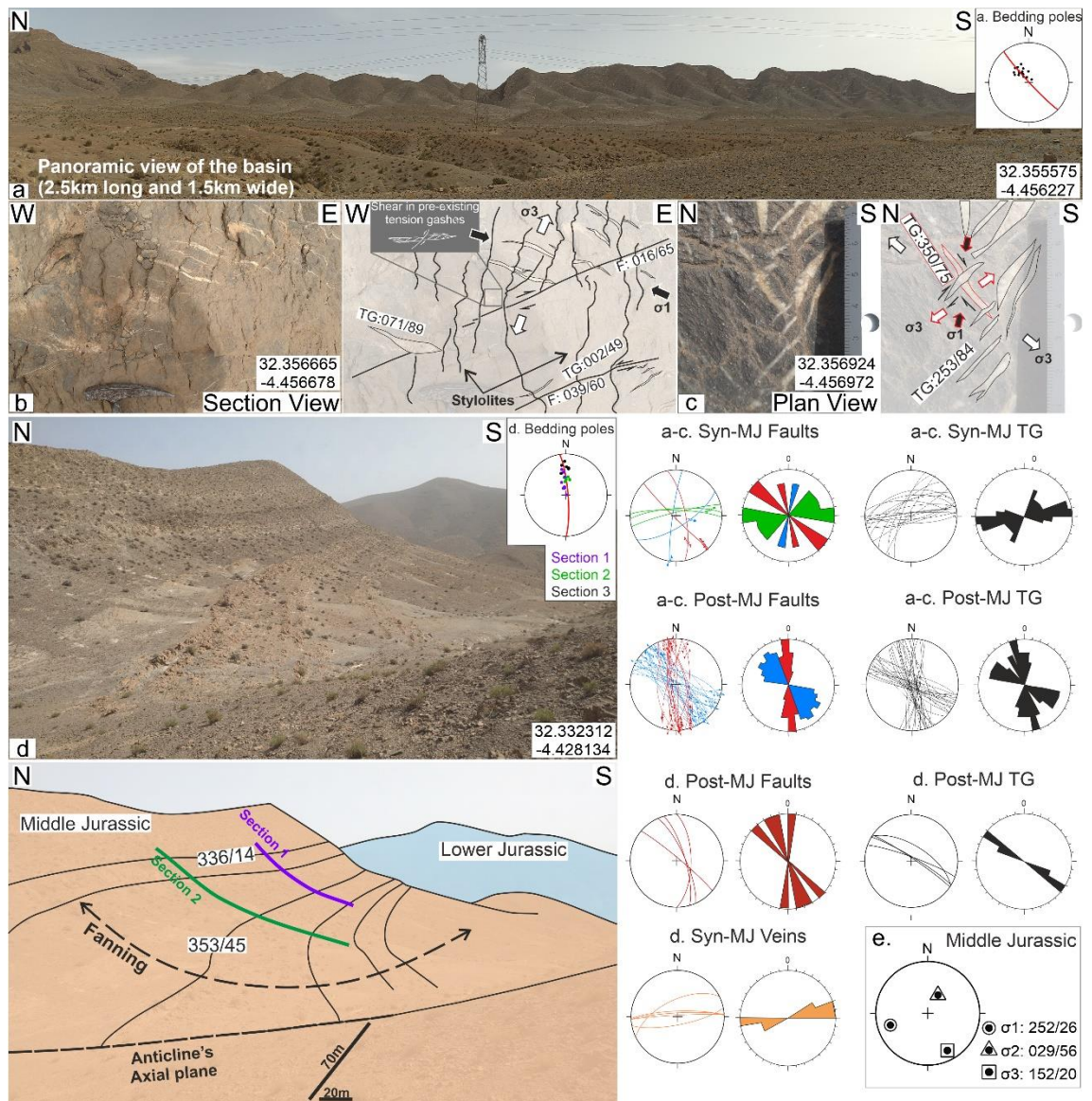


Figure 2.8: Er-Rich region localities presented in Figure 2.1C. (a) Panoramic view of the syncline, and restored bedding poles that show fanning towards the SE. (b) Representative Middle Jurassic shear zone with dominant contractional shear, (c) an older (red) tension gash deformed by younger tension gashes (black). (d) Middle Jurassic antiform with syn-kinematic bedding, and the bedding poles that indicate fanning towards the south. (e) Paleostress analysis in the Middle Jurassic. TG: tension gashes; MJ: Middle Jurassic. Field data are presented in appendix Tables A-13 and A-14.

2.4.6 Bou Annane

2.4.6.1 Area overview

The Bou Annane region (Figures 2.1D and 2.9a) is located in the Eastern High Atlas, distinct from the Central High Atlas due to frequent exposures of the Paleozoic basement. This region, located at the southern boundary of the High Atlas, is characterised by regional scale ENE-WSW trending faults (Figure 2.1D). Stratigraphic analysis was performed from north to south to unravel sediment-structure interaction, understand the interaction between the pre-existing basement structures and younger sequences, and determine the paleostress regime that prevailed in this region. Due to limited access to Middle Jurassic sequences, four additional cross-sections (Figures 2.1D and 2.9d) were constructed, to characterise the Paleozoic basement to Lower Jurassic stratigraphic and structural configurations.

2.4.6.2 Field observations

The Paleozoic basement is marked by deformed schists and quartzite, with minor pre-existing Hercynian thrusts that have not been reactivated during the later stages of the Atlas system's evolution. In contrast, the regional scale faults associated with the basement exhibit brittle deformation and have shaped geomorphic valleys due to multiple phases of activity (Figure 2.9a). The Triassic sequence consists of pillow lavas and is unconformably overlying the basement, along with the shallow water Lower Jurassic carbonates (Figure 2.9a; Ellouz et al., 2003; Fedan, 1989; Frizon de Lamotte et al., 2008; Milhi et al., 2002; Pierre et al., 2010). The Triassic and Lower Jurassic sequences are several metres thick, while the Middle Jurassic exhibits thicker growth strata (Figure 2.9d) based on the cross-sections. Field observations and cross-section analyses indicate that the Triassic pillow lavas can reach a thickness of 300 metres, while the Lower Jurassic carbonates have a minimum thickness of 100 metres but could extend up to 270 metres, as suggested by growth strata in the lower layers of the sequence. However, the early Lower Jurassic, which is deposited on the basement, maintains a consistent thickness (Figure 2.9a), and the Middle Jurassic carbonates conformably overlie the Lower Jurassic carbonates. Stratigraphic analysis, cross-sections, and restored sections suggest that the Triassic, Lower, and Middle Jurassic sequences are accommodated by

reactivated regional-scale faults, which appear as zones of brittle deformation (i.e., F1, F2, and F3; Figure 2.9d). As previously noted, uncertainties exist in the restored sections due to the observed strike-slip movement depicted on the maps (Figure 2.1D).

Within the Lower-to-Middle Jurassic carbonates, two sets of tension gashes were observed (Figure 2.9b), one sub-perpendicular to bedding and the other sub-parallel to bedding. The sub-perpendicular tension gashes, trending NE-SW, indicate sinistral shear, while the ~E-W sub-parallel tension gashes, which align with bedding, demonstrate dextral shear. In the field, I did not recognise any interaction between these two sets of tensions gashes. The first set of NE-SW (green; Figure 2.9b) indicate approximately an E-W orientation for σ_3 , and a N-S orientation for σ_1 , which could correspond to the Alpine orogeny. The second set of tension gashes (purple; Figure 2.9b), when restored, their corresponding paleostress regime suggests orthogonal-influenced extension, with σ_3 oriented NNW-SSE (Figure 2.9c) and inclined σ_1 .

2.4.6.3 Interpretation

Based on the aforementioned observations, it appears that there was a period of tectonic quiescence during the Early Jurassic when constant thickness sediments were deposited on the basement (Figure 2.9a) in Bou Annane. Orthogonal extension likely initiated the earliest during the later stages of the Early Jurassic (Figure 2.9a), although the duration of this activity remains uncertain.

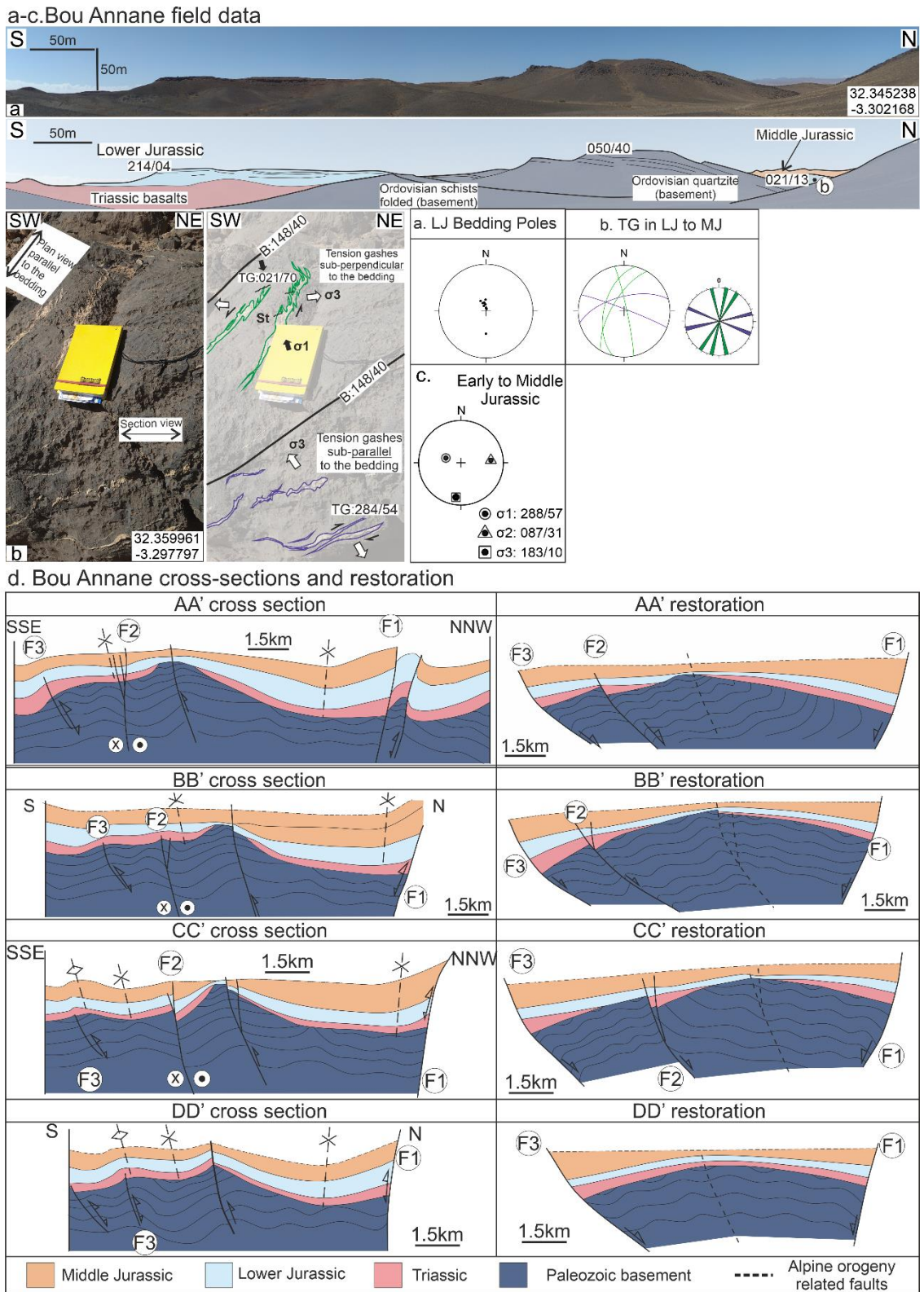


Figure 2.9: (a) Panoramic view of the basement and the rifting sequences of Triassic and Lower Jurassic in Bou Annane. Middle Jurassic in the background towards the N. (b) NE-SW and ~E-W trends of tension gashes within the Lower Jurassic carbonates, which are sub-perpendicular and sub-parallel to the bedding, respectively. (c) Paleostress analysis. d. Cross-sections and schematic cross-section restorations in the Bou Annane region that cover the basement exposure

(Figure 2.1D). LJ: Lower Jurassic; TG: tension gashes. Field data are presented in appendix Table A-15.

2.5 Discussion

The Atlas system underwent different phases of extension from the Triassic onwards (Ellouz et al., 2003; Frizon de Lamotte et al., 2008; Laville et al., 2004). This was due to the synchronous opening of the Atlantic and the Tethys Oceans. In this section, the extensional events in the Atlas rifting are classified based on their timing and characteristics. Then, these are distinguished as orthogonal extension, the true rifting with pure shear, and oblique extension. In summary:

- Early Jurassic: fault-driven growth strata towards the north or the south
- Upper Early Jurassic (Toarcian): simple shear observed on the bedding; extensional faults without any growth strata
- Middle Jurassic: extensional growth strata; extensional dip-slip, oblique-slip, and strike-slip faults; sheared involved inherited structures; magmatic-related growth strata; syn- and post-Middle Jurassic volcanism.
- Cretaceous: Gently folded beds. No structures were identified within this sequence.

2.5.1 Orthogonal extension

During the Late Triassic to Early Jurassic, the Atlas system underwent rifting processes due to the break-up of Pangaea and the opening of the Atlantic Ocean (Ellouz et al., 2003; Fernandez, 2019; Frizon de Lamotte et al., 2008; Lachkar et al., 2009). Previous studies have proposed that the deformation mechanism during the later stages of this rifting, in the Early Jurassic, was primarily associated with Triassic evaporites movement (Bouchouata et al., 1995; Ettaki et al., 2007; Moragas et al., 2018; Saura et al., 2014; Teixell et al., 2003, 2017; Vergés et al., 2017). This halokinesis may partially explain the development of Early and Middle Jurassic growth strata. However, the exposed outcrops in Ouaouizaght (Figure 2.4a), Zawyat-Ahancal (Figure 2.5a), and Bou Annane (Figure 2.9) reveal characteristics of tectonic driven extension during both the Triassic and Early Jurassic, despite the presence of evaporites in the regions. These observations have been integrated to investigate the paleostress and carry

a kinematic analysis (Figure 2.10) at each of these localities in the Central and Eastern High Atlas. The aim is to assess the degree of obliquity during extension, the role of reactivation of pre-existing structures, and the formation of growth strata during the Triassic and the Early Jurassic (Laville et al., 2004).

The Triassic basalts are well-exposed in the Bou Annane region of the Eastern High Atlas, where the Paleozoic basement is present (Figures 2.1D and 2.9a). These Triassic sequences are associated with pillow lavas and notably lack evaporites due to the transgression from the Tethys during the Late Triassic – Early Jurassic boundary (Laville et al., 2004), indicating lithological variations along the Atlas system during the Triassic. The Triassic sequence of the Bou Annane region is deposited in half-grabens controlled by ENE-WSW trending faults in the basement (Figure 2.9a). Similarly, in Zawyat-Ahancal and Ouaouizaght, Early Jurassic growth strata are observed along NE-SW (e.g., Laville and Harmand, 1982; Figure 2.4a) or ENE-WSW (Figure 2.5a) trending faults. While the Early Jurassic growth strata may have been influenced by salt tectonics (Martín-Martín et al., 2017; Moragas et al., 2018; Saura et al., 2014; Teixell et al., 2017; Vergés et al., 2017), the sediment-structure interaction analyses conducted both near and away from the evaporitic exposures (Zawyat-Ahancal; Figure 2.1B) support a fault-controlled driving mechanism in the Central High Atlas (Figure 2.5a) and the Eastern High Atlas (Figure 2.9), where Early Jurassic analysis was possible.

A series of tension gashes as compelling evidence observed in the Zawyat-Ahancal (Figure 2.5d) and Bou Annane (Figure 2.9a-b) regions, supports the idea of orthogonal extension that dominated during the Late Triassic to Early Jurassic. In this context, σ_1 is oriented vertically or sub-vertically, while σ_3 exhibited an NW-SE orientation (Figure 2.10). This timeframe aligns with the Atlantic opening and the reactivation of NE-SW and ENE-WSW Hercynian regional scale faults in the mentioned regions, including Aït Attab (Aït Attab; Figure 2.1B), Ouaouizaght (Figure 2.4a), and throughout the broader Atlas system (Figure 2.1A; Laville and Piqué, 1991; Charriere, 1996; Ellouz *et al.*, 2003; Laville *et al.*, 2004; Frizon de Lamotte *et al.*, 2008, 2011, 2015; Fernandez, 2019). The reactivation of pre-existing faults resulted in the formation of grabens, half-grabens, and both hard and soft-linked relay ramps (e.g., Ouaouizaght; Figures 2.1B and 2.10-2), where

Triassic and Early Jurassic growth strata developed against these faults (Figures 2.5a and 2.9d).

However, in Bou Annane, the tension gashes and potential orthogonal extension appear during the transition from the upper Early to Middle Jurassic, indicating a different timing of orthogonal extension along the Atlas system. Thus, there was a shift of the orthogonal extension towards the east (Figures 2.9a and 2.10-6), resembling the proposed model by Escosa *et al.* (2021), which suggests rift migration in the Atlas system during this age. It is worth noting that Triassic and Lower Jurassic sequences are thinner in the Bou Annane region (Figure 2.1D) compared to the outcrops in the Central High Atlas outcrops (Figure 2.1B), suggesting that the Central Atlantic Opening predominantly influenced the Triassic and Jurassic sequences in the Central High Atlas without significantly affecting the Eastern Atlas system. Lastly, following the cessation of the orthogonal rifting, the formation of the carbonate platform took place (e.g., Ellouz *et al.*, 2003; Laville *et al.*, 2004; Hafid *et al.*, 2006; Frizon de Lamotte *et al.*, 2008, 2009, 2011; Moragas *et al.*, 2018), which, based on the field data is suggested to be pre-Toarcian in age.

2.5.2 Oblique extension

During the syn-to-post-kinematic phase of the Atlas system, oblique extension with sinistral slip has been inferred to have been active in the Atlas system based on subsidence analysis (Fernandez, 2019; Gouiza *et al.*, 2010; Laville *et al.*, 2004; Moragas *et al.*, 2018) and plate reconstruction models (Fernandez, 2019; Labails *et al.*, 2010). This oblique extension occurred during the Middle Jurassic and left its imprint in the Toarcian. The Atlas system experienced the effects of oblique motion, with Africa exhibiting ongoing separation from America and relative movement with respect to Iberia (Charriere, 1996; El Kochri & Chorowicz, 1996; Ellouz *et al.*, 2003; Fernandez, 2019; Frizon de Lamotte *et al.*, 2008; Labails *et al.*, 2010; Laville, 1985; Laville & Piqué, 1991; Piqué *et al.*, 2002; Schwarz & Wigger, 1988). This motion led to the reactivation of pre-existing rift structures, creating a transtensional stress regime within the basin during the Middle Jurassic (Mattauer *et al.*, 1977; Laville and Petit, 1984; Laville, 1985; Laville and Piqué, 1991; Laville *et al.*, 2004).

2.5.2.1 Thin vs thick-skinned deformation

This study reveals that in the regions of the Central High Atlas (Figure 2.1B-2.1D), both the Toarcian (Figures 2.3e and 2.5c; Laville *et al.*, 2004) and the Middle Jurassic sequences (Figures 2.3-2.8) exhibit a distinct sheared deformation pattern characterised by the presence of extensional faults. While minor growth strata were identified within the Toarcian, the Middle Jurassic sequence displays growth strata at both mesoscopic and megascopic scales. The normal faults are associated with strike-slip faults featuring extensional component (Figures 2.3a, 2.4d-e, and 2.6), and locally, they show signs of contractional strike-slip deformation (Figure 2.8). The interpreted local stresses (Figures 2.3g, 2.4f, 2.6f, 2.8e) correspond to a different tectonic phase, distinct from the previously mentioned orthogonal phase (Figures 2.5, 2.10-2.11) and the latter orogenic event, whose regional stress was NW-SE (e.g., Frizon de Lamotte *et al.*, 2000; Ait Brahim *et al.*, 2002; Ellouz *et al.*, 2003; Teixell *et al.*, 2003; Ellero *et al.*, 2020). It is important to highlight that the field data indicate that this event had a relatively limited impact on the overall Atlas system, given the sparse network of faults and structures compared to the orogenic event.

Cross-sections (Rolley & Etienne, 1978) along the Aït Attab syncline suggest thin-skinned tectonics involving evaporites at the decollement (Figure 2.1-II1); however, the faults identified in the region (Figure 2.3a-d) may indicate reactivation and involvement of pre-existing thick-skinned NE-SW and ENE-WSW structures. South of the Aït Attab region, the structures in Figure 2.3c-d feature a principal displacement zone (Figure 2.11-1), with the strike-slip fault (Figure 2.3c) in the centre of the zone, and extensional sidewalls (Figure 2.3d). This structural arrangement is reminiscent of previous models of pull-apart basins, resulting from the reactivation of NE-SW trending extensional faults into strike-slip faults surrounded by extensional faults (e.g., Woodcock and Fischer, 1986; Sylvester, 1988; Mann, 2007), and it involves minor halokinesis (Figure 2.3c). The extensional faults (Figures 2.3c and 2.11-1) are either hard or soft-linked to the main strike-slip fault in accordance with prior 4D analogue modelling on transtensional basins (Wu *et al.*, 2009). However, the precise nature of the fault linkage is unclear due to erosion. Similarly, the bounding fault in Aït Attab in Figures 2.1B, 2.3a, and 2.11-1, represents a pre-existing en-echelon structure that has evolved into an extensional oblique-slip horsetail termination as

previously suggested in transtensional basins in California (John C Crowell, 1974) with extensional sidewalls.

2.5.2.2 Relay ramps and folding

Field data (e.g., Peacock and Sanderson, 1995; Fodor, 2007; Rotevatn and Peacock, 2018) and analogue modelling (Wu et al., 2009) have proposed the formation of breached relay ramps under a transtensional stress regime. In contrast, relay ramps under transpression would result in areas of uplift, contractional deformation, and a network of faults that accommodate shortening within the relay ramp or the fault bends (e.g., Peacock and Sanderson, 1995; Rotevatn and Peacock, 2018). In Ouaouizaght, oblique-slip faults with extensional component of approximately E-W trend (Figure 2.4e), which are oblique to the NW-SE fault (Ouaouizaght; Figures 2.1B and 2.4d), were found within the relay ramp of the NE-SW trending faults (Ouaouizaght; Figures 2.1B and 2.1B-A.1). The E-W oblique-slip faults possibly intersect the NW-SE normal fault (Figure 2.4d-e), suggesting the formation of a relay ramp during the orthogonal rifting (Figure 2.10-2) and its reactivation during the oblique extension and the formation of E-W structures (Figure 2.11-2). Whereas, the NW-SE trending fault (Figure 2.4d) may act as a transfer fault.

Extensional and contractional structures have previously been documented in tectonic settings involving oblique divergence (Fossen et al., 2013; Harding, 1974; Kristensen et al., 2018; Sanderson & Marchini, 1984; Venkat-Ramani & Tikoff, 2002), where folding can develop obliquely to direction of extension (e.g., Fossen et al., 2013). In the Agoudal and Er-Rich regions, the Middle Jurassic sequence exhibits extensional and contractional features, with synchronous syn-extensional and syn-contractional growth strata associated with the activity of ENE-WSW and NE-SW inherited structures. Some of the tension gashes and faults observed and analysed in the Middle Jurassic (post-Middle Jurassic faults and tension gashes; Figures 2.6 and 2.8) exhibit consistency to the Cenozoic orogenic stress field and do not show any subsequent deformation. The structures and the syn-kinematic growth strata related to the oblique extension, with the contractional or partly contractional deformation would result in σ_1 trending WNW-ESE (Figure 2.6f) and ENE-WSW (Figure 2.8e) in the Middle Jurassic, for the regions of Agoudal (Figure 2.11-4) and Er-Rich (Figure 2.11-5), respectively. Additionally, in the Er-Rich region, field data (Figure 2.8) and the

restored sections (Figure 2.7) suggest concurrent extensional and contractional features. As a result, the stress regime is more likely to be transtensional (Figure 2.11-5), where local open transtensional folding can occur (Figure 2.8d; e.g., Fossen et al., 2013). In contrast, the Agoudal region appears to display pure strike-slip or contractional strike-slip (Figure 2.11-4) in the Middle Jurassic, due to the lack of extensional growth strata.

2.5.2.3 Magmatism

The Agoudal and Er-Rich regions have been associated with coeval passive salt mobility, causing salt diapirism and welding in the Middle Jurassic, at which point rift-related extension ceased (Bouchouata et al., 1995; Calvín et al., 2018; Ettaki et al., 2007; Martín-Martín et al., 2017; Moragas et al., 2018; Saura et al., 2014; Teixell et al., 2017; Torres-López et al., 2016; Vergés et al., 2017). Consequently, the growth strata were interpreted as salt-driven. In Er-Rich, I believe the evaporites is a key factor for the Middle Jurassic sequence development, which was laterally stretched based on the tectonic regime, and formed a diapir consistent with the transtensional folding. In Agoudal, the strike-slip event may be linked to the Middle Jurassic magmatic intrusions (Laville & Piqué, 1992), which interacted with the evaporites (Bouchouata et al., 1995; Calvín et al., 2018; Ettaki et al., 2007; Saura et al., 2014; Teixell et al., 2017; Torres-López et al., 2016; Vergés et al., 2017) and produced magmatic diapirism (He et al., 2009). The interpretation presented here may be summarised as a synchronous activity of mild tectonism, halokinesis, and potential magmatism along the ENE-WSW faults, similar to the Eastern High Atlas (Allouban et al., 2021).

The Middle Jurassic to Cretaceous magmatic intrusions occur mostly in the Central High Atlas (Armando, 1999), and they are transitional, moderately to purely alkaline (Armando, 1999; Bensalah et al., 2013; Essaifi & Zayane, 2018; Moratti et al., 2018). Their emplacement is believed to have happened during the oblique extensional event (Laville, 1988; Laville & Piqué, 1992). Radiometric dating of the Jurassic to Cretaceous magmatic rocks in the Central High Atlas has given two age ranges of 175-155±5Ma (Toarcian to Kimmeridgian) and 135-110±5Ma (Early Cretaceous) (e.g., Armando, 1999; Frizon de Lamotte et al., 2008). Recent dating of basalts from the southern Central High Atlas using ⁴⁰Ar - ³⁹Ar (Moratti et al., 2018) yielded an age of 120Ma, which is similar to ages from the northern border of the Central High Atlas (e.g., Armando, 1999). However,

the magmatic activity in the core of the Central High Atlas might have occurred during the Middle to Late Jurassic eruption, which triggered halokinesis and diapirism (Figures 2.6b-c and 2.6e; Calvín et al., 2017). This scenario suggests that magmatic activity likely commenced during the Middle to Late Jurassic within the core of the Atlas, and subsequently this volcanism migrated towards the southern and northern borders, manifesting itself through thick-skinned faults during the Early Cretaceous.

On the other hand, if, indeed, the magmatic rocks in the Central Atlas are Early Cretaceous in age, as found in the northern and southern borders of the High Atlas (Armando, 1999; Moratti et al., 2018), they could mark the end of the transtensional event, as previously have been observed in multiple transtensional settings (e.g., Aydin and Nur, 1982; Ngako *et al.*, 2003; Mann, 2007; Fu *et al.*, 2012). Although this determination is uncertain due to the lack of dating in these rocks, and the erosion of the younger sequences, which prevents direct observations (Figure 2.2B). Hence, if the age of magmatic rocks is consistently attributed to the Early Cretaceous, the deformation observed in Agoudal (Figure 2.6) would be predominantly linked to halokinesis.

2.5.2.4 Deformation and stress variation along the Atlas in the Middle Jurassic

The Middle Jurassic sequence reveals features indicative of a tectonic event during this period. The paleostress analysis suggests a regional transtensional tectonic regime (Figure 2.11), where σ_1 exhibits an NE-SW orientation and σ_3 shows a NW-SE orientation, indicating a sinistral movement in the Atlas system. However, variation in the lateral stress field was observed in the Agoudal, Er-Rich, and Bou Annane regions, suggesting complexity at a local scale. The western part of the Central Atlas system experienced transtension (Figures 2.11-1 and 2.11-2), leading to the reactivation of pre-existing troughs (Figure 2.10-1) and relay ramps (Figure 2.10-2) resulting in horsetail terminations (Figure 2.3a) and negative flower structures (Figure 2.3c-d; Mattauer et al., 1977; Schaer and Rodgers, 1987; Laville, 1988; Laville and Piqué, 1992). The core of the Central Atlas experienced strike-slip stress regime, synchronously associated with salt tectonics (Martín-Martín et al., 2017; Moragas et al., 2018; Saura et al., 2014; Teixell et al., 2017; Vergés et al., 2017) and the potential Middle Jurassic volcanism (Figures 2.6 and 2.11-4) that formed open synclines and overturned

anticlines. While, towards the east of the system, the stress regime changes to transtensional with local folding (Figures 2.7 and 2.11-5). Finally, orthogonal extension occurred in the Bou Annane region (Figure 2.10-6), which as earlier mentioned suggests rift migration to the east (Escosa et al., 2021). Finally, the oblique extension ceased during the late stages of the Middle Jurassic to Cretaceous, followed by multiple phases of dextral transpression since the Cretaceous, leading to the inversion of the Atlas system (e.g., Frizon de Lamotte et al., 2009).

Orthogonal extension

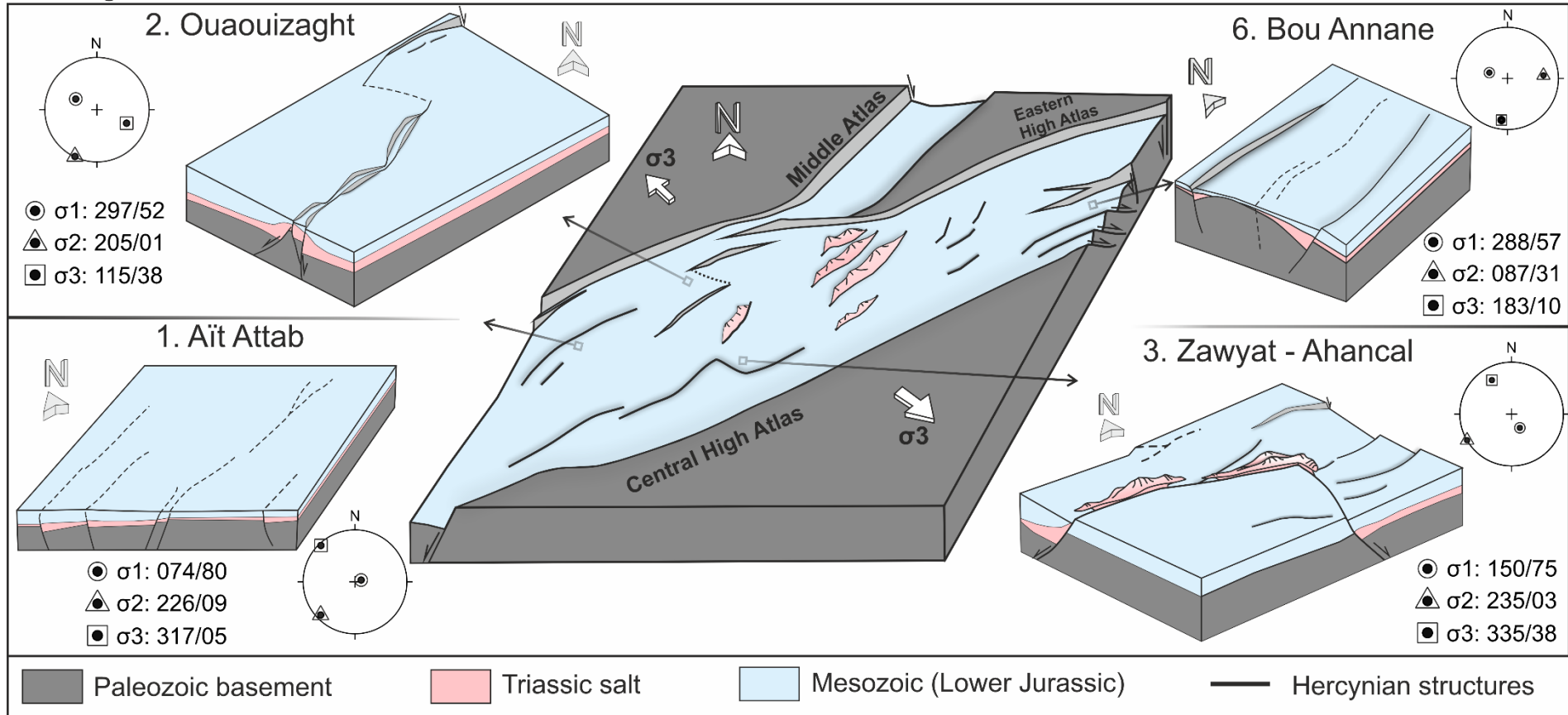


Figure 2.10: Schematic 3D tectonic model of the Atlas rift system during the orthogonal phase in the Late Triassic to late Early Jurassic. Detailed representation of the outcrops where orthogonal extension was observed and their calculated local stress. 1. Aït Attab; the orthogonal extension occurred mostly in the Triassic than Jurassic and produced grabens. 2. Ouaouizaght; the orthogonal extension influenced both Upper Triassic to Lower Jurassic sequences and formed a soft or hard-linked relay ramp. 3. Zawyat – Ahancal; the orthogonal extension occurred during the Late Triassic to Early Jurassic, which reactivated ENE-WSW faults and developed half grabens. 6. Bou Annane; Two distinct orthogonal extensional events occurred during the Late Triassic and Early Jurassic to Middle Jurassic boundary. The stereonet refers to the latest orthogonal event.

Oblique extension

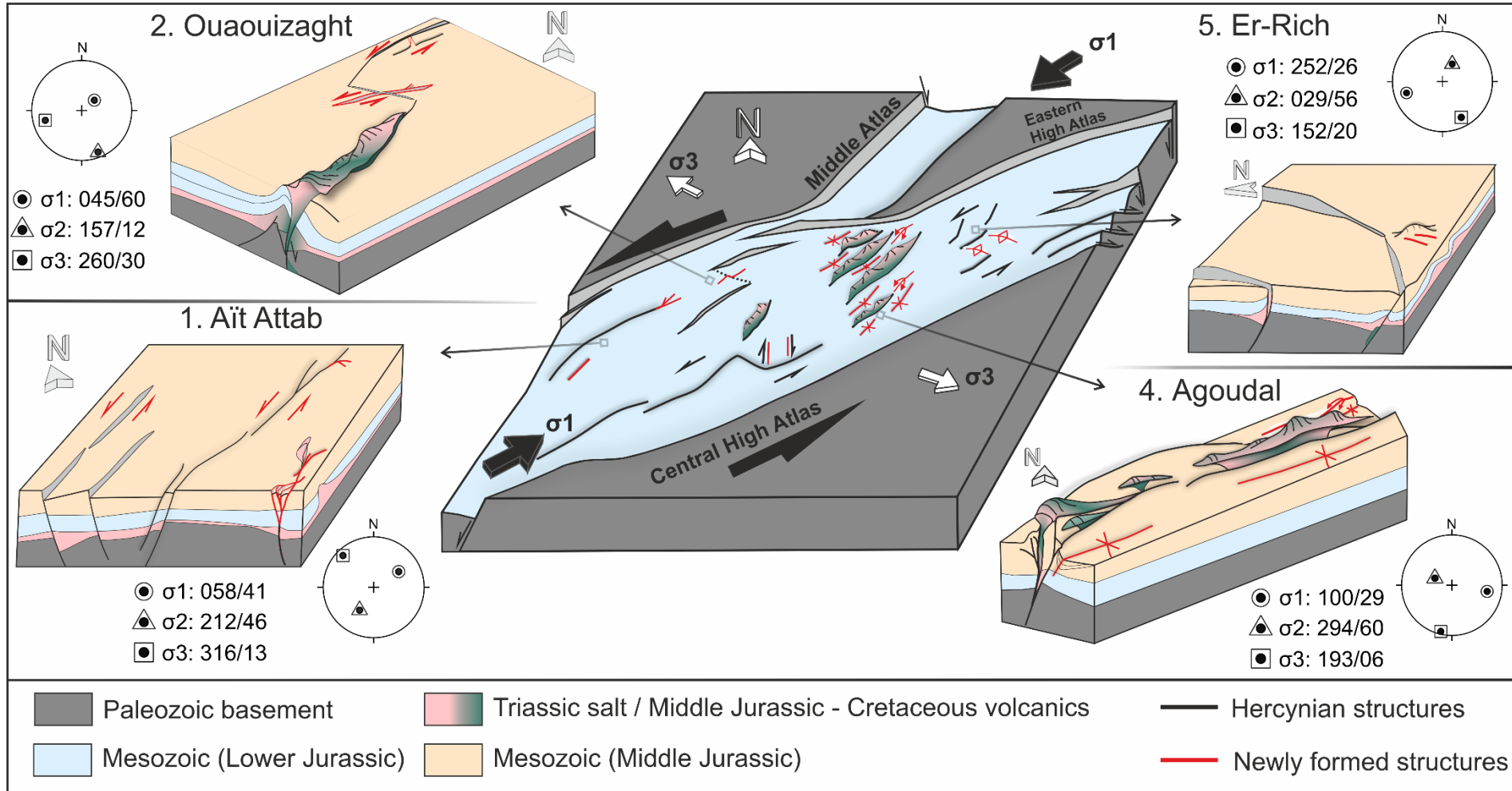


Figure 2.11: : Schematic 3D tectonic model of the Atlas rift system during the oblique extensional phase in the late Early Jurassic to Middle Jurassic. Detailed representation of the outcrops where oblique extension was identified, and their calculated local stress. 1. Aït Attab; the oblique extension reactivated the structures and evolved the structures to strike-slip splays and negative flower structure, which involved halokinesis. 2. Ouaouizaght; the oblique extension reactivated the pre-existing structures and developed the core of the hard-linked relay ramp with ENE-WSW extensional oblique-slip faults. Magmatism might have been occurred in the southern fault. 4. Agoudal; gentle oblique transpression associated with evaporites and potential magmatic activity in the ridge. 5. Er-Rich; the oblique extension reactivated the pre-existing normal faults, and developed open folding.

2.6 Conclusion

The Moroccan High Atlas Mountains is an aborted rift system that underwent different phases of extension during the Mesozoic. The extensional phases are related to the coeval Central Atlantic and Tethyan opening; and the relative left-lateral oblique movement between Africa and Iberia.

Field data in the Central and Eastern High Atlas focuses on the structural and stratigraphic development within the rifted basin, and identified a phase of Late Triassic to Early Jurassic orthogonal extension and a phase of Middle Jurassic oblique extension. The results of the field analyses can be summarised as follow:

- Late Triassic- Early Jurassic:
 - Orthogonal extension reactivated mostly ENE-WSW and NE-SW pre-existing Hercynian structures,
 - The regional stress regime was extensional, with σ_3 exhibiting NW-SE orientation and the σ_1 axis predominantly vertical to inclined. Consequently, the influence of the Atlantic opening was more dominant than that of the Tethyan opening.
 - Orthogonal extension formed half-grabens and troughs along ENE-WSW and NE-SW faults. Pre-existing structures were locally reactivated as oblique-slip features, resulting in relay ramps.
- Middle Jurassic (- Early Cretaceous?):
 - The regional stress regime became an oblique extension in the Central Atlas system, with σ_1 and σ_3 exhibiting orientations of NE-SW and NW-SE, respectively. The deformation recorded in the Middle Jurassic was limited in response to the rift-related processes.
 - The oblique extension developed a stress variation lengthwise in the Atlas system involving the pre-existing structures.
 - In the western Central High Atlas, the paleostress regime remained similar to the orthogonal phase, with a slight change in the inclination of the σ_1 axis. This alteration led to the formation of oblique-slip and strike-slip features in pre-existing structures,

characterised by the development of horsetail terminations, transtensional flower structures, and NW-SE transfer faults.

- The core of the Central High Atlas, experienced pure or contractional strike-slip deformation, with the synchronous halokinesis and possibly Middle Jurassic volcanism, that led to contractional features (e.g., Agoudal).
- In the Central to Eastern High Atlas transition, the transtensional structures (e.g., Er-Rich) coincided with transtensional folding.
- In the Middle Jurassic, the potential for magmatic activity within fault zones coinciding with halokinesis at the core of the central Atlas system is present. This magmatic activity could have migrated from the core to the borders of the Atlas system over time. The occurrence of volcanism is linked to the oblique extension, either synchronous taking place in the Middle Jurassic or indicating the end of the regional oblique extension in the Atlas system in the Early Cretaceous.

Chapter 3 - Florida margin, Eastern Gulf of Mexico: Identifying strike-slip activity during rifting

This chapter has been published as:

Vasileiou, A., Gouiza, M., Mortimer, E., Paton, D., Nanfito, A., Lewis, D. 2023. New insights into the crustal architecture and tectonic evolution of the Eastern Gulf of Mexico. Basin Research. 10.1111/BRE.12812

Summary

The Gulf of Mexico is an intraplate oceanic basin where rifting commenced in the Late Triassic, leading to drifting and ensuing oceanic accretion by Middle-Late Jurassic, which ceased by the Early Cretaceous. Its tectonic evolution encompasses multiple rifting phases dominated by orthogonal extension, variable magmatism, and salt deposition. This complex tectonic history is recorded within the rifted margins of the Gulf of Mexico, including along the eastern part of the basin, where considerable uncertainty remains regarding the tectonic evolution and resulting crustal configuration.

This chapter presents new insights into the crustal types and an updated tectonic framework for the Florida margin. An integrated analysis of seismic and potential field data allows to characterise the nature of the crust, which shows wide zones of hyperextended continental crust, seaward dipping reflection (SDR) packages, exhumed mantle and magmatic crust.

The results propose elements that could improve the plate model of the Gulf of Mexico, by accounting for the polyphase nature of rifting, the counter-clockwise rotation of the Yucatan block, and the observed increase in magmatic supply.

3.1 Introduction

The Gulf of Mexico (GOM) is an oceanic basin located within the southern part of the North American plate and bound to the south by the Caribbean plate. The GOM is a tectonically complex basin that formed during the Mesozoic due to the break-up of Pangaea and the counter-clockwise rotation of the Yucatan block in the south (Marton & Buffler, 1994; Marton & Buffler, 1999; Pindell, 1985; Pindell & Kennan, 2009; Pindell & Dewey, 1982; Pindell & Kennan, 2001). In the past two decades, a number of adjustments to the rotational tectonic model have been proposed for the evolution of the GOM margin (e.g., Pindell and Kennan, 2001; Bird et al., 2005; Kneller and Johnson, 2011; Hudec, Norton, et al., 2013; Eddy et al., 2014; Minguez et al., 2020; Pindell et al., 2021; Izquierdo-Llavall et al., 2022; Pindell and Heyn, 2022; Filina and Beutel, 2022). These models provide some constraints on the crustal architecture and the timing of salt deposition and its subsequent mobility. However, it is only recently that the margin's rift to drift evolution and subsequent crustal configuration has begun to be better understood (Filina et al., 2022; Filina & Beutel, 2022; Filina & Hartford, 2021; Izquierdo-Llavall et al., 2022; Pindell et al., 2011).

Some efforts to better understand the region were made with the Gulf of Mexico Basin Opening (GUMBO) project, in which four regional refraction sections were undertaken in the GOM. Two GUMBO sections, Lines 3 and 4 (Figure 3.1) are located within the eastern Gulf of Mexico (EGOM) and were analysed by Christeson et al. (2014) and Eddy et al. (2014) to gain further insights into the margin's evolution. The GUMBO Lines in the Florida margin reveal different crustal types within the transitional domain with interpreted SDRs in Line 3 (Eddy et al., 2014) and attenuated continental crust in Line 4 (Christeson et al., 2014). The crustal and magmatic variability from the northern to southern province of Florida has also been supported by seismic reflection data (Curry et al., 2018; Eddy et al., 2014; Izquierdo-Llavall et al., 2022; Liu et al., 2019; Pindell et al., 2011). In addition, aeromagnetic data analysis suggests the presence of hyperextended continental crust and exhumed mantle along the Florida margin (Curry et al., 2018; Minguez et al., 2020; Pindell et al., 2016). However, despite the different approaches the nature of the crust in the distal domain of the margin remains controversial.

The location of the inner limit of the oceanic crust (ILOC) and the nature of the continent-ocean transition are usually difficult to image in seismic data due to their equivocal seismic characteristics, the presence of salt, and magmatic additions (Erlich & Pindell, 2020; Heatherington & Mueller, 1999, 2003). Different interpretations of the continent-ocean boundary and extinct spreading ridges have been proposed (Figure 3.1) using plate reconstructions, seismic data, gravity data, and/or magnetic data (e.g., Bird et al., 2005; Pindell and Kennan, 2009; Kneller and Johnson, 2011; Hudec, Norton, et al., 2013; Eddy et al., 2014; Sandwell et al., 2014; Nguyen and Mann, 2016; Pindell et al., 2016; Deighton et al., 2017; Lundin and Doré, 2017; Filina et al., 2020; Minguez et al., 2020; Izquierdo-Llavall et al., 2022; Filina and Beutel, 2022).

Here, we use good resolution regional seismic reflection profiles (Figure 3.1) and potential field data (Sandwell et al., 2014; Meyer et al., 2017) to unravel the tectono-stratigraphic architecture of the EGOM. We interpret the different crustal types across the EGOM, map these crustal domains, and then use these interpretations to constrain forward gravity modelling to quantify the deep crustal structure and validate the different crustal types invoked across the margin. These new crustal and structural interpretations are integrated to propose further adjustments to the tectonic model for the evolution of the EGOM.

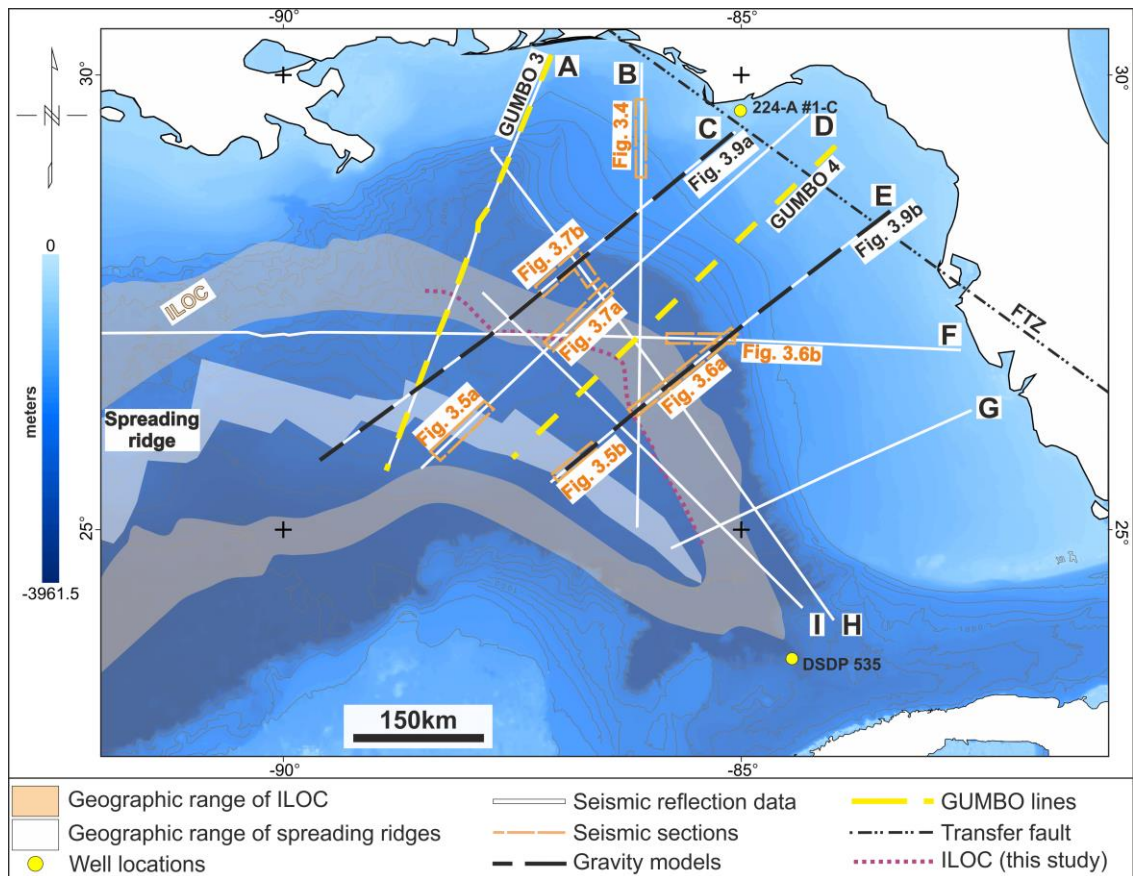


Figure 3.1: Bathymetry map (Smith & Sandwell, 1997) in the Florida margin, Eastern Gulf of Mexico, which includes: the transparent orange and white zones that correspond to the geographic range of the inner limit of the oceanic crust (ILOC) and the extinct spreading ridges, respectively, previously interpreted in the EGOM (Bird et al., 2005; Pindell and Kennan, 2009; Kneller and Johnson, 2011; Hudec, et al., 2013; Christeson et al., 2014; Sandwell et al., 2014; Nguyen and Mann, 2016; Pindell et al., 2016; Deighton et al., 2017; Lundin and Doré, 2017; Filina et al., 2020; Minguez et al., 2020; Izquierdo-Llavall et al., 2022; Filina and Beutel, 2022); black dotted/dashed line traces represent formerly proposed NW-SE trending transfer fault (FTZ: Florida Transfer Zone; Pindell, 1985); yellow dashed line traces are the GUMBO refraction lines 3 and 4; seismic lines used in this study are shown in white, with portion of interest displayed in Figures 3.4-3.7 highlighted in orange, and black dashed traces indicating the 2-D gravity models presented in Figure 3.9. The location of the well 224-A #1-C (Babcock, 1970) in the north, and the DSDP Leg 77, site 535 (Schlager, 1984; Buffler et al., 1984) in the south which were used to further analyse the age and nature of volcanism, and the top of syn-rift sequence. Seismic data courtesy of TGS.

3.2 Geological Background

The Gulf of Mexico formed due to two phases of rifting, the first of which is related to the breakup of Pangea and separation of North America from Africa, initiating in the Late Triassic and continuing until the Middle Jurassic (Pindell and Dewey, 1982; Pindell, 1985; Marton and Buffler, 1994; Pindell and Kennan, 2009; Kneller and Johnson, 2011; Hudec, et al., 2013; Eddy et al., 2014; Nguyen and Mann, 2016). Extension was oriented NW-SE (Figure 3.2a) and resulted in NE-SW trending rift basins, which were filled by fluvio-lacustrine sediments (Bird et al., 2005; Buffler & Sawyer, 1985; Curry et al., 2018; Eddy et al., 2014; MacRae & Watkins, 1996; Pindell & Kennan, 2001; Rowan, 2014; Salvador, 1987; Steier & Mann, 2019). Houston Magnetic Anomaly (HMA), Florida Magnetic Anomaly (FMA) and the Campeche Magnetic Anomaly (CMA; Figure 3.2b) are major magnetic anomalies that formed in relation to the emplacement of volcanic flows (i.e., seaward dipping reflections – SDRs) in the EGOM (Eddy et al., 2014; Filina & Beutel, 2022; Hall, 1990; Imbert & Philippe, 2005; Kneller & Johnson, 2011; Liu et al., 2019; Mickus et al., 2009; Pindell et al., 2011; Rowan, 2014; Steier & Mann, 2019). Salt deposition also occurred at the end of this phase of continental rifting. The salt deposits were initially assumed to be Callovian (Salvador, 1991), however, strontium isotope records (e.g., Posey et al., 1987) and a recent isotope analysis (Snedden and Galloway, 2019; Pulham et al., 2019; Pindell et al., 2019) suggest an older Bajocian age, but could be Bathonian and possibly Callovian in the younger salt sequences.

Counter-clockwise rotation of the Yucatan block initiated at the end of this first rifting phase leading to a second extensional phase oriented NE-SW locally in the north-east Gulf of Mexico and roughly NNE-SSW in the central and southern parts of the Gulf (Eddy et al., 2014; Pindell & Kennan, 2001). However, due to the continuous separation of North America from Africa, the regional extension remained WNW during the second phase of rifting (Müller et al., 2019). This eventually led to oceanic spreading between Yucatan and North America (Hudec et al., 2013; Sandwell et al., 2014). By the Berriasian, the Yucatan block had rotated along the Western Main Transform (Figure 3.2d) fault to the SW of the GOM (Marton & Buffler, 1994; Pindell, 1985). Yucatan's rotation could have been accommodated by the sinistral system of the parallel North Oaxaca and Florida-Bahamas Transfer Faults to the SW and the NE of the GOM, respectively (Pindell

et al., 2021). The rotation was about ca. 42° around a pole that migrated southwards, relative to North America, along the western margin of Florida into the Florida Straits or even south of Cuba (Bird et al., 2005; Buffler & Sawyer, 1985; Marton & Buffler, 2016; Pindell, 1985; Pindell et al., 2016, 2021; Salvador, 1987). The age of seafloor spreading is also uncertain, and could have commenced either in the Bathonian-Oxfordian or Kimmeridgian (Hudec et al., 2013; Eddy et al., 2014; Pindell et al., 2020b). Spreading ceased either in the Late Jurassic (Kneller & Johnson, 2011) or in the Early Cretaceous, between the Berriasian and Valanginian (Pindell, 1985; Marton and Buffler, 1994; Bird et al., 2005; Eddy et al., 2014).

In addition to the orthogonal structures formed during the NW-SE and NE-SW extensional phases, strike-slip structures have been suggested to be active during the rifting by several authors (e.g., Klitgord et al., 1984; Pindell, 1985; MacRae and Watkins, 1996; Pindell and Kennan, 2009). The most significant and well-studied transfer fault in the NE GOM is the sinistral Florida-Bahamas Transfer Zone (FTZ; Figures 3.1 and 3.2a), which accommodated 300 to 400 km of displacement during the first phase of rifting (Erlich & Pindell, 2020; Pindell, 1985; Pindell & Kennan, 2009; Pindell et al., 2021) and allowed the south-eastward motion of the Florida Straits.

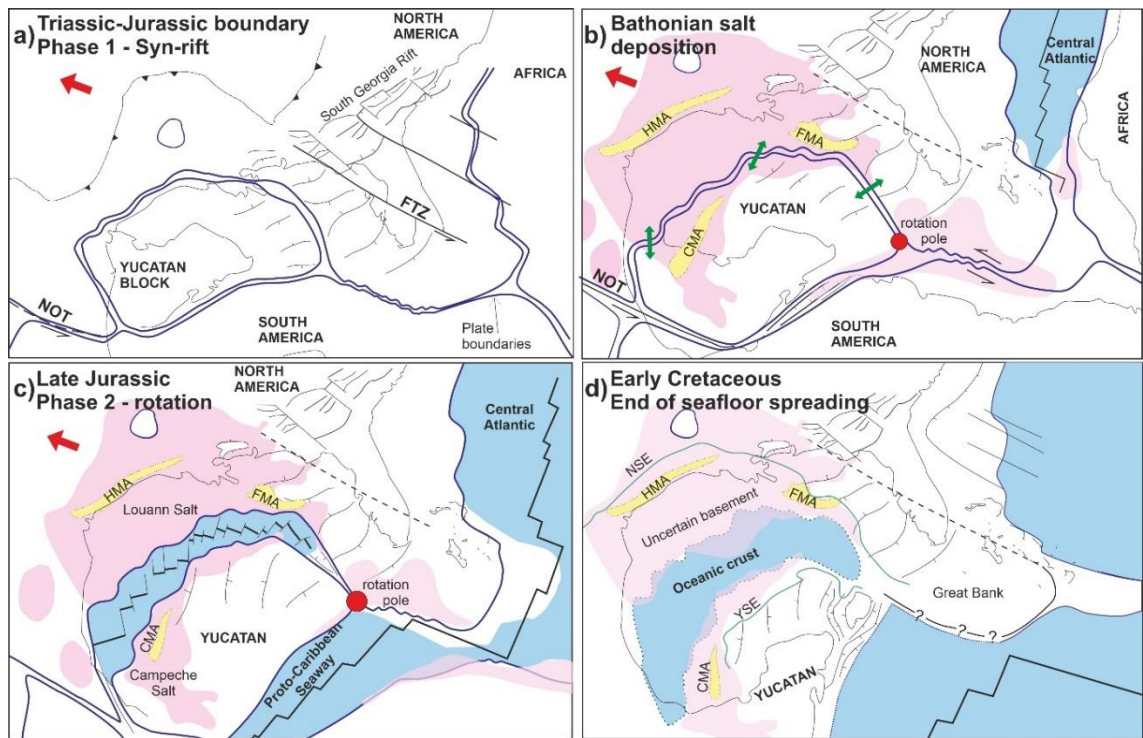


Figure 3.2: (a-d) Tectonic evolution of the Gulf of Mexico (modified from Steier and Mann, 2019; Pindell et al., 2020a; Pindell and Heyn, 2022). (a) Initiation of Pangaea’s breakup with North America plate WNW synchronous motion (Müller et al., 2019; red arrow). The first phase of rifting was NW-SE with sinistral slip of the Florida-Bahamas Transfer Zone (FTZ). (b) Middle Jurassic continental extension, formation of Houston Magnetic Anomaly (HMA), Florida Magnetic Anomaly and Campeche Magnetic Anomaly (CMA) (Pindell et al., 2016) and deposition of Middle Jurassic salt. Green arrows indicate the local orientation of extensional between North America plate and Yucatan Block. (c) Yucatan’s counter-clockwise rotation and oceanic seafloor spreading during the Late Jurassic. (d) End of seafloor spreading in the Early Cretaceous. Green lines indicate the Cretaceous shelf in Florida and Yucatan margins.

3.3 Data and Approach

3.3.1 Data

This study utilises a suite of nine 2D seismic reflection profiles (Figure 3.1) provided by TGS in two-way travel time (tw) recorded to 14 s. They are oriented NE-SW, E-W and NW-SE with lengths ranging from 500km to 1,500km. These seismic lines partially image the Moho discontinuity; while the basement, syn-rift and post-rift sequences are well imaged, where evaporites are not present. Our seismic data were complemented by integrating published seismic interpretations and well data (Buffler et al., 1984; Marton and Buffler, 1999; 2016) from DSDP leg 77 (site 353; Figure 3.1). These data are located to the southeast of our study area and were used to correlate the top syn-rift sequence previously identified in DSDP leg 77, site 535 (Buffler et al., 1984; Marton and Buffler, 1999; 2016) into our seismic reflection lines and construct the structural framework at the southwestern part of the Florida margin.

Public domain satellite free air gravity (Figure 3.3a; Sandwell et al., 2014), residual gravity (Figure 3.3b), its vertical gradient (Figure 3.3c) and Earth Magnetic Anomaly Grid (Figure 3.3d; EMAG2v3; Meyer et al., 2017) were used alongside the seismic profiles to refine our structural and crustal interpretations. The residual gravity map was calculated from the free air gravity by removing the effect of the water column, to enhance the anomalies related to crustal boundaries in the deep offshore. It was calculated assuming a water density of 1.03 g/cm^3 and an average rock density of 2.67 g/cm^3 . The magnetic data were primarily used to identify the extent of the oceanic crust and rift-related magmatism. Nevertheless, magnetic anomalies in the Eastern Gulf of Mexico are not all rift-related (Babcock, 1970; Heatherington & Mueller, 1991, 2003). Onshore and offshore drillhole sample analysis in the Florida region suggests that some magnetic anomalies could be related to Gondwanan or Pan-African Palaeozoic magmatic activity, the Central Atlantic Magmatic Province (CAMP), and/or the diachronous magmatic activity of the Suwannee terrane (Erlich & Pindell, 2020; Heatherington & Mueller, 2003) and should therefore be treated with some caution.

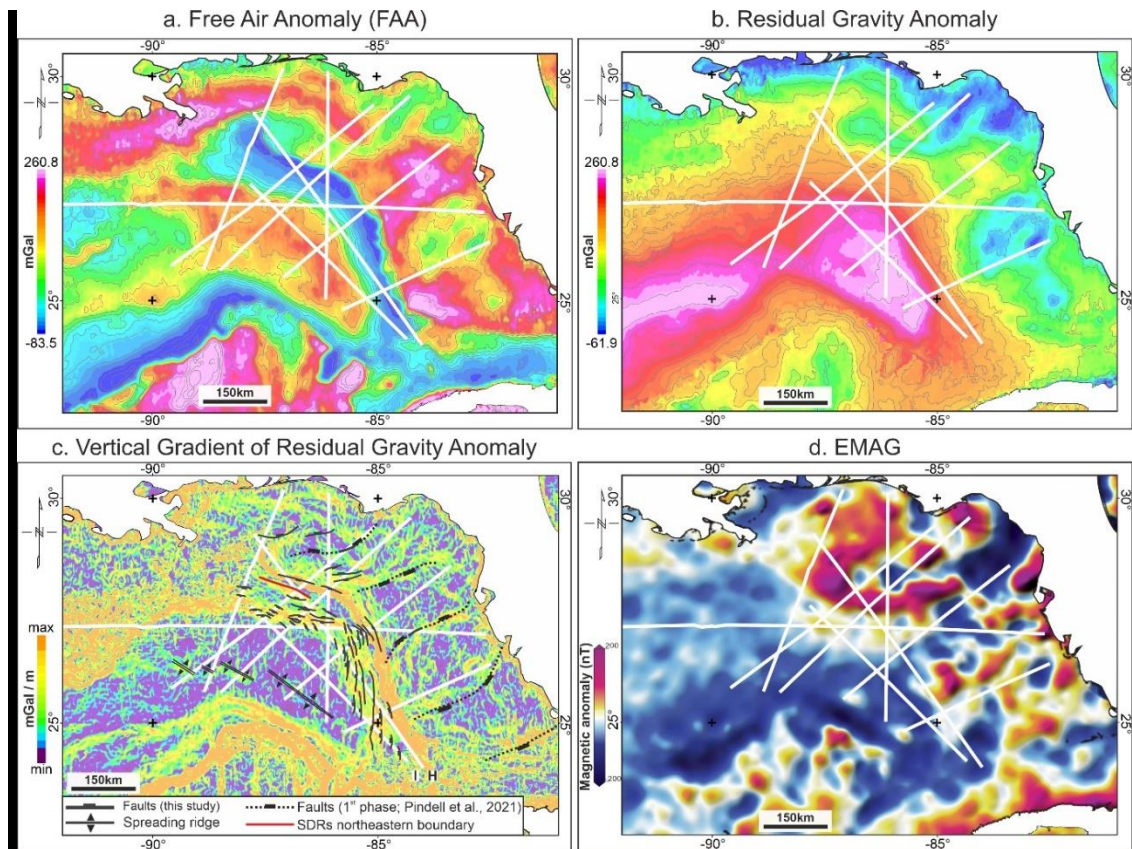


Figure 3.3: (a) Free Air Gravity Anomaly (FAA; Sandwell et al., 2014); (b) Residual gravity anomaly; (c) Vertical gradient of Residual gravity anomaly with structures trends, and (d) Earth Magnetic Anomaly Grid (EMAG; Meyer et al., 2017) in the Eastern Gulf of Mexico. Seismic data courtesy of TGS.

3.3.2 Approach

Sedimentary sequences and crustal types were interpreted along the seismic reflection profiles primarily based upon their seismic character. We identify key seismic reflections from stratal terminations, internal reflection geometry (e.g., divergence and thickening of syn-rift sequences) and seismic facies (i.e., reflection amplitudes and continuity) that enables us to define distinct packages: post-rift and syn-rift sedimentary sequences, a salt unit, and a post rift carbonate platform.

Due to the lack of publicly available well data, the age of the interpreted seismic horizons and packages was inferred from published literature. The age of the transition from syn-rift to post-rift remains ambiguous, as different well data along the margin indicate either Berriasian (Figure 3.1, DSDP 535, SE GOM; Marton and Buffler, 1999; 2016) or Tithonian (Hudec, Norton, et al., 2013) ages. However, in this study, due to the diachronous breakup along the Gulf of Mexico, the younging direction of rifting and drifting towards the south (Deighton et al.,

2017; Filina & Beutel, 2022; Lundin & Doré, 2017; Minguéz et al., 2020; Nguyen & Mann, 2016; Pindell & Heyn, 2022; Sandwell et al., 2014), and the lack of published well data in the Florida margin, we interpreted the syn- to post-rift transition to be Tithonian (Late Jurassic) in age, based on the unpublished well data of (Hudec, Norton, et al., 2013), which is located in the NE GOM.

The different crustal types were interpreted in the 2D seismic data based on their seismic facies, and are further addressed in the following section. Crust types were then used to create a crustal domain map. High amplitude reflections imaged at -10 to -12 s (twt) in the majority of the 2D seismic data were interpreted as Moho reflections. Despite the good coverage of the seismic data, the wide spacing between sections requires an extrapolation of crustal types across tens of kilometres, something that is of particular importance when considering the mapping of crustal boundaries. To assist with this, and reduce this uncertainty, potential field data were used to characterise these boundaries and aid their interpolation throughout the study area.

The presence of salt and thick carbonates on the shelf reduces the seismic imaging quality of the underlying sediments and basement and increases the uncertainty in our interpretation. In addition, the interpretation of the salt bodies could vary, due to the low seismic resolution where salt is present.

3.4 Stratigraphic and Crustal Architecture

Representative sections showing the interpreted stratigraphic and crustal architecture of the basin are presented in Figures 3.4-3.7. We first consider the main sedimentary packages before examining the underlying Moho and crustal structure.

3.4.1 Rift to drift sedimentary sequences

The pre-rift sequence is identified only in the shelf domain at the northern part of the Florida margin. We distinguish this sequence by high amplitude reflections with consistent original thickness, which are tilted and truncated (Figure 3.4; see also Pindell et al., 2011; Liu et al., 2019; Izquierdo-Llavall et al., 2022). This sequence has previously been interpreted as a syn-rift volcanoclastic sequence (Liu et al., 2019; Menzies et al., 2002), but could also be Appalachian deformed

section (Eddy et al., 2014). Furthermore, well 224-A #1-C (Figure 3.1), located close to this volcanic sequence, encounters Triassic volcanic material (Babcock, 1970; Heatherington & Mueller, 2003); and recent zircon analysis (Erlich & Pindell, 2020) supports igneous activity offshore North Florida and the western Bahamas in the Middle Triassic that expanded to the onshore of North Florida and South Georgia in Late Triassic to Early Jurassic. We believe that this sequence is likely to be related to a pre-rift magmatic event or local volcanism before or during the earliest stages of rifting. This pre-rift sequence is not observed in the southern part of the shelf domain.

Due to the lack of well data and poor subsalt seismic imaging, there is high degree of uncertainty within the syn-rift sequence. The syn-rift sequence exhibits variable seismic characteristics, with either chaotic low amplitude reflections (Figure 3.4, 3.6a and 3.7a) or more continuous high amplitude reflections (Figure 3.7). It is capped by downlap terminations and can be recognized by the presence of growth strata. It is, however, difficult to image where salt deposits are present. The syn-rift is interpreted to be thin within the shelf domain with chaotic but high amplitude reflections and no apparent growth strata. The lack of syn-rift growth geometry could be related to the orientation of the seismic lines, which are perpendicular to the NW-SE Late Triassic extension. Within the syn-rift sequence, the Middle Jurassic Bajocian salt (Figure 3.6 and 3.7a) is characterised by chaotic and low amplitude reflections and shows an irregular geometry due to halokinesis. In the south of the margin, salt was deposited onto the basement, and the growth strata above the salt are well imaged (Figure 3.7a). In the north, where salt deposits are considerable and have been extensively mobilised, syn-rift sediments are less well imaged and are difficult to interpret with confidence (Figure 3.7a). The salt is primarily autochthonous, with major salt diapirs in the NW and minor local salt diapirs and pillows in the SE. Local allochthonous salt appears to be fault controlled and is observed primarily south of seismic line F (see location on Figure 3.1) along the shelf (Figure 3.6).

The post-rift package comprises a thick carbonate sequence (thickness between 2.3 and 3.5 s twt) in the shelf domain and siliciclastic sequences in the deep basin (Dobson & Buffler, 1997; Snedden et al., 2014). The carbonate platform forms a continuous package of high amplitude reflections (Figure 3.4 and 3.6b), whereas the post-rift siliciclastics increase in thickness in the NW and are affected by the

post-rift salt movement. In contrast, the siliciclastic post-rift sequences in the south are relatively undisturbed. The thickness of the carbonate platform increases from NW to SE between seismic lines B-C and E-F, which could be related to the first rift-phase related NE-SW trending horsts of the continental crust.

3.4.2 Structural configuration

Faults were identified in the shelf domain and in the deep oceanic basin with a variety of dip angles and orientation. Seismic data show that the basement in the shelf domain is affected by NW-SE trending extensional faults (Figure 3.4). Other faults orientation, i.e., parallel to the directions of the seismic lines, may exist, but would not be clearly imaged in the 2D data. Oceanward and landward dipping normal faults have previously been identified at the hinge of the carbonate platform (Izquierdo-Llavall et al., 2022; Pindell et al., 2011), however, we interpreted these faults with low confidence on our seismic data (Figure 3.6; dashed extensional faults).

In the deep basin, listric normal faults are identified dipping SW, in seismic line E (Figure 3.6a), and W, in seismic line F (Figure 3.6b). In both cases, the faults reach a deep high amplitude reflection, which could be mid-crustal detachment level or the Moho. In seismic line E (Figure 3.6a), tilted blocks bounded by normal faults are well imaged and define half-grabens with syn-rift infill. The dip direction of these normal faults was established using the syn-rift growth strata geometry. Most seismic lines show SW-dipping normal faults; however, in seismic line D (Figure 3.7a) the dip-direction changes locally to the NE. It is worth noting that due to the 2D nature of the seismic data, the imaged dip direction of faults is the apparent dip.

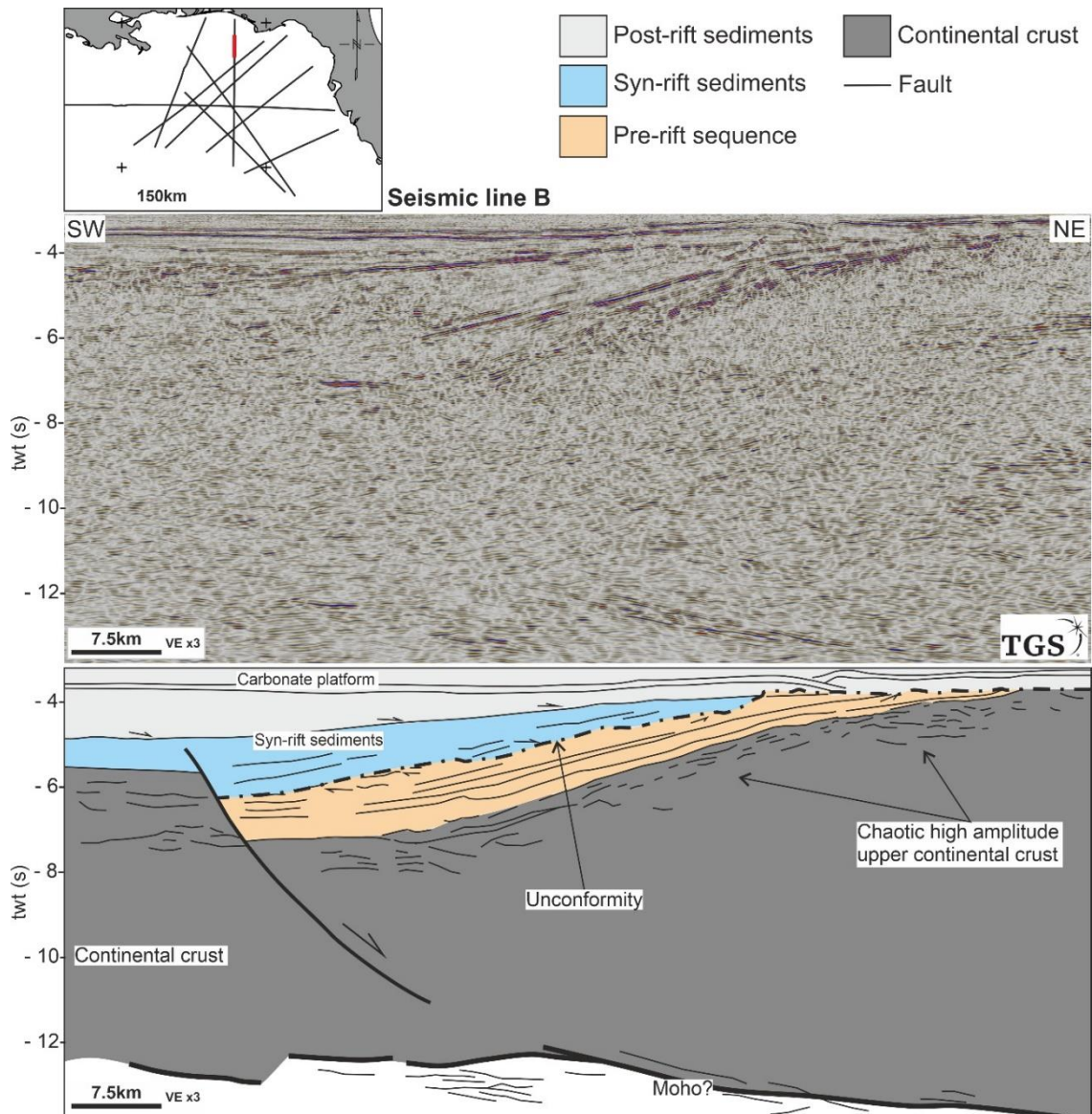


Figure 3.4: High amplitude eroded pre-rift sequence in the shelf domain, which is placed between syn-rift sediments and continental crust. Full seismic line of high resolution is provided in Appendix (Figure B.1). Seismic data courtesy of TGS.

3.4.3 Crustal Types

The Moho is partly imaged in the data as a high amplitude reflection occurring at depths between -10 and -12 s (twt). Different crustal types were identified between top basement and the Moho, based on their distinct seismic characters.

Oceanic crust (Figure 3.5a and 3.5b) is presented in the distal domain of the margin. It is defined by high amplitude reflections at the top, a relatively well imaged high amplitude Moho at the base, and a fairly consistent thickness (~2.5-3.0 s twt), typical for oceanic crust (Hoggard et al., 2017; Paton et al., 2017). Extinct spreading ridges are imaged along the southern edge of the study area, and can be up to 30 km wide, forming trough geometries filled with post-spreading

sediments and underlain by thinner oceanic crust (Figure 3.5a). Variable scale medium to high amplitude geometries are found close to the spreading ridge segments, with Moho reflection pull-up underneath them. These geometries are up to 10km wide and are likely to be submarine volcanoes (Figure 3.5a; Lin et al., 2019) due to their amplitude reflectivity, the pull-up seismic imaging beneath them, and the onlaps on both their sides. High amplitude reflections offset the oceanic crust and Moho (Figure 3.5b) and could indicate either faults or dykes (Ding et al., 2018). Faults are mainly imaged close to the spreading ridge (Figure 3.5a and 3.5b), while dykes are imaged cutting the oceanic crust from the base (i.e., Moho) to the middle of the crust (Figure 3.5a).

Continental crust is presented in both the proximal and distal domains of the margin (Figures 3.6 and 3.7a). In the proximal domain, continental crust is imaged beneath the carbonate platform (Figure 3.4 and 3.6) with seismic facies characterised by parallel to sub-parallel reflections of low to medium amplitude and discontinuous high amplitude reflections at depth in some locations. The underlying continental Moho is poorly imaged and was picked (with low confidence) around -12 s (twt), along beneath sets of deep and discontinuous high amplitude reflections (Figure 3.6). Irregular high amplitude reflections are imaged within the continental crust along the shelf in both proximal and distal domains. In the proximal shelf, the high amplitude reflections are located in the lower continental crust and could represent magmatic intrusions and/or ductile shear within the lower continental crust (e.g., Harry and Sawyer, 1992); however, these are not imaged in all seismic reflection lines. Consequently, the upper and lower continental crust are difficult to distinguish. In the deep domain of the margin, continental crust is characterised by more chaotic, high amplitude reflections, while the Moho exhibits a weak seismic signature. Moho is difficult to pick in places where there is salt in the overlying basin (Figure 3.7a), whereas its depth is uncertain under the more prominent high amplitude reflection of faults detachment (Figure 3.6). In seismic lines E and F, strong and discontinuous reflections are found beneath the high amplitude reflection (Figure 3.6), which could indicate the existence of a lower crustal layer, magmatic intrusions, or partly serpentinized mantle, which will be further examined in the gravity analysis section. Overall, regardless of the Moho depth, the imaged and identified continental crust in the deep margin predominantly consists of listric normal fault-

bounded tilted blocks between 1.0 and 2.5 s (tw) (Figures 3.6 and 3.7a). Lastly, the geometry of the faults in seismic line D (Figure 3.7a) indicate a trough geometry, which juxtaposes against the oceanic crust, and could be interpreted as an outer marginal trough (Curry et al., 2018; Hudec, Jackson, et al., 2013; Hudec & Norton, 2019; Pindell et al., 2014).

An undifferentiated crustal domain is observed along the margin, where the nature of the crust (i.e., continental vs. oceanic) remains ambiguous. The crust in this domain can be divided into two unknown types with different seismic characteristics, which juxtapose the thin continental crust of the distal domain in different seismic lines (Figure 3.6). For simplicity, we will refer to them as crust type I and crust type II. Crust type I (Figures 3.6b and 3.7b) consists of a zone of chaotic, medium amplitude reflections that juxtaposes the continental crust. It is found beneath a small number of salt deposits, and is bound by continental crust, crust type II, and a sequence of high amplitude dipping reflection that will be examined below. SW of the hinge and the carbonate platform, the top of crust type I is almost a second (tw) shallower than the continental crust (Figure 3.6b), which could indicate potential exhumed mantle. Crust type II (Figure 3.6) is located between continental and oceanic crust. This crust has a consistent thickness of 2.4 s (tw), but thickens closer to the continental crust, locally thins, and is faulted in its upper part (Figure 3.6). The transition between crust type II and the continental crust is equivocal, and different interpretations are possible. The Moho is partly imaged beneath crust type II, it is shallower close to the oceanic crust and deeper close to the continental domain. Top crust type II is characterized by low amplitude reflections with medium amplitude small geometries similar to the oceanic crust (Figure 3.5a). Within and close to the top of the crust, high amplitude reflections are frequent, dipping both oceanward and continent-ward, and high amplitude reflections penetrate the crust close to the continental crust (Figure 3.6a). These characteristics suggest that this crust is different from the true oceanic crust and from the unambiguous continental crust.

Some high amplitude reflections, shown in Figure 3.7b, are bound by continental crust and crust types I and II. Their geometry, seismic characteristics, associated high magnetic anomaly (Figure 3.3d), and deep nature (between -6.5 s and -11.5 s (tw)) suggest that these reflections could be SDRs. Low amplitude reflections observed beneath these in seismic line C (Figure 3.7b) could potentially

correspond to the Moho or the continental basement. The interpreted SDRs in seismic lines C and H are dipping to the SSW. High amplitude reflections with geometries, similar to volcanoes interpreted before, are located on the SDRs; which we interpret these as post-SDR volcanic edifices (e.g., Norcliffe et al., 2018). The presence of Moho or potential continental crust beneath the SDRs is questionable and further investigation is required. A distinct boundary between the SDRs and the surrounding crust cannot be distinguished due to poor imaging, which is partly related to the overlying salt deposits.

North-east of the SDRs, we identified some tilted high amplitude reflections in seismic lines A and B (Figure 3.4) in the shelf, which have a high magnetic anomaly (Figure 3.3d) similar to the SDRs south of the shelf. However, as mentioned above, they have consistent thickness, without a wedge geometry. Based on these characteristics, we interpret them as pre-rift features, possibly composed of volcanic rocks, deposited on the continental crust prior to rifting.

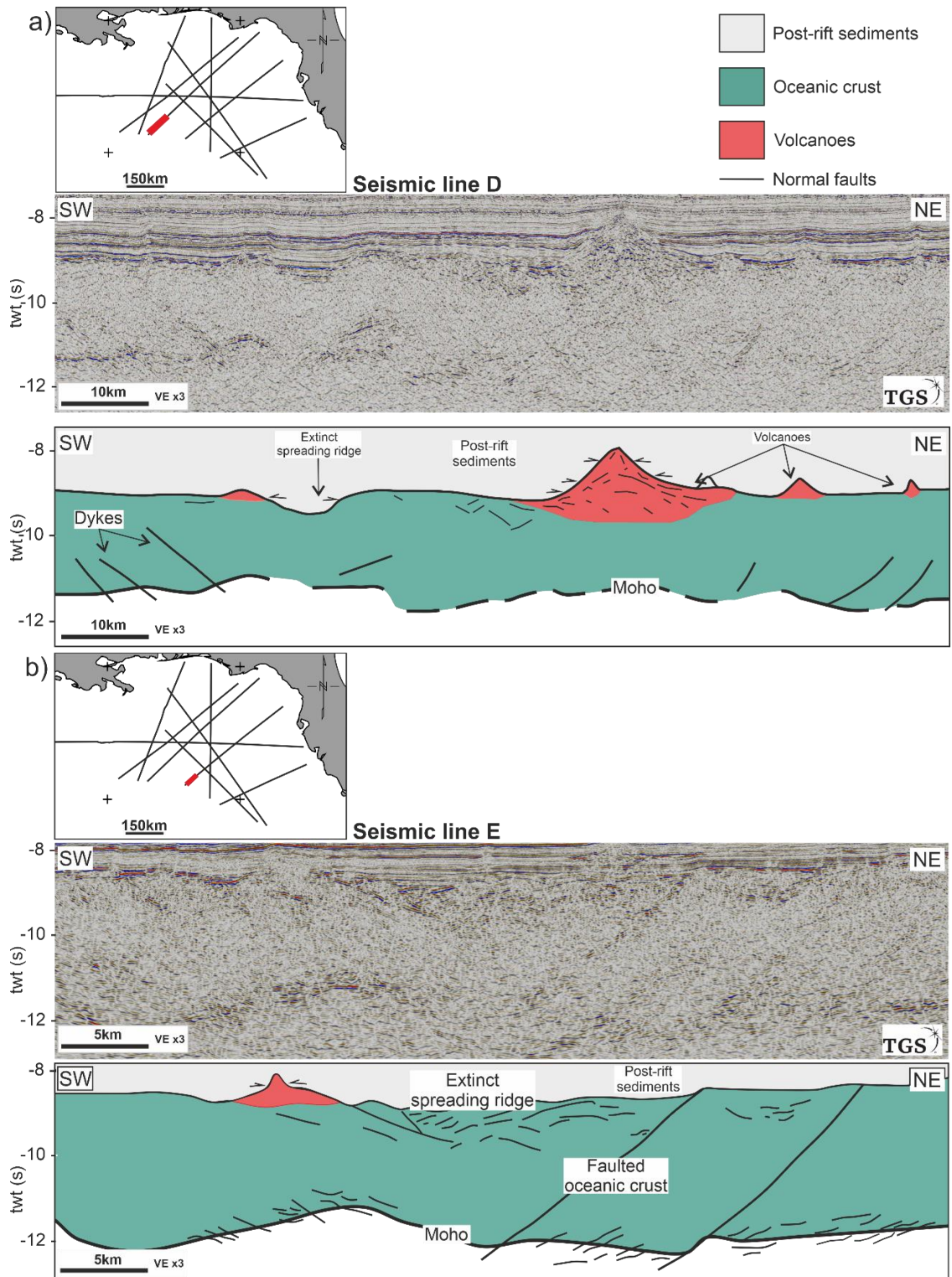


Figure 3.5: Representative seismic lines and interpretation of oceanic crust. Oceanic crust characteristics with a smaller (a) and a bigger scale (b) spreading ridge (post-spreading basin), interpreted volcanoes on the top crust and, faults and dykes influence the crust. Full seismic lines of high resolution are provided in Appendix (Figures B.3-B.4). Seismic data courtesy of TGS.

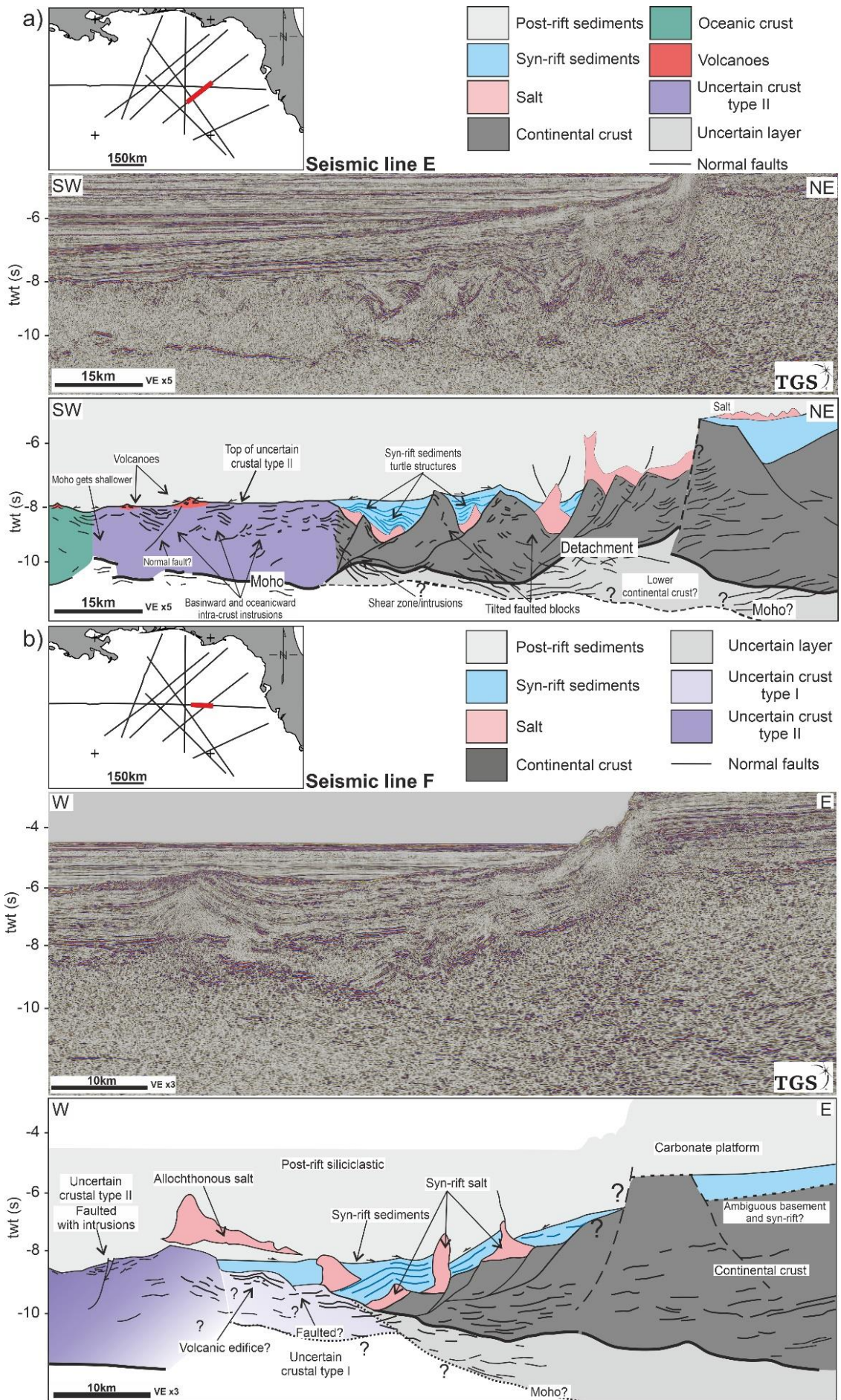


Figure 3.6: (a) Representative seismic line and interpretation of thinned continental crust at the proximal domain and an uncertain crust type II with intra-basement magmatism. (b) Representative seismic line and interpretation image the continental crust and the two different uncertain crustal domains. Uncertain crust type I (right) and uncertain crust type II (left). Full seismic line E of high resolution is provided in Appendix (Figure B.4). Seismic data courtesy of TGS.

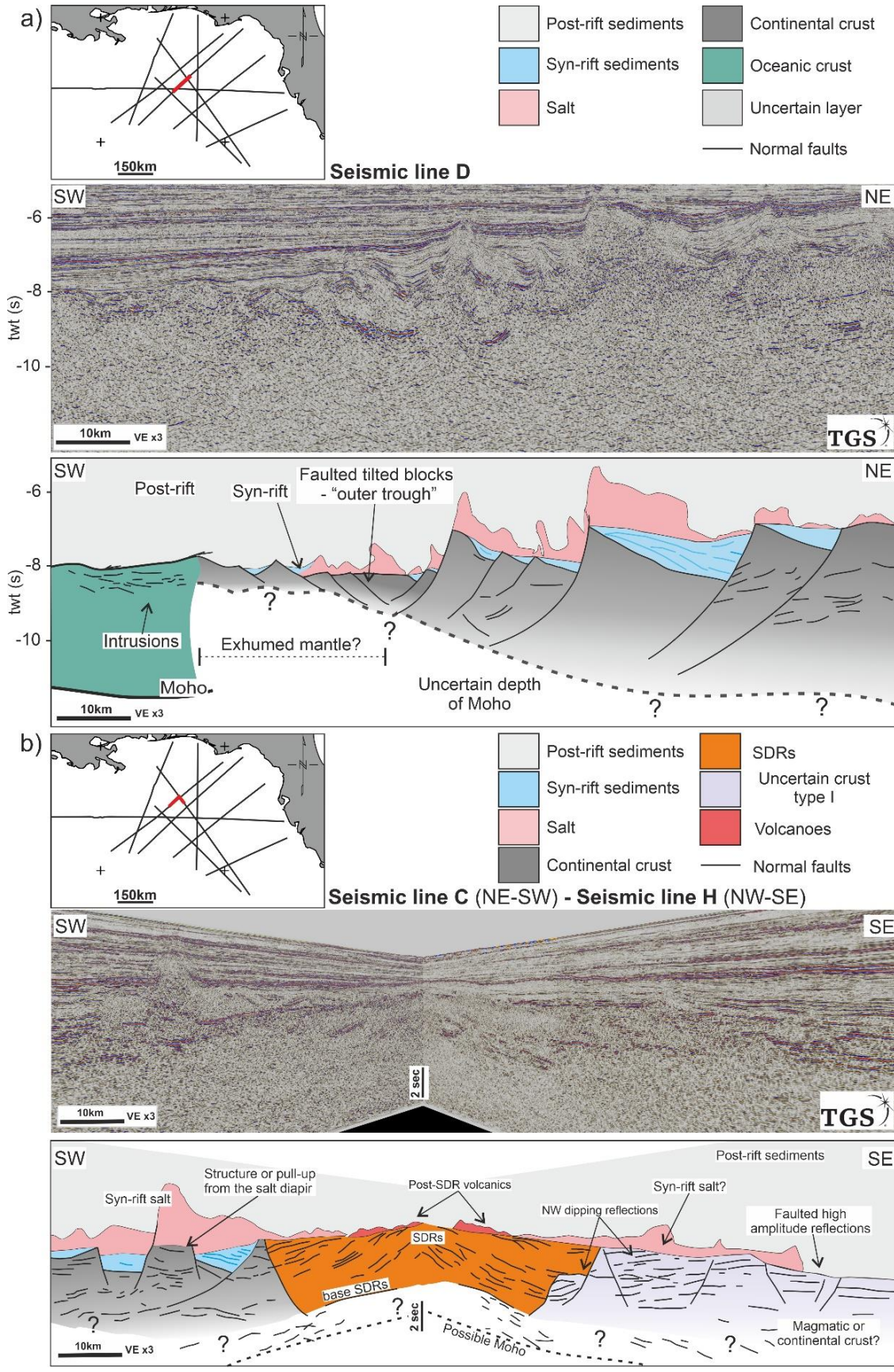


Figure 3.7: (a) Representative seismic line and interpretation of sedimentary sequences and ambiguous continental crust beneath the salt deposits that juxtapose to the oceanic crust, and (b) Possible Seaward Dipping Reflections (SDRs) overlaying by post-SDR volcanoes and surrounded by the uncertain crust type I and continental crust with uncertain depth of Moho. Full seismic lines of high resolution are provided in Appendix (Figures B.2-B.3 & B.5). Seismic data courtesy of TGS.

3.5 Gravity analysis

A crustal map (Figure 3.8) was produced from the seismic analysis of the different crustal types. These consist of the proximal to distal continental domain of the Florida margin and the deep oceanic domain up to the mid-oceanic ridge. In between lies a region of basement of uncertain nature but where SDR packages were identified at the intersection of lines C and H. This undifferentiated domain extends along the margin slope and widens toward the west where salt deposits are predominant. To address this area of uncertainty we conducted 2D gravity modelling along the seismic lines to test different crustal scenarios (Figure 3.9). Furthermore, we calculated the vertical gradient of residual gravity anomaly to support the structural trends (Figure 3.3c).

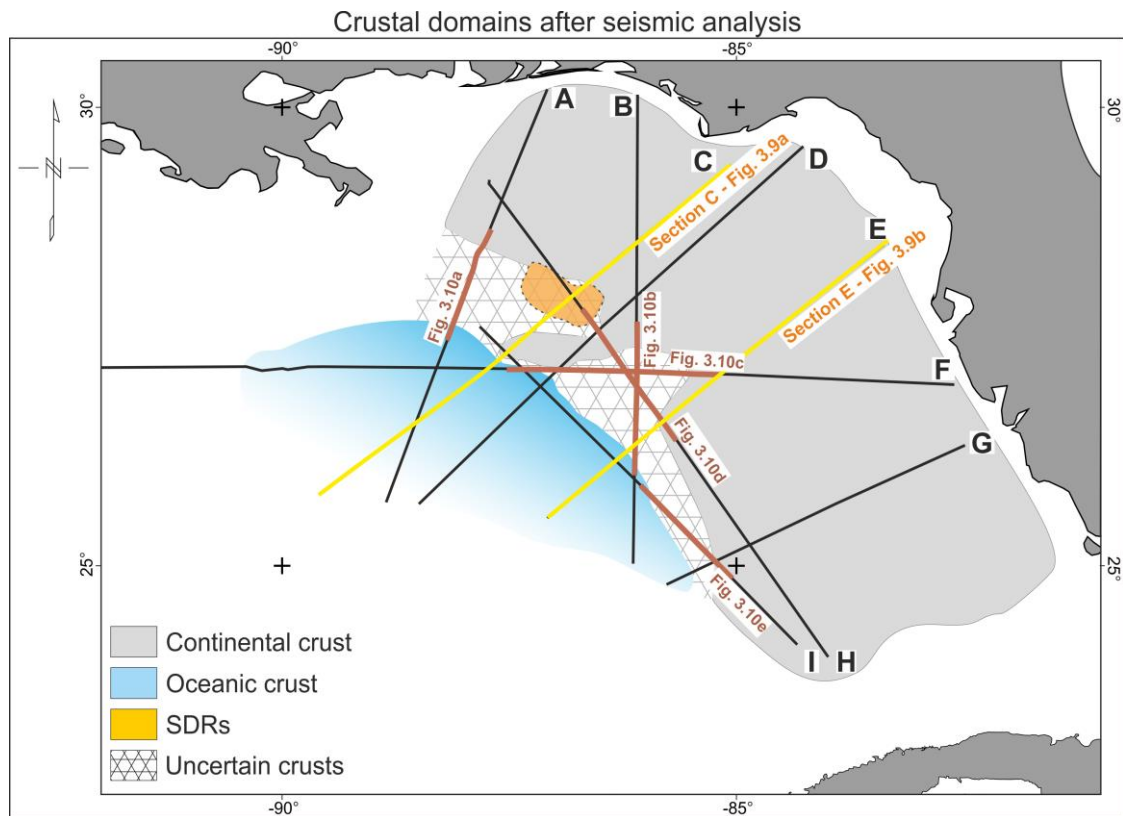


Figure 3.8: Crustal domains map based on the seismic characteristics. Yellow and brown traces show the location of the gravity models in Figure 3.9 and Figure 3.10, respectively. Seismic data courtesy of TGS.

3.5.1 Methodology

To validate the crustal types, better define their limits and improve the constraint of the Moho depth, we carried out forward 2D gravity modelling in Geosoft Oasis Montaj (GM-SYS profile modelling; Pouliquen et al., 2017) along interpreted seismic lines. First, a time-to-depth conversion was performed using constant interval velocities (Table 3-1). Average interval velocities were calculated from stacking velocities using Dix's equation (Dix, 1955):

$$v_{int} = [(t_2 * v_{RMS2}^2 - t_1 * v_{RMS1}^2) / (t_2 - t_1)]^{1/2}$$

where v_{int} is the interval velocity, t_1 & t_2 are the top and the base respectively (in twt) for each interval, and v_{RMS1} & v_{RMS2} are root-mean-square velocity at the top and the base respectively.

For the gravity modelling, average density values (Table 3-1) for the sedimentary sequences were calculated using Gardner's equation (Gardner et al., 1974):

$$\rho = 0.23 * v_P^{0.25} \text{ km/m}^3$$

where v_P is the average interval velocity.

Table 3-1: Velocity model with the average interval velocities and densities used in this study for the depth conversion and the gravity models, respectively, and the GUMBO lines 3 and 4 velocity models derived by refraction data (Christeson et al., 2014; Eddy et al., 2014).

	Average interval velocity model (km/s)	Density (g/cm ³)	GUMBO Line 3 velocity model (km/s)	GUMBO Line 4 velocity model (km/s)
Water	1.50	1.03	≤ 1.6	≤ 1.6
Sediments on the shelf	2.36-4.77	2.45-2.54	1.8-4.5	3.0-5.5
Sediments in the deep ocean basin	2.3-4.0	2.40-2.57	2.0-4.5	2.1-4.5
Salt	5.0	2.175	2.0-4.5	-
Continental crust	6.19	-	5.5-7.5	6.1-7.1
Oceanic crust	6.26	-	~ 8.0	~7.0

SDRs	6.11	-	6.0-7.5	-
Undifferentiated	6.14	-	-	-

The post-rift and syn-rift clastic sequences in the deep basin, SW of the shelf, have an average density of 2.40 and 2.57 g/cm³, respectively. Whereas on the shelf, the carbonates and syn-rift sediments have an average density of 2.45 and 2.54 g/cm³, respectively. The obtained salt density ranges between 2.1 and 2.9 g/cm³, with an average of 2.61 g/cm³. This wide range could highlight the uncertainty in the interpretation of the salt base, or variable salt composition (e.g., anhydrite - Alger and Crain, 1966; Dobson and Buffler, 1997; Snedden and Galloway, 2019). A low-end salt density of 2.175 g/cm³ was assumed due to its mobility and Bird's et al. (2005) interpretation of salt density in the western Gulf of Mexico. Standard density values were used for continental crust (2.75-2.9 g/cm³), oceanic crust (2.9-3.0 g/cm³), SDRs (2.65-2.75 g/cm³), magmatic underplating (2.9-3.0 g/cm³), serpentinized mantle (2.7-3.2 g/cm³), and mantle (3.3 g/cm³) (Bassetto et al., 2000; Holbrook et al., 1994; Mjelde, Raum, Myhren, et al., 2005). In the Eastern Gulf of Mexico, a gravity model was previously applied on the seismic line coincident with the GUMBO line 3 (Liu et al., 2019) using continental crust densities based on the DSDP well Site 537, located on a structural high close to Campeche Escarpment (Buffler et al., 1984). In this study, we used density values of 2.75 g/cm³ and 2.85 g/cm³ for the attenuated and thicker continental crust, respectively. The value of 2.85 g/cm³ describes the average density of the upper and lower continental crust as they were difficult to distinguish within the seismic reflection data. Similar values have previously been used for gravity models in the GOM (Bird et al., 2005; Nguyen and Mann, 2016; Lin et al., 2019). The remainder of the crust in the gravity profiles has an average density value or the best-fit value from the previously mentioned crustal density ranges.

The validity of our gravity models relies on the depth-conversion velocity model and the assigned density values. Dix's equation, used to calculate interval velocities, tends to underestimate velocities in deep layers, which has minor impact on the interpreted crustal boundaries, but can result in an overestimation of the crustal thickness. The densities of the sedimentary layers are relatively well constrained using Gardner's empirical equation. Those assigned to the different

crustal layers are based on a range of values, previously mentioned, and are consistent with densities derived from seismic refraction (Christensen & Mooney, 1995; Christeson et al., 2014; Eddy et al., 2014; McDermott et al., 2019). Density, however, remains the main source of uncertainty, especially when differentiating between SDRs and serpentinized mantle, whose density depends on the sediment-volcanics ratio and the degree of mantle hydration, and can vary laterally. Overall, gravity models are non-unique and reflect our interpretation of the seismic data within the context of a valid geological model.

3.5.2 Gravity Modelling Results

In our gravity modelling, we consider different scenarios to test the nature of the crust in the uncertain domain for each profile. In Figure 3.9, we show the different models that were tested for seismic lines C and E; whereas in Figure 3.10, we display only the best-fit models.

Three possible scenarios were considered in both sections. First, a transitional domain of high-density crust of 3.0 g/cm^3 (Scenario 1; Figure 3.9), due to the wide range of ILOC (Figure 3.1) and the presence of thick undifferentiated crust that is similar to oceanic crust (Figure 3.6a). In section C, we applied a thick high-density crust as the Moho is not imaged in the seismic data, which is extended beneath the SDRs. Previous gravity models have proposed a high-density of 2.9 g/cm^3 beneath SDRs (e.g., Paton et al., 2017). In section E, the thickness is fixed in accordance with the seismic interpretation (Figure 3.6a) and the depth-converted Moho (Figure 3.9). In both sections, there is a significant misfit between the calculated and observed gravity. For this reason, in the second scenario (Figure 3.9b), we applied a low and an average-density crust considering their seismic characteristics.

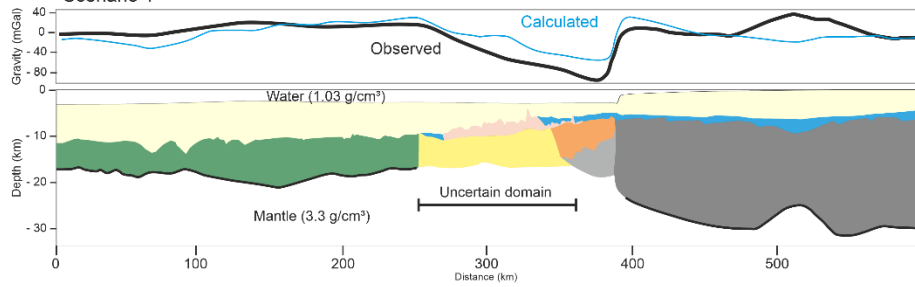
In scenario 2 for section C (Figure 3.9a.2), we applied a density of 2.75 g/cm^3 , and a thinner crust, which does not extend beneath the SDRs. Therefore, we retained a 3.3 g/cm^3 mantle density beneath the SDRs and only evaluated the transitional crust between the SDRs and oceanic crust. Here, the misfit between the calculated and the observed gravity is less than in the first scenario, although it is still significant. In scenario 2 for section E (Figure 3.9b.2), we applied an average density of 2.85 g/cm^3 , which produces the best fit between calculated and observed gravity in the uncertain domain. Hence, the transitional domain

between continental crust and oceanic crust consists of an average density of 2.85 g/cm^3 with similar thickness to the oceanic crust (6 km).

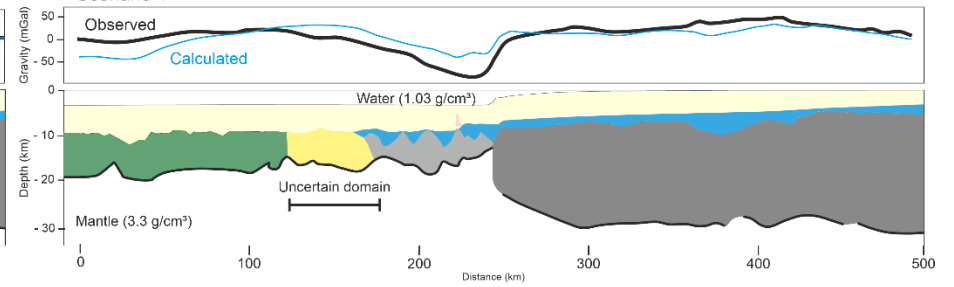
In the second scenario, both models minimised the misfit by applying a lower density crust. However, both sections also exhibit a major misfit between the oceanic and the thick continental crust. In section C, the misfit occurs along the thin continental crust, the SDRs and the low-density crust (Figure 3.9a.2). In section E, the misfit is mainly along the thin continental crust (Figure 3.9b.2), where we identified the low amplitude reflections (uncertain layer; Figure 3.6) and the uncertain crust (Figure 3.6a). This could only be corrected with a high-density layer of 3.0 g/cm^3 at depth (Figure 3.9a.3 and 3.9b.3), which is not imaged in the seismic reflection data. Our preferred scenario is the third one (Figure 3.9; Scenario 3), which has a low density crust (2.75 g/cm^3) in the north (Section C; Figure 3.8) and an average density crust (2.85 g/cm^3) in the south (section E; Figure 3.8).

We used the same density and crustal configuration as scenario 3 when modelling the uncertain domain in the other sections (Figure 3.10). The uncertain domain in section A (Figure 3.10a) consists of a 2.75 g/cm^3 low density thin crust underlain by the 3.0 g/cm^3 high density layer. Section I (Figure 3.10e) located in the southernmost part of the margin has similar crust densities, with the exception that the deep high-density domain is extended underneath the thin continental crust and partly underneath the low-density crust. In section H (Figure 3.10d), the deep high-density layer is located underneath the SDRs and the low density crust, similar to section C (Figure 3.10a.3).

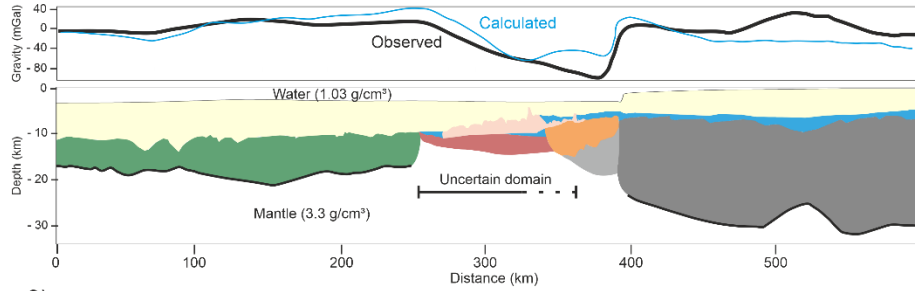
a.1) Section C
Scenario 1



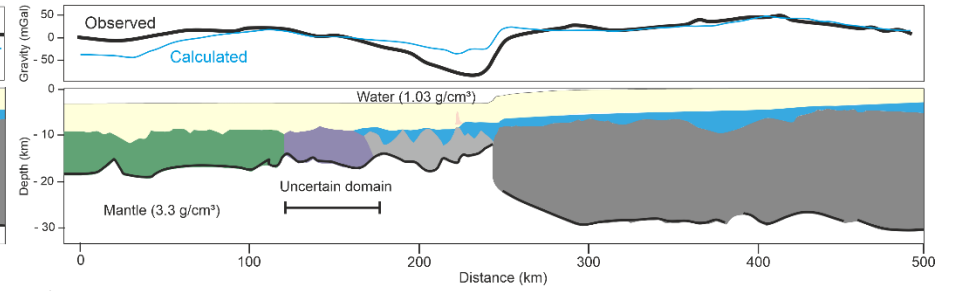
b.1) Section E
Scenario 1



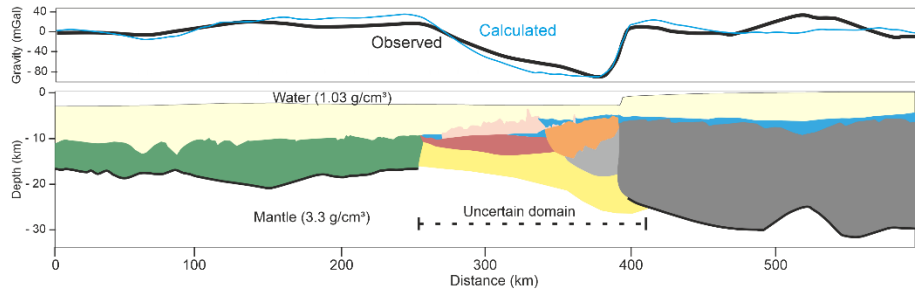
a.2) Scenario 2



b.2) Scenario 2



a.3) Scenario 3



b.3) Scenario 3

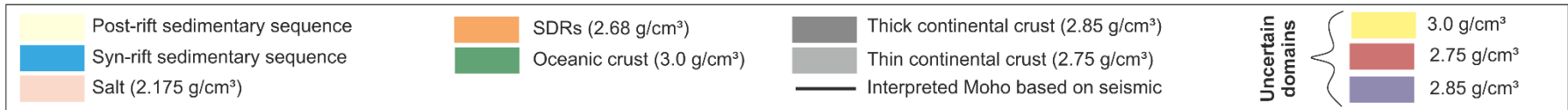
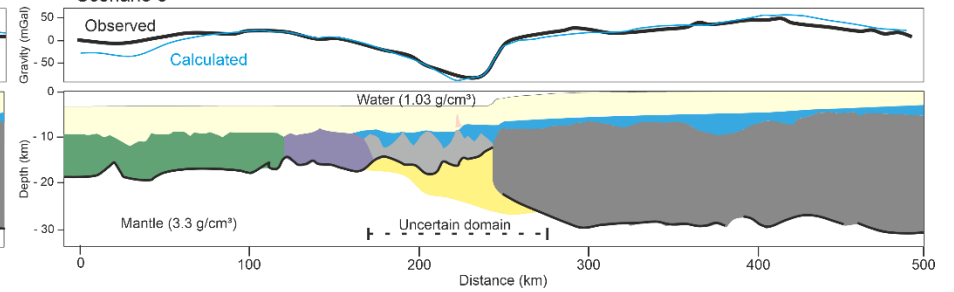


Figure 3.9: Gravity modelling of the depth converted profiles C and E, whose locations are presented on Figures 3.1 and 3.3c. In the first scenario, high density was applied in the uncertain domain. In the second scenario, different low densities were applied for each section best fit in the model. In section C, dashed line represents the uncertain crust beneath the SDRs. Scenario three, proposes an extra high-density sequence (marked with dashed uncertain domain), which is partly detectable in the seismic reflection data.

In the centre of the margin the uncertain domain shows a more complex configuration, with a 2.85 g/cm^3 average density crust in sections B, F and H (Figure 3.10b-d). In section B (Figure 3.10b), it is located between thin continental crust and oceanic crust, similarly to seismic line E (Figure 3.9b.3). In sections F and H (Figures 3.10c and 3.10d), the uncertain domain is located between thin continental crusts.

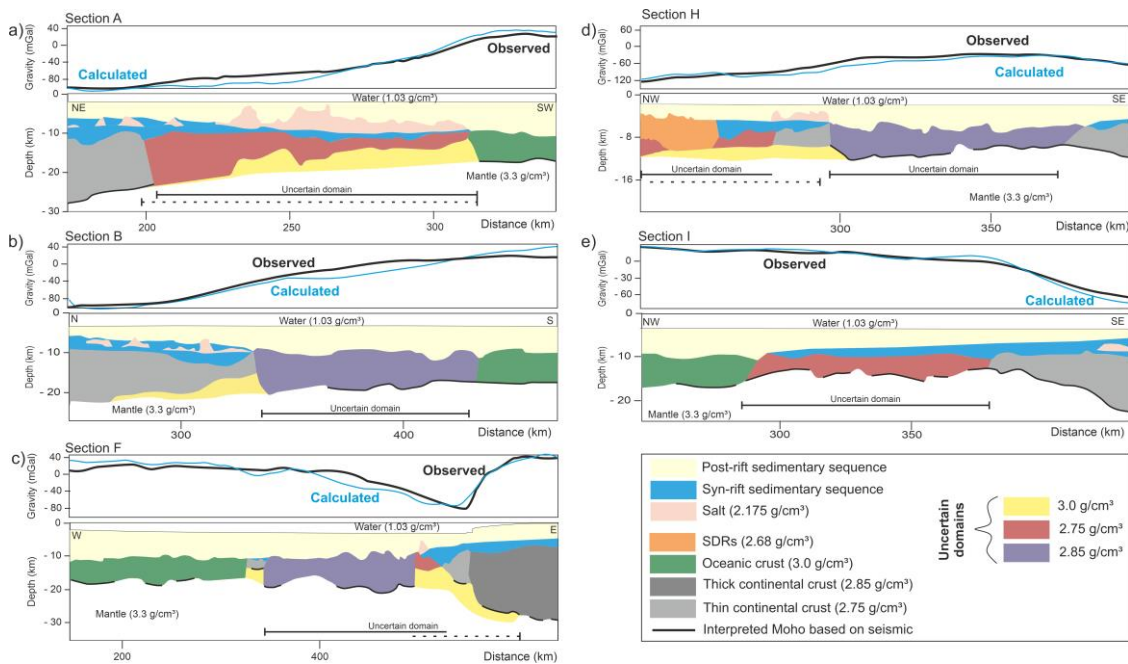


Figure 3.10: Gravity modelling results along the uncertain crustal domain. Line locations are presented in Figure 3.8. The uncertain domains identified in the seismic reflection data are marked with solid black line, while dashed line highlights the misfit of observed and calculated gravity anomaly, which was corrected with the 3.0 g/cm^3 high density layer.

3.6 Proposed crustal model for the Eastern Gulf of Mexico

The integration of seismic reflection, potential field data and gravity modelling has enabled us to produce a new and refined structural and tectonic map for the Eastern Gulf of Mexico (Figure 3.11a) in which several crustal domains have been identified and mapped across the area. Our crustal model illustrates the crustal configuration of the Florida side only, as we have not examined data from the conjugate side. In Figure 3.11b, we present representative cross-sections of depth-converted seismic lines C and E, which integrate the seismic interpretation (Figures 3.5-3.7) and the gravity modelling (Figure 3.9). These sections illustrate the crusts' geometry from NW to SE, and in depth.

The continental crust has been divided into stretched continental crust, with a thickness of ~ 25 km, and hyperextended continental crust, which is less than 10 km thick. Both continental domains are NW-SE trending. The first phase of normal faults formed NE-SW basins along the shelf (Pindell and Kennan, 2001; Pindell and Kennan, 2009). The NE-SW faults (in blue in Figure 3.11a) are based on Pindell et al. (2020a) and were partly identified in seismic lines C and F. The second phase of NW-SE trending normal faults are restricted to the hyperextended continental crust. These are developed in the upper part of the continental crust and form tilted blocks (e.g., Figures 3.6a and 3.7a).

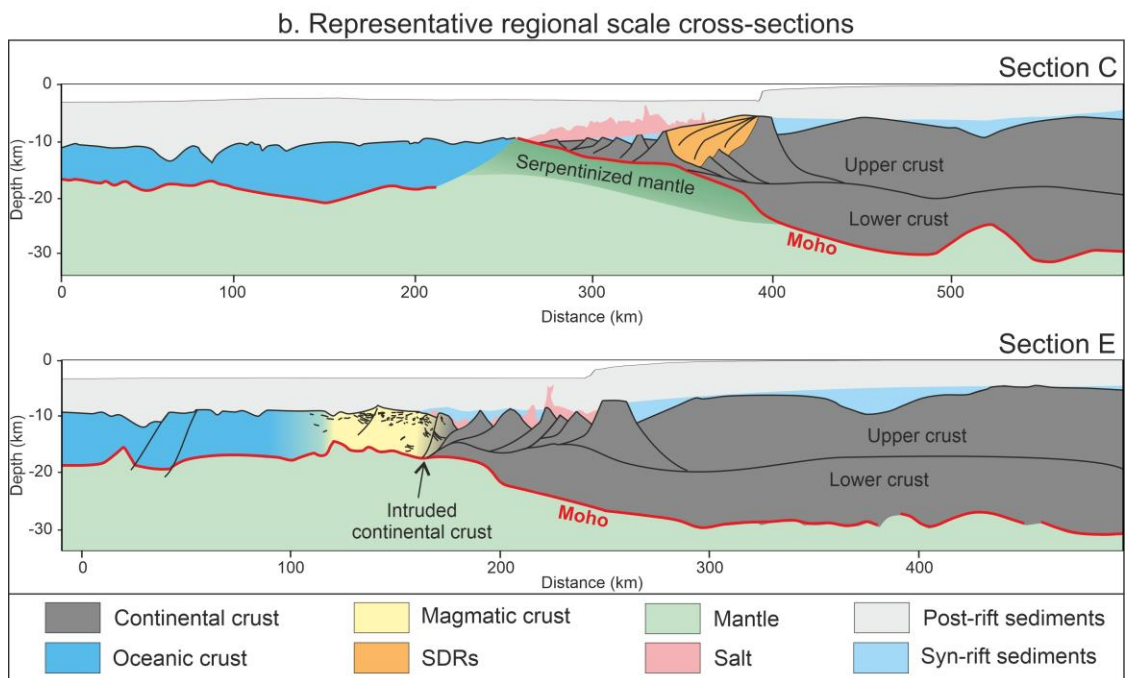
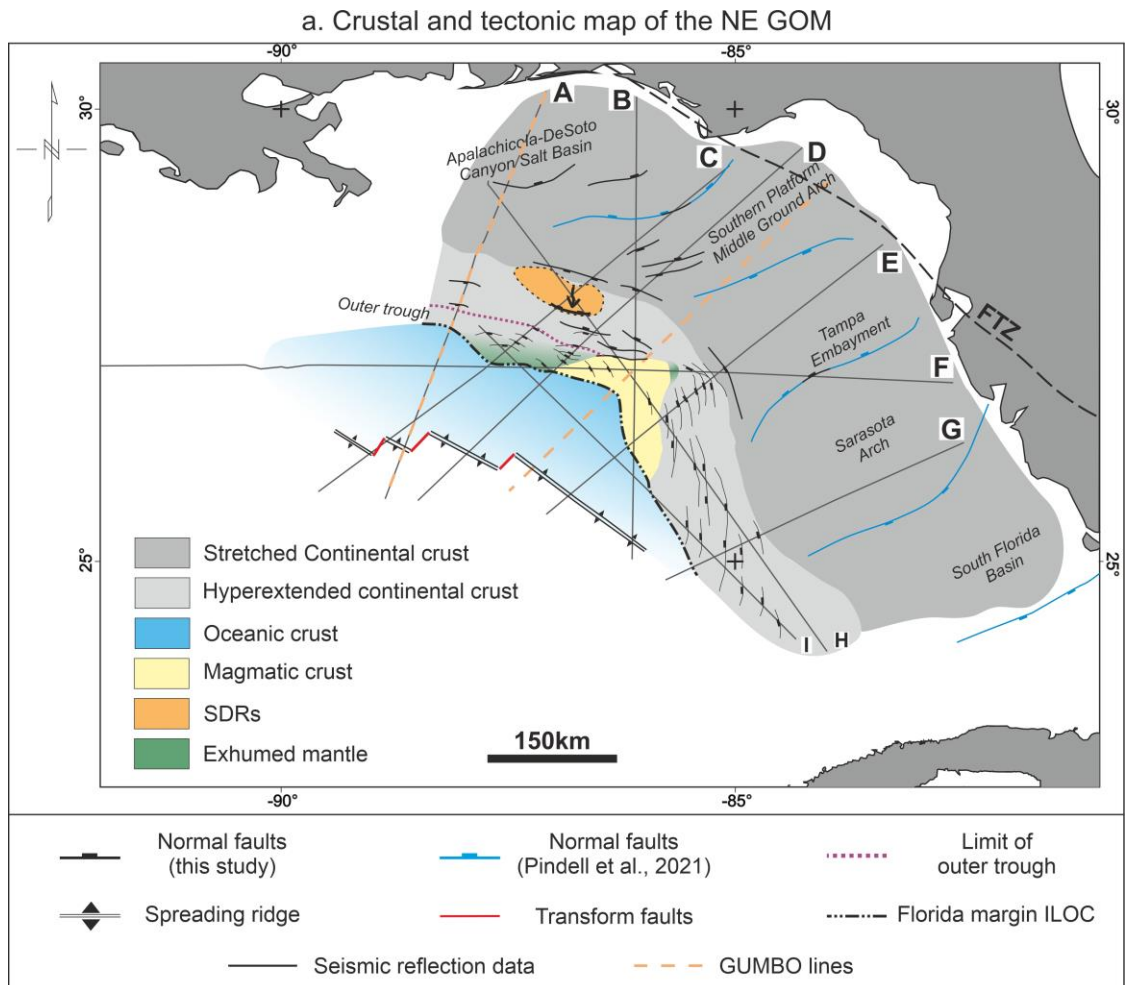


Figure 3.11: (a) Crustal and tectonic map of the NE Gulf of Mexico. The arrow on the SDRs shows the dip direction. FTZ: Florida-Bahamas Transfer Zone. Seismic data courtesy of TGS. (b) Representative regional scale cross-sections of seismic lines C and E.

Hyperextended continental crust is mapped between stretched continental crust, the magmatic crust, and the oceanic crust. However, in the gravity modelling, scenario 3 (Figure 3.9) suggests the presence of a high density layer (3.0 g/cm^3) beneath low density continental crust. Therefore, the high amplitude reflections interpreted with bold lines in Figures 3.6 and 3.7a, are more likely to be a detachment for the titled blocks (e.g., Pindell et al., 2011; Izquierdo-Llavall et al., 2022), which separate the upper and lower continental crusts. The lower crust is poorly imaged in Figures 3.6 and 3.7a, and the continental Moho could only be inferred from the gravity models (Figures 3.9b.3 and 3.10c). Therefore, the high density layer is inferred to be a continental crust towards the southeast of the margin.

Hyperextended continental crust is affected by NW-SE trending normal faults in the north and almost N-S trending normal faults in the south of the study area. The presence of salt on the hyperextended continental crust and the lack of first phase syn-rift sediments in the south support the eastern migration of rifting (Izquierdo-Llavall et al., 2022; Pindell & Heyn, 2022). In seismic lines E and F (Figure 3.6), the occurrence of Middle Jurassic salt, growth strata on the tilted continental blocks (Izquierdo-Llavall et al., 2022; Pindell & Heyn, 2022), and the lack of pre-salt sediments indicates that either there was no accommodation (the continental crust was above sea level, (Pindell & Heyn, 2022)) or they have been eroded or that poor imaging beneath salt has obscured thin pre-salt sediments such that they cannot be seismically resolved. Finally, a 10 km thick package of SDRs, which extends for approximately 100 km along the shelf (Imbert, 2005; Pindell et al., 2014; Pindell et al., 2011), is placed on the hyperextended continental crust.

Our interpreted ILOC is comparable with the one proposed by Izquierdo-Llavall et al. (2022) especially in the south of the study area. Geometrically, the oceanic crust is narrow in the southeast and widens in the northwest. Towards the southwest, it appears un-faulted (Figure 3.5a) across the region; and overlain by volcanoes of different sizes, with the majority of them occurring close to the extinct spreading segments. The Florida margin has at least four segments of NW-SE trending extinct spreading ridges that are segmented by NE-SW trending transform faults. The oceanic crust thickness is typical to thin ranging between 7

and 3 km (Figure 3.9 and 3.10). The thin oceanic crust portions are found where the extinct spreading ridges are located (Figure 3.5a).

Based on the seismic characteristics and gravity modelling, we can provide an interpretation for the two uncertain crustal types. Uncertain crust type I could be exhumed mantle or continental crust due to its low density, which is consistent with known hyperextended continental crust (Figures 3.6, 3.7a and 3.8). In seismic line H (Figure 3.7b), uncertain type I is more likely to be a low density continental crust than exhumed mantle, due to the presence of the SDRs NW of the crust, and its inboard position. Uncertain crust type II is considered to be a magmatic crust, which has an average thickness of 8.5 km with local variations (i.e., 5 to 10 km thick). Its upper portion can be locally affected by normal faults (Figure 3.6). This magmatic domain is only found in the central part of the margin, bounded by hyperextended continental crust and/or exhumed mantle to the SE and NW, and by oceanic crust to the S and W.

Gravity modelling suggests the presence of a deep high-density layer (i.e., 3.0 g/cm³; Figures 3.9a.3, 3.9b.3 and 3.10) beneath the hyperextended continental crust that extends up to the shelf. Three different scenarios could explain its occurrence beneath the seismic Moho (e.g., Figure 3.6a): (i) magmatic underplating of a mafic layer located close to the Moho, consistent with the presence of the SDRs in the northern part of the margin, and typical of magma-rich rifted margins (Franke, 2013; White & McKenzie, 1989); (ii) (partially) serpentinized mantle beneath the attenuated continental crust (Eddy et al., 2014; Filina et al., 2020; Hudec, Norton, et al., 2013; Nguyen & Mann, 2016), which is consistent with possible mantle exhumation identified in seismic line F (crustal type I; Figure 3.6b) and seismic line D (Figure 3.7a), and typical of magma-poor rifted margins (e.g., Peron-Pinvidic et al., 2013a); or (iii) thicker continental crust, as previously suggested for seismic lines E and F. We interpret the high density layer beneath the hyperextended continental crust in the majority of the lines (Figures 3.9 and 3.10) as a deeper continental crust in the proximal domain or partly serpentinized (i.e. 3.0 g/cm³) mantle in the distal domain, which locally could be exhumed in the “*outer trough*” (Minguez et al., 2020; Pindell et al., 2016; van Avendonk et al., 2015) and close to the magmatic and the oceanic crusts (Figure 3.11a). The tilted blocks (Figure 3.7a) could correspond to stretched continental crust remnants on the potential exhumed mantle.

Our analysis highlights that the Florida margin changes character considerably from east to west. Hyperextended continental crust appears to occupy most of the distal domain between the ~25 km thick stretched continental crust and unambiguous oceanic crust. A restricted transitional domain in the central part of the margin exhibits a narrow area of magmatic crust and a potential exhumed mantle. A restricted domain with SDRs is also found in the north-western part of the margin. Their emplacement before salt deposition might indicate their formation prior to Yucatan's rotation and the transition from NW-SE to NE-SW extension.

3.7 Discussion

The Florida margin does not appear to fit the well-defined end-members of magma-poor or magma-rich margins (Franke, 2013; Peron-Pinvidic et al., 2013). The presence of hyperextended continental crust with different trends in structures, limited serpentized exhumed mantle, SDRs, and magmatic crust suggest that the Florida margin is a non-typical magma-rich margin in the early stages of Yucatan's rotation, and is affected by amagmatic tectonics prior to the breakup (Rowan et al., 2012; Pindell et al., 2014; 2016; Curry et al., 2018; Liu et al., 2019; Minguez et al., 2020; Filina et al., 2022; Filina and Beutel, 2022).

3.7.1 Structural evolution

In the Florida margin, we recognise different fault trends in the shelf domain and the deeper basin that could be active at different stages of the margin evolution. It is clear that the NE-SW trending faults (Figure 3.11a) in the shelf domain were active during the first, NW-SE oriented, phase of rifting associated with the Atlantic opening.

In the deeper basin, the activity of faults becomes more complex due to their different orientations (WNW-ESE in the west and NNW-SSE in the east), the SDR formation, and the salt deposits. If we assume a synchronous salt (Bajocian) along the margin, then we could use the salt as a temporal marker to classify the timing of faults activity in the deeper basin. In the west, seismic lines C, D, and H (Figure 3.7a) indicate that the faults were active mostly prior to and during salt deposition and less active during the Middle Jurassic. The WNW-ESE trending

faults that were active prior to the salt deposition are not related to the first NW-SE extension, and therefore we propose an Early Jurassic extensional phase 2, with a local extensional stress regime oriented approximately N-S. While in the east, seismic line E (Figure 3.6a) shows faults were active during and after salt deposition, with significant post-salt growth strata against faulted tilted blocks. Based on the observations in these seismic lines (Figures 3.6 and 3.7a), strain migrated from west to east in the Florida margin (Christeson et al., 2014; Kneller & Johnson, 2011; Marton & Buffler, 1994; Pindell & Heyn, 2022) from the Early Jurassic to Middle-Late Jurassic.

3.7.2 SDRs

The presence of subaerial SDRs within the EGOM has been debated. Seismic reflection and refraction data, potential field data, and seismic velocity analysis have been previously used to investigate the presence of SDRs or interbedded igneous and sedimentary sequences at the northern part of the Florida margin and the Yucatan conjugate margin (Christeson et al., 2014; Curry et al., 2018; Filina & Hartford, 2021; Imbert, 2005; Imbert & Philippe, 2005; Izquierdo-Llavall et al., 2022; Liu et al., 2019; Pindell et al., 2014; Pindell et al., 2011; Rowan, 2014; Rowan, 2018; Steier & Mann, 2019).

In the Florida margin, two seaward dipping reflection sequences were identified along seismic line A, which is coincident with GUMBO line 3 (Figure 3.1, Eddy et al., 2014). We recognised the northern sequence of these high amplitude seaward dipping reflections, which we interpret as a pre-rift sequence at the north-eastern part of seismic lines A and B (Figure 3.4) in the Apalachicola basin beneath the carbonate platform. The northern magmatic sequence located within the Apalachicola basin is approximately 100 km to the north of our interpreted SDRs (Figure 3.11) under the intermediate to high magnetic anomaly (Figure 3.3d).

Eddy et al. (2014) identified a questionable southern sequence of SDRs in FUGRO seismic line 533 (Seismic line A; Figure 3.1). Our interpretation instead invokes continental crust, which is overlain by salt, similar to that observed in seismic line D (Figure 3.7a). However, further to the south-east, we identified a sequence of SDRs (Figures 3.7b, 3.9a and 3.10d), which has an associated high magnetic anomaly (e.g., Paton et al., 2017), but is bound by hyperextended

continental crust south-west of the hinge line (Curry et al., 2018; Pindell et al., 2011). We interpret this sequence as SDRs (Filina & Beutel, 2022; Filina & Hartford, 2021; Imbert, 2005; Imbert & Philippe, 2005; Liu et al., 2019; Pindell et al., 2014; Pindell et al., 2011) instead of sediments (Curry et al., 2018; Minguez et al., 2020; Rowan, 2018), based on their high amplitude reflectivity (Figure 3.7b), their dip direction towards the SSW, the occurrence of volcanic edifices on top (e.g., Norcliffe et al., 2018), the density derived from the gravity model (2.68 g/cm^3 , Figures 3.9a and 3.10d), and the referred SDR in the northern Yucatan margin (Filina et al., 2022). Typically, SDR formation models suggest an oceanward emplacement on continental crust and/or on magmatic material and juxtapose the oceanic or embryonic oceanic crust. Since the first extensional phase was NW-SE and the second NE-SW, they are likely to coincide with the transition between the two rifting phases with approximately N-S trend, which was associated with Yucatan's counter-clockwise rotation. However, the autochthonous salt observed on top of the SDRs (Figure 3.7b) indicates that the N-S extensional phase was active prior to the Yucatan rotation, and the deposition of salt in Bajocian time, thus SDRs can be inferred to be older than Bajocian.

The SDRs do not juxtapose the oceanic crust or any magmatic transitional crust as seen in typical magma-rich margins and their accepted conceptual model (e.g., Franke, 2013), but they are surrounded by continental crust. Gravity modelling results suggest that the SDRs are emplaced partly on the continental crust and partly on a high-density crust (3.0 g/cm^3 ; Figures 3.9a.3 and 3.10d, respectively). We interpreted the latter as a highly intruded lower continental crust. SDRs could be generated by a small volume of mafic magma (Eddy et al., 2014) trapped underneath the NW of the Florida margin and local sills intruded in the continental crust (e.g., North Atlantic margins; White et al., 2008; Thybo and Artemieva, 2013), or by a plume that migrated eastwards to the Florida-Bahamas region (e.g., Burke and Torsvik, 2004; Dale, 2013; Basile et al., 2020; Pindell and Heyn, 2022). However, the hotspot activity in the Demerara plateau has been reported to be active during Aalenian (173.4 Ma; Basile et al., 2020), which could be the latest possible time formation of the SDRs in the Florida margin (Figure 3.7b). Therefore, the activity of the plume and its movement towards the east should be older than 173.4 Ma, and the SDR formation is possibly not related to

the plume activity. The formation of the SDRs on the continental crust could be an incipient breakup that was subsequently aborted due to the strain migration to the east, when interbedded volcanics and sediments placed within a half-graben, due to the lack of the full SDR system in the Florida margin.

3.7.3 Magmatic crust

Our model (Figure 3.11) suggests the formation of a magmatic crust with an average density of 2.85 g/cm³ (Figure 3.9b.3), a high volume of magmatic intrusions, and variable thickness (5-10km; Figures 3.6a, 3.9 and 3.11) averaging ~7 km. Similar seismic reflection characteristics were interpreted in the East Indian margin (Nemčok, Sinha, et al., 2013), in Iberia-Newfoundland (Structural Comparison of Archetypal Atlantic Rifted Margins: A Review of Observations and Concepts, 2013), the Eastern US Atlantic margin (Bécel et al., 2020), the Australia-Antarctica conjugate margins (Gillard et al., 2015) and SE India-East Antarctica (Tugend et al., 2018). The oceanward and continentward dipping reflections, volcanic domes overlying volcano-clastic sediments, and elevated Moho reflection marking the transition to unambiguous oceanic crust (Figure 3.6a; Gillard et al., 2016) are key characteristics identified in the Florida margin.

Seismic data from the south margin (e.g., Izquierdo-Llavall et al., 2022) also show elevated Moho reflection (Figure 3.6a) between the magmatic and the oceanic crust, which was interpreted to be the ILOC against continental crust. However, the characteristics of our unknown crust type II, namely, its discontinuous nature, variable thickness (Figures 3.9 and 3.10), the presence of faults in the upper portion (Figure 3.6) without growth strata, and the presence of oceanward and continent-ward reflections (Figure 3.6a), are consistent with an unstable magma supply prior to the steady state oceanic crust formation (e.g., Nemčok et al., 2013; Gillard et al., 2015). Alternatively, it could be the continuation of the continental crust (Izquierdo-Llavall et al., 2022) and/or exhumed mantle (Curry et al., 2018; Minguéz et al., 2020; Pindell et al., 2016), which were highly intruded (e.g., Tugend et al., 2018) prior to the seafloor spreading.

3.7.4 Serpentinized subcontinental mantle

Previous studies supported by gravity and magnetic data identified a narrow zone of uncertain basement along the north-western and north-eastern Gulf of Mexico. This zone may represent hyperextension along an Alleghenian lower crustal

decollement surface and exhumed mantle with or without magmatic intrusions (Curry et al., 2018; Marton & Buffler, 1994; Pindell et al., 2016, 2021). Further studies of seismic refraction data from the north-western Gulf of Mexico, offshore Texas, have interpreted zones of exhumed mantle and highly stretched continental crust (GUMBO Line 1 (van Avendonk et al., 2015); GUMBO Line 2 (Eddy et al., 2018)). However, in the Eastern Gulf of Mexico, GUMBO lines 3 and 4 (Figure 3.1; Christeson et al., 2014; Eddy et al., 2014) indicate the presence of high velocity crustal bodies (van Avendonk et al., 2015). The high velocities in GUMBO line 3 suggest high velocity lower crust (HVLC) which could represent intrusions into the middle and lower continental crust (Eddy et al., 2014; Holbrook & Kelemen, 1993; White & McKenzie, 1989), or mafic underplating formed due to high mantle temperature during rifting (Franke, 2013; Menzies et al., 2002). The HVLC is imaged above low mantle velocities (i.e., 7.6 km/s; Eddy et al., 2014) that could be explained by partial serpentinization of the mantle, facilitated by deep seated crustal faults which reach the upper mantle.

Exhumed mantle (e.g., Pindell et al., 2016; Curry et al., 2018; Minguéz et al., 2020), continental crust (Eddy et al., 2014; Filina et al., 2020; Hudec, Norton, et al., 2013; Nguyen & Mann, 2016) or even an exhumation of lower continental crust (Filina & Beutel, 2022) has previously been interpreted in this domain of the northern part of the Florida margin. Even though we recognised hyperextended continental crust (Figures 3.6-3.7 and 3.11) in the distal domain, it is very hard to discern if there is mantle exhumation. We could interpret a ~10-15 km wide zone of exhumed mantle on seismic lines C, and D (Figures 3.7a and 3.11, outer trough; Pindell et al., 2014; Curry et al., 2018) between the hyperextended continental crust and oceanic crust, where we identified a low-density basement (2.75 g/cm^3 , Figure 3.9c), which caps the high-density layer (3.0 g/cm^3). In addition, we could interpret local mantle exhumation in seismic line F (crustal type I; Figure 3.6b), where top basement is shallower than top continental crust with a low-density of 2.75 g/cm^3 (Figure 3.10c). If there is mantle exhumation, then the high-density layer (3.0 g/cm^3 , Figures 3.9a.3 and 3.10) in the northern margin, could be either continental crust, which is not imaged in the seismic lines or serpentinized mantle, with a lower degree of hydration (e.g., Toft et al., 1990). Whilst, the same high density layer could be continental crust beneath the SDRs (Figures 3.9a.3 and 3.10d), and low density continental crust in the more proximal

domain (Figure 3.9b.3), where continental crust is not imaged on seismic (Figure 3.6a).

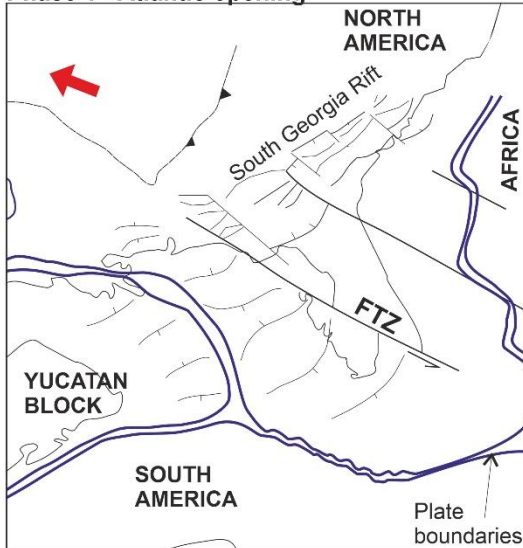
3.7.5 Evolutionary model for the EGOM

Based on our findings, we propose further adjustments to the rotational tectonic model (e.g., Pindell, 1985) for the Florida margin in the Eastern Gulf of Mexico that captures different phases of extension, Yucatan's counter-clockwise rotation, and the varying crustal nature in the continent-ocean transitional domain (Figure 3.12).

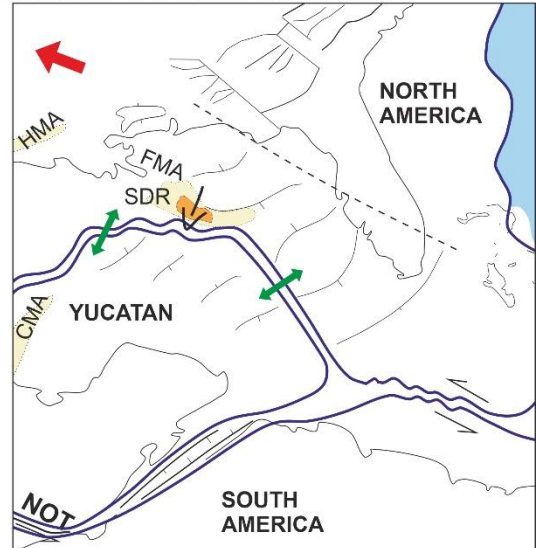
During the Late Triassic-Early Jurassic (Figure 3.12a), the Florida margin underwent sub-orthogonal NW-SE extension, accommodated by NE-SW trending normal faults, structural highs and grabens. In addition, the NW-SE Florida-Bahamas Transfer zone, accommodated 300-400 km of displacement during this first phase of rifting (Pindell, 1985; Pindell & Kennan, 2009; Pindell et al., 2021). In the Early Jurassic (Figure 3.12b), the local extension orientation shifted from NW-SE to approximately NE-SW in the Eastern Gulf of Mexico, prior to the Yucatan's rotation and separation from South America. The northern part of the Florida margin accommodated syn-rift volcanism (SDRs) during the late Early Jurassic, prior to the salt deposition. The SDR sequences emplaced on continental crust (Type I; e.g., McDermott et al., 2018), volcanism was shut down, probably due to eastward strain migration (Figure 3a; post-salt fault activity).

During the Middle Jurassic, i.e., Bajocian, rotation of the Yucatan commenced, SDRs were aborted, and the continental crust underwent hyperextension. Mantle exhumed synchronously with salt deposition (Figure 3.12c) as the rifting propagated to the south-east. Hyperextension of the continental crust continued after salt deposition had ceased, evident by the presence of salt on faulted tilted blocks, overlain by younger growth strata (Figure 3.6a). Prior to the seafloor spreading, unstable magma supply overprinted the hyperextended continental crust and possibly exhumed mantle, which formed the ocean-like magmatic crust (Figure 3.12d). Finally, the magma supply stabilized during the Late Jurassic, leading the emplacement of a proper mid-oceanic ridge and marking the onset of true steady-state oceanic accretion (Figure 3.12e).

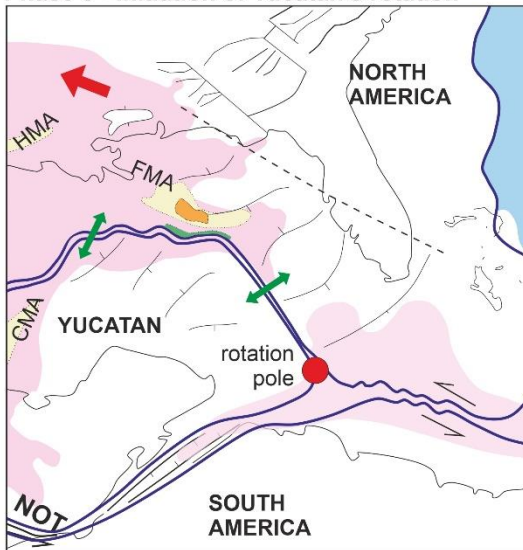
a) Triassic-Early Jurassic
Phase 1 - Atlantic opening



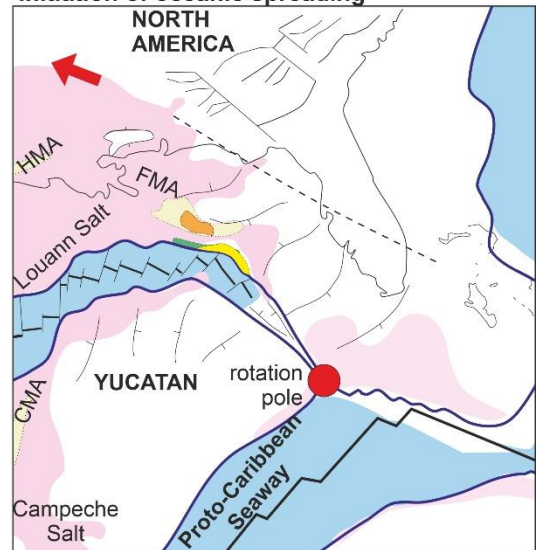
b) Early Jurassic
Phase 2 - Pre-salt SDR formation



c) Bathonian salt deposition
Phase 3 - Initiation of Yucatan's rotation



d) Late Jurassic
Initiation of oceanic spreading



e) Early Cretaceous
End of seafloor spreading

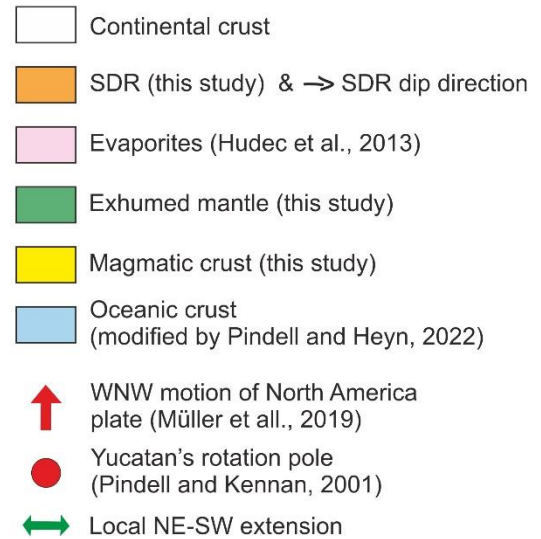
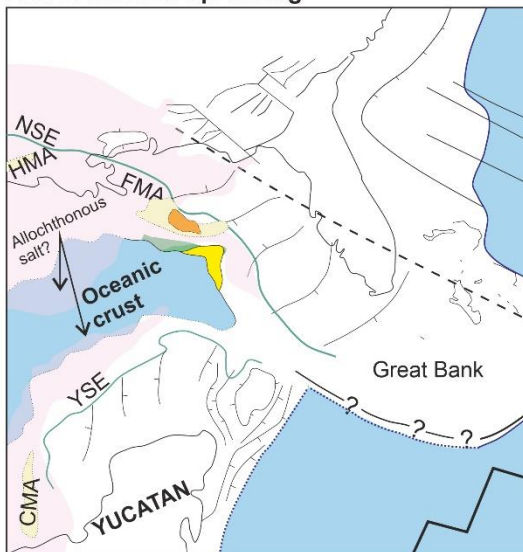


Figure 3.12: Tectonic evolution focusing on the Florida margin, Eastern Gulf of Mexico (modified from Steier and Mann, 2019; Pindell et al., 2021; Pindell and Heyn, 2022). a) Late Triassic-Early Jurassic phase of rifting with NW-SE extension. b) SDR formation in the continental domain of the northern Florida margin during the transition from NW-SE phase to Yucatan's rotation. Arrow on the SDR indicates the dip direction, parallel to the local extension. Yellow arrow indicates that the rotation pole of North America is further north (see Pindell, Villagómez, et al., 2020). c) Initiation of Yucatan's rotation in the Middle Jurassic, salt deposition, continuous extension of the continental crust and possible mantle exhumation. d) Late Jurassic post-salt formation of magmatic crust and continental break-up. e) Early Cretaceous cessation of seafloor spreading. FTF: Florida Transfer Fault; HMA: Houston Magnetic Anomaly; FMA: Florida Magnetic Anomaly; CMA: Campeche Magnetic anomaly; NSE: Northern Cretaceous shelf edge; YSE: Yucatan shelf edge. Red arrow indicates the regional WNW-ESE extension from the America and Africa separation. Green arrows indicate the local extension in the conjugate margins of Florida and Yucatan at the Eastern Gulf of Mexico.

3.7.6 Further discussion

The Gulf of Mexico has been characterised as a strike-slip influenced margin, a conclusion drawn from plate reconstruction models (Pindell & Kennan, 2009; Pindell et al., 2021). The classification is rooted in the sinistral movement of the Florida Transfer Fault and North Oaxaca Transfer, situated at the boundaries of Yucatan microplate, which induced a counter-clockwise rotation of the microplate (Pindell et al., 2021).

In the Eastern Gulf of Mexico, the presence of the Florida Transfer fault can be observed in magnetic data, yet elusive in seismic reflection data, particularly in the distal domain where the seismic reflection data have a greater resolution. Notably, the overall interpretation and the tectonic model for the Eastern Gulf of Mexico do not support the notion of any strike-slip or transfer faults. Even though later stages of rifting do not support the activity of strike-slip faults, it is important to focus on the Florida Transfer Zone and the nearby strike-slip faults at the failed rift system of South Georgia.

The South Georgia rift system, preceding the late Triassic rifting of Florida Transfer Zone, was once active but later ceased, and capped by CAMP basalts around ~200Ma (Marzoli et al., 1999; McBride, 1991). Subsequently, the Florida Transfer Zone became active, following the South Georgia rift activity, as the Florida Straits block migrated southward approximately 400km (Erlich & Pindell, 2020; Pindell, 1985; Pindell & Kennan, 2009; Pindell et al., 2021).

It is possible that minor strike-slip faults emerged south of the Florida Transfer Zone, and got aborted before the onset of the Gulf of Mexico rifting, akin to the South Georgia rift system. These strike-slip faults may have been either overprinted by the multiphase extension in the Florida margin, potentially evolving into normal faults as previously suggested in models indicating the development of oblique normal faults from strike-slip faults (Farangitakis et al., 2019). Alternatively, they could have been obscured concealed by the magmatic intrusions affecting the region during and after the rifting (Erich & Pindell, 2020; Heatherington & Mueller, 1999, 2003). Furthermore, if the strike-slip faults did exist in the eastern Gulf of Mexico, they could form migration paths for magma supply, potentially explaining the formation of SDRs in a half-graben and the high volume of magma within the continental crust, as observed in the gravity and magnetic data.

3.8 Conclusion

The nature of the EGOM margin has long been debated, in particular the presence of exhumed mantle or SDRs, and the continent-ocean transition location. Previously, the margin has been interpreted to have either or both SDRs and exhumed mantle (e.g., Hudec, Norton, et al., 2013; Eddy et al., 2014; Nguyen and Mann, 2016; Pindell et al., 2016; Rowan, 2018; Liu et al., 2019; Minguez et al., 2020; Filina and Beutel, 2022).

Our integrated study of seismic reflection and potential field data, supported by 2D gravity modelling, introduces new insights into the crustal architecture of the margin. Our analysis reveals that the margin underwent different tectonic phases, which in a chronological order, resulted in:

- (i) stretched continental crust, which was influenced by the NW-SE Triassic-Jurassic phase and accommodates NE-SW trending normal faults;
- (ii) aborted SDRs, which are placed on the continental crust, formed by a magmatic activity during the transition of NW-SE to NE-SW extensional phases;
- (iii) hyperextended continental crust SW of the hinge line, which was influenced by different orientations of local stresses during the

Yucatan's counter-clockwise rotation, and imprints the strain migration to the east;

- (iv) serpentized exhumed mantle formed prior to the breakup;
- (v) a magmatic crust overprinted the hyperextended continental crust and the possible exhumed mantle; and
- (vi) an oceanic crust, which formed during different states of magma supply.

The margin's characteristics suggest that:

- (vii) the transitional crust of the Florida margin comprising SDR and exhumed mantle, indicates the transition from magma-rich to magma-poor margin, and
- (viii) the geometry and the formation timing of pre-salt SDRs, and syn-to-post salt mantle exhumation, indicate the strain migration towards the east, where post-salt extension is observed.

Chapter 4 – The transform margin of Ghana

Summary

The Ghanaian margin, a prominent transform margin in the Equatorial Africa plate, experienced oblique rifting during the Cretaceous due to the progressive rifting from the South Atlantic. Previous plate reconstructions and analogue modelling have utilised the Ghanaian margin as a case study, contributing to conceptual models for a global understanding of transform margins development and the Mesozoic Equatorial Atlantic opening. Despite these extensive studies, the structural architecture and crustal nature along the margin remain poorly understood.

This study employs an extensive survey of 2D seismic reflection data, complemented by free air anomaly gravity data, to discern the characteristics of the Ghanaian transform margin. The investigation aims to understanding the crustal nature, crust-structure interactions, and the relationships between structures and sediments occurring during the multiple deformation events associated with rifting.

The results reveal a margin influenced by diverse stress regimes in various segments, evident in both the sedimentary sequences and the crustal configuration. Additionally, the study sheds light on the implications of magmatic supply, contributing to the formation of a transitional crust in the outer corner of the margin. Lastly, a conceptual reconstruction model is presented with respect to the conjugate side, integrating the key results of this work.

4.1 Introduction

Transform margins have received relatively less attention when compared to their rifted counterparts, despite their recognition nearly half a century ago (Masclé, 1976). This can be attributed to the challenges associated with the seismic reflection imaging, due to the sharp changes along the margin, (Basile, 2015; Sage et al., 2000), the structural complexity of strike-slip faults formed along the tectonic plates that cannot be understood by sparse 2D data (Basile, 2015). However, the study of transform margins holds significant implications for both academic research, due to the key role of transform margins in plate tectonics, and industry, since the discovery of the Jubilee oil field offshore Ghana in 2007 and the Liza oil field offshore Guyana in 2015. The last few years have witnessed an increased focus on these regions, particularly since the conceptual model of Masclé & Blarez (1987) improved by Basile (2015), including the key elements of the transform margins (Figure 4.2B; fault activity, thermal uplift and subsidence, and the characteristics of inner and outer corners), and the review of Mercier de Lépinay et al. (2016) that summarised the transform margins worldwide, and the improvement in seismic reflection data quality. In recent years, notable contributions to this area of research have been made (e.g., Antobreh et al., 2009; Attoh et al., 2004; Markwick et al., 2022; Nemčok et al., 2013; Nemčok, Rybár, et al., 2016; Nemčok et al., 2022, 2023; Paton et al., 2023; Polteau et al., 2020; Roche et al., 2023; Tavares et al., 2020, 2022). These studies focus on identifying the processes involved in oblique separation of plate boundaries, differences observed on various transform margins, the role of inherited structures on the transform margins' development, and the underlying crustal nature and geometries.

The Ghanaian margin, situated in West Africa and the east Equatorial Atlantic, has been a focal point of research aimed at enhancing our understanding of the tectonic processes during the opening of transform margins (Antobreh et al., 2009; Attoh et al., 2004; Basile et al., 1993; Basile et al., 1998; Edwards et al., 1997; Masclé & Blarez, 1987; Nemčok et al., 2013, 2023; Nemčok et al., 2022; Sage et al., 2000). Nevertheless, the majority of published data are found in the Côte d'Ivoire and the Côte d'Ivoire-Ghana Ridge (Masclé and Blarez, 1987; Blarez and Masclé, 1988; Basile et al., 1993; Masclé et al., 1996; Edwards et al., 1997; Clift et al., 1997; Bouillin et al., 1998; Clift and Lorenzo, 1999; Sage et al.,

2000; Tari, 2006; Scarselli et al., 2020), while limited research has focused specifically on the Ghanaian transform margin and its characteristics (Antobreh et al., 2009; Attoh et al., 2004; Attoh & Brown, 2008; Nemčok et al., 2022; 2023).

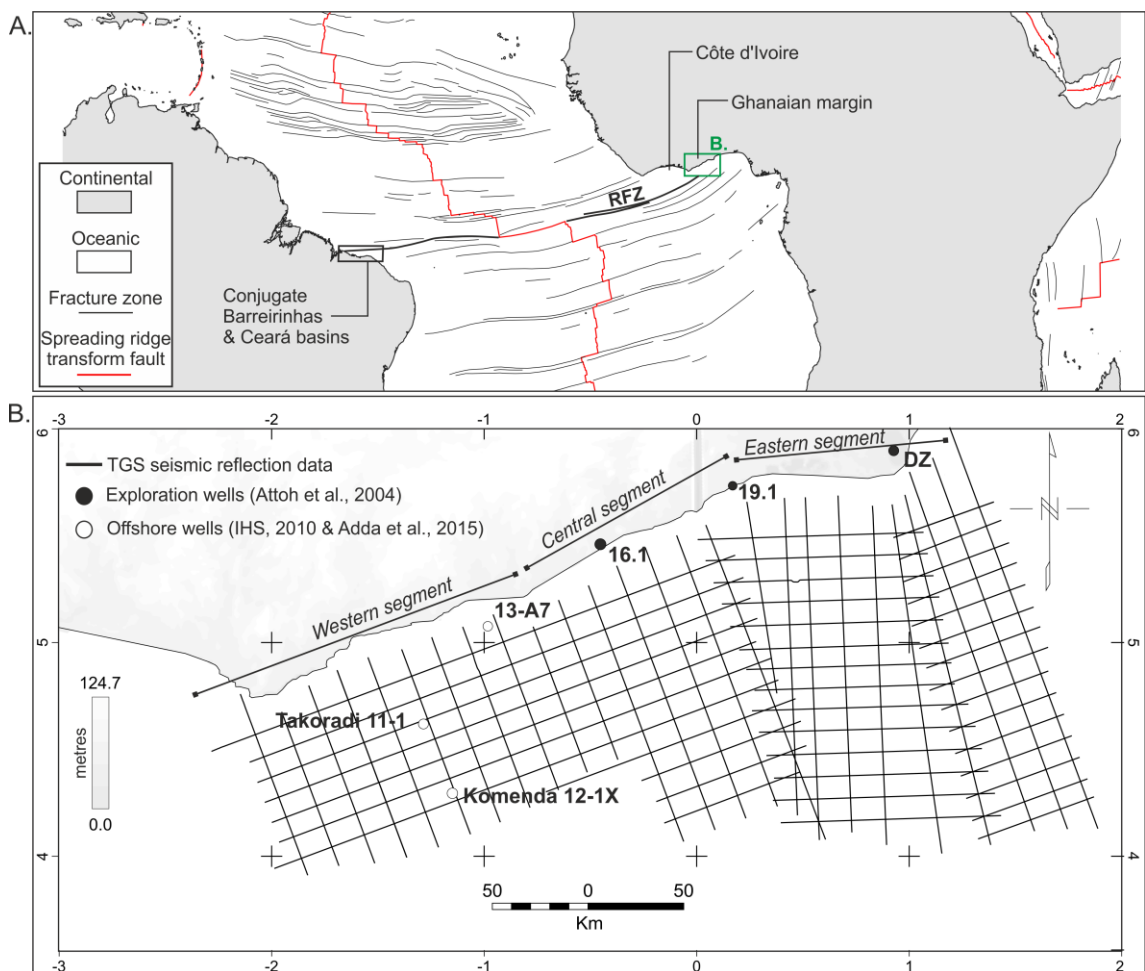


Figure 4.1: A. Equatorial Atlantic with plotted major fracture zones, spreading ridges, and key areas of the Ghanaian margin (B.), the conjugate basins of Barreirinhas and Ceará, and the Côte d'Ivoire basin (modified from Matthews et al., 2011; Müller et al., 2008). RFZ: Romanche Fracture Zone. B. Onshore topography (Sandwell & Smith, 1997) of the Ghanaian Margin, West Africa, which includes: TGS offshore seismic reflection data in black traces; the location of the onshore exploration wells (Attoh et al., 2004) and offshore wells (Adda, et al., 2015; IHS, 2010); white dashed lines as the oceanic transform faults based on FAA (Sandwell et al., 2014). Seismic data courtesy of TGS.

Even though there is a tectonic model dedicated to transform margins (Masclé & Blarez, 1987), the current study focuses on refining our understanding of the crustal architecture and tectonic framework of the Ghanaian margin (Figure 4.1), which records a series of deformation events during the Equatorial Atlantic opening, and investigates the relationship between crustal types and structures over time in accordance with the conjugate Brazilian margin. The study places a

specific emphasis on the role of magmatic material and its implications along the margin's transform zone during the syn-to-post transform phases (Antobreh et al., 2009; Nemčok et al., 2023; Nemčok, Henk, et al., 2016). It explores the presence of unknown nature transitional crustal types and underplating (Antobreh et al., 2009), and the distinct role of structures in each type of crust. The findings are presented in the form of a comprehensive tectonic model for the Equatorial Atlantic margins of Ghana and Barreirinhas-Ceará. 2D regional scale seismic reflection data, integrated with velocity and gravity analysis indicate a transform margin with a complex tectonic background. In summary, along the margin, the continental crust juxtaposes the oceanic crust in most of the studied area, while transitional magmatic crust can be found in the south-western part and along the main transform zone. Lastly, the continental faults and the main transform zone of Ghana, the Romanche Fracture Zone (RFZ) that appears segmented, show both extension and contraction related to multiple phases of deformation.

4.2 Geological Background

In the Ghanaian margin, pre-rift structures, inherited from the Pan African Orogeny (Tidjani et al., 1997) and observed onshore (Trompette, 1994), played a major role in the margin's evolution. NE-SW and NNE-SSW fold belts and strike-slip faults were formed during the Pan African orogeny under dextral shear (Affaton et al., 1980; Attoh et al., 1997; Tidjani et al., 1997; Trompette, 1994) and formed the template for the Mesozoic rifting.

The opening of the Equatorial Atlantic is considered to have begun in the Early Cretaceous when West Africa and South America started to separate (Masclé et al., 1988; Masclé & Blarez, 1987). This resulted from the northward propagation of the South Atlantic seafloor spreading (e.g., Rabinowitz and Labrecque, 1979; Nürnberg and Müller, 1991; Eagles, 2007; Pérez-Díaz and Eagles, 2014) and the NW-SE spreading between the African plate and the North America (e.g., Nürnberg & Müller, 1991).

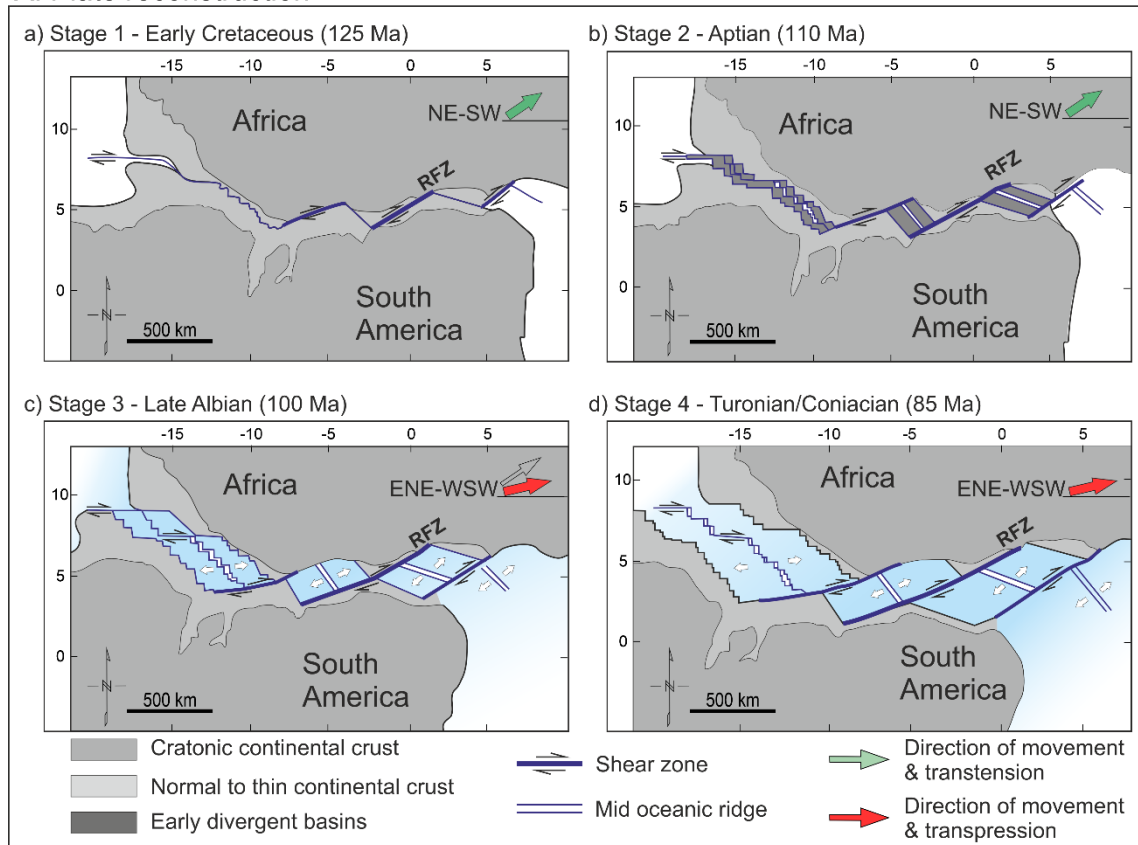
The Ghanaian margin has been classified as a transform margin, which evolution was described by four diachronous stages (Masclé and Blarez, 1987; Masclé et al., 1988; Sage et al., 2000; Basile, 2015). These stages are described using different terms, either based on (i) the type of crustal contact across the basin: "*continental-continental*", "*active continental-continental*", "*continental-oceanic*", and "*oceanic-oceanic*" (Antobreh et al., 2009; Masclé & Blarez, 1987; Sage et al., 2000) or (ii) the tectonic context: "*intracontinental rifting*", "*continental transform*", "*syn-transform*", and "*post-transform*" (Figure 4.2A; Attoh et al., 2004; Basile, 2015; Mercier de Lépinay et al., 2016; Tavares et al., 2020).

In the Ghanaian margin, the first stage, continental-continental or intracontinental rifting (Figure 4.2Aa), was controlled by the E-W trending transform zone of the Romanche Fracture Zone (RFZ; Masclé and Blarez, 1987). This phase began in the Early Cretaceous, and it is believed to have started specifically in the early Aptian (Tavares et al., 2020; Trosdorf et al., 2007) and continued through the early Albian (Antobreh et al., 2009; Attoh et al., 2004; Tavares et al., 2020; Zalán, 2004). During this phase, it is proposed that the inherited structures of NE-SW trend were reactivated and controlled the margin's geometry (Antobreh et al., 2009; Attoh et al., 2004). These structures experienced a dextral transtensional regime, leading to the development of pull-apart basins and transtensional

splays, and the rifting of the continental crust (Harding et al., 1985; Mascle and Blarez, 1987; Attoh et al., 2004; Antobreh et al., 2009).

In the second stage, active continental-continental or continental-transform (Figure 4.2Ab), the continental crust started thinning, while the African and South American plates remained connected. This period lasted for approximately 10 Ma (Basile et al., 1998; Klitgord & Schouten, 1986; Nürnberg & Müller, 1991; Tavares et al., 2020). Although the onset of continental break-up cannot be distinguished by the magnetic anomalies due to the mid-Cretaceous magnetic quiet zone (Campan, 1995), the initiation of the continental-oceanic or syn-transform phase is estimated to have occurred at around 110 Ma (Antobreh et al., 2009; Bigot-Cormier et al., 2005; Nemčok, Rybár, et al., 2016; Sage et al., 2000; Soares Júnior et al., 2008; Tavares et al., 2020). This age is based on erosional unconformities at ODP Leg 159 sites 959 and 960, as well as apatite fission-track analysis, which yielded similar ages as those identified in the ODP Leg 159 (Basile et al., 1998; Bouillin et al., 1998; Clift et al., 1998; Clift and Lorenzo, 1999; Nemčok et al., 2013). The aforementioned alternative methods of dating were used due to the lack of magnetic anomalies, which are usually used to date the early break-up (Campan, 1995) and the difficulty of directly dating the oceanic crust due to the thick sediments on the crust (Clift et al., 1998).

A. Plate reconstruction



B. Three stage model with transform margin elements

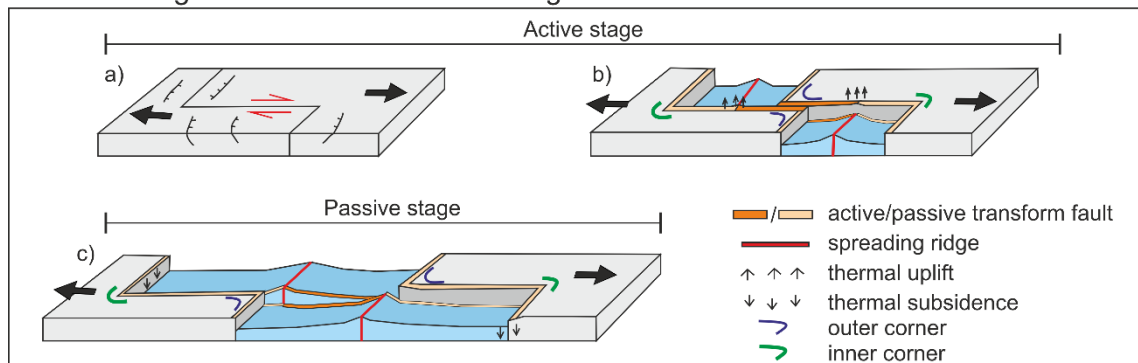


Figure 4.2: A. Plate reconstruction of the Equatorial Atlantic opening (modified after Mascle et al., 1988; Antobreh et al., 2009). Arrows indicate the direction of movement for Africa plate. (a) Stage 1: “continental-continental” or “intracontinental rifting”; (b) Stage 2: “active continental-continental” or “continental transform”; (c) Stage 3: “continental-oceanic” or “syn-transform”; (d) Stage 4: “oceanic-oceanic” or “post-transform”. RFZ: Romanche Fracture Zone. B. Three stage model for transform margin formation with key elements of active and passive transform faults, thermal uplift and subsidence, and inner and outer corners during the (a) intra-continental and active continental-continental, (b) continental-oceanic and (c) passive margin stages (after Basile, 2015; Lorenzo, 1997; Mascle & Blarez, 1987).

The third stage, of continental-oceanic or syn-transform deformation (Figure 4.2Ac), involves the juxtaposition of continental and oceanic crusts along the

transform fault of Romanche Fracture Zone (e.g., Mascle and Blarez, 1987). During this phase, the direction of movement of the African plate shifted to ENE-WSW (Davison et al., 2016; Klitgord & Schouten, 1986; Zalan et al., 1985). This change led to a dextral transpressional regime with respect to pre-existing structures, and along the Romanche Fracture Zone (Antobreh et al., 2009; Attoh et al., 2004; Basile et al., 2005; Davison et al., 2016; Huguen et al., 2001; Nemčok et al., 2013; Tavares et al., 2022; Ye et al., 2017). The transpressional regime and the thermal uplift on the continental side (Figure 4.2Bb) inverted the sediments from the intracontinental and continental-transform stages, which resulted in an erosional unconformity (Clift & Lorenzo, 1999; Clift et al., 1998; Lorenzo, 1997; Mascle & Blarez, 1987; Nemčok et al., 2022). Thus, in the deeper basin, the spreading ridges shifted to a more N-S strike direction, becoming more orthogonal to the main transform zones (i.e., RFZ; Tavares et al., 2020). A continental sliver or an exotic block is also believed to have been located in the RFZ and the plates contact (Davison et al., 2016; Gasperini et al., 2001) prior to the break-up, which migrated during the Equatorial Atlantic opening towards the west.

The final stage, oceanic-oceanic or post-transform (Figure 4.2Ad), occurred when the oceanic crusts along the E-W trending sheared fractures were juxtaposed against each other. This sheared segment is active only within the oceanic crust, without influencing the continental crust (Blarez & Mascle, 1988; Mascle & Blarez, 1987). The passive stage of the Ghanaian margin has previously been dated to start at 80 Ma, based on various plate reconstructions (Antobreh et al., 2009; Attoh et al., 2004; Basile et al., 1998; Huguen et al., 2001; Klitgord & Schouten, 1986; Nemčok, Rybár, et al., 2016; Nürnberg & Müller, 1991). Thermal subsidence occurred during this stage on both continental and oceanic crusts at the passive transform fault (Figure 4.2Bc; Lorenzo, 1997; Mascle & Blarez, 1987).

The aforementioned stages are applicable to any transform margin. However, the presence of transitional crusts in the transform and divergent parts of the margin, the structures activity and role influencing the various crusts still remains ambiguous.

4.3 Data and Methodology

4.3.1 Data

This study utilises 66 2D seismic reflection profiles (Figures 4.1 and 4.3) along the Ghanaian margin, courtesy of TGS. The acquisition parameters are as follows: (1) airgun volume: 3200 cu; (2) gun depth: 7m; (3) SP interval: 37.5m; (4) fold: 106; (7) group interval: 12.5m; (8) streamer length: 7950m; (9) streamer depth: $8\text{m}\pm 1\text{m}$; and (10) sample rate: 2ms. The seismic reflection data have undergone Kirchhoff post-stack time migration. Both time and depth migrated profiles were provided by TGS, along with their respective migration velocities. The two-way-travel time (twt) lines extend down to 14s, while the depth migration was carried out down to a depth of 18 km only, without capturing all the reflections observed in time. Thus, the seismic interpretation was carried out in the twt lines. The migration velocities were used to create a velocity model for the depth conversion. The seismic lines predominantly run in north-south (N-S) and north-northwest to south-southeast (NNW-SSE), east-west (E-W) and east-northeast to west-southwest (ENE-WSW) orientations. The dip lines (i.e., N-S to NNW-SSE) vary in length from 80 km to 250 km, while the strike lines (i.e., E-W to ENE-WSW) range from 54 km to 290 km. In the seismic survey, the spacing between seismic lines falls within the range of 120 to 200 km. This spacing significantly affects the correlation and interpretation of faults and crustal features. The varying line spacing highlights the uncertainty, particularly in fault correlations, which influences the imaging the relationship of neighbouring fault segments.

To enhance the value of the provided seismic reflection data, they were integrated with onshore exploration (Attoh et al., 2004) and offshore wells from the Ghana National Petroleum Corporation (GNPC; IHS, 2010; Adda et al., 2015). The exploration well data are situated in the northern and the eastern parts of the margin, while the offshore wells are found in the western region. Whenever possible, the wells were tied to the seismic lines to identify the different seismo-stratigraphic units (Figure 4.3).

Public domain satellite free air gravity (Figure 4.4a; Sandwell et al., 2014) was utilised alongside the seismic data to constrain the interpretation of the crustal domains and the structural features. It transpires that magnetic data (Figure 4.4b) is not useful for identifying crustal nature and contacts due to the magnetic

quiescence (e.g., Campan, 1995) during the Cretaceous, which coincided with the margin's evolution. Magnetic quiescence refers to a period that lacks magnetic anomalies, which provide insights into the age of the oceanic crust (e.g., Eagles, 2007).

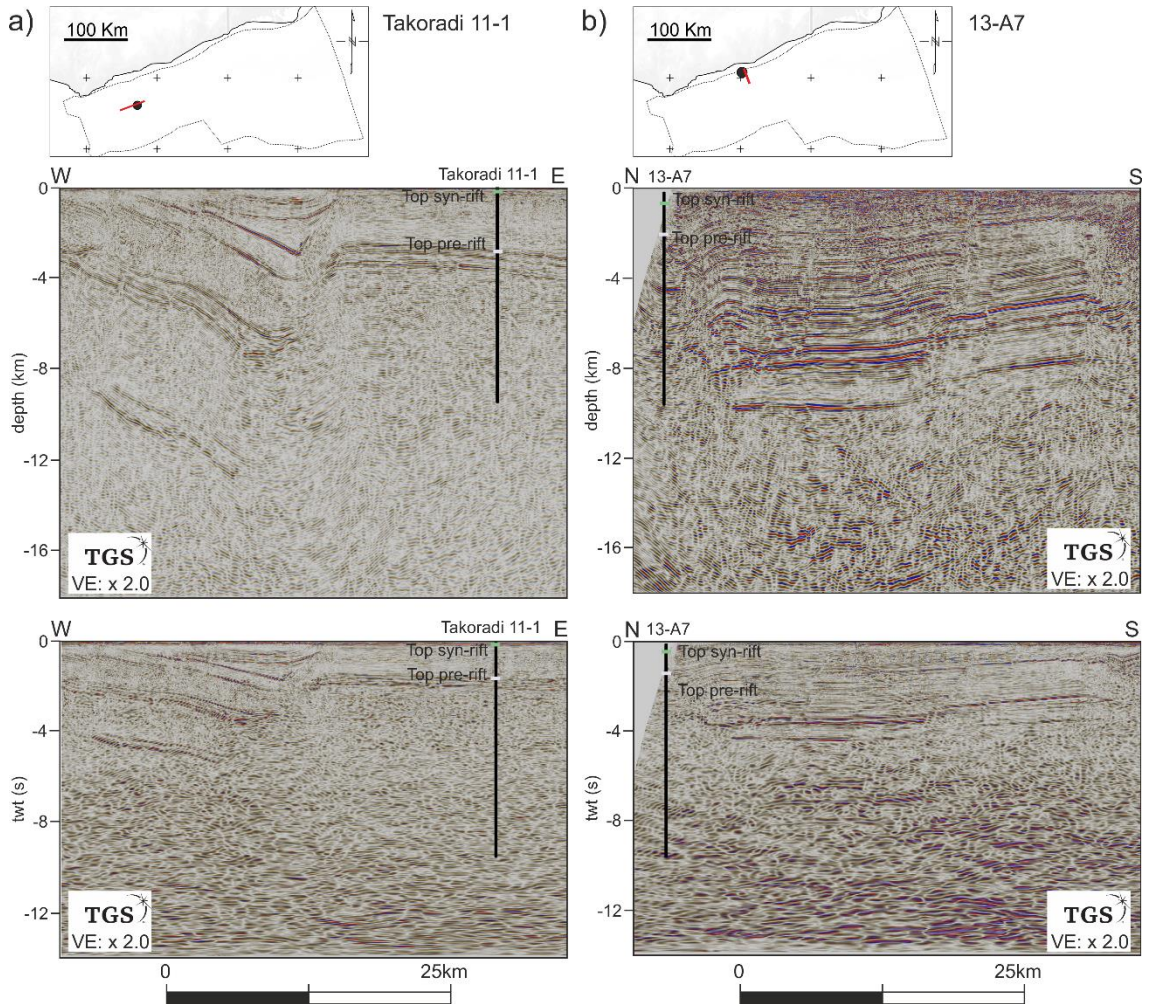


Figure 4.3: Seismic-well-tie at the offshore wells Takoradi 11-1 (a) and 13-A7 (b) in depth and time and the correspondent reflections of top syn-rift and top post-rift.

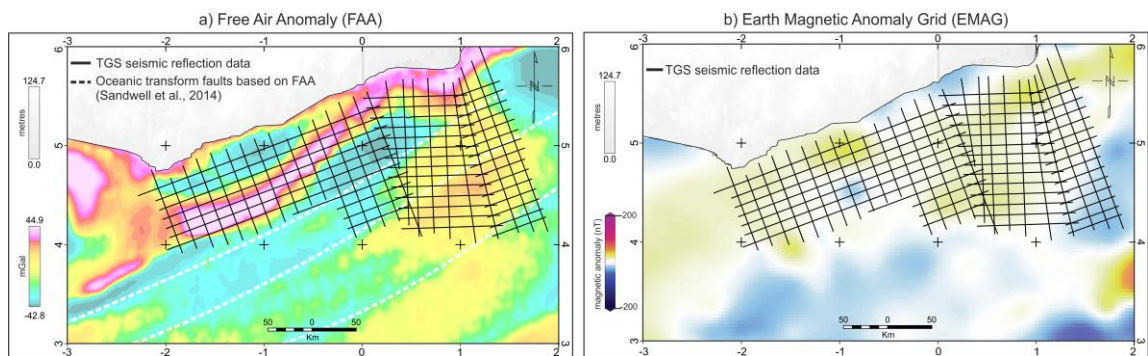


Figure 4.4: Onshore topography (Smith & Sandwell, 1997) with offshore a) Free Air Anomaly (Sandwell et al., 2014) and b) Earth Magnetic Anomaly Grid (EMAG; Meyer et al., 2017) along the Ghanaian region.

4.3.2 Methodology

The interpretation of seismo-stratigraphic units, crustal types, and structures was carried out in the time domain. Well data (Figures 4.1 and 4.3) were utilized to identify the seismo-stratigraphic sequences in the depth lines, which were then aligned with their corresponding reflection in the time lines (Figure 4.3). The wells presented in Figure 4.3, are located on structural highs, therefore the correlation of the stratigraphic sequences are based on similar seismic characteristics. The seismo-stratigraphic units were divided into three sequences of post-rift, syn-rift, and pre-rift, and their correlation away from the wells was based on stratal terminations and seismic facies (i.e., reflection amplitude and continuity). Ghana experienced multiple deformation events, and for simplicity, the pre-, syn-, and post-rift seismo-stratigraphic units are defined in line with earlier studies (Antobreh et al., 2009; Attoh et al., 2004). The ages of the mega-sequences are as follows: a) Devonian to Carboniferous, with Jurassic volcanics in places pre-rift; b) Aptian to Albian syn-rift, and c) Campanian to Holocene post-rift (Adda et al., 2015; Antobreh et al., 2009; Attoh et al., 2004; IHS, 2010).

Table 4-1: Sequence's depth based on published wells in the Ghanaian margin (Attoh et al., 2004; IHS, 2010; Adda et al., 2015).

Wells (tops)	Takoradi 11-1	Komenda 12-1X	13-A7	16.1	19.1	DZ
Syn-rift (m)	160	591	664	166	528	861
Pre-rift (m)	2,851	1,877	1,759	3,055	1,944	3,361

The well data show that the top of the pre-rift sequence lies at depth between 1,759 and 3,361 m, while the top syn-rift sequence can be found at depths between 160 and 861 m (Table 4-1). The correlation of the sequences is treated with highly confidence in close proximity to the wells and towards the western part of the margin, where the sequences seem continuous. On the other hand, the correlation becomes less confident towards the east, either due to the wells being situated significantly distant from the seismic lines or changes in the seismic characteristics of the sequence, leading to increased discontinuities.

Fault interpretation occurred utilising the aforementioned seismo-stratigraphic sequences and the discontinuities observed within them. Faults were classified according to pre-rift deformed sediments, syn-extensional sediments, locally inverted, and discontinuities flanking the faults. As previously noted, uncertainties in fault arise from the spacing between the seismic lines. In this study, I correlated the faults on the map using the simplest interpretation, given the dense distribution and varied orientations of the faults.

The identification of different crustal types was accomplished using seismic facies in the 2D seismic data, as further addressed in the following section. These crustal types were then used to create a map of interpreted crustal domains. The reflection of the Moho is clearly imaged in the deep basin as a high amplitude continuous reflection or a zone of chaotic discontinuous reflections around -11.5 s (twt), which is approximately 17.5 km in the depth domain. In the proximal domain, the Moho reflection is generally not imaged in most of the seismic reflection data. However, it could be imaged as a high amplitude reflection at -13.8 s (twt) towards the east of the margin. Typically, this reflection is too deep and not imaged in the depth migrated seismic data.

Lastly, based on variations in the margin's geometry and the lateral distinct characteristics identified in faults and crusts, the margin was divided into western, central, and eastern segments (Figure 4.1), in addition to the proximal domain and the deeper basin.

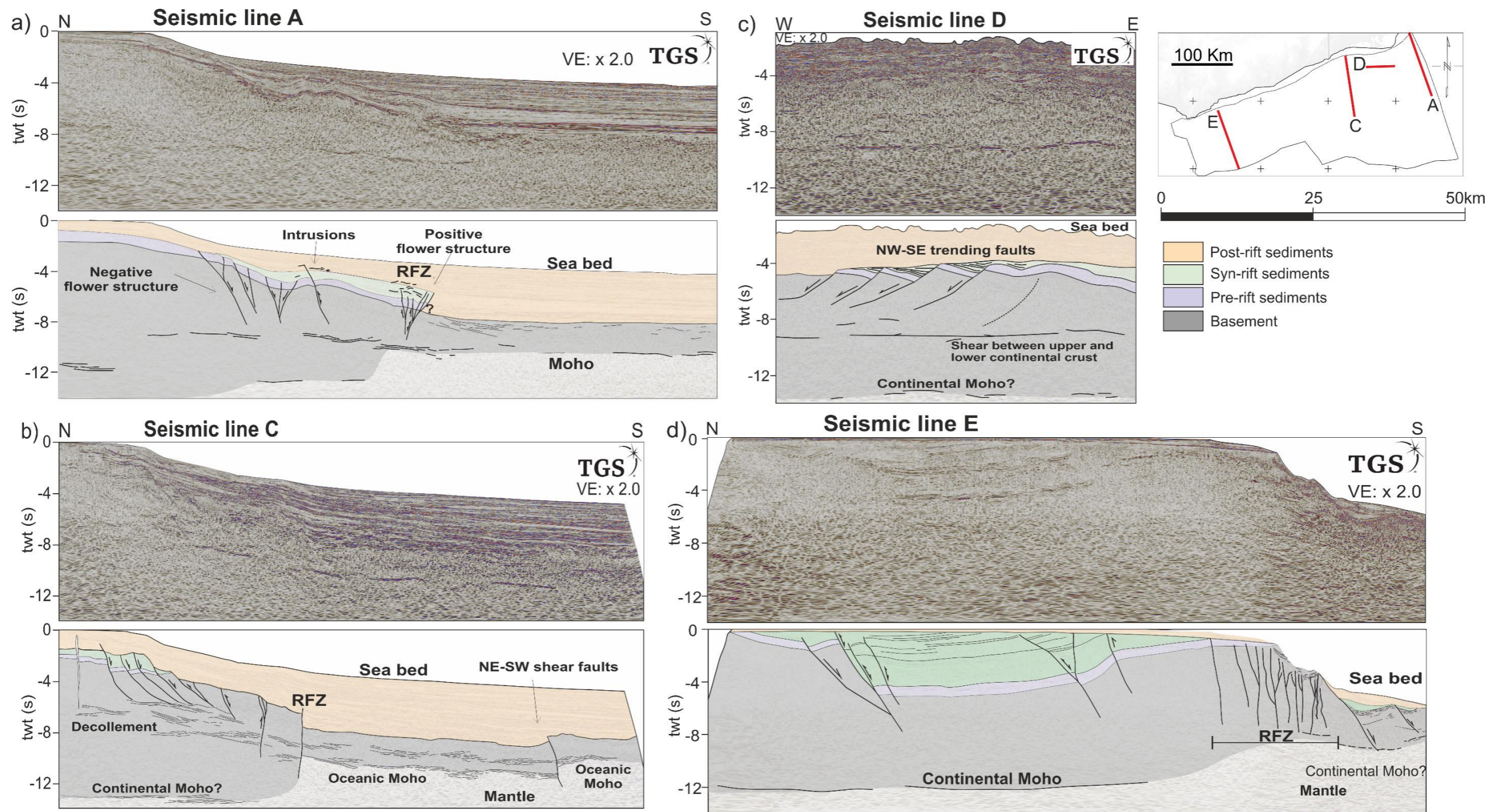


Figure 4.5: Key seismic lines illustrating the structural features and seismo-stratigraphic sequences along the margin. RFZ: Romanche Fracture Zone. Seismic data courtesy of TGS.

4.4 Seismic Analysis

In this section, the stratigraphic, structural and crustal architectures of the margin are presented, which are based on the interpretation and analysis of seismic and well data. Figure 4.5 illustrates fully interpreted key seismic lines focusing on the seismo-stratigraphic and structural characteristics along the Ghanaian margins.

4.4.1 Seismo-stratigraphic sequences

The pre-, syn-, and post-rift seismo-stratigraphic units were primarily identified using well data (Figure 4.3 and Table 4-1), and they are presented from shallow to deeper depths.

4.4.1.1 Post-rift

The post-rift sequence (Figures 4.5-4.6) consists of variable thickness carbonates (Figures 4.5-4.6a) in the shelf domain and marine shales to turbiditic sandstones in the deep basin (Figure 4.5-4.6b; MacGregor et al., 2003). In both proximal and distal domains, both turbidites and carbonates can be identified by continuous high amplitude reflections. In the proximal domain, the base of the post-rift is marked by onlaps, underlain by an unconformity with the syn-rift sequence (Figures 4.5, 4.6a and 4.7). In the eastern segment of the margin and the deeper basin, the post-rift sequence is characterised by a series of unconformities, while high amplitude reflections could correspond to post-rift intrusions (Figures 4.5a). In the deeper basin, the post-rift sequence overlies the basement directly. Notably, the thickness of the post-rift (Figure 4.6c) decreases towards the west (ranging between 0.0 and 0.2 s twt) and increases towards the east (ranging between 2.94 and 4.87 s twt), while remains relatively constant (3.5-4 s twt) in the deeper basin.

4.4.1.2 Syn-rift

The syn-rift sequence (Figures 4.5- 4.7) is characterised by consistent mid to high amplitude reflections. These reflections are primarily marked by toplap terminations, indicating a truncation unconformity at the top of the syn-rift sequence, which is upper Albian to Turonian of age (~110 - 89.8 Ma; Zalan et al., 1985; Blarez and Mascle, 1988; Mascle et al., 1988; Strand, 1988; Basile et al., 1993; Attoh et al., 2004; Antobreh et al., 2009; Basile, 2015; Mercier de Lépinay

et al., 2016). The syn-rift sediments appear sub-horizontal (Figures 4.3b, 4.7c and 4.8a) without the typical geometry of growth strata (Figure 4.7c-d), therefore the interpretation of the base and top syn-rift was based on the published well data (Table 4-1; Adda et al., 2015; IHS, 2010). However, locally in the western and eastern segments of the margin, some growth strata can locally be observed, reaching a time-thickness of 0.8 s twt (1.3 km) and juxtaposing against regional-scale continental faults (Figure 4.7a and 4.7c). On average, the syn-rift sediments have a thickness of 7.5 km, but can reach up to 10 km in the western segment of the margin based on the provided depth-converted seismic lines.

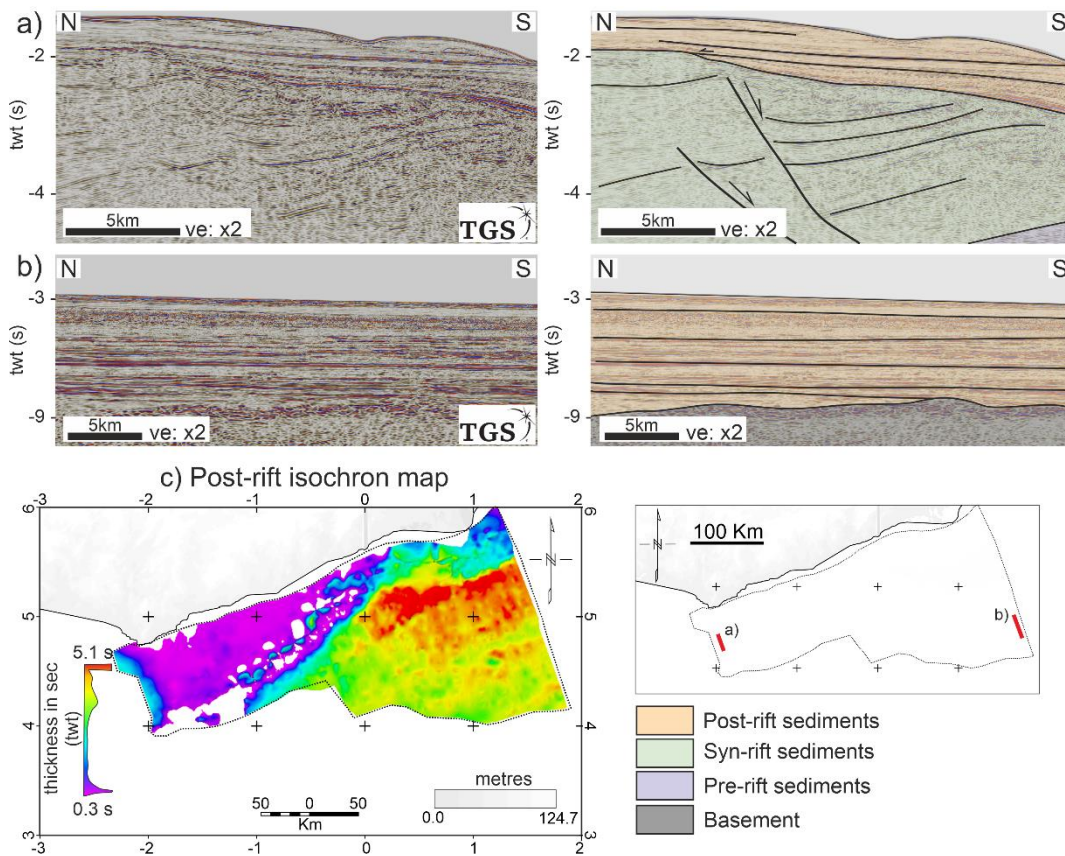


Figure 4.6: Representative seismic lines and interpretation of sedimentary sequences, focusing on the post-rift sequence in the proximal (a) and the distal domain (b). (c) Post-rift distribution and thickness map in time (twt). Seismic data courtesy of TGS.

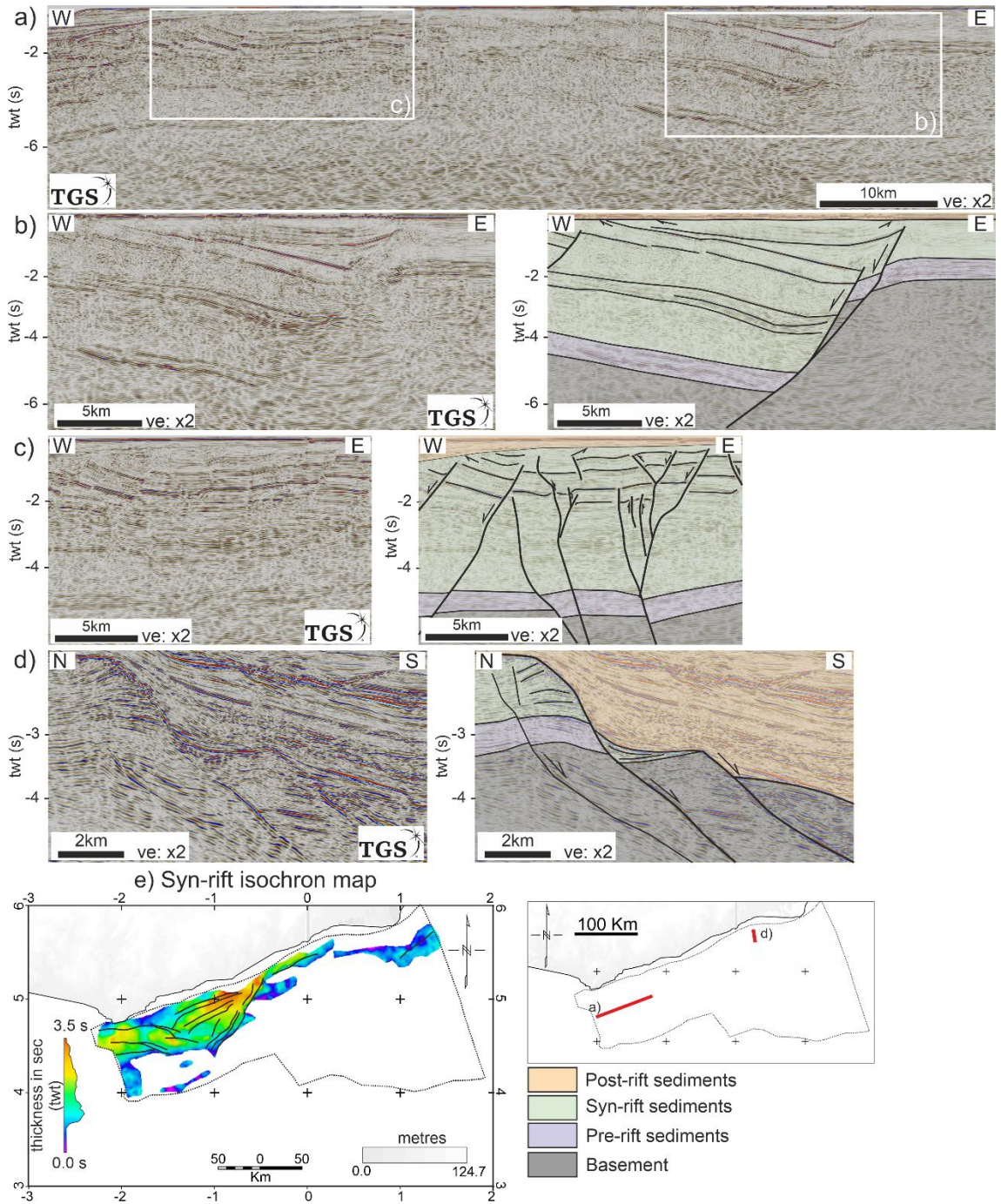


Figure 4.7: (a-c) Representative seismic lines and interpretation of sedimentary sequences in the western and eastern segments, focusing on the syn-rift sequence. Regional scale (a) extensional fault with growth strata, (b) positive flower structure in the syn-rift sequence in the western segment. (d) Minor syn-rift growth strata in the eastern segment. (e) Syn-rift sequence distribution and thickness map in time (twf) with the major faults influencing the syn-rift sediments. Seismic data courtesy of TGS.

4.4.1.3 Pre-rift

The pre-rift sequence exhibits two prominent spatial variations, which differ in their pre-rift deformation. The first one (Figures 4.5, 4.7-4.8) has consistent seismic facies and thickness similar to the aforementioned syn-rift sequence. In the western segment, a continuous, high amplitude reflection marks the contact between the pre- and syn-rift. In the well data, Jurassic volcanics with variable thickness of up to 100 m form the boundary between the pre- and syn-rift sediments (Attoh et al., 2004; IHS, 2010). This boundary can be identified as a single high amplitude reflection in the seismic lines. This reflection is either disrupted by contractional deformation (Figure 4.8a) or thins towards the central and eastern segments of the margin, where it is not observed. In the western segment, the pre-rift sequence has a time-thickness of 1.0 s twt, approximately equivalent to 1.7 km thickness in depth converted seismic data. In the central segment, the pre-rift sequence (Figure 4.8a) is characterised by pre-rift deformed sediments forming a series of antiforms by NNE-SSW trending thrust faults, and can reach time-thickness of 2 s twt (Figure 4.8c). This sequence forms a topographic high and could be related to the syn-rift sediments' inconsistent distribution between western and eastern segments (Figures 4.7d and 4.8c). Northwest of the thrusts, steep extensional normal faults can be imaged, which are primarily trending ENE-WSW (Antobreh et al., 2009; Nemčok et al., 2013). In the pre-rift sequence, salt has also been identified at the southwest edge of the western segment (Figure 4.8b). However, the influence of salt tectonics on the margin's formation history is minimal and is not further discussed. Distribution maps and thickness profiles of the post-, syn-, and pre-rift sequences in time are displayed in Figures 4.6-4.8.

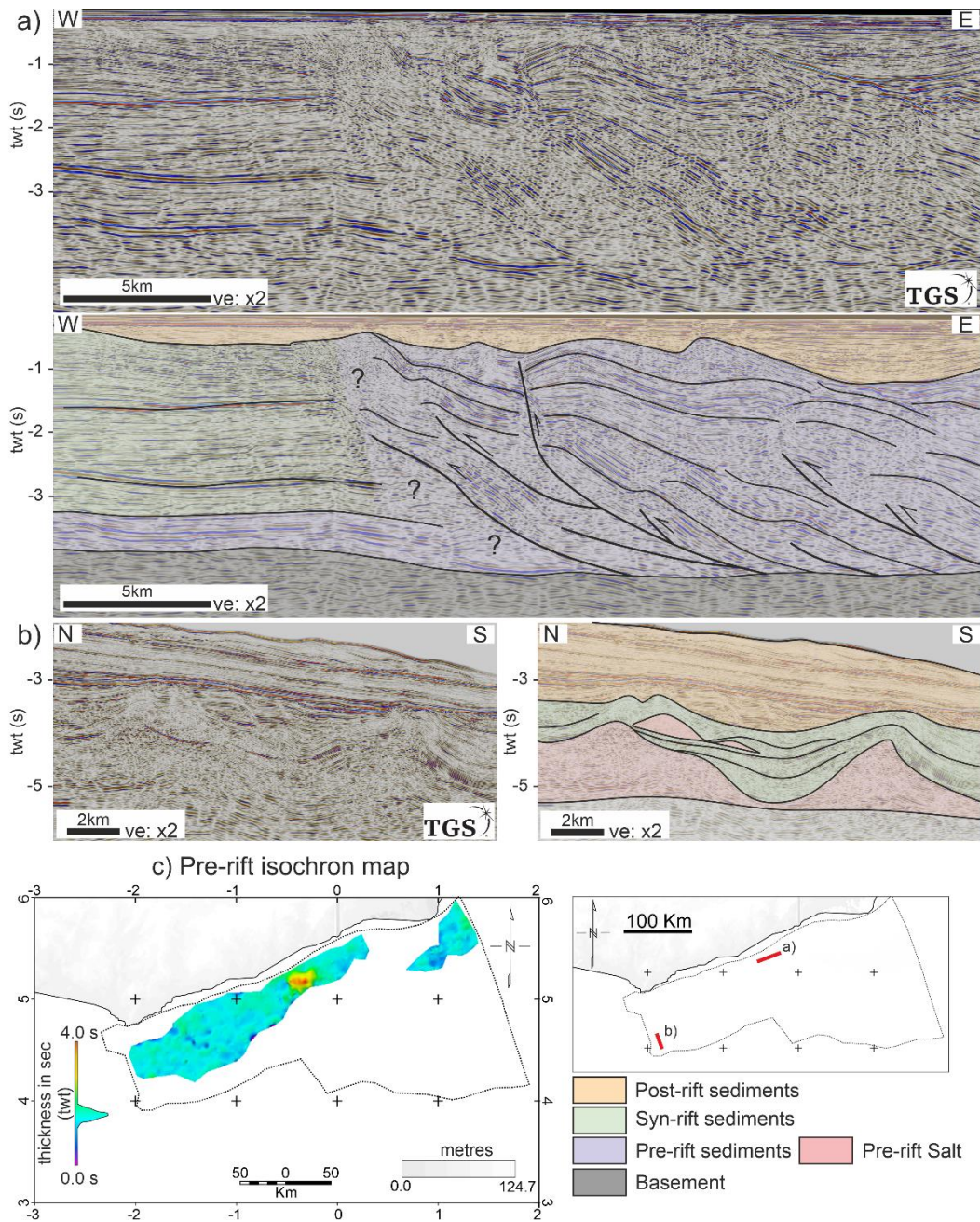


Figure 4.8: (a-c) Representative seismic lines and interpretation of sedimentary sequences, focusing on the pre-rift sequence. (a) Pre-rift sequence of antiforms, which are related to pre-rift orogeny, and (b) pre-rift salt identified in the western region. (c) Post-rift sequence distribution and thickness map in time (twf). Seismic data courtesy of TGS.

4.4.2 Faults

Faults have been identified in both the shelf domain and the deeper basin. In the depth-converted seismic lines (e.g., Figure 4.3), where the structural geometry is accurately portrayed, various fault types can be differentiated. The western segment of the margin stands out for its two NW-SE trending basins, which formed due to continental NW-SE extensional normal faults, resulting in the development of extensional growth strata (Figure 4.7a). These faults cut through the upper and lower continental crust, if not down to the Moho, exhibit thick-skinned faults, and form the largest accommodation space for the syn-rift sediments with significant growth strata (Figure 4.7a,e). The western segment of the basin reveals a system of vertical to sub-vertical contractional strike-slip faults and gentle folds, forming a positive flower structure (Figure 4.7b; Basile et al., 1993; Attoh et al., 2004; Antobreh et al., 2009; Mercier de Lépinay et al., 2016). Observing the syn-rift sediments (Figure 4.7a) exhibiting continuity from the extensional fault to the positive flower structure, it seems that the contraction occurred after the extension in the Ghanaian margin.

In the eastern segment of the margin, ENE-WSW extensional normal faults dipping towards the deeper basin are imaged, alongside vertical to sub-vertical extensional and contractional faults. These latter faults form negative flower structures at the eastern edge of the data (Figure 4.5a). Similar to the western segment of the margin, NW-SE trending normal faults are observed (Figure 4.5b,c), with less extensional deformation than the eastern segment faults. These faults are positioned between the ENE-WSW trending faults.

Between the shelf domain and the deeper basin, a series of faults trending ENE-WSW could potentially correspond to the Romanche Fracture Zone (Figure 4.5, RFZ; Mascle and Blarez, 1987; Basile et al., 1993; Attoh et al., 2004; Antobreh et al., 2009; Nemčok et al., 2013; Davison et al., 2016; Andrade et al., 2018). The RFZ displays varying characteristics along the margin. In the western segment, it is characterised by south-dipping extensional and vertical to sub-vertical faults (RFZ; Figure 4.5d), which transition into contractional strike-slip faults towards the central segment (RFZ; Figure 4.5a), forming positive flower structures. In the eastern segment, the RFZ displays extensional or strike-slip and contractional deformation (RFZ; Figure 4.5b). The western segment shows less contractional

deformation than the eastern and the central segments. It is important to note that due to the 2D nature of the seismic data, the imaged dip direction represents the apparent dip. However, the proximity of the seismic lines to one another allows fault correlation based on similarities in sediments and fault geometries. The inversion, which was described mostly by the positive flower structures observed in the sediments (Figure 4.6b) and along the Romanche Fracture Zone (Figure 4.5a), postdates the extension and the breakup. It caused deformation in the syn-rift sediments (e.g., Figure 4.7c) and persists during the post-rift phase, as illustrated in the post-rift sequence (Figure 4.5a).

In the deeper basin, two distinct groups of faults can be recognized. The first set trends NE-SW (Figure 4.5b), showing contraction towards the northwest and extension towards the southeast of the deeper basin. The second set of faults trends NW-SE to NNW-SSE (e.g., Figure 4.5c), showing extensional deformation in the upper crust. These faults will be further analysed in the crustal analysis.

4.4.3 Crustal types

In the seismic data, the Moho discontinuity is imaged as a single high amplitude reflection or a zone of discontinuous high amplitude reflections. It is observed at time-depths between -10 and -12 s twt (Figures 4.9a and 4.10a) in the deeper basin. In contrast, in the shelf domain, the Moho is rarely and partly imaged at -13.8 s twt (Figures 4.9a, 4.10b and 4.11) in the eastern segment of the margin. Even though it is partly imaged, the Moho's depth at the shelf domain is consistent, with a minor variation in the western segment, where it was interpreted shallower at approximately -7.5 s twt (Figures 4.9a and 4.12a).

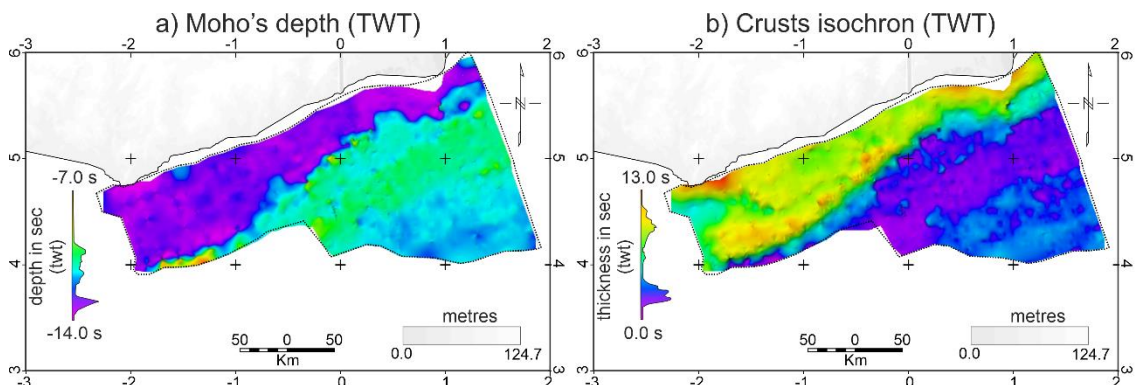


Figure 4.9: (a) Depth in time (twt) of the interpreted Moho, and (b) isochron map between the top crusts and Moho.

Between the basement and the observed Moho, different crustal types were recognised based on their seismic characteristics (Tables 4-2 and 4-3) and their isochron observed in the seismic reflection data (Figure 4.9b). The distinction between the continental and oceanic crust was based on the stratigraphy, the presence or lack of syn-rift and pre-rift sediments, and their seismic characteristics. I distinguished the oceanic crust based on the presence of high amplitude reflections, the consistent thickness and the lack of rift-related faults. The continental crust was mostly identified based on the sediments. However, these are absent towards the eastern segment (Figure 4.7) and the interpretation of the continental crust was based on the thickness and the seismic facies. In the western segment, an additional crustal type was interpreted, where the distinction between the continental and oceanic crust was ambiguous.

Four different configurations of oceanic crust (Table 4-2 and Figures 4.10-4.13) can be differentiated in the seismic data, which can be distinguished based on their seismic characteristics. From the proximal towards the distal domain:

- i) Oceanic crust type-1 (1.Oc; Table 4-2 and Figure 4.11a), which is the closest to the RFZ, appears as a two layered crust. Moho is imaged as a single high amplitude reflection between -11.5 and -10.8 s (tw). The top crust was interpreted between -9 and -7.0 s (tw). The crust layers are divided by a zone of continuous high amplitude reflections, which has a consistent depth between approximately -8.0 and -9.0 s (tw).
- ii) Oceanic crust type-2 (2-3.Oc; Table 4.2 and Figures 4.10-4.12) is the thinnest type (Figure 4.8b; purple). Here, the Moho is imaged as a continuous high amplitude reflection between -10 and -11 s (tw), and the top crust between -9.0 and -7.5 s (tw) with chaotic low to high amplitude reflections. In the eastern segment (Figure 4.13a), the oceanic crust type-2 changes seismic characteristics with dipping reflections reminiscent of seawards dipping reflections in the upper part of the crust, which are dipping towards the west, and an additional high amplitude reflection imaged between -10.5 s and -12.5 s (tw). The latter reflection (3.Oc-purple; Table 4-2 and Figure 4.13a), is imaged at a greater depth than the adjacent oceanic Moho, exhibiting local variations in depth, forming steep geometries, and occasionally merging with the surrounding oceanic Moho.

These features contradict the typical oceanic crust characteristics identified in this region. The nature of this reflection will be further analysed with gravity. For both oceanic crusts type-1 and type-2, the top basement was interpreted based on the stratal terminations, where the top crust is imaged as chaotic with low amplitude reflection characteristics.

- iii) Oceanic crust type-3 (4.Oc; Table 4-2 and Figure 4.10a) has a Moho at depths from -9.2 down to -10.5 s (twt) as a zone of chaotic, high amplitude reflections. The basement of oceanic crust type-3 has chaotic low amplitude seismic characteristics. This type of seismic characteristics is continuous down to the Moho, but some high amplitude, partly continuous reflections can be locally imaged.
- iv) Oceanic crust type-4 (5.Oc; Table 4-2 and Figure 4.10a) is made of three layers. The Moho consists of a zone of high amplitude discontinuous reflections from -10 to -11.8 s (twt). The top crust is characterised by continuous to discontinuous high amplitude reflections from -8.2 to -9.0 s (twt), while the mid crust consists of a chaotic low amplitude zone.

The different layers in the oceanic crust could indicate changes in composition (e.g., Pirajno, 2000), while the high amplitude dipping reflections observed within the crust could be interpreted as dykes. Usually, the oceanic crustal types are divided by NE-SW trending faults (Figure 4.10), which cut the crust from basement to Moho, and sometimes show contractional deformation and flexural uplift interpreted to have been induced by thermal contraction (e.g., Figure 4.11a; Basile & Allemand, 2002; Bonatti et al., 2005). However, locally there is a smooth transition between the oceanic crustal types. Lastly, NW-SE to NNW-SSE trending faults can be observed. These faults have been developed within the upper oceanic crust, forming localised growth strata, indicating synchronous activity with the oceanic crust formation. These features are illustrated as having high amplitude reflections (Figure 4.12c).

In the proximal domain of the margin, the seismic reflection data provides clear imaging of the continental crust. The seismic characteristics of the continental crust vary from the western to the eastern segment. In the western and central segments, a shallow surface of continental basement at approximately -1.5 s (twt) could be interpreted as the marginal ridge (refer to the terminology list and Figure

C1 in appendix) of the Ghanaian margin (Figure 4.12a; e.g., Blarez and Mascle, 1988; Basile et al., 1993; Sage et al., 1997). This ridge marks a sharp transition between the crusts, and its orientation aligns with the NE-SW trend of the RFZ. The seismic characteristics of the marginal ridge are marked by chaotic continuous high amplitude reflections, which can be attributed to acoustic noise due to their “*smile*” geometry (3.Cc; Table 4-3), due to the high density of strike-slip faults in the basement (Figure 4.12a). In the western segment, a post-rift sequence is observed at the top of the marginal ridge, which is flanked by extensional structures dipping towards the distal domain (Figure 4.12a), forming faulted tilted blocks towards the south. The marginal ridge does not appear in the central and eastern segments, indicating significant variations along the margin.

Table 4-2: Key seismic facies and reflection relationships for the crustal type “Oceanic crust” (Oc) and “Magmatic crust” (Mc). Highlighted in red indicates the specific reflections of interest. Highlighted in blue indicates the reflections that are not directly linked to the oceanic crustal type.

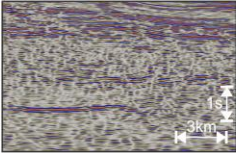
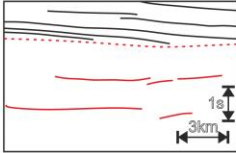
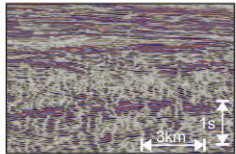
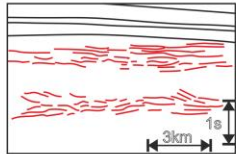
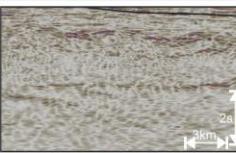
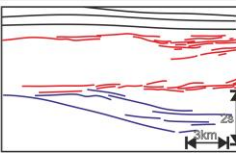
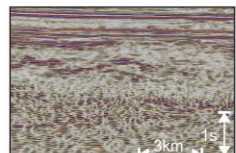
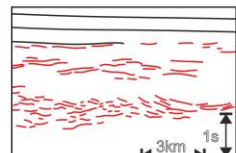
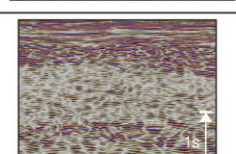
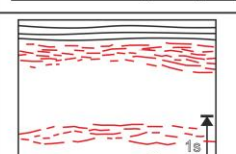
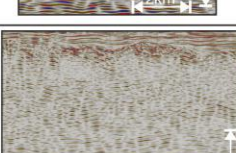

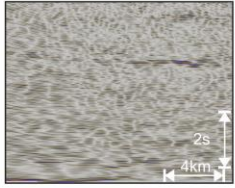
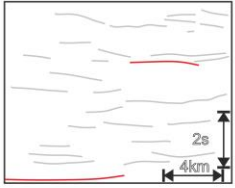
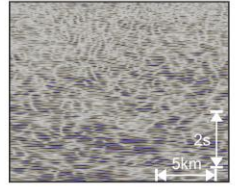
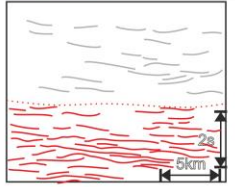
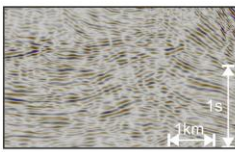
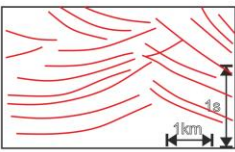
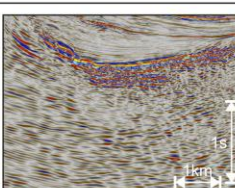
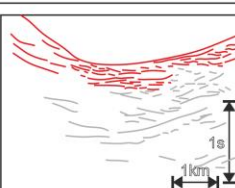
Crustal type	Seismic facies	Key reflection relationships	Reflection characteristics	Seismic facies association
1.Oc			Chaotic and low amplitude top crust (dashed line). High amplitude, continuous reflections at the middle and base crust.	Classified as a two-layer oceanic crust.
2.Oc			Continuous to discontinuous, high to low amplitude reflections at the top and base of crust.	Classified as a one-layer oceanic crust. The thinnest oceanic crust with relatively consistent thickness.
3.Oc			Similar to (2.Oc). Continuous to discontinuous, high to low amplitude reflections at the top and base of crust. High amplitude reflections underneath the base of crust with irregular geometry.	Classified as a one-layer oceanic crust. Additional type of reflection underneath the crust.
4.Oc			Chaotic low amplitude reflections at the top crust. High amplitude, discontinuous reflections in the upper and base crust.	Classified as a three-layer oceanic crust with some abnormal high amplitude reflections in the upper-middle crust, and a relatively consistent thickness.
5.Oc			High amplitude, discontinuous sets of reflections at the top and base crust. Chaotic seismic characteristics in the middle of the crust.	Classified as a three-layer oceanic crust with a consistent thickness.
6.Mc			High amplitude, continuous top crust, with underlying high amplitude discontinuous reflection. Chaotic low amplitude middle crust, and low amplitude discontinuous reflections at the base of the crust	Classified as a magmatic crust with variable geometries of volcanoes. The crust has variable thickness.

Table 4-3: Key seismic facies and reflection relationships for the crustal type “Continental crust” (Cc). Highlighted in red indicates the high amplitude reflections in the crust. Highlighted in grey indicates the low amplitude reflections in the crust.

Crustal type	Seismic facies	Key reflection relationships	Reflection characteristics	Seismic facies association
1.Cc			Discontinuous, low amplitude reflections (grey) from top to base crust, with high amplitude reflections (red) in the middle and low crust.	Continental crust. High amplitude reflection in the middle crust, the contact between lower and upper crust. Moho - the deepest high amplitude reflection.
2.Cc			Discontinuous, low amplitude reflections (grey) in the upper crust, and semi-continuous, high amplitude reflection in the lower crust.	Continental crust with different seismic characteristics in the upper and lower crust. The difference marks their contact (dotted line).
3.Cc			High amplitude, reflections form geometries of "smiles".	Thick continental crust.
4.Cc			Discontinuous, high amplitude reflections at the top of the crust (red). The reflections decrease their amplitude (grey) with depth.	Thin continental crust.

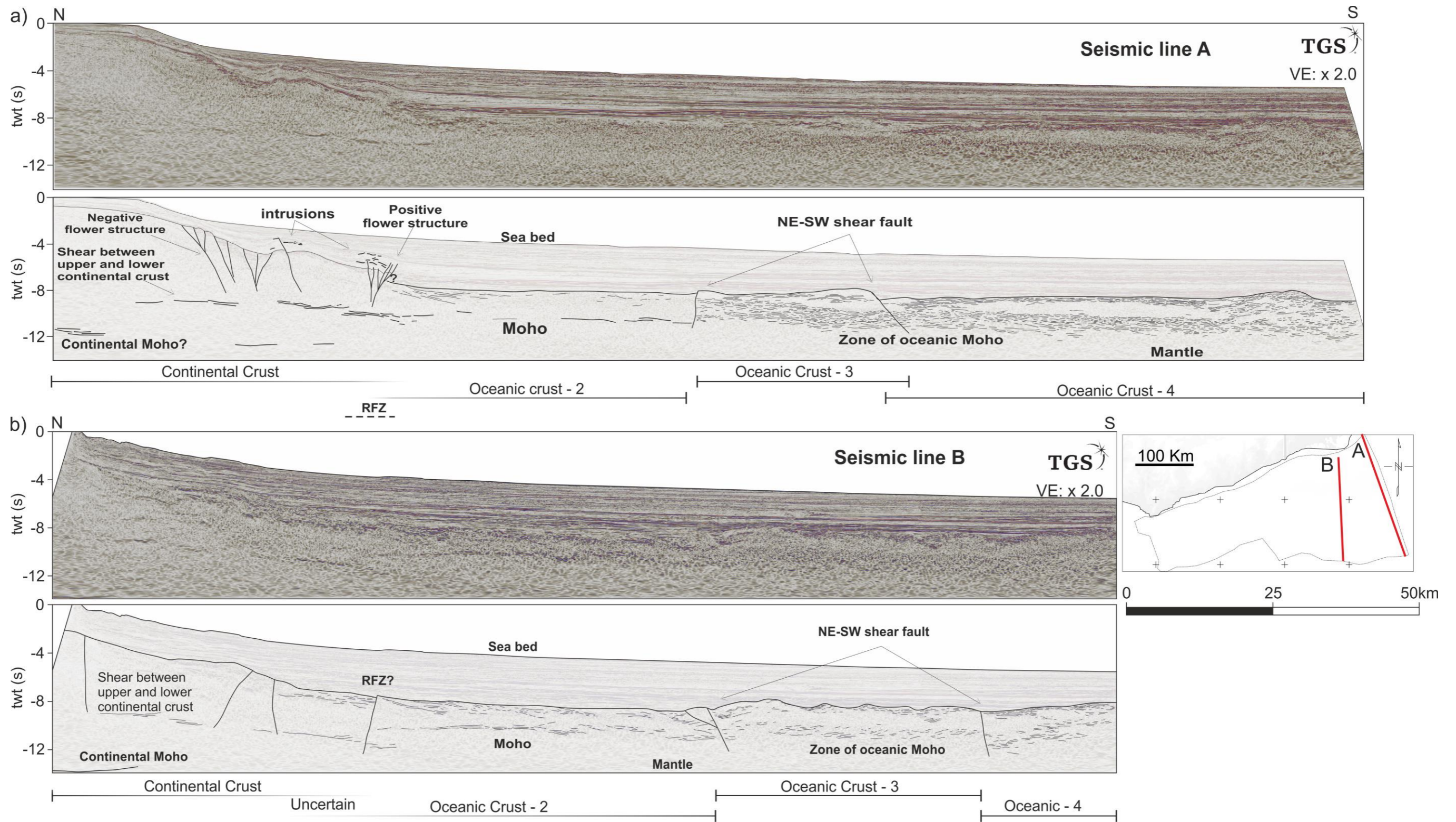


Figure 4.10: The seismic line A (a) and B (b) illustrate representative seismic characteristics of the different oceanic crustal types, the continental crust, and the uncertain crustal type, and the Romanche Fracture Zone (RFZ) at the eastern segment of the margin. Seismic data courtesy of TGS.

In the western segment, northwest of the marginal ridge, the continental crust is imaged with low amplitude and chaotic reflectivity. It is affected by a series of faults which form several half-graben basins (Figures 4.7b and 4.12a). The top basement is imaged at -7.5 s (tw) with high amplitude reflections, though the continental Moho remains elusive in the seismic reflection data (4.Cc; Table 4-3 and Figure 4.11a). In the central segment, the top basement is imaged consistently at approximately -4.5 s (tw; Figure 4.11a). Here, the seismic characteristics of the continental crust change compared to the previous segment. From the top basement up to -7.0 s (tw), the crust appears with very low amplitude, akin to what is observed in the western segment. However, at depths exceeding -7.0 s (tw), the crust exhibits discontinuous high amplitude reflections (2.Cc; Table 4-3). The base of these high amplitude reflections could signify the Moho discontinuity, and the difference in the seismic facies between low and high amplitude could mark the boundary between the upper and lower continental crust.

In the eastern segment, the crust maintains the low amplitude seismic character, similar to the western segment. However, a high amplitude reflection is imaged at -8.0 s (tw; 1.Cc; Table 4-3 and Figures 4.10 and 4.12a) which could potentially indicate the contact between the upper and the lower crust. As previously mentioned, a high amplitude reflection of the Moho can be seen at -13.8 s (tw; Figure 4.10b). The top basement is imaged between -1.5 to -4.0 s (tw). Within the continental crust, high amplitude continuous to discontinuous reflections could refer to structures or magmatic intrusions. Moreover, the eastern segment crust seems less affected by the deformation, exhibiting localised faulting by oceanward-dipping normal faults (Figure 4.11a) and gentle folding through inverted structures (Figure 4.10a).

A magmatic crust can be found in the western segment (Figure 4.13b) and is potentially defined as a transitional crust. This magmatic crust forms the transition between the continental crust and the oceanic crustal types 1 and 2. The top of the crust is imaged between -6.6 and -8.0 s (tw) as high amplitude reflections (Mc; Table 4-2), which could indicate volcanics as potential volcano geometries are observed (Figure 4.13b). The crust's Moho is partly imaged at -11.5 s (tw) and appears as an array of mid amplitude, discontinuous reflections, merging

with the oceanic Moho, and fades towards the continental crust. The classification as a magmatic crust is supported by its characteristics, including high amplitude reflection on its basement, consistent thickness exceeding that of the oceanic crust (Figure 4.9b), the absence of faults that could suggest a continental crust presence, and the gentle transition from continental to oceanic crust.

Lastly, in the eastern segment, there is an uncertain type of crust situated between the unambiguous continental and oceanic crusts (Figures 4.10b and 4.11a). This crust is defined by its consistent thickness, a high amplitude semi continuous reflection of Moho between -10.7 and -11.6 s (tw), low amplitude discontinuous reflections from basement to Moho with a high amplitude reflection in the middle crust, and high amplitude discontinuous reflections from -7.3 to -8.5 s (tw) for top crust. While it could tentatively be interpreted as oceanic crust type-1 due to its thickness and seismic characteristics, the ongoing connection with the continental crust and the similar seismic characteristics complicates the characterisation. This crust is also locally divided by strike-slip faults, marking the boundary between the continental and oceanic domains. To identify the nature of this crustal type, it will be further investigated with gravity.

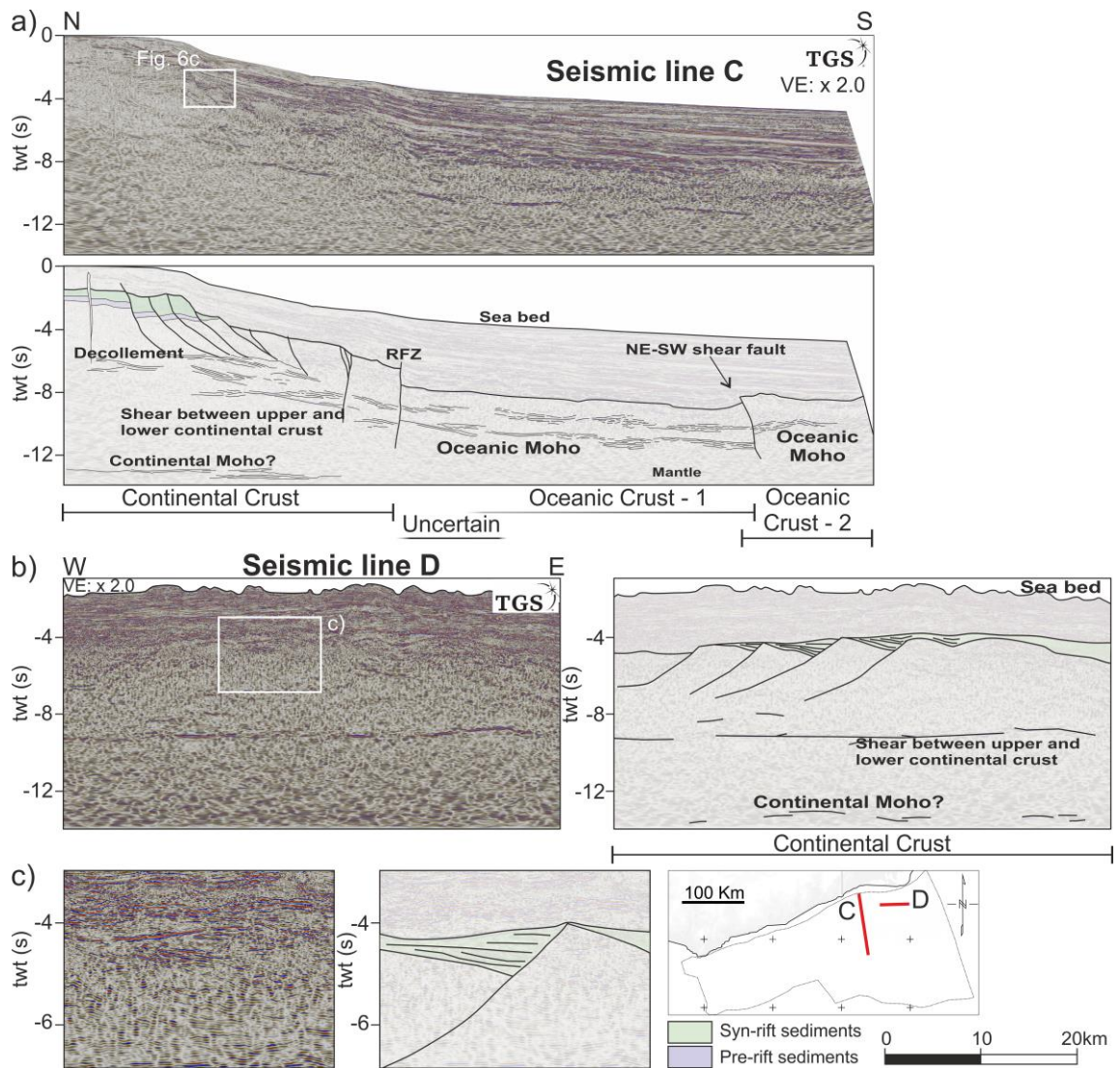


Figure 4.11: Seismic lines C and D illustrate characteristics of the eastern and central segments of the margin. Seismic line C (a) illustrates representative seismic characteristics of the different continental and oceanic crusts, and the Romanche Fracture Zone (RFZ). Uncertain crustal type is imaged at the continental-oceanic transition. Seismic line D (b,c) illustrates the continental crust's NW-SE trending faults. Seismic data courtesy of TGS.

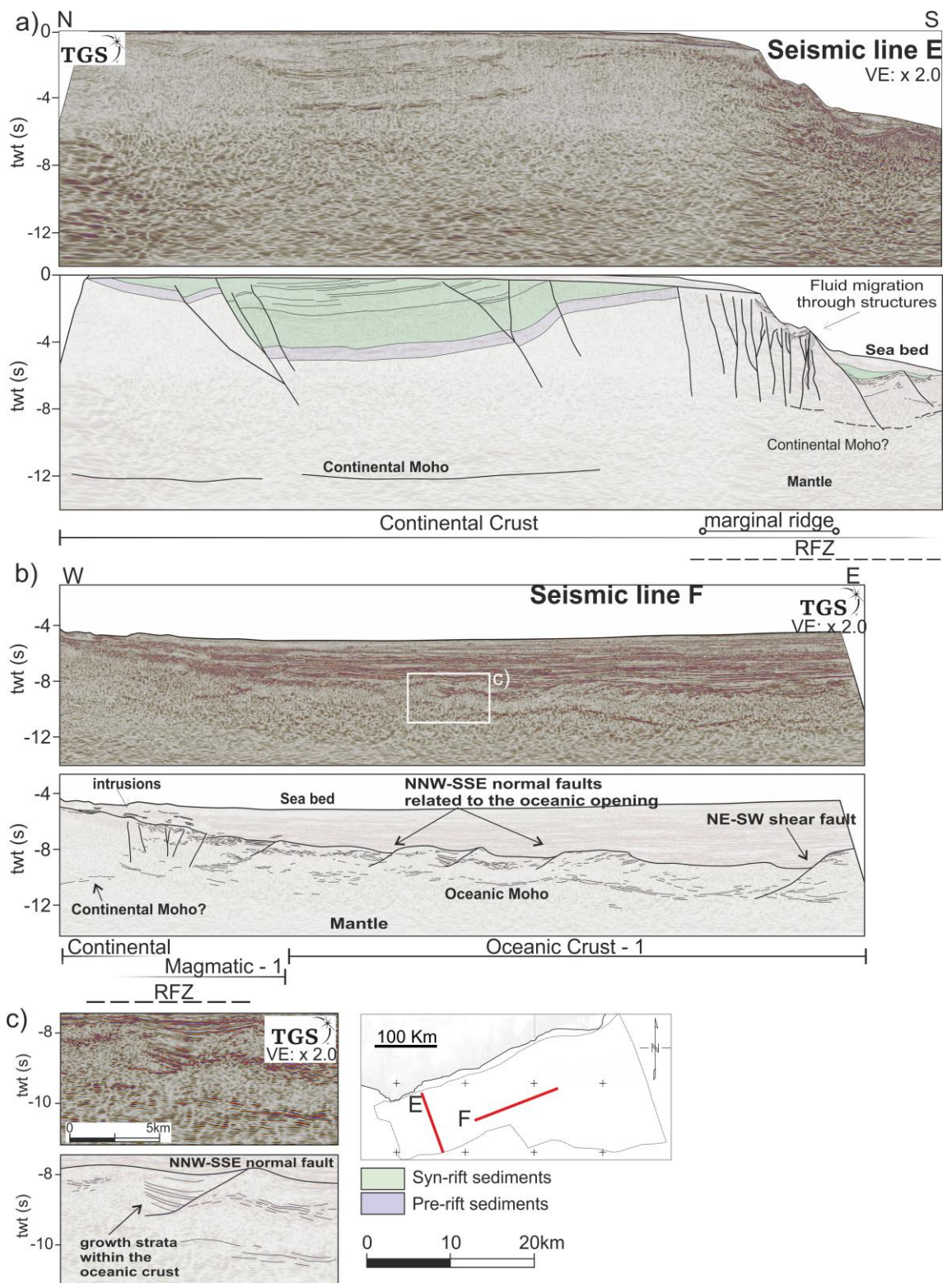


Figure 4.12: Seismic lines E and F illustrates the margin's characteristics in the western segment. The continental crust in (a) changes thickness south of the marginal ridge in the Romanche Fracture Zone (RFZ). Seismic line F (b,c) illustrates the transition from continental to oceanic crust, and the oceanic crust's structures along the strike line, with zoom-in (c) on the growth strata. Seismic data courtesy of TGS.

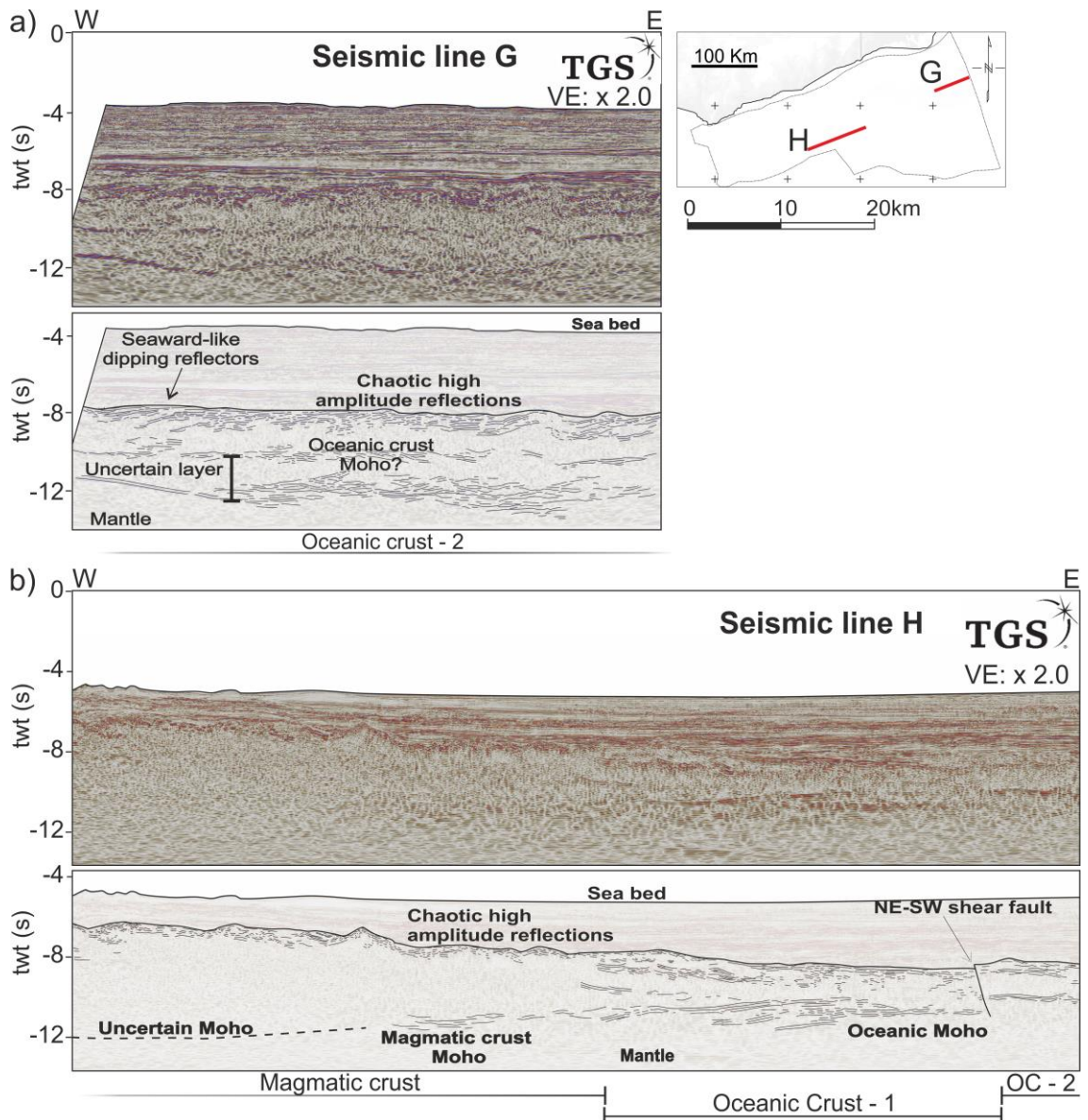


Figure 4.13: Representative seismic line of the oceanic crust type-2 with the uncertain underlying high amplitude reflection (a) and the magmatic crust (b). (a) Oceanic crust type-2 illustrates seaward-like dipping reflectors on the upper crust. The irregular high amplitude reflection is imaged deeper than the surrounding oceanic Moho. (b) Geometries of potential volcanoes are imaged on the magmatic crust basement, and Moho is not imaged. Seismic data courtesy of TGS.

Following the seismic analysis, a map (Figure 4.14) of different crustal types was produced. In general, the region is confidently mapped, primarily based on the seismic reflection data. However, in the eastern segment, the uncertainties become more pronounced. The two main uncertainties are: i) the precise boundary between oceanic and continental crust within the uncertain domain (e.g., Figure 4.10b), and ii) the nature of the uncertain layer (Figure 4.13a),

underlies the oceanic crust type-2 with an irregular basal geometry (Figure 4.13a). To address these aforementioned uncertainties, velocity and 2D gravity modelling along specific seismic lines were conducted.

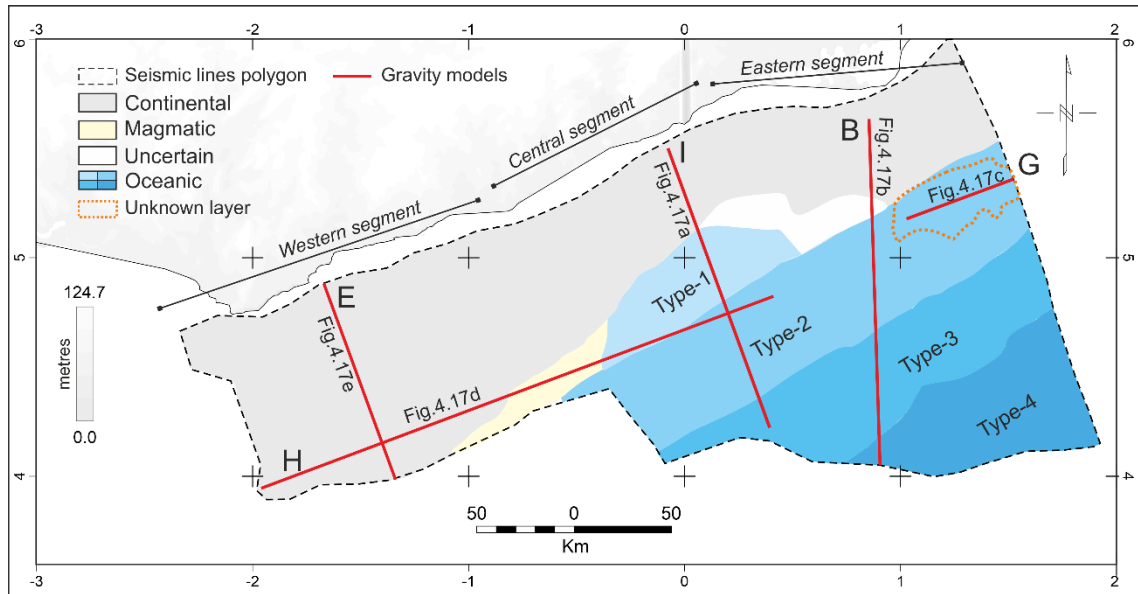


Figure 4.14: Crustal types and displayed uncertainties based on the seismic characteristics. Red traces indicate the gravity models location in Figure 4.17.

4.5 Velocity and Gravity Analysis

4.5.1 From time-to-depth

To validate the crustal types, refine their limits, reduce the uncertainties regarding their nature, especially the uncertain crust (Figure 4.10b) and the layer beneath the oceanic crust type-2 (Figures 4.13a and 4.14), and enhance constraints on the Moho depth underneath the continental and the magmatic crusts, a comprehensive workflow was conducted. This involved velocity analysis, time to depth conversion, and forward 2D gravity modelling using Geosoft Oasis Montaj (GM-SYS profile modelling; Pouliquen et al., 2017) along interpreted seismic lines.

First, to produce the velocity model, migration velocities were extracted from the 2D velocity lines provided by TGS (Figure C.2 in appendix) by building a grid for each sequence, i.e., seabed, post-, syn-, and pre-rift, continental, magmatic,

uncertain, and oceanic crusts, and converted to interval velocities using Dix's equation (Dix, 1955):

$$v_{int} = [(t_2 * v_{RMS2}^2 - t_1 * v_{RMS1}^2) / (t_2 - t_1)]^{1/2}$$

where: v_{int} is the interval velocity, t_1 & t_2 are the top and the base respectively (in twt) for each interval, and v_{RMS1} & v_{RMS2} are root-mean-square velocity at the top and the base respectively.

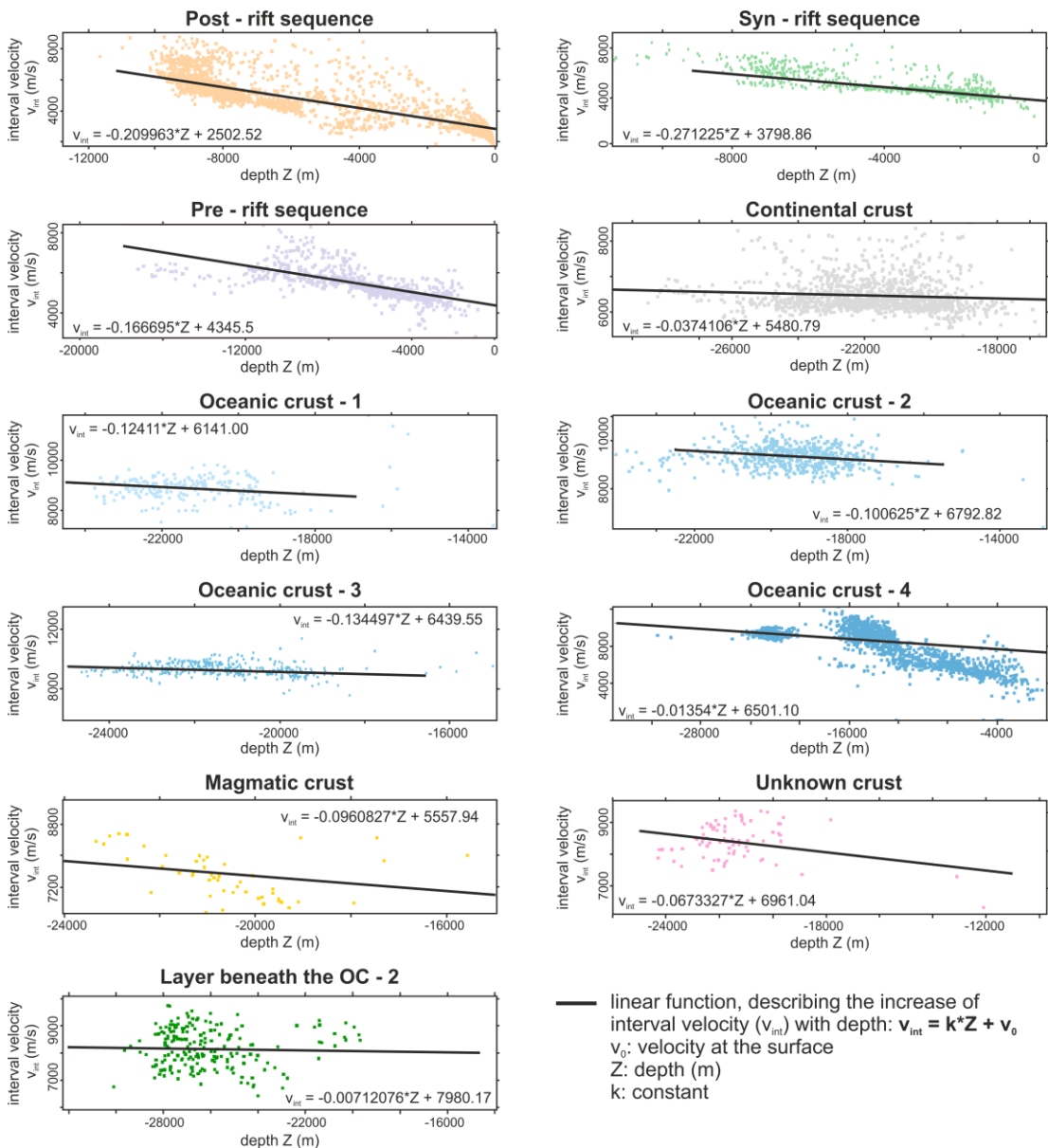


Figure 4.15: Plots of interval velocity and depth pairs [interval velocity, depth] for each seismo-stratigraphic and crustal unit calculated from the extracted migration velocities using the Dix's formula (Dix, 1955).

The obtained interval velocities were then analysed to infer interval velocity functions for each seismo-stratigraphic layer and crustal unit (Figure 4.15 and Table 4-4). It is noteworthy that using migration velocities to construct a velocity model for the depth conversion might cause major uncertainties as the migration velocities are used for imaging rather than true depth conversion (Etris et al., 2001; Schultz, 1999). This type of velocities, their laterally distributed anisotropy, and the complex nature of the subsurface structures increase the uncertainty in the depth conversion, and can overestimate the depths.

Lastly, average density values (Table 4-4) were calculated for all sequences using the Gardner's equation (Gardner et al., 1974), which were later used for the gravity modelling:

$$\rho = 0.23 * V_P^{0.25} \text{ km/m}^3$$

where: V_P is the average interval velocity.

Table 4-4 summarises the average and interval velocities that were used during the depth conversion, and the calculated densities for each sedimentary sequence and crustal types during the depth conversion. The mantle's average velocity and density exhibited smaller values, possibly linked to a shallower interpretation of the continental Moho, where the reflections could not be effectively imaged. To mitigate the uncertainty, typical values of 8000 m/s and 3.30 g/cm³ were applied for mantle (e.g., Mjelde et al., 2005). Similarly, standard velocity (1500 m/s) and density (1.03 g/cm³) were used for the water column.

The seismic lines and horizons were depth converted based on average and linear interval velocity (Figure 4.15 and Table 4-4). For the pre-, syn-, and post-rift, I used average velocities instead of using the velocity function, due to the presence of variable lithology in the sequences and the unconformities that were observed in the seismic analysis.

Here, it is important to emphasise on the identified velocities for each crust, which are used to refine and interpret the crustal interpretation. The different types of oceanic crust have a maximum and minimum velocity of 6792.82 and 6141.00 m/s, respectively, with average velocity of 6466.91 m/s. The velocity of the uncertain crust (6961.04 m/s) aligns with the range of the calculated velocities in

the oceanic crust. The continental crust has a velocity of 5480.79 m/s, which is slightly lower than the magmatic crust's velocity of 5557.94 m/s. Lastly, the undifferentiated layer beneath the oceanic crust type-1 has a velocity as high as 7980.17 m/s, which is similar to the typical value for the mantle's velocity. The continental and magmatic crusts could be classified as low velocity crusts, the oceanic and uncertain crusts as intermediate velocity crusts, while the mantle and the undifferentiated layer could be classified as high velocity sequences.

Table 4-4: Summarised table of the different velocities and the applied density values of each unit. The asterisk (*) indicates the units where typical values were applied for the depth conversion and the gravity models.

	k	Velocity (V ₀)	Density (g/cm ³)
Water*	-	1500	1.03
Post - rift	-	2502.52	2.54
Syn - rift	-	3784.14	2.59
Pre - rift	-	4345.5	2.66
Continental crust	-0.0374106	5480.79	2.78
Oceanic crust - 1	-0.12411	6141.00	3.01
Oceanic crust - 2	-0.100625	6792.82	3.04
Oceanic crust - 3	-0.134497	6439.55	3.05
Oceanic crust - 4	-0.01354	6501.10	2.90
Magmatic crust	-0.0960827	5557.94	2.89
Uncertain crust	-0.0673327	6961.04	2.97
Undifferentiated layer	-	7980.17	2.94
beneath OC -2	0.00712076		
Mantle*	-	8000	3.30

As previously mentioned, the calculated velocity values could overestimate the thickness and the depth of the horizons and subsequently affect the crust's density. In this approach, the depth of the top basement, upon conversion, ranged from -7.5 to -9 km depth in the deep basin, and -12.7 to -1 km for the shelf domain. The Moho is estimated to range between depths of -16 and -22 km depth for the oceanic crust, and between -24 and -43 km for the continental crust (Figure 4.16a). The thickness of the continental crust ranges between 21 and 40 km,

while the oceanic crust ranges between 5 and 10 km (Figure 4.15b). These thickness values align consistently with findings from prior studies (Kusznir et al., 2020; Nemčok et al., 2023; Nemčok et al., 2022). These depth converted data were further incorporated into Geosoft Oasis Montaj for the purpose of gravity modelling, with the aim of mitigating the uncertainties that were raised during the seismic interpretation.

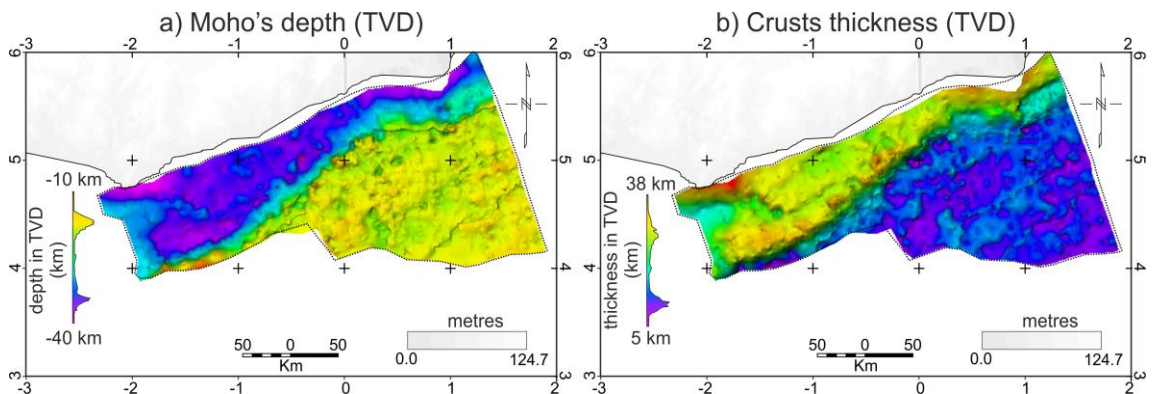


Figure 4.16: (a) Depth in km of the interpreted Moho, and (b) thickness between the top crusts and Moho after the depth conversion.

4.5.2 Gravity analysis

The Free Air Anomaly (Figure 4.4a) illustrates a high anomaly strip trending NE-SW that corresponds to either the Romanche Fracture zone, the marginal ridge (Figure 4.12a), or the antiforms (Figure 4.8a). In the western segment, the exposure of the continental basement at the marginal ridge and the absence of sediments contribute to the increased gravity anomaly. On the other hand, the low gravity anomaly (Figure 4.4a) indicates the presence of thick sediments in the NW-SE trending basins identified from the seismic lines (Figures 4.7a and 12a). In the central segment, the transition from a continental to an oceanic domain is more pronounced, although a gradual transition is observed towards the eastern segment, where the uncertain crustal type was identified (Figure 4.14).

Given the high quality of seismic imaging, a high degree of confidence is attributed to the crustal architecture in most of the seismic sections (Figure 4.14) and, therefore, the gravity modelling was used to clarify if the observed response is consistent with the current interpretation. The gravity modelling results are

presented in Figure 4.17, however, even though the models are non-unique, they reflect the interpretation within a valid geological model.

In the gravity modelling, the depth of the Moho underwent minimal changes after the depth conversion (Figure 4.16a). In the seismic analysis, the interpretation of the continental Moho was ambiguous due to the chaotic seismic characteristics. In the gravity modelling, continental Moho remained the same and only the density changed in some lines. The density of continental crust was initially interpreted to be 2.78 g/cm^3 based on Gardner's equation (Table 4-4). This value was applicable in seismic line E (Figure 4.17e), while a value of 2.85 g/cm^3 was applied when modelling in seismic line I, B and H (Figure 4.17). This variability could be explained by compositional changes within the continental crust.

The thickness of oceanic crust remained relatively the same, with the exception of certain parts within the oceanic crust type-3, where the depth conversion overestimated the depth of Moho and consequently the crust's thickness. This moderation was only a couple of kilometres shallower. The density of oceanic crust was also modified within the range of the calculated values (Table 4-4). In seismic lines B and G (Figure 4.17a and 4.17c) located in the eastern segment, employing a density of 2.94 g/cm^3 in the oceanic crust underplating yielded the optimal gravity error. This result aligns with the interpretation of a comparable high-density layer by Antobreh et al. (2009).

After implementing the previously mentioned modifications, primarily focusing on the density variations in both the continental and the oceanic crust, the average thickness of the unknown crust was calculated to be 7 km, the magmatic crust 14 km, and the layer beneath the oceanic crust type-2 has an average thickness of 11 km, thinning towards the west (Figure 4.17). Overall, the gravity models exhibit a robust response when considering the aforementioned adjustments and the associated density values (Table 4-4).

To finalise the crustal interpretation, the integration of seismic, velocity, and gravity analysis is required. Density is a key characteristic in the gravity modelling, where the continental crust shows an average density of 2.82 g/cm^3 , while the oceanic crust shows a range of densities between 2.90 and 3.05 g/cm^3 .

The densities of the magmatic and the uncertain crusts, as well as the underplating, fall within the range of oceanic crust densities.

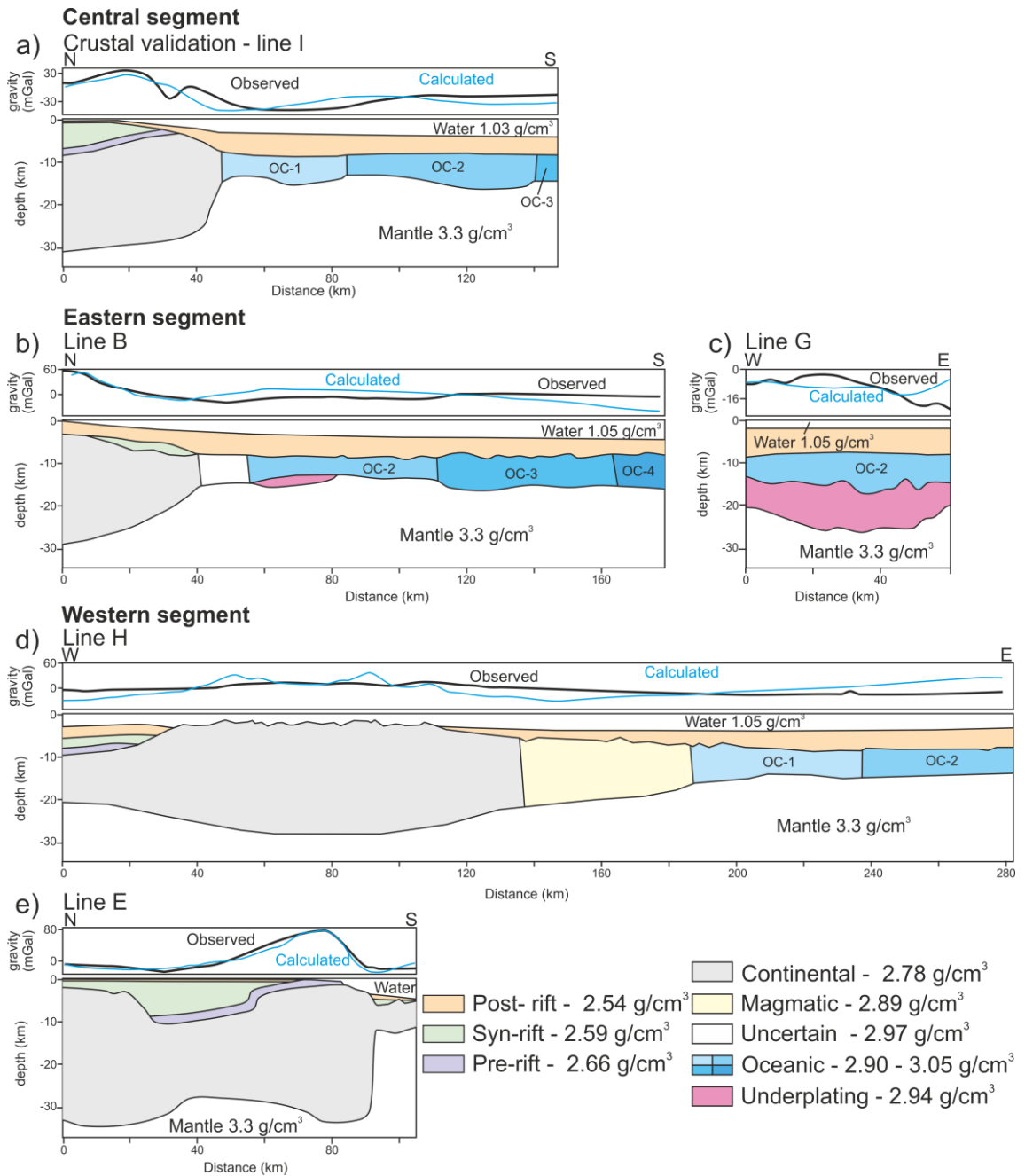


Figure 4.17: Gravity modelling of different sections and segments of the margin. (a) Crustal validation and Moho's modification occurred in the central segment line I. (b-c) Gravity models of eastern segment lines B and G, and (d-e) western segment lines H and E.

4.6 Discussion

4.6.1 Crustal-tectonic model for the Ghanaian margin

The integration of seismic interpretation, velocity analysis, and gravity modelling has allowed the production of a crustal and tectonic map for the Ghanaian margin, where different domains were identified across the area (Figure 4.18a). This map illustrates the crustal configuration within the study area, which is defined by the coverage of the seismic reflection data. A typical transform margin (e.g., Mascle & Blarez, 1987) is characterised by the sharp transition from continental to oceanic domains, as described by Sage et al. (2000) and Ye et al. (2019), and lacks a transitional domain (Basile, 2015). In this case, this transition is exemplified by the presence of the complex Romanche Fracture Zone. However, the margin exhibits certain features that may suggest a more complicated tectonic process beyond the typical transform zone activity. In Figure 4.18b, representative cross-sections combine both seismic interpretation and gravity modelling to illustrate the key characteristics of the margin.

4.6.1.1 Continental crust

In the proximal domain, the continental crust extends from west to east, gradually narrowing towards the east (Ye et al., 2019). The thickness alternates (Figures 4.17-4.18) with a thinner profile in the eastern segment and a thicker configuration towards the western segment. In the western segment, localised thinning of the continental crust occurs due to fault activity. Specifically, in the eastern segment, the continental crust is approximately 26km thick, while in the western and the central segments, it exceeds 30km, particularly within the Pan African Dahomeyide orogenic belt and antiforms (Figure 4.8a; Affaton et al., 1980; Trompette, 1994; Attoh et al., 1997; Tidjani et al., 1997) in the central segment. These thrust faults did not experience any reactivation during the rift process. However, to the southeast of these structures, vertical to sub-vertical faults with a similar NE-SW trend suggest gentle extensional deformation and inversion in the sediments, forming negative flower structures (e.g., Figures 4.5 and 4.10a). The continental crust accommodates two main basins in the western segment, which are trending NW-SE and E-W, while the eastern and central segments lack significant basins. In the western segment, the crust appears stretched (Figures

4.12a and 4.17e), which aligns with observations by Markwick et al. (2022) and Nemčok et al. (2023).

The continental structures (Figure 4.18a) exhibit diverse orientations, activity and deformation. These continental crust faults have been categorised based on their trends and their interpreted deformations evident in seismic reflection data (Figures 4.10-4.13). Within the Ghanaian margin, these faults were classified into four distinct categories:

Group 1: These faults extend throughout the region and trend in a NE-SW direction. In the central segment, they constitute the continuation of the pre-existing Pan-African orogenic structures, particularly notable in the pre-rift sediments of the central segment of the margin (antiforms; Figure 4.8a). Faults of group 1 suggest a syn-rift deformation, the deposition of syn-rift sediments, and inversion in the central segment. Negative flower structures are found in both the eastern and central segments of the margin.

Group 2: This consists of faults with the largest displacements and they accommodate sub-horizontal syn-rift sediments (e.g., Figure 4.3b). Group 2 faults trend roughly E-W and can be identified across all three segments of the margin.

Group 3: These faults trend NW-SE and are present in the eastern and western segments, displaying distinct characteristics. In the eastern segment, they depict faulted upper continental crust with minor displacement (Figure 4.11b). In the western segment, they form significant basins that cut through the upper and possibly lower continental crust.

Group 4: These faults trend WNW-ESE and are found exclusively in the western segment. They form positive flower structures and appear to have had a more pronounced impact on sediments than on the continental crust (Figure 4.7a-c). It is possible that these faults are related to Group 3 faults and are indicative of the transpressional phase of the margin, with minimal deformation of the continental crust.

4.6.1.2 Oceanic crust

In the deeper basin, the oceanic crust juxtaposes the continental crust in the central and eastern segments, while in the western segment, it interfaces with a

magmatic crust. The continental-oceanic contact is characterised by the RFZ, where one or both crusts display significant deformation. This is associated with the alternation of transtensional and transpressional deformation. The oceanic crust type-1 primarily exhibits the majority of the deformation from the RFZ, which is not observed in oceanic crust type-2, with local instances of overlapping by the continental crust (Figures 4.10b, 4.11a and 4.17b). In contrast, there is a gradual transition from the oceanic to the magmatic crust in the western segment of the margin.

In addition to the RFZ deformation, the oceanic crust is affected by primary NE-SW trending oceanic transform faults (Figures 4.10 and 4.18) and secondary NW-SE trending extensional faults in the upper part of the crust (Figure 4.10). Seismic reflection data suggests that the primary NE-SW trending transform faults are discontinuous, contradicting earlier interpretations (e.g., Antobreh et al., 2009; Kuznir et al., 2020; Matthews et al., 2011; Müller et al., 2008), and they show extensional or extensional deformation towards northwest or southeast, respectively along the margin. The secondary NW-SE faults showing extensional deformation, run parallel to the spreading axes, indicating the opening direction of the oceanic crust and their synchronous activity. Across the oceanic crust, their orientation shifts from NW-SE to NNW-SSE, aligning with the rotated spreading axes of the Brazilian margin (Tavares et al., 2020). Both gravity modelling and seismic reflection data have identified variations of oceanic crust thicknesses, ranging from 5 to 10 km (Figure 4.17; Kuznir et al., 2020; Nemčok et al., 2022, 2023). These thickness variations typically coincide with the presence of NE-SW trending transform faults, where the crust is segmented. Lastly, in the eastern segment, the previously uncertain layer beneath the oceanic crust (Figure 4.13a) is now interpreted as serpentized mantle, due to the irregular geometry of the high amplitude reflection (Figure 4.13a), the high velocity of almost 8000 m/s (Table 4-4), and the high density of 2.95 g/cm³. Its thickness reaches 10km (Figure 4.17c), which, if it was assumed to be oceanic crust would exceed the normal thickness of oceanic crust. The serpentized mantle extends up to the RFZ (Figure 4.18), where it thins out, potentially bearing substantial implications for the evolution of the margin.

4.6.1.3 Magmatic – transitional crust

Lastly, the magmatic crust (Figure 4.13b) identified in the western segment can be interpreted as a transitional magmatic crust (Figure 4.18). The magmatic crust is distinguished from both the oceanic and continental crusts due to distinct characteristics identified through seismic, velocity and gravity analysis. As mentioned in the seismic analysis, the seismic reflection data illustrates the magmatic nature of this crust, characterised by the high amplitude reflectivity and the presence of interpreted volcanoes on the basement (Figure 4.13b). The velocity analysis indicates a crust with low velocity of approximately 5500 m/s (Table 4-4), which is akin to the average velocity of the continental crust. Additionally, based on the gravity modelling, its thickness (Figure 4.17d) surpasses 8km and has a density of 2.89 g/cm³. The transition from the magmatic crust to the oceanic, as previously mentioned, is gradual, and while it extends along the RFZ, the shift towards the continental crust appears to exhibit locally a gentle transition (Figure 4.13b).

In general, the proposed model exhibits numerous resemblances in terms of structural framework and crustal architecture, as supported by several studies (Antobreh et al., 2009; Kuszniir et al., 2020; Nemčok et al., 2013; Nemčok et al., 2022; Ye et al., 2017, 2019). The majority of the region features faults with a similar orientation, exhibiting minor variations primarily in the eastern segment. The model introduces the concept of additional ENE-WSW and NW-SE trending normal faults (Figure 4.18a; Groups 2 & 3 – eastern segment). The model challenges the conventional understanding of transform margins by proposing the existence of a new magmatic crust in the western segment, which contradicts the classic model that does not incorporate a transitional crust in transform margins (Basile, 2015; Mercier de Lépinay et al., 2016).

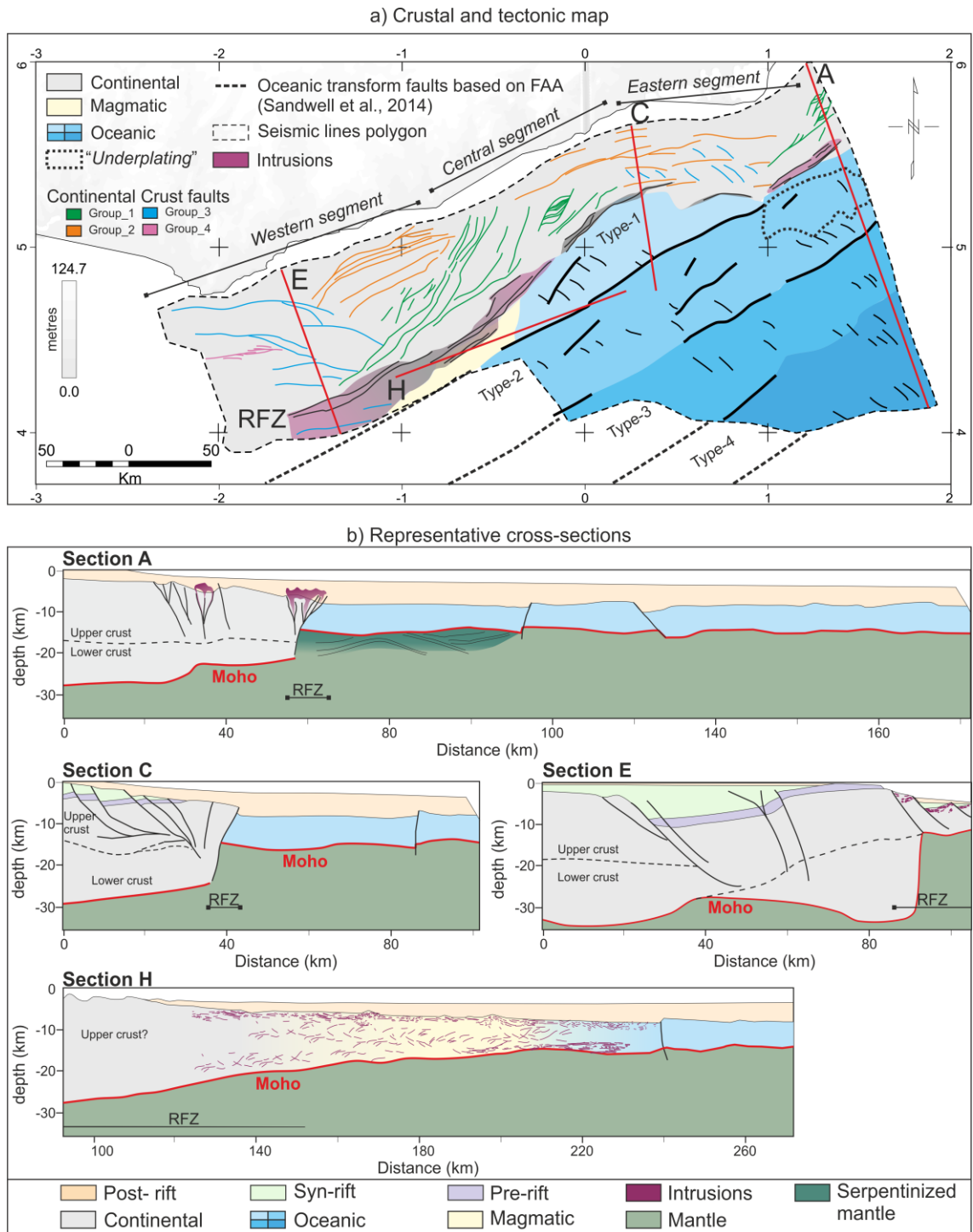


Figure 4.18: (a) Crustal and tectonic map of the Ghanaian margin, bounded by seismic reflection data polygon. Marked traces indicate the location of the depth converted sections presented in (b). RFZ: Romanche Fracture Zone, marked with a transparent grey polygon.

4.6.2 Magmatic material

The Ghanaian margin is considered to be a magma-poor transform margin (Markwick et al., 2022; Sage et al., 2000). However, associated magmatism can be emplaced during the break-up (Nemčok et al., 2013, 2023; Scarselli et al., 2020), which is associated with the oceanic ridge, especially transforms that have been influenced by transtension (Clarke & Beutel, 2020; Lundin et al., 2022). Two magmatic elements suggest elements of magmatic activity in the Ghanaian margin. The presence of the magmatic crust in the western segment and the intrusions along the RFZ (Figure 4.18) are evident before and after the breakup, respectively.

The potential presence of magmatic underplating has previously been suggested in the Ghanaian margin and the adjacent Côte d'Ivoire - Tano basin (Figure 4.1A) based on seismic, gravity and magnetic data, and thermo-tectonostratigraphic reconstructions in the proximal domain (Antobreh et al., 2009; Kuszniir et al., 2020; Loncke et al., 2020; Rüpke et al., 2010). However, this study's observations contradicts the notion of the underplating beneath the continental crust (Antobreh et al., 2009; Edwards et al., 1997), as this is not supported by either seismic data (Figures 4.5, 4.10-4.13) or gravity modelling (Figure 4.17).

On the other hand, a distinct layer with high velocity (7980.17 m/s) and high density (2.94 g/cm³) has been identified in the eastern segment, beneath the oceanic crust and in close proximity to the RFZ (Figures 4.13a, 4.17b,c and 4.18). A similar layer has been previously recognised to the west of the Ghanaian margin, along the Ivorian Marginal Ridge in the Côte d'Ivoire margin (Sage et al., 2000). Comparable sequences have been interpreted in various margins, either as underplating (e.g., US East Coast; LASE Study Group, 1986; North Atlantic; White et al., 1987; Exmouth Plateau; Lorenzo et al., 1991) or as a result of partial serpentinization of the upper mantle (Ritzmann et al., 2004; Sage et al., 2000). In the case of the underplating, this may be attributed to the significant lateral thermal contrast between continental and oceanic crust in a transform margin and the generation of secondary melting beneath the continental crust (Lorenzo et al., 1991; Lundin et al., 2022). In the Svalbard transform margin, serpentinized mantle has been proposed in a similar context as the eastern segment of the studied margin. In the Svalbard margin, the oceanic crust is characterised by its

thin crust, faulting, and a slow spreading rate, which can allow the migration of water through the faulted crust and promote the upper mantle serpentinization (Minshull et al., 1998; Nemčok et al., 2023 and references therein; Ritzmann et al., 2004). Both interpretations may hold validity in the context of the Ghanaian margin, primarily due to the presence of magmatic material evident in the seismic data (Figures 4.10-4.13). In this case, the preferred interpretation would be the serpentinized mantle (Figure 4.18), due to the slow Equatorial Atlantic opening (Granot & Dymont, 2015; Müller et al., 2008) preventing the formation of significant magmatic crusts. The magmatic material identified in the margin (Figures 4.9a & 4.14b) is likely to be related to the thermal uplift due to the continental and oceanic contact during the syn-transform or continental-oceanic phase.

Magmatic crusts have previously been recognised in various margins and can exhibit associations with both continental or oceanic characteristics (Bastow & Keir, 2011; Direen et al., 2007; Nirrengarten et al., 2020; Planke et al., 2000; Reeve et al., 2021; Skogseid et al., 1992, 2000), indicating magmatic activity during rifting. Similarly, in the Ghanaian margin, the presence of magmatic transitional crust and post-rift intrusive material suggests magmatic activity during and after the continental break-up, without forming a fully magmatic margin where Seaward Dipping Reflections are formed (e.g., Franke, 2013). The emergence of a magmatic crust along the RFZ in the western segment (Figures 4.13b and 4.18) and the Côte d'Ivoire margin and volcanic ridge (Nemčok et al., 2013; Scarselli et al., 2020), and the post-rift intrusions along the fractures (Figures 4.10a, 4.12b and 4.18b; Markwick et al., 2022) could be explained by melting occurring beneath the transform fault zone. The temperature variations between the adjacent continental and oceanic crusts, led to the magmatic crust formation along the RFZ during the continental break-up, the continental-oceanic or syn-transform phase (Edwards et al., 1997; Mercier de Lépinay et al., 2016; Rey et al., 2008; Scarselli et al., 2020). Leaky faults exist at the transform fault zone due to thermal conductivity between the continental and the oceanic crusts, and formed the magmatic crust, overprinting the continental crust as suggested by the seismic, velocity, and gravity analysis (Figures 4.17d and 4.18b, Table 4-4).

For the Ghanaian margin, the magmatic crust was developed by magmatic intrusions migrating through a releasing bend or a pull-apart basin in the continental crust, as previously has been suggested in the Dead Sea Transform, the California and the Norwegian margins (Busby et al., 2018; Libak et al., 2012; Rosenthal et al., 2019), and from the juxtaposition between the oceanic and continental ridges in the western segment. Similarly, heavily intruded magmatic crust, resembling the oceanic, has been proposed in the Cuvier Abyssal Plain in NW Australia, with increase magma supply towards the oceanic crust (Nirrengarten et al., 2020; Reeve et al., 2021). The formation of the magmatic crust might suggest a local shift in the stress regime during the syn-transform phase, evident by the locally smooth transition towards the continental and oceanic crusts (Figure 4.18b). Additionally, minimal intrusive activity occurred during the post-transform phase observed along the RFZ, primarily within the continental domain. This activity could be linked to the existence of pre-existing continental and oceanic transform faults facilitating the upwelling of deeper fluids.

4.6.3 Comparison with the conjugate Barreirinhas-Ceará

The NE Brazilian Equatorial margin represents the conjugate counterpart of the Ghanaian margin, encompassing the Ceará Basin and the southern section of the Barreirinhas Basin, influenced by the Romanche Fracture Zone (Figures 4.1A and 4.19). The morphology and stratigraphy of the Ghanaian and Barreirinhas-Ceará margins reveals similarities in the structures formed during the rifting, uplift due to the transpressional characteristics of the Romanche Fracture Zone, and flexural uplift and erosion at various stages of the margin evolution. The RFZ forms the boundary between the continental and oceanic crusts in the eastern and central segments of Ghana (Figure 4.18), and the Ceará Basin (Tavares et al., 2022). Meanwhile, in the western segment of Ghana (Figures 4.12a and 4.18) and the Barreirinhas basin (Montenegro et al., 2021; Trosdorf et al., 2007) the RFZ influences the continental crust by cross-cutting it .

In the southern part of the Barreirinhas Basin, high-angle NE-SW faults, both south and north dipping, form well-developed grabens and horsts (de Castro et al., 2022; Montenegro et al., 2021). WNW-ESE and NW-SE faults are intersected by NE-SW strike-slip faults highlighting the complex and diachronous

deformation in the Barreirinhas Basin (Montenegro et al., 2021). These structures resemble those in the western segment of the Ghanaian margin (Figure 4.18; Faults Group 3), accommodating half grabens with significant thicknesses of syn-rift sediments (Figure 4.12a; de Castro et al., 2022; Montenegro et al., 2021). Both the Barreirinhas and the western segment of Ghana exhibit gentle deformation due to transpression, featuring open folds and positive flower structures (Figures 4.7c, 4.12a and 4.18; Faults Group 4).

The Ceará Basin displays five major sets of faults: (1) NE-SW trending Brasiliano-Pan African orogeny structures, (2) two major NE-SW trending normal faults forming half-grabens, parallel to the first set, (3) NE-SW trending half-grabens controlled by E-W structures northwest of the orogeny related structures, (4) NE-dipping NW-SE trending faults southeast of the orogeny-related structures, and (5) a dense set of basement-related vertical to sub-vertical faults associated with the RFZ (Andrade et al., 2018; Basilone et al., 2023; Destro et al., 1994).

The first set of the Brasiliano-Pan African-related structures correlates with Pan African thrusts interpreted in the Ghanaian margin (Figure 4.8a; Andrade et al., 2018; Antobreh et al., 2009; Attoh et al., 2004; Destro et al., 1994). The second set of NE-SW faults, parallel to the Pan African structures (Andrade et al., 2018; Basilone et al., 2023) aligns with reactivated NE-SW faults (Figure 4.18; Faults Group 1) identified in the margin. However, the similar trend of faults controlled by the E-W structures northwest of the previously mentioned faults are unique to the Ceará Basin, as they do not have corresponding structures in the Ghanaian margin. In the Ghanaian margin, the seismic data only support E-W structures northwest of the Pan African structures and the faults of Group 1 (Figure 4.18; Faults Group 2). In the southern part of the Ceará Basin, NW-SE trending faults on the shelf can be associated with the NW-SE trending faults in the eastern segment of Ghana (Figures 4.11b and 4.18; Faults Group 3). Notably, both margins feature a series of basement-related strike-slip faults forming the Romanche Fracture Zone.

Lastly, magmatism has been observed in both the Ceará-Barreirinhas and Ghana margins. In NE Equatorial Brazil, radiometric age data have revealed occurrences of pre-rift (228 ± 38 Ma) and syn-rift (124 ± 06 Ma, 109 ± 08 Ma)

magmatism in the Barreirinhas Basin (Basilone et al., 2023; Mizusaki et al., 2002; Thomaz Filho et al., 1974). In the Ceará Basin, magmatism is primarily post-rift (44-32 Ma) or precedes the continental break-up (83 ± 06 Ma; Basilone et al., 2023; Mizusaki et al., 2002; Mizusaki & Saracchini, 1991). In Ghana, seismic data indicate post-rift magmatism manifesting as sills within the post-rift sequence (Figures 4.10a and 4.12b). However, the western segment reveals syn-rift magmatism occurring before the break-up, contributing to the formation of the magmatic crust (Figures 4.13b and 4.18).

4.6.4 Structural and crustal evolution

Based on the findings, a tectonic model of the Equatorial Atlantic opening is proposed, primarily focusing on the evolution of the faults, and their interaction with the associated crustal types. The model (Figure 4.19) is a schematic reconstruction with fixed the African plate and the north arrow corresponding to the present day orientation. It integrates onshore structures of both conjugate margins (Akpaki, 1978; Attoh et al., 1997; Pinéo et al., 2020; Tidjani et al., 1997), the presence of magmatic material, the interpreted structures in the Ghanaian margin and the conjugate Barreirinhas and Ceará (Andrade et al., 2018; Davison et al., 2016; Morais Neto et al., 2003; Tavares et al., 2022; Vasconcelos et al., 2004), based upon the crustal types inferred from the seismic reflection data (Figures 4.7, 4.10-4.13), and the gravity models (Figure 4.17). The evolutionary model was categorised into different stages, each being further linked to a potential transform opening phase (Figure 4.2A).

In the early stages of the Equatorial Atlantic opening, orthogonal extension to dextral transtension occurred (Stage-1; Figure 4.19a) during the Early Cretaceous. This extension likely triggered ENE-WSW trending normal faults in the central and eastern segments of the Ghanaian margin and the Ceará Basin. These normal faults exhibit noticeable normal displacement under dextral movement (Figure 4.11). The identification of typical syn-rift growth strata in Ghana implies the influence of an orthogonal or slightly oblique tectonic regime, particularly evident in the central and eastern segments of the margin (Figures 4.7d and 4.11a). In the central segment of Ghana, these normal faults demonstrate an orthogonal influenced tectonic regime, without having the typical

geometry of syn-rift growth strata (Figure 4.3b). Analogue modelling in pull-apart basins (Wu et al., 2009) suggests sub-horizontal infilling of the syn-kinematic sediments, mirroring the sediment characteristics observed in the Ghanaian margin. However, towards the eastern segment, some of the ENE-WSW trending faults display extensional normal faults with a significant decollement, and the typical growth strata (Figure 4.11), suggesting an orthogonal phase prior to the transtension, akin to the paleo-stress analysis conducted in the Brazilian Equatorial margin (de Matos, 1992; Tavares et al., 2022). During this phase, the central segment probably experienced more stretching than the eastern segment, due to the present day thinner continental crust (Figure 4.9b). Additionally, the RFZ faults, forming the boundary between the South American and African plates, were reactivated in an orthogonal extensional manner (Figure 4.19a; e.g., Tavares et al., 2020). This phase could be classified as part of the early stages of the intra-continental tectonic phase (Figure 4.2Aa).

Stage-2 (Figure 4.19b) is marked by diverse deformation events along the margin from Aptian to Early Albian. In the eastern and central segments, transtension influenced the margins, reactivating NE-SW trending structures, inherited from the Brasiliano-Pan African Orogeny, which resulted in a series of negative flower structures (e.g., Figure 4.10a). In the eastern segment, a Riedel-like sheared zone (e.g., Sylvester, 1988) evolved, initiating NW-SE extensional faults. In the western segment, there was NW-SE trending extension (Figures 4.7b and 4.12a) which is likely to have been caused by orthogonal extension. The orthogonal extension propagated westward, accompanied by younger sediments, as previously proposed by Nemčok et al. (2013, 2022). The continental crust in the western segment of Ghana and Barreirinhas Basin experienced more stretching under an orthogonal regime, and accommodated more sediments, exceeding a thickness of 5 km in half grabens (Figure 4.17e; Basile et al., 1998, 2005; de Castro et al., 2022; Guiraud et al., 1997; Mascle et al., 1988; Mercier de Lépinay et al., 2016; Montenegro et al., 2021). The aforementioned elements are likely to be associated with the intracontinental phase of the Ghanaian margin evolution (Figure 4.2Aa).

Towards the end of Stage-2, intrusions started feeding the continental crust along the RFZ, developing magmatic crust in the western segment, while in the central

segment continental break-up occurred, forming the oceanic crust type-1. The formation of the oceanic crust occurred in the inner corner of the margin (Figure 4.2B; Basile, 2015) in an orthogonal-to-oblique manner, similar to the pre-existing tectonic model of Antobreh et al. (2009) in the inferred Eastern Ghana Slope basin. The onset of seafloor spreading is dated during the Aptian-Albian boundary (Moulin et al., 2010; Pontes & Asmus, 1976). In the gravity modelling, the continental crust was calculated to be as thin as 6km in the western segment (Figures 4.17e and 4.18b) south of the RFZ. The juxtaposition between the warmer oceanic crust with the cooler continental crust generated thermal anomalies, which increased the heat flow at a regional scale. These thermal anomalies led to the continental stretching south of the RFZ in the western segment (Figures 4.12a and 4.17e; Kaspereit et al., 2016; Nemčok et al., 2023; Prol-Ledesma et al., 2016). If this stretching occurred during this event, it is likely to have occurred under an orthogonal extension, due to the well-developed growth strata. The migration of the orthogonal extension and the formation of the NW-SE trending faults in the western segment of Ghana and Barreirinhas may partly be associated with the Cote d'Ivoire margin opening (Gillard et al., 2017; Ye et al., 2017, 2019). Progressing from west to east, the tectonic phases alternate between the synchronous continental-transform (Figure 4.2Ab) activity in the western segment of Ghana and Barreirinhas, the continental-transform to syn-transform (Figure 4.2Ab,c) where the magmatic crust is situated, transitioning to syn-transform in the central segment, ultimately leading to the oceanic crust formation.

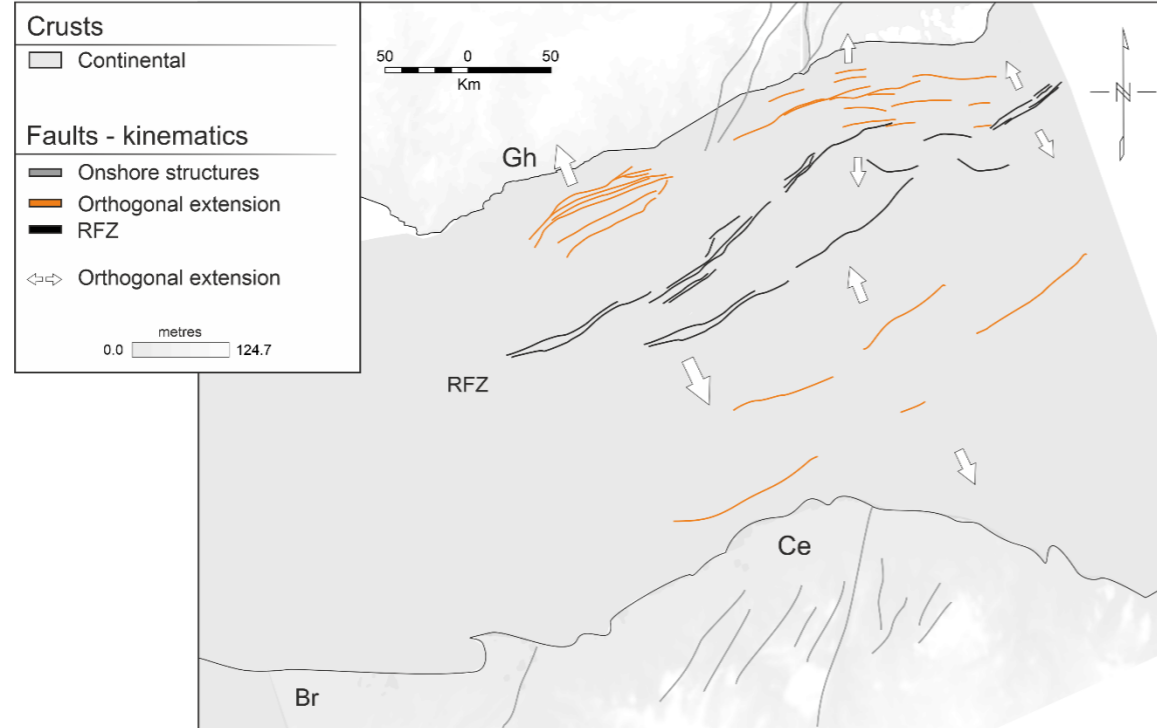
Stage-3 could be associated with the syn-transform phase (Figure 4.2Ac), when the Equatorial margins underwent the transpressional deformation (Figure 4.19c) in Late Albian. During this stage, dextral transpression influenced the entire region, leading to inversion of pre-existing faults, the formation of positive flower structures, the uplift of the continental crust, and the deformation of the RFZ and oceanic crust type-1. Simultaneously, new oceanic crust (type-2) was emplaced along the NE-SW trending oceanic transform faults. Uplift in the continental crust is evident throughout the margin and the RFZ (Figures 4.10-4.12; Andrade et al., 2018; Attoh et al., 2004; Basile, 2015; Basile & Allemand, 2002; Benkhelil et al., 1995; Cliff & Lorenzo, 1999; Nemčok et al., 2013; Tavares et al., 2022).

The continental uplift caused by the different mechanisms of tectonic movement (Andrade et al., 2018; Attoh et al., 2004; Basile et al., 1993; Blarez & Mascle, 1988; Costa et al., 1990; Zalan et al., 1985) and thermal heating (Holmes, 1998; Mascle & Blarez, 1987; Todd & Keen, 1989) is evidenced by the crust's vertical offset at the transform zone and the erosional surface of the syn-rift (Figures 4.7-4.12). In general, the marginal ridge in the western segment underwent significant uplift while the plates were still in contact. On the other hand, the eastern segment's continental crust might have experienced most of the inversion during the continental-oceanic phase, especially when compared to the other segments. This is attributed to the limited observable syn-rift and pre-rift sediments (Figures 4.10a and 4.11a). Contractional deformation is observed along the RFZ, which is caused by transpression, the magmatic material intruded in the RFZ and the thermally weakened margin (Basile & Allemand, 2002; Nemčok et al., 2013; Nemčok et al., 2022), although it is not uniform. Oceanic crust type-1 was deformed by transpression in the eastern and central segments (e.g., Figure 4.10a), suggesting that this crust had already formed during this stage. Conversely, oceanic crusts types 2-4 exhibit uplift along the NE-SW oceanic transform faults, whose geometry is more likely to fit with the intra-oceanic transform faults uplift (Bonatti et al., 2005; Chen, 1988; Sandwell & Schubert, 1982), and differs from the RFZ deformation. These oceanic crust types were only deformed by the oceanic transform faults (Figures 4.10-4.13 and 4.18) and were formed during the later post-transform stage (Figures 4.2d, 4.13b and 4.19d).

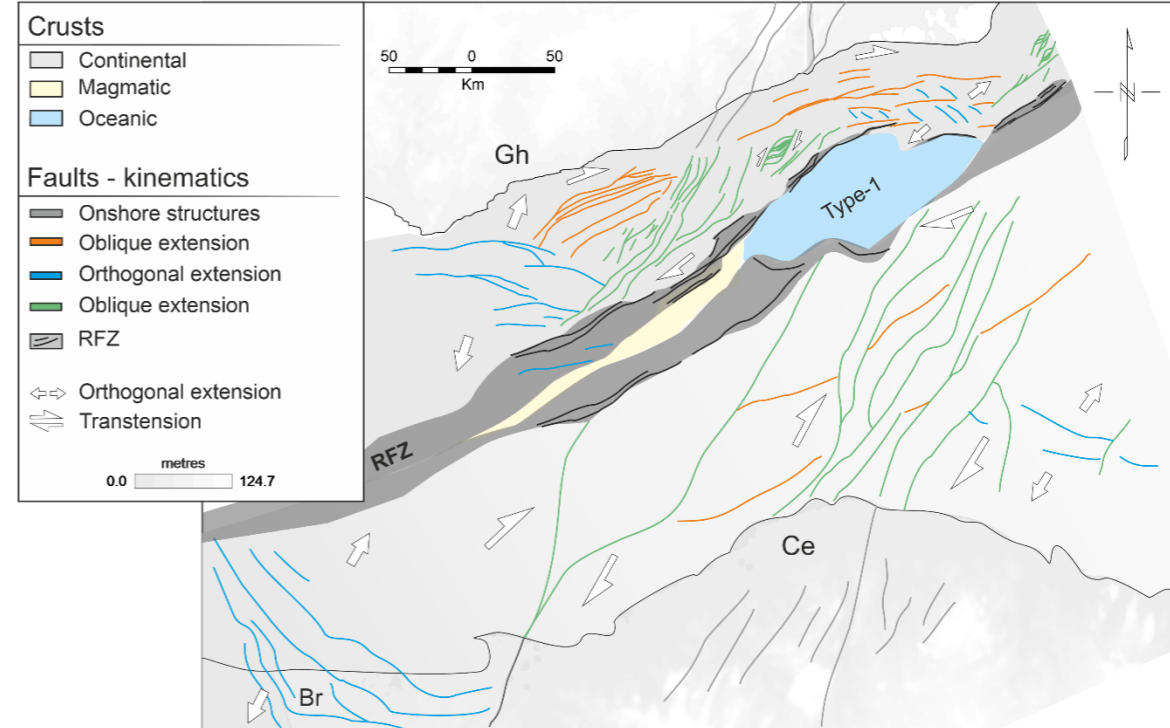
During Stage-4, there is only intra-oceanic deformation and it can be associated with the post-transform stage during the Late Cretaceous (Figures 4.2Ad and 4.19d). As previously mentioned, the oceanic crust was affected by the NE-SW trending oceanic transform faults (Bonatti et al., 2005; Chen, 1988; Sandwell & Schubert, 1982), which are locally discontinuous and form transform troughs (e.g., Figure 4.9a; Basile & Allemand, 2002). These oceanic transform faults may not have developed uniformly (Figure 4.18a) or have been covered across the region due to high temperatures and magma intrusions. Additionally, minor NW-SE extensional faults (Figures 4.13b and 4.18a) evolved on the upper oceanic crust in an oblique manner to the dextral shear, resembling extensional Riedel

structures (Sylvester, 1988). Finally, during the post-transform stage, intrusions migrated through the RFZ faults not only in the Ghanaian margin (Figures 4.10a and 4.12b), but in the Brazilian Equatorial margin as well (Basilone et al., 2023; Mizusaki et al., 2002; Mizusaki & Saracchini, 1991). The magmatic activity towards the end of the tectonic processes may be attributed to the friction and melting between the continental and oceanic crust near the continental transform fault of RFZ.

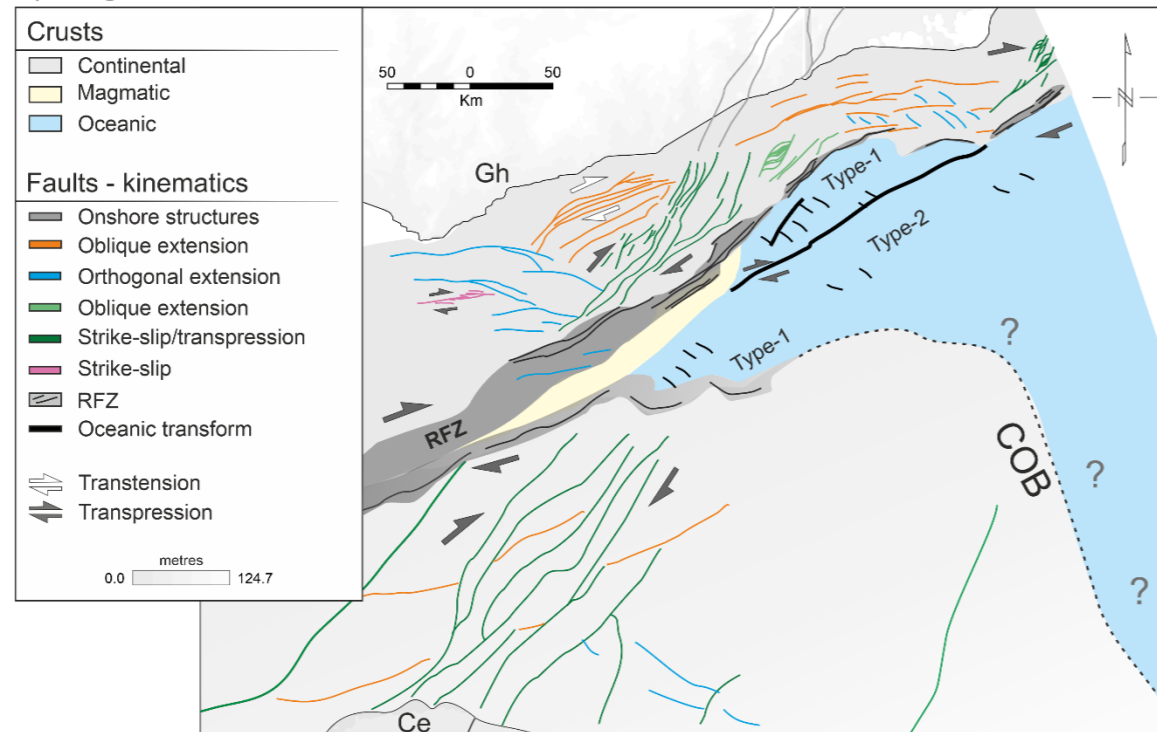
a) Stage-1 – Early Cretaceous



b) Stage-2 – Aptian to Early Albian



c) Stage-3 – Late Albian



d) Stage-4 – Late Cretaceous

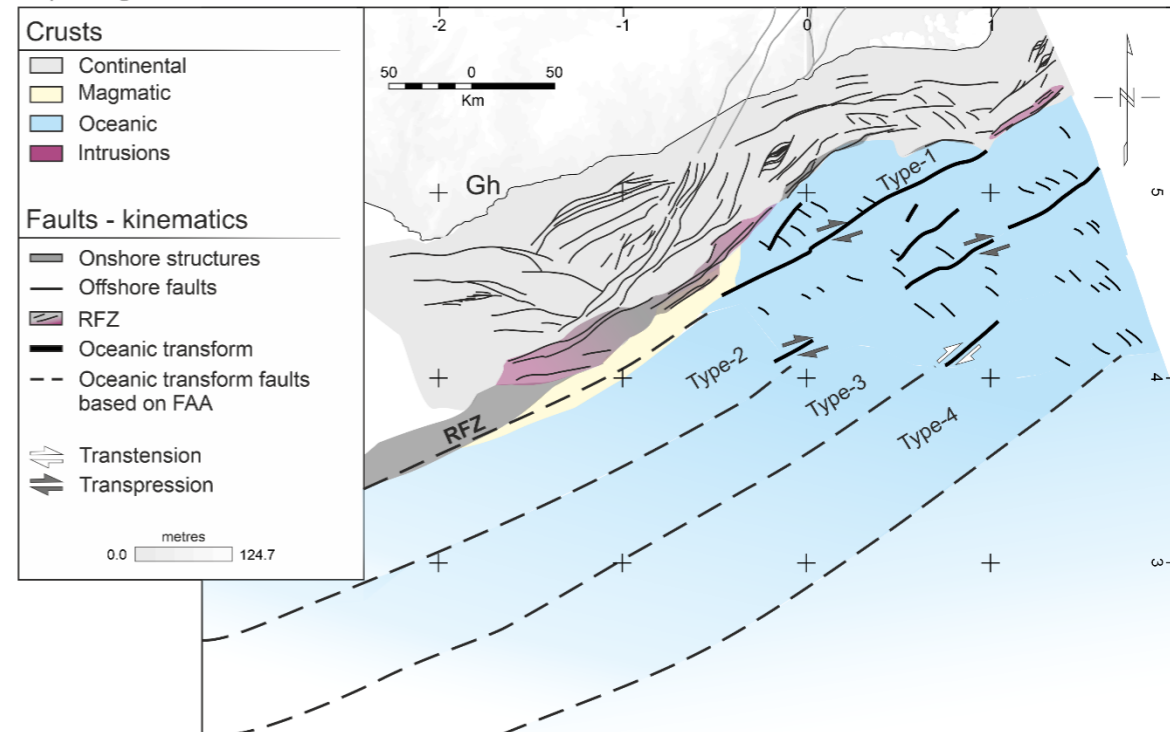


Figure 4.19: Structural and tectonic evolution of the Equatorial Atlantic margins, with a specific focus on the Ghanaian margin. The positions of the African plate and the north arrow are presented in reference to the present day, remaining fixed for orientation. (a) Stage-1 of NNE-SSW orthogonal extension. (b) Stage-2 of dextral transtension in the eastern and central segments of Ghana and Ceará basin, which formed pull-apart basins and sheared structures in the continental crust. Migration of the ENE-WSW orthogonal extension towards the western segment and Barreirinhas basin. Intrusions within the RFZ in the western segment that formed the magmatic crust. Potential formation of oceanic crust type-1 at the end of the transtensional phase and the separation of Africa and South America plates. (c) Stage-3 of dextral transpressional phase caused inversion, oceanic crust type-1 deformation, and oceanic spreading. (d) Stage-4 of post-transform stage with oceanic crust formation cessation, and post-rift intrusions along the RFZ. Gh: Ghana; Br: Barreirinhas; Ce: Ceará; RFZ: Romanche Fracture Zone. Structural framework compilation for the conjugate Barreirinhas and Ceará basins from Andrade et al. (2018), de Castro et al. (2022), Davison et al. (2016), Morais Neto et al. (2003), Pinéo et al. (2020), Tavares et al. (2022) and Vasconcelos et al. (2004). Onshore structures of the Ghanaian margins from Akpaki (1978), Attoh et al. (1997) and Tidjani et al. (1997). Oceanic transform faults based on Free Air Anomaly from Sandwell et al. (2014). Ages are derived by Adda et al. (2015), Antobreh et al. (2009), Attoh et al. (2004), IHS (2010), Mascle & Blarez (1987) Scarselli et al. (2020), Tavares et al. (2020), and the seismic interpretation of this study.

4.7 Conclusion

This study integrates 2D seismic reflection data, gravity data, and 2D gravity modelling to present a refined interpretation of the various crustal types in the Ghanaian margin, and their relationship with the structural changes that occurred during the continental transform opening. The results indicate that the margin underwent a sequence of distinct tectonic processes during this event, as follow:

1. Phase 1: This phase occurred during the “*continental-continental*” or “*intracontinental*” stage. The margin initially experienced local NE-SW orthogonal extension, leading to the activation of ENE-WSW normal faults.
2. Phase 2: This phase occurred during the transition between the “*continental-continental*” or “*intracontinental*” and the “*active continental-continental*” or “*continental transform*” stages. The orthogonal extension was followed by a significant phase of transtension, which led to the reactivation of pre-existing structures, the formation of pull-apart basins, and new NW-SE shear faults in the east. The orthogonal extension migrated south-westward.
3. Phase 3: The phase occurred during the transition between the “*active continental-continental*” or “*continental transform*” and the “*continental-oceanic*” or “*syn-transform*” stages. The shift between the two phases was characterised by magmatic activity. A narrow transitional crust formed in the western segment, while seafloor spreading commenced in the eastern segment of the margin.
4. Phase 4: The phase occurred during the “*continental-oceanic*” or “*syn-transform*” stage. Transpressional deformation leading to basin inversion and deformation along the RFZ.
5. Phase 5: The phase occurred during the “*oceanic-oceanic*” or “*post-transform*” stage. Upper-crust normal faults developed during the oceanic crust formation, while discontinuous oceanic transform faults deformed the oceanic crust.

The characteristics of the margin suggest:

1. Sediments deposited under oblique extension appear fairly sub-horizontal, in contrast to the sediments deposited under orthogonal extension, forming the typical growth strata.
2. Migration of magmatic material through the RFZ: Two events of magma migration occurred in the margin. The first one, was synchronous to the margin's opening and altered the continental crust into a transitional magmatic crust. The second event occurred after the tectonic cessation and marked the end of continental transform activity.

Chapter 5 – Discussion, future work and conclusions

5.1 Introduction

In Chapters 2 to 4, a methodical approach was undertaken to examine, identify, and assess the influence of strike-slip movement on the aborted rift of the Atlas system (Chapter 2), identify such movement and its characteristics in the rifted margin of the Eastern Gulf of Mexico (Chapter 3), and analyse the tectonic characteristics in the transform margin of Ghana (Chapter 4). The analysis of the Eastern Gulf of Mexico reveals an absence of significant strike-slip characteristics capable of influencing the divergent margin. However, Chapter 3 delves into an extensive discussion on the potential implications of strike-slip faults, particularly if they were active before the rifting processes.

This chapter encapsulates the discussion on strike-slip tectonics in divergent systems, outlines areas for future work, and presents key conclusions. Initially, it explores basin characteristics and examines the relationship between crusts and structures identified within the tectonic settings of a failed rift system and a transform margin. Based on the studied areas, it discusses the differences between orthogonal divergent and oblique divergent margins, and integrates the kinematic evolution of the previous chapters into the Pangaea's break-up.

Subsequently, a comparative analysis is drawn with divergent rift systems influenced by strike-slip. The discussion is followed by a series of potential future studies that could be done building upon the work presented in this thesis and aims to enrich the understanding of the explored topic. The chapter concludes with remarks summarising the key findings.

5.2 Stress-regime and tectono-stratigraphy

5.2.1 Stress regime

Both case studies of the Atlas system and Ghana indicate lateral stress-field variation, despite the predominant regional oblique extension. An exception arises in Ghana during the break-up, when certain parts of the continental crust and sediments were influenced by transpression. However, during the regional transtensional phase, the findings from Atlas (Figure 2.11) and Ghana (Figure 4.19) reveal the coexistence of transtension, pure strike-slip, orthogonal extension, and transpression. In the case of Ghana, there is a discernible alternation between transtension or strike-slip and orthogonal extension. Meanwhile, in the Atlas system, there is a sequence of orthogonal extension, transtension with local folding (e.g., Chapter 2 – Er-Rich transtensional folding, Figure 2.8; Fossen et al., 2013), and transpression or zones of exhumation caused by volcanic intrusions (Chapter 2 – Agoudal, Figure 2.6; Girard and van Wyk de Vries, 2005). Pre-existing faults accommodate deformation based on the stress regime and their geometry, with newly formed structures more likely to develop under a low obliquity stress regime.

3D numerical modelling in rift systems (Brune, 2014) supports the stress variation along the rift systems with obliquity. According to Brune (2014), rift systems with low obliquity exhibit a stress field that predominantly features orthogonal extension, with some strike-slip component in the centre of the system. Moderate obliquity systems resemble low obliquity ones, but with more pronounced strike-slip movement in the centre of the margin, and well-developed Riedel structures accommodating orthogonal extension. High obliquity rift systems predominantly exhibit strike-slip (Agostini et al., 2009; Brune, 2014) and transtensional stress regime, with minor orthogonal extension surrounding the strike-slip. Based on this numerical modelling (Brune, 2014), the Atlas system would likely be classified as having low to moderate obliquity, with some stress variation as mentioned earlier and in accordance with the paleostress analysis (Chapter 2; Figures 2.10-2.11). Meanwhile, the Ghanaian margin (Chapter 4; Figure 4.19) would be categorised as a high obliquity rifted system.

5.2.2 Faults

In both case studies examining the Atlas rift system (Chapter 2) and the Ghanaian margin (Chapter 4), the evolution of these regions is notably shaped by pre-existing structures, playing a significant role compared to the emergence of newly formed structures, and establishing the structural template for the systems mentioned above. In the Atlas system, ENE-WSW and NE-SW trending structures (Figure 2.1) were established during the preceding Hercynian Orogeny and were reactivated during the failed orthogonal rifting (Chapter 2; Laville and Petit, 1984; Beauchamp, 1988; Laville and Piqué, 1992; Piqué et al., 2002; Michard et al., 2008; Frizon de Lamotte et al., 2015). While in Ghana, NE-SW to NNE-SSW (Figure 4.19) structures formed during the Pan-African orogeny influenced the transform margin formation (Chapter 4; Affaton et al., 1980; Trompette, 1994; Tidjani et al., 1997; Attoh et al., 2004). These structures accommodate the initial motion of transtension or strike-slip movement (Basile, 2015; Mercier de Lépinay et al., 2016).

Typical transform margins and transtensional settings exhibit complex fault networks (Antobreh et al., 2009; Benkhelil et al., 1995; Farangitakis et al., 2019; Mascle & Blarez, 1987; Nemčok et al., 2016; Scrutton, 1979) likely associated with stress-regime alternations (Mercier de Lépinay et al., 2016) that can be found in such tectonic settings. The stress regime, deformation, fault activity, and consequently sediment distribution adapt based on the regional stress induced by plate activity and the geometry of pre-existing structures, which are mobilised first. Field data (Bellahsen et al., 2013), seismic reflection data (Abd-Allah et al., 2014), and analogue modelling in strike-slip tectonic settings (Agostini et al., 2009; Corti et al., 2020; de Souza Rodrigues et al., 2023; Farangitakis et al., 2019; Richard & Krantz, 1991; Viola et al., 2004; Zwaan et al., 2016) indicate that pre-existing faults are the first to be reactivated under strike-slip movement, giving space for new structures to get developed as Riedel shear structures (Viola et al., 2004; Zwaan et al., 2016) and parallel to sub-parallel in orientation to the strike-slip movement (Corti et al., 2020) as similarly observed in Chapters 2 and 4.

The analogue modelling carried out by Corti et al. (2020) provides valuable insights into the effect of the pre-existing structures on the pull-apart basins (Figure 5.1i-viii). Their models, run under normal gravity conditions, consisted of

two crustal blocks simulating simple shear deformation (Corti et al., 2020). To simulate the brittle behaviour of the upper crust, the models used a sand pack composed of a mixture of quartz and K-feldspar sand. In terms of scaling, 1 cm in the model corresponds to 3 km in nature, allowing for a lateral displacement of 12 km in a 12 km thick upper crust (Corti et al., 2020). Despite the model setup corresponding to small-scale natural basins, the lateral displacement and thickness of the upper crust enable comparisons with the Atlas system.

Corti's et al. (2020) models align with the Atlas system, whose pre-existing structures are both parallel and oblique to the opening due to prior orthogonal failed rifting (Figure 5.1ix). Sinistral transtensional influence led to the formation of new structures, partly intersecting the pre-existing ones, yet predominantly manifesting within the basin (Figure 5.1x). In the case of the Atlas system, the basin's characteristics, as identified in Chapter 2, align with phases shown in Figures 5.1iii, 5.1vi and 5.1vii. The main characteristics extracted from the analogue modelling of Corti et al. (2020) that best describe the transtensional evolution of the Atlas system are: i) significant linear faults formed along the pre-existing basin's border faults, parallel to the opening, and ii) the reactivation of oblique to the borders inherited structures, notably prominent in the central part of the basin (Figure 2.11). However, the reactivation of the oblique faults experiences a delayed onset.

The analogue modelling by de Souza Rodrigues et al. (2023) was designed to simulate the brittle upper and ductile lower continental crust, which was compared with the Equatorial Atlantic (Figure 5.2i-iii). Natural dry quartz sand or corundum sand was used to represent the upper crust, while high-viscosity silicone layer simulated the lower continental crust (de Souza Rodrigues et al., 2023). This generic model, with a thickness of 4 cm, corresponds to a natural upper crust thickness of 20 km and a lower continental crust of 10 km (de Souza Rodrigues et al., 2023).

The model of de Souza Rodrigues et al. (2023) provides an overview without a detailed depiction of all structures outlined in Chapter 4 (Figures 4.18 and 5.2iv-v). Nevertheless, their model (Figure 5.2i-iii) effectively captures the reactivation of pre-existing ENE-WSW and NE-SW structures, and the formation of newly developed NW-SE structures, in line with the insights presented in Chapter 4 and summarised in Figure 5.2iv-v. The chronological sequence of initial reactivation

of pre-existing structures followed by the formation of new structures aligns with the established models in strike-slip and transtensional settings (Agostini et al., 2009; Corti et al., 2020; Farangitakis et al., 2019; Richard & Krantz, 1991; Viola et al., 2004; Zwaan et al., 2016).

The new structures may intersect pre-existing ones, as exemplified in Chapter 2 with the Ouaouizaght case (Figure 2.4) – a strike-slip fault cross-cutting a pre-existing and reactivated relay ramp (Figure 2.11-2). New structures develop in accordance with the stress regime (Viola et al., 2004; Zwaan et al., 2016), forming mesoscopic and megascopic Riedel structures. These are illustrated in Chapter 4 with the NW-SE structures in the eastern segment of Ghana (Figure 4.18), and in Chapter 2 with the transtensional folding in the Er-Rich region (Figure 2.8d), and the newly formed extensional oblique-slip faults in the Ouaouizaght region (Figure 2.4e) of the Atlas system. According to Fossen et al. (2013), transtensional folding requires a more ductile volume of rocks. Generally, a substantial presence of either salt or shale can contribute to the development of these geometries. In the Atlas system, salt plays a significant role, and its mobility could facilitate the formation of such geometries.

Pull-apart basin opening (i-viii) and Atlas system opening (ix-x)

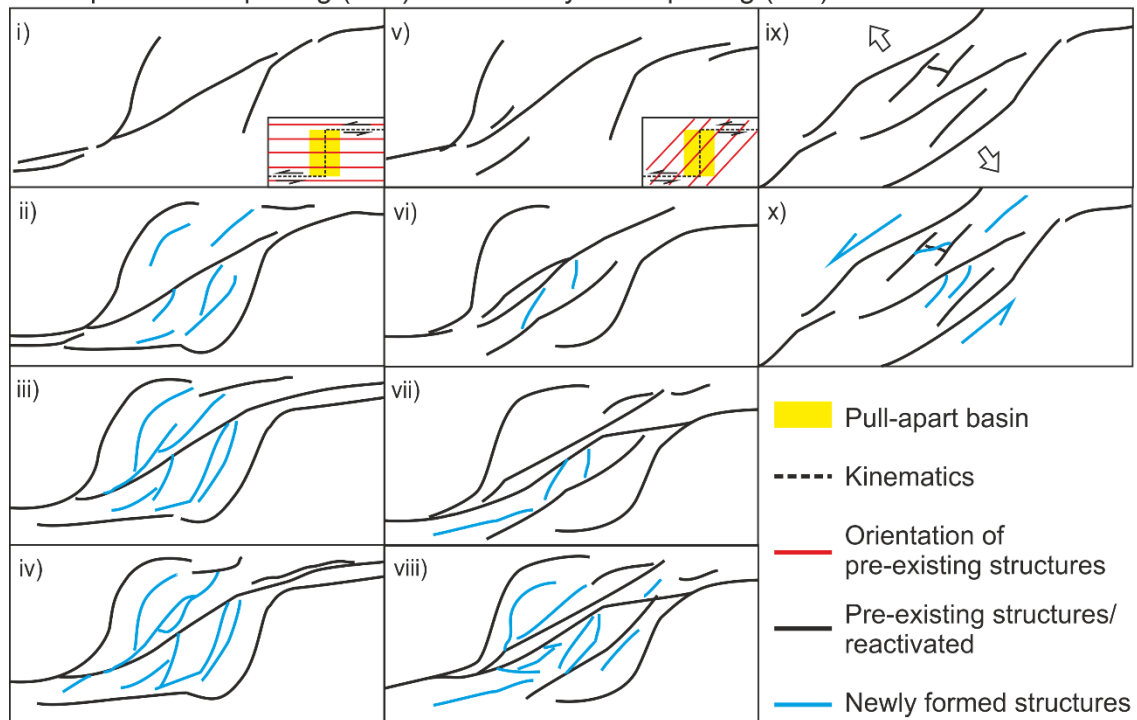


Figure 5.1: Analogue modelling (modified from Corti et al., 2020) of pull-apart basin with different orientations of pre-existing structures – parallel (i-iv) and oblique to the opening (v-viii), and Atlas system opening (ix-x) based on Chapter 2.

Equatorial Atlantic opening

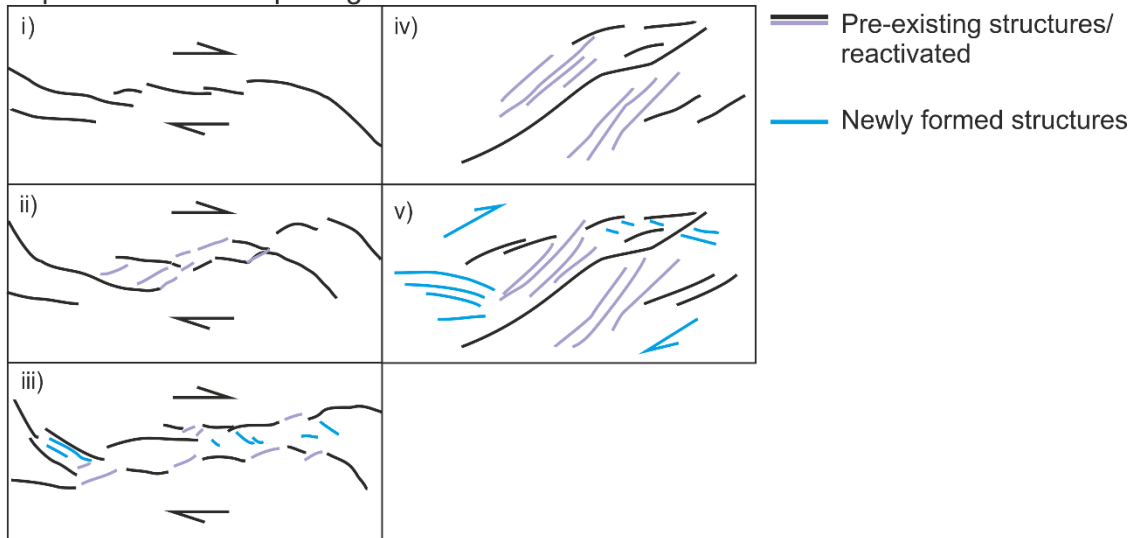


Figure 5.2: Equatorial Atlantic opening – analogue modelling (i-iii; modified from de Souza Rodrigues et al., 2023), and schematic diagram (iv-v) based on Chapter 4.

5.2.3 Sediment characteristics

In response to the prevailing stress regime, the structures demonstrate variable sediment geometries. Insights from seismic reflection data, field analogues (Figures 5.3-5.4; Chapters 2 and 4), and analogue modelling in transtensional pull-apart basins (Wu et al., 2009) and transform margins (Figures 5.3-5.4; de Souza Rodrigues et al., 2023) reveal comparable characteristics. Under an orthogonal stress regime, faults give rise to graben and horst formations, exhibiting a potential listric geometry, and facilitating the accumulation of growth strata with associated growth wedges. Segments of Ghana influenced by orthogonal extension (Figure 4.19) and the Atlas system's orthogonal rifting phase (Figure 2.10), despite later deformation and inversion, exhibit well-developed growth strata characterised by the typical wedge geometry (Figure 5.3a-b). This corresponds to the analogue modelling cross-section in orthogonal grabens of de Souza Rodrigues et al. (2023) (Figure 5.3c).

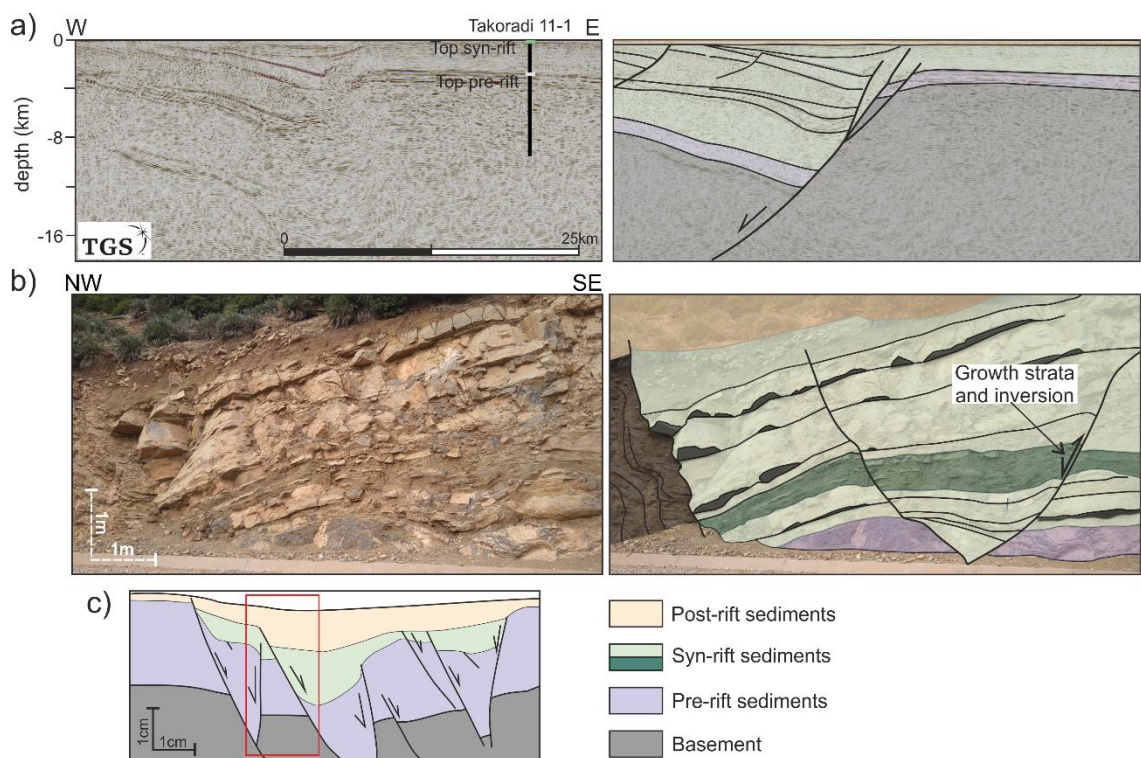


Figure 5.3: Orthogonal influenced growth strata. (a) seismic data indicating growth strata in the orthogonal influenced segment of the Ghanaian margin. Seismic data courtesy of TGS. (b) Inverted growth strata from the orthogonal failed rifting of the Atlas system. (c) Analogue modelling cross-section modified from de Souza Rodrigues et al. (2023). Red rectangular corresponds to the seismic and field data observations.

On the other hand, during the oblique tectonic phases, both cases and analogue modelling indicate the formation of pull-apart basins bounded by strike-slip faults (Figure 5.4). The pull-apart basins, reflecting the degree of obliquity, accommodate growth strata with sub-horizontal to horizontal geometry, resulting in symmetrical depositional troughs, as previously proposed by Wu et al. (2009) and de Souza Rodrigues et al. (2023). Therefore, the interpretation of oblique-influenced growth strata should be grounded in similar units demonstrating thickness variation around the strike-slip fault (Figure 5.4b) or rely on well data (Figure 5.4a) where feasible.

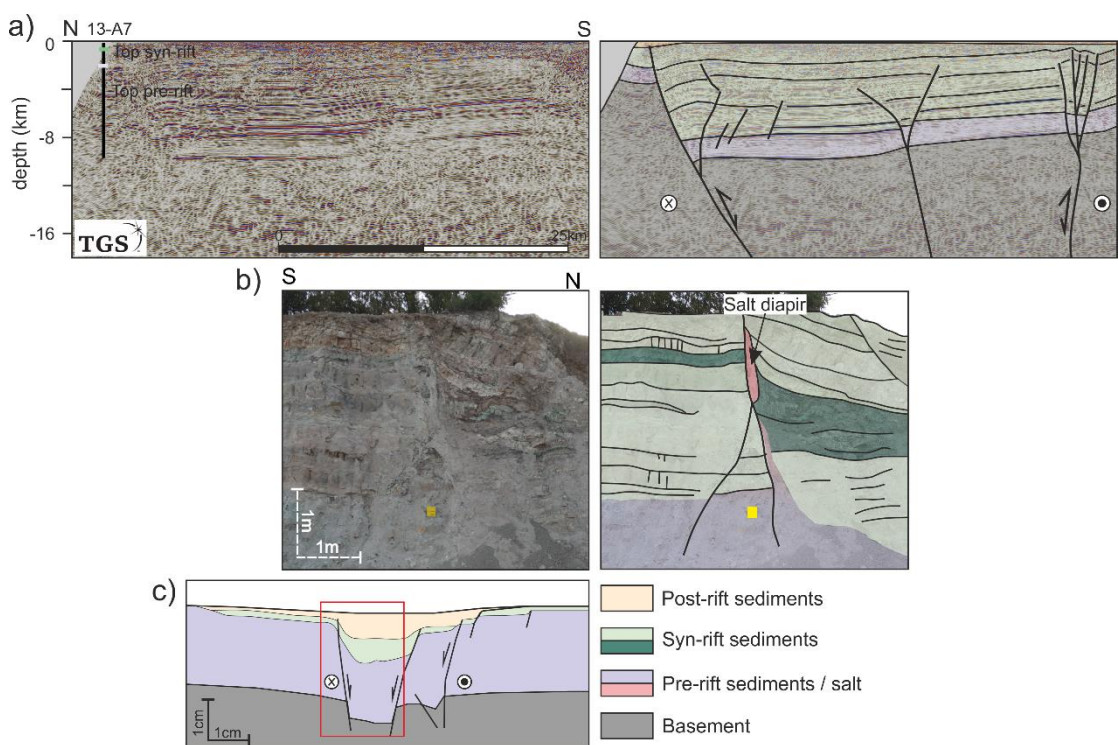


Figure 5.4: Oblique influenced growth strata. (a) seismic data indicating growth strata in the strike-slip influenced segment of the Ghanaian margin. Seismic data courtesy of TGS. (b) Growth strata occurred in the Atlas system during the transtensional phase. (c) Analogue modelling cross-section modified from de Souza Rodrigues et al. (2023). Red rectangular corresponds to the seismic and field data observations.

5.3 Crustal types-fault relationships and magmatism

The examination of the Atlas system and the Ghanaian margin in the corresponding chapters (Chapters 2 and 4) involves tectonic processes of plate movement, activity at major strike-slip zones, and associated magmatism. The timing of magmatic activity associated with transform margins remains a subject of debate (Berndt, Mjelde, et al., 2001; Loncke et al., 2020). Previous research has documented magmatic intrusions, lava flows, and underplating along some transform margins (Antobreh et al., 2009; Berndt, Planke, et al., 2001). These phenomena are linked to the formation of the oceanic crust and its juxtaposition against the cooler continental crust (Mutter et al., 1988) at the strike-slip fault zone (Figure 5.5A). This interaction can lead to additional melting in the later stages of the transform movement (Lorenzo et al., 1991), indicating diachronous melting from active rifting and break-up, generated through decompression (Mutter & Larson, 1989), toward the passive margin phase. Moreover, the thermal gradient at the strike-slip fault zone would result in a temperature decrease in the upper mantle, leading to melt production caused by the transportation of the oceanic crust to the adjacent continental crust (Berndt, Mjelde, et al., 2001).

Although the Ghanaian margin is considered magma-poor, it shows magmatic supply influenced by active strike-slip tectonics, as discussed in Chapter 4 (Figure 4.18). Two magmatic events align with the previously mentioned mechanisms and timing. The first activity, associated with the tectonic processes, occurred during the early phases of break-up, and the second one during the post-rift phase, both occurring at the strike-slip fault zone. The first magmatic phase altered the continental crust into a magmatic crust at the continental-oceanic boundary, which is the transform or the strike-slip fault zone. Similar characteristics have been observed in the Davis Strait located between Canada and Greenland, where stretched continental crust has been highly intruded, described as a new igneous crust (Suckro et al., 2013). Crustal thickening by intrusions at the continental-oceanic transition has been noted in the shear-influenced Norwegian Vøring transform margin, classified as magma-rich, with key characteristics including intrusive and extrusive materials, underplating and sills (Skogseid et al., 1992; Skogly, 1998; Berndt et al., 2001).

In the Atlas system, despite the passive nature of transtensional movement, aligned with Mann's (2007) cratonic strike-slip (Figure 5.5A) faults, similar

characteristics are observed. Post-transension and potential syn-transension (Figure 2.6) magmatism was discussed in Chapter 2. Magmatism has extensively been observed in pull-apart basins, which intruded either during or at the end of pull-apart basin evolution (Aydin et al., 1990; Aydin & Nur, 1982; Bellier & Sébrier, 1994; Corti & Dooley, 2015; De Paola et al., 2005; El-Sawy & Masrouhi, 2019; Filatova, 2008; Girard & van Wyk de Vries, 2005; Mann et al., 1983; Mann, 2007; Mao et al., 2021; Ngako et al., 2003; Sagong et al., 2001; Suo et al., 2015; Tatar et al., 2007). North Anatolia (e.g., Aydin and Nur, 1982; Tatar et al., 2007), Gulf of California (e.g., Aydin and Nur, 1982), the Yeongdong pull-apart basin in southwestern Korea (Sagong et al., 2001), the east China Sea (Suo et al., 2015) and intra-cratonic pull-apart basins in China (Fu et al., 2012) constitute some of these pull-apart basins. In addition, the low obliquity Main Ethiopian Rift (Abebe et al., 2007; Corti, 2009; Rooney et al., 2007), and the areas covered in this thesis, support the model proposed by Dewey et al. (1986) (Figure 5.5B). This model suggests that the depth of the fracture zone, the elastic lid beneath the pull-apart basin, and the rapid extension may contribute to volcanic activity in the fracture zone.

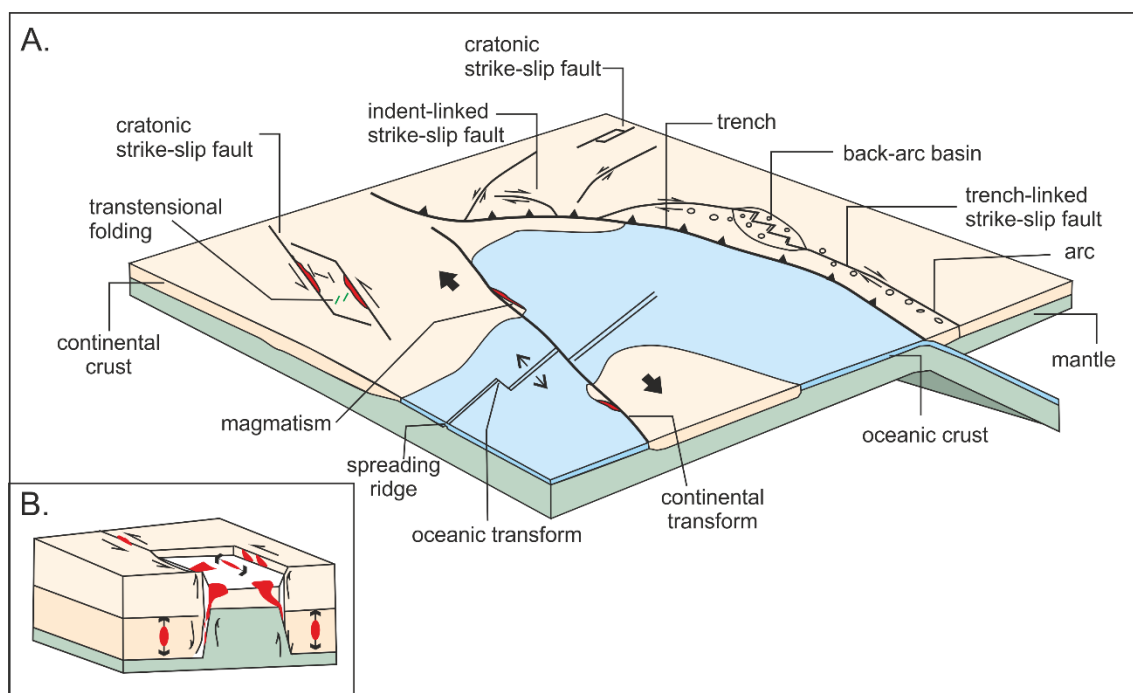


Figure 5.5: A. Updated strike-slip tectonics 3D model capturing both contractional and extensional tectonics (after Woodcock, 1986). Red illustrates the intrusions occur in a pull-apart basin and a continental transform margin. B. Schematic illustration of a pull-apart basin with intrusions (after Dewey et al., 1986).

5.4 Classic rifted margins vs strike-slip influenced margins

In the previous chapters, various types of divergent systems with distinct characteristics were identified. This section will summarise the key results and highlight the differences between the diverse extensional systems analysed in Chapters 2-4.

5.4.1 Rifted margins

The Florida margin exhibits typical characteristics of a passive rifted margin, as analysed in Chapters 1 and 3, and illustrated in Figures 1.1 and 3.11, respectively. Passive rifted margins can be classified as either magma-poor or magma-rich depending on the magma-supply and the relative tectonic processes (Figure 1.1; Doré & Lundin, 2015; Franke, 2013; Lister et al., 1991; Peron-Pinvidic et al., 2013; Planke & Eldholm, 1994; Sutra & Manatschal, 2012). Although, the Florida margin displays both types. Figure 3.11 illustrates Seaward Dipping Reflectors (SDR), hyperextended continental crust, and potential exhumed mantle, resulting from variable tectonic events during the rift-to-drift transition, the shift of the rotation pole, and the migration of the magma supply away from the rifting processes (more details on Chapter 3).

Additionally, significant syn-rift sediment characteristics within the basin are identified by their geometry, developing against the footwall, forming a wedge shape, as well illustrated in seismic lines D, E and F in Figures 3.6-3.7. These geometries are consistent to the magma-poor margin model (Figure 1.1Ab; Doré & Lundin, 2015; Franke, 2013; Lister et al., 1991; Peron-Pinvidic et al., 2013; Sutra & Manatschal, 2012).

5.4.2 Transform margins

Transform margins exhibit distinct characteristics compared to passive rifted margins in terms of crustal structure, magma supply, and basin development. At the crustal scale, as shown in the Ghanaian margin (Chapter 4), there is typically an abrupt transition between continental and oceanic crust, as proposed by Basile (2015), Loncke et al. (2020), and Mercier de Lépinay et al. (2016) (Figure 1.1B). However, in addition to the juxtaposition of oceanic and continental crusts, seismic analysis of the Ghanaian margin (Figures 4.13 and 4.18) reveals a magmatic transitional crust. This suggests that magma supply can alter the

continental crust during the syn-transform phase of the transform margin, as discussed in Chapter 4 and section 5.3. Furthermore, magma-supply can leak through transfer or thick skinned faults and intrude the sediments, as observed in both the Atlas system and the Ghanaian margin, in Chapters 2 and 4, respectively (Figures 2.6, 2.11, 4.10, 4.12, and 4.18).

Lastly, the oblique movement, as observed and discussed in both the Atlas system and the Ghanaian margin, forms depocenters that accommodate sediments (e.g., Figures 4.5 and 5.4; and Antobreh et al., 2009). These depocenters differ from the typical growth strata observed in the passive margins (Figures 3.6 and 5.3).

5.5 Atlantic opening

The previous kinematic analysis and schematic reconstructions of the three study areas in the Atlas system, along with the Florida and Ghanaian margins, allow us to constrain kinematic information on the break-up of Pangaea from the Late Triassic to Late Cretaceous (Figure 5.6).

Based on chapters 2-4, rifting in Pangaea began with localised NW-SE trending extension in the North Atlantic in the Triassic (Figure 5.6; Norian). This rifting extended southward with the same trend, influencing the Gulf of Mexico region (Figure 5.6; Tr-Jr Boundary). Concurrently, rifting started with dextral shear in the transform margin of the South Atlantic.

In the Early Jurassic (Figure 5.6; Toarcian), the transform movement in the South Atlantic persisted, but the stresses at the core of Pangaea altered. In the Gulf of Mexico, stresses shifted to a NE-SW extensional trend, while North Africa began experiencing passive transtensional sinistral movement from the synchronous opening Atlantic and Tethyan opening (e.g., Escosa et al., 2021). By the Middle Jurassic (Figure 5.6; Bajocian-Bathonian), the stresses remained under a stable state, accompanied by the counterclockwise rotation of the Yucatan block, continuing until the Tithonian (Figure 5.6; Tithonian). Seafloor spreading at the core of Pangaea began during the Tithonian and the Jurassic-Cretaceous Boundary (Figure 5.6; Jr-Cr) in the Gulf of Mexico and the North Atlantic, respectively.

With continued extension in the South Atlantic and the propagation of the seafloor spreading northward (Granot & Dymant, 2015; He et al., 2008; Malinverno et al., 2012; Moulin et al., 2010; Nürnberg & Müller, 1991; Pérez-Díaz & Eagles, 2014), extension began in the Equatorial Atlantic in the Early Cretaceous (Figure 5.6; Barremian). This continuous movement of the African plate towards the NE caused dextral oblique extension (Figure 5.6; Early Aptian) until the Albian (Figure 5.6; Early Albian), when the African plate shifted its movement towards the ENE (e.g., Antobreh et al., 2009), causing dextral-transpression in the Equatorial Atlantic (Figure 5.6; Late Albian-Cenomanian). This transpression in the Equatorial Atlantic represents the final stage of tectonism in the Pangea break-up until the Campanian (Figure 5.6), when seafloor spreading became evident along the Atlantic.

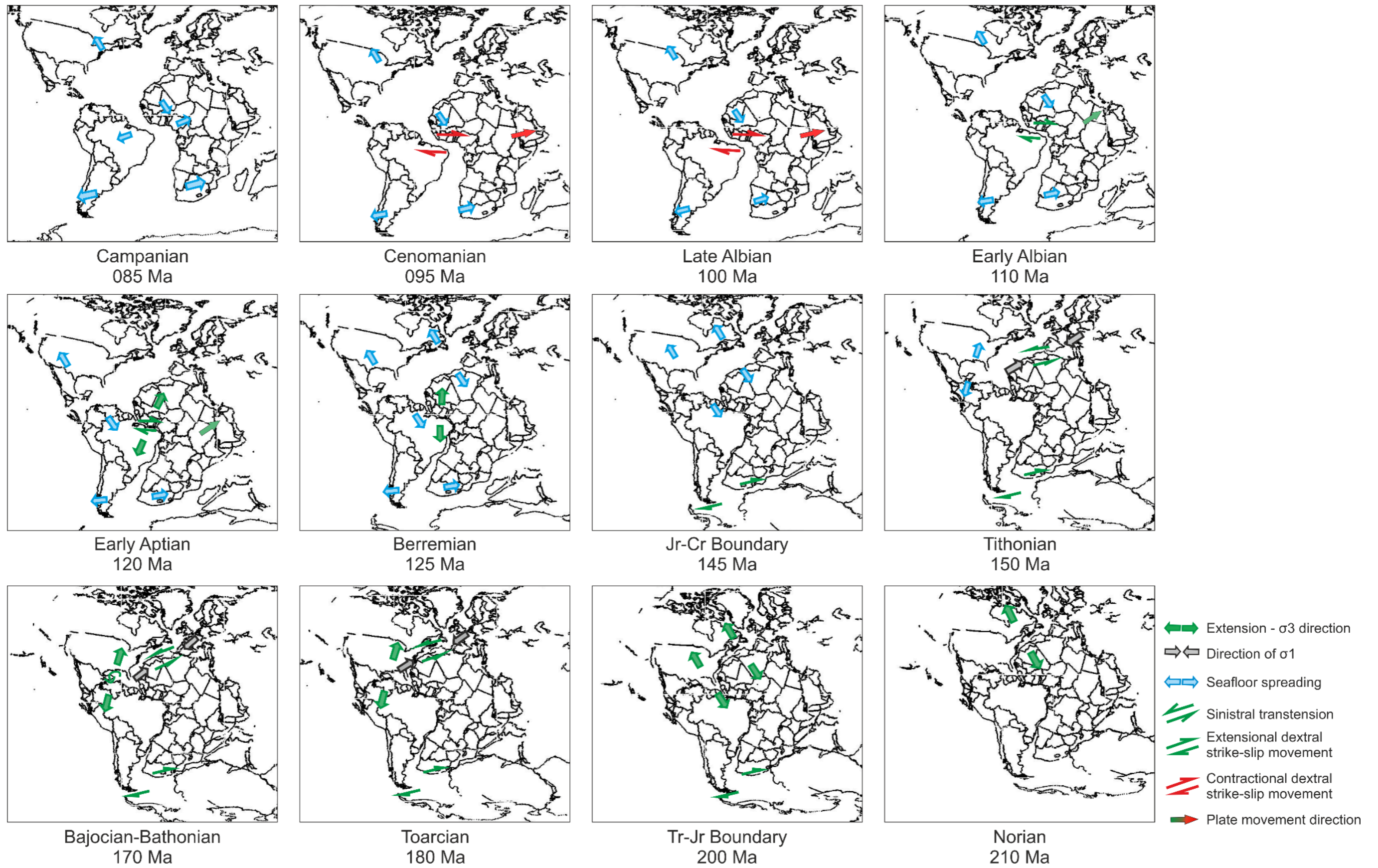


Figure 5.6: Pangaea's break-up evolution integrating the kinematic characteristics from Chapters 2-4. Kinematic characteristics in North and South Atlantic opening are based on previous studies (Antobreh et al., 2009; Granot & Dymant, 2015; He et al., 2008; Malinverno et al., 2012; Moulin et al., 2010; Scotese, 2016), (model from Scotese, 2016). Tr-Jr Boundary: Triassic-Jurassic Boundary. Jr-Cr Boundary: Jurassic-Cretaceous Boundary.

5.6 Comparison with other divergent systems influenced by strike-slip faults

In the previous chapters and sections, the discussion focused on the stress regime, tectono-stratigraphy, and the relationship between the crustal types and the faults in oblique systems. The analysis drew from analogue models, complemented by comparisons with natural examples to enrich the observations of this work. This section further compares in detail these findings with other systems under a distinct rifting phase and obliquity.

5.6.1 East Africa Rift and the Main Ethiopian Rift

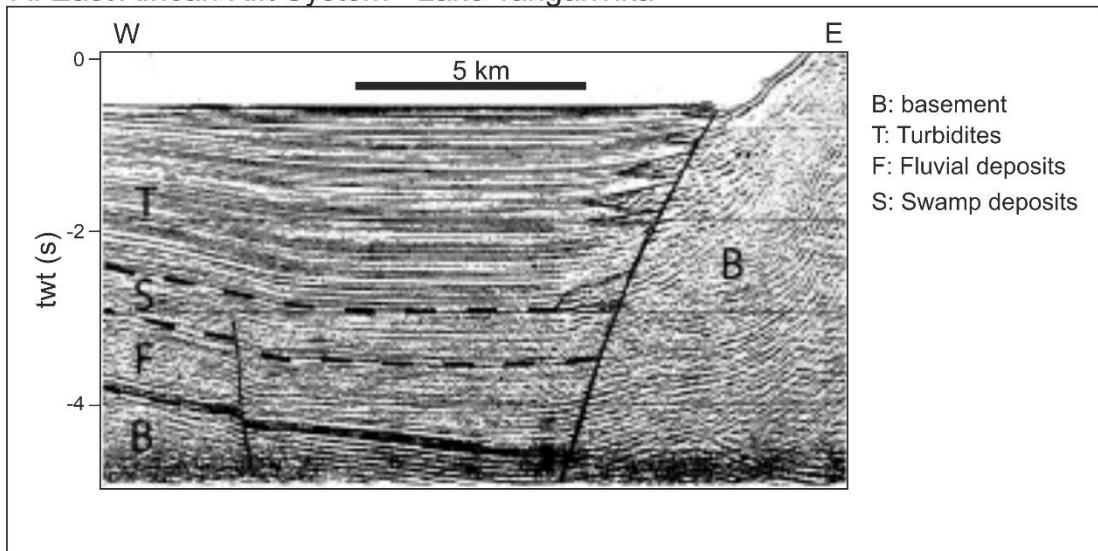
The East Africa Rift serves as an insightful natural example for comparing observations from both Ghana and Atlas. The East African Rift displays various fault types, reactivation of pre-existing structures, sub-horizontal syn-rift sediments, and volcanism.

The East African Rift features diverse fault types, such as normal faults, dextral or sinistral strike-slip and oblique-slip faults, and local reverse faults (Chorowicz, 1989; Chorowicz & Mukonki, 1979; Chorowicz, 2005; Daly et al., 1989; Ebinger, 1989; Kazmin, 1980; Kilembe & Rosendahl, 1992; Tiercelin et al., 1988; Wheeler & Karson, 1994). This variation corresponds to lateral stress differences and varying degrees of obliquity, akin to observations in the Atlas system. Along the East African rift, a series of lithospheric pre-existing weaknesses are inferred to have been reactivated (Bosworth & Morley, 1994; Delvaux, 2001; Ebinger, 1989; Smith & Mosley, 1993). The Main Ethiopian Rift, a segment of the East African Rift, consists of two fault trends at the boundary and the centre of the rift system, with the latter constituting the reactivated structures (Chorowicz et al., 1994; Corti, 2009). This reactivation mirrors observations in both Ghana and Atlas, where main faults correspond to reactivated pre-existing structures. However, in this thesis' study areas, the pre-existing structures can either be at the boundary or the centre of the system. Based on the analogue modelling in the Main Ethiopian Rift by Corti (2008), rifting propagates from the boundaries to the centre (Corti, 2009; Ebinger, 2005). In the Atlas system, the propagation of the rifting cannot be distinguished only based on the current field data, and further analysis is required. The Equatorial Atlantic's higher obliquity introduces different characteristics, preventing a direct comparison with the current system.

Sedimentation within the East African Rift System varies with the obliquity influence. Seismic profiles across Lakes Rukwa (Kilembe & Rosendahl, 1992) and Tanganyika (Figure 5.7A; Project PROBE, 1986; Chorowicz, 2005) in Tanzania reveal distinct characteristics. These profiles depict listric faults forming a pull-apart basin, demonstrating thickness variation in syn-rift sediments with sub-horizontal geometry. Additionally, Tanganyika exhibits characteristics of a half-graben filled with sub-horizontal growth strata. In both cases, the seismic profiles allow us to attribute similar elements to Figure 5.4. These elements are associated with either variations in sediment thickness on each side of the faults or the presence of thick sedimentation within half-grabens. In addition, the Main Ethiopian Rift's central segment displays more pronounced oblique characteristics than the northern counterpart (Abebe et al., 2005; Wolfenden et al., 2004). However, the limited availability of seismic reflection data in this basin introduces ambiguity in assessing sediment characteristics (Corti, 2009). On the other hand, a seismic profile in Lake Malawi indicates a more orthogonal extension with the typical growth strata (Specht and Rosendahl, 1989; Rosendahl et al., 1992; Figures 5.3 & 5.7B).

Volcanic activity has been observed along the East African Rift System, particularly in the northern region (Chorowicz, 2005). In the north, where the Main Ethiopian Rift is situated, magmatism is linked to pre-existing structures experiencing oblique movement at the centre of the system (Ebinger & Casey, 2001; Rooney et al., 2007). Ebinger (2005) proposed a rift evolution for the Main Ethiopian Rift, highlighting similarities with both the Atlas system and Ghana. As mentioned earlier, magmatic activity is concentrated in the central faults of the rift system, mirroring the Atlas system. Magmatic intrusions, sills, and dykes modify the continental crust, resulting in heavily intruded zones and the formation of new oceanic crust. Similar intruded zones were observed in the Ghanaian margin, aligning with the proposed model (Figure 5.5). However, in the Main Ethiopian Rift the lower obliquity compared to Ghana facilitates the development of seaward dipping lavas (Ebinger, 2005).

A. East African Rift System - Lake Tanganvika



B. Lake Malawi

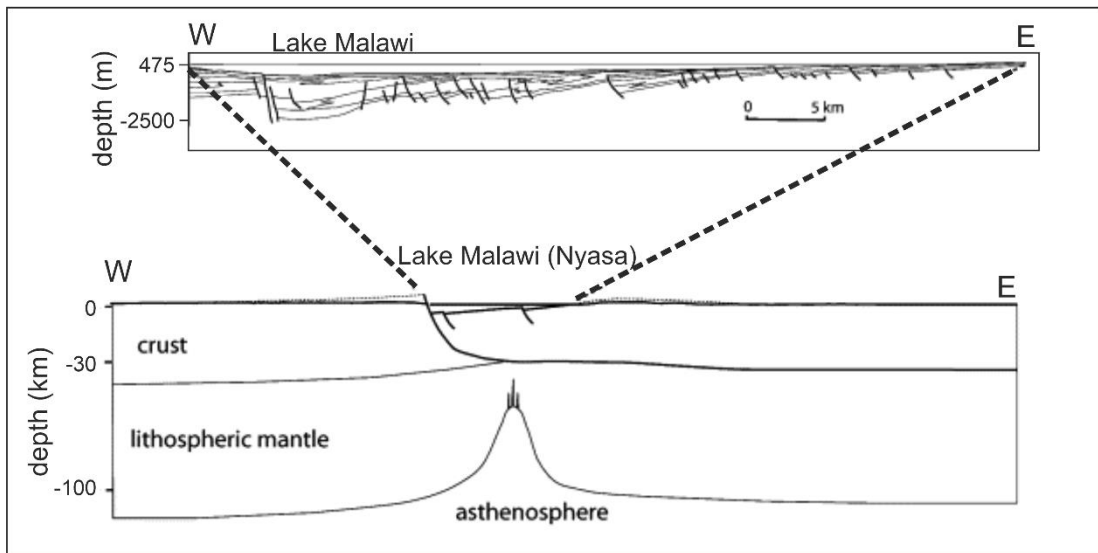


Figure 5.7: A. Seismic profile in the Tanganvika Lake of the East African Rift System (modified from Project PROBE, 1986; Chorowicz, 2005). B. Seismic reflection profile of Lake Malawi (modified from Specht and Rosendahl, 1989; Rosendahl et al., 1992) and inferred lithospheric cross-section of the northern Kenyan rift.

5.6.2 Agulhas transform margin – South Africa

The Agulhas transform margin (Figure 5.8) in South Africa shares similar resemblances with the proposed model (Figure 5.5A) and the transform margin of Ghana (Figure 4.19). Inherited Proterozoic structures (Illsley-Kemp et al., 2018; Meert & Lieberman, 2008) underwent reactivation during the transform movement (Paton et al., 2023). However, their orientation is parallel to the opening in contrast to the pre-existing structure of Ghana. The behaviour of pre-existing structures parallel to the opening in pull-apart basins is described by Corti et al. (2020) (Figure 5.1).

The initiation of the Agulhas Falklands Fracture Zone caused a change in the stress distribution in the region according to the orientation of the pre-existing structures. The stress was divided among different geological features, including areas where strike-slip dominated and areas experiencing simultaneous stretching and compression (Paton et al., 2023). Due to the synchronous contraction, extension, and strike-slip deformation in the Agulhas margin, the stratigraphic geometries cannot be compared with the Ghanaian margin, where the contractional and extensional events occurred in a sequential manner.

Lastly, similarly to the Ghanaian margin (Figure 4.18), the Agulhas transform margin exhibits seamounts and localised magmatism along the transform fault (Markwick et al., 2022; Paton et al., 2023). Magmatic intrusions form narrow stripes of mixed continental and magmatic crust along the line of Agulhas Falklands Fracture Zone and Agulhas Ridge (Markwick et al., 2022; Paton et al., 2023; Uenzelmann-Neben & Gohl, 2004).

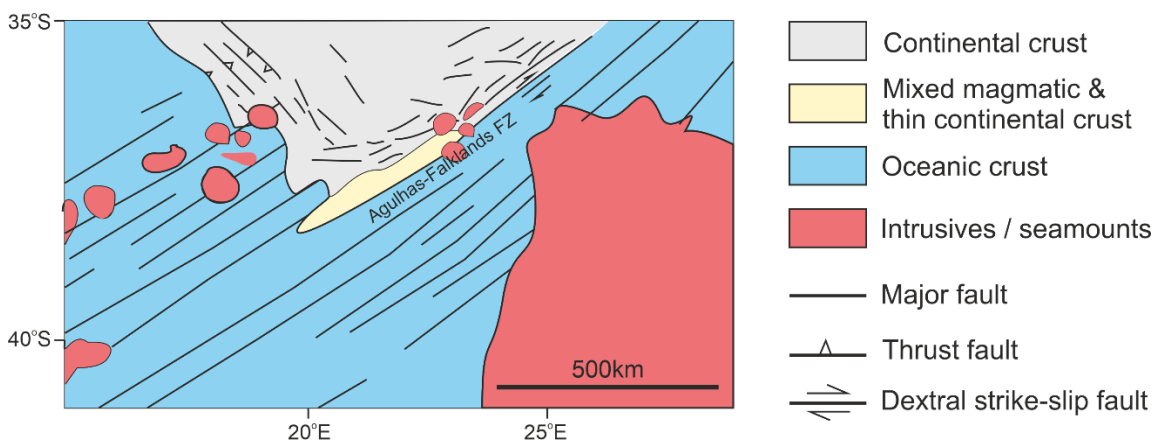


Figure 5.8: Crustal distribution in the South African margin with key structural elements and igneous features (modified from Markwick et al., 2022; Paton et al., 2023). FZ: Fracture Zone.

5.6.3 Barents Sea and Norwegian transform margins

The Norwegian – Greenland Sea is distinguished by alternating sheared and rifted margins (Figure 5.9). The Vøring margin exhibits characteristics of a shear-influenced rifted margin, while the Svalbard margin is identified as a sheared margin (Faleide et al., 2008). The architecture of the Vøring margin suggests orthogonal extension, with a transfer zone marking the boundary between the margin and the Vøring Plateau. The region is associated with lithospheric stretching and breakup-related magmatism (Breivik et al., 2006; Eldholm et al., 2002; Mjelde et al., 1993, 2003; Mjelde, Raum, Breivik, et al., 2005; Olesen et al., 2002; Steltenpohl et al., 2004; Tsikalas et al., 2005). The Barents Sea-Svalbard margin developed along a shear zone, with different segments influenced by orthogonal or oblique extension (Faleide et al., 2008), each exhibiting distinct crustal properties, structural features, and magmatic characteristics (Breivik et al., 1999; Eldholm et al., 1987; Faleide et al., 1988; Jepsen & Faleide, 1998; Ritzmann, 2003; Ritzmann et al., 2004).

Within the Svalbard margin, both transtensional and transpressional features, and potentially inherited structures can be observed, along with break-up-related volcanic activity, observed by prominent volcanoes and intrusions in the outer margin (Breivik et al., 1999; Faleide et al., 1988; Jepsen & Faleide, 1998; Ritzmann, 2003; Ritzmann et al., 2004). Notably, magmatism is specifically observed in rift-influenced shear segments of the Svalbard margin.

Considering these characteristics, the Norwegian – Greenland Sea shares significant similarities with the Ghanaian margin and the proposed model (Figure 5.5A), yet notable differences exist. Both margins are segmented with varying degrees of obliquity, as outlined in Chapter 4 (Figure 4.19) and proposed by Antobreh et al. (2009), leading to distinct lateral stress regimes. Reactivation of inherited structures is a possibility in the Svalbard margin, although the extent of their activity remains unclear. Breakup-related magmatism is evident in both areas, with the Svalbard margin having similar magmatic characteristics of thinned intruded crust at the continental-oceanic boundary (Eldholm et al., 1987), but also in segments influenced by orthogonal extension, contrasting with observations in Ghana. This variability may be related to the Norwegian – Greenland sea margins' magmatic nature. Additionally, in the shear-influenced Vøring rifted margin, SDRs were interpreted (Eldholm, 1989; Mjelde, Raum,

Myhren, et al., 2005; Planke et al., 1999), which is not a characteristic identified in the Ghanaian margin.

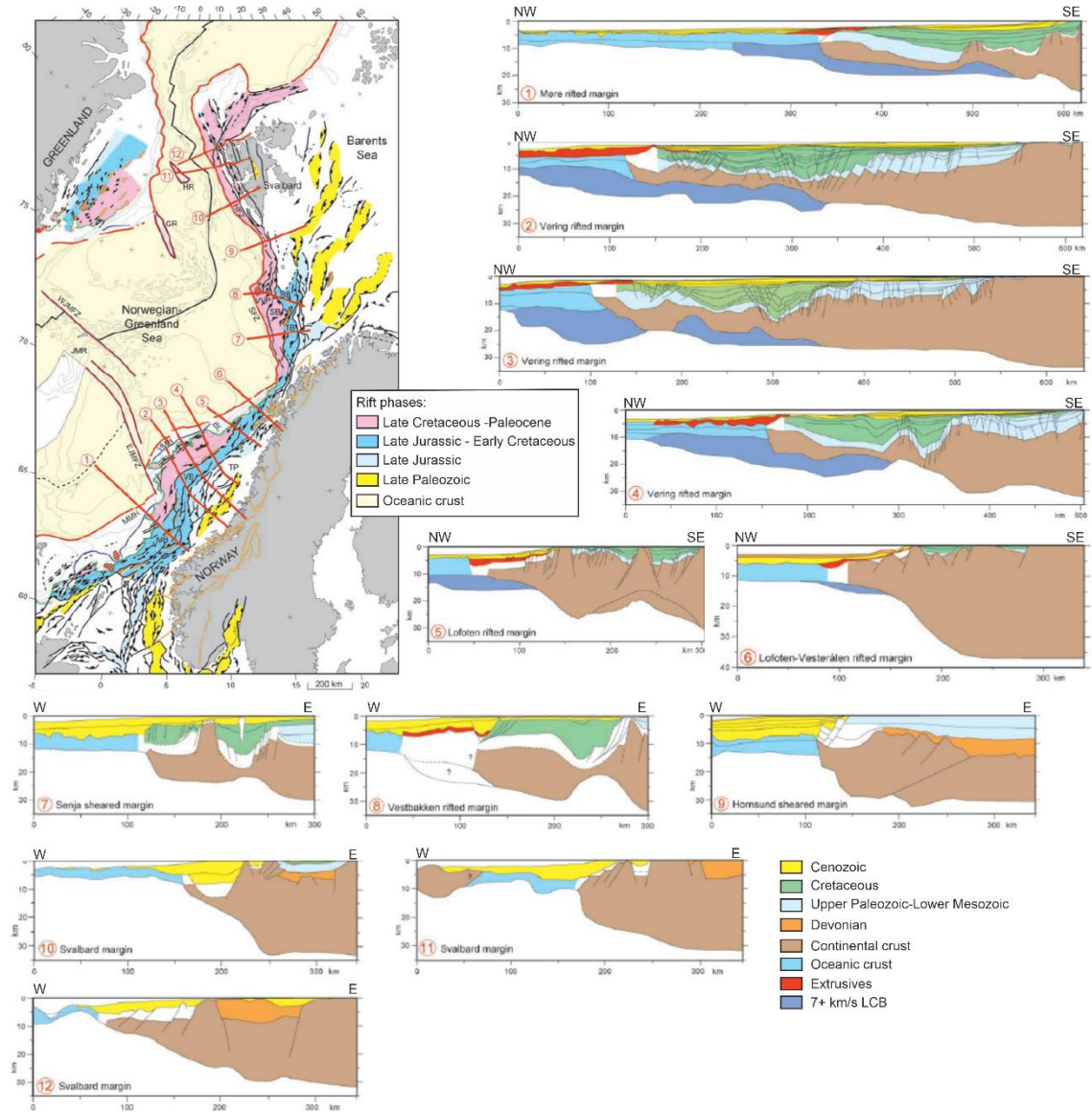


Figure 5.9: Regional structural map with structural elements related to different rift phases and crustal transects across the rifted margin of mid Norway (1-6), and the mainly sheared western Barents Sea-Svalbard margin (7-12) (modified from Faleide et al., 2008).

5.6.4 Gulf of California

The Gulf of California is a young transtensional margin, which is bounded by en-echelon NW-SE trending strike-slip faults, delineating the pull-apart basin (Figure 5.10; e.g., Lizarralde et al., 2007; Bennett et al., 2013). In the northern region, active rifting is prevalent (Martín-Barajas et al., 2013), while the southern and central Gulf exhibit ongoing seafloor spreading (Lizarralde et al., 2007). In addition to the bounding strike-slip faults, the basin features NE-SW trending normal and strike-slip faults (Aragón-Arreola & Martín-Barajas, 2007; Axen & Fletcher, 1998; Bennett, 2013; Bennett et al., 2013; Fletcher & Spelz, 2009; Gastil & Krummenacher, 1977; Harding, 1990; Lewis & Stock, 1998; Martín-Barajas et al., 1995; Martín-Barajas et al., 2013; Oskin, 2002; Persaud et al., 2003; Sanchez-Zamora et al., 1991; Seiler et al., 2010).

The boundaries of the Gulf of California are influenced by oblique movement, while the basin experiences primarily orthogonal extension (Farangitakis et al., 2020). The faults in the Gulf of California are newly formed, without any evidence of reactivated structures. Magmatic intrusions and volcanic deposits in the sedimentary sequences (Aragón-Arreola & Martín-Barajas, 2007; Persaud et al., 2003; Sanchez-Zamora et al., 1991), along with syn-rift volcanism, contribute to the development of a hybrid magmatic-continental crust along the strike-slip fault zones (Martín-Barajas et al., 2013), resembling characteristics observed in the Ghanaian margin (Figure 4.18).

Seismic analysis of the Gulf of California (Aragón-Arreola & Martín-Barajas, 2007; Martín-Barajas et al., 2013) reveals the presence of listric faults forming half-grabens accommodating syn-rift sediments and locally forming antiforms. The antiforms may also be attributed to the strike-slip fault activity. The sediment geometries and fault characteristics suggest a predominant transtensional margin with major depocenters, differing significantly from the Ghanaian transform margin. In the Ghanaian margin, the major depocenters developed in pull-apart basins (e.g., Figure 4.3b). Furthermore, the Gulf of California lacks tectono-stratigraphic similarities with the transtensional Atlas system, possibly attributed to inherited structures, as the Atlas system had a well-developed fault system prior to the onset of the transtensional phase.

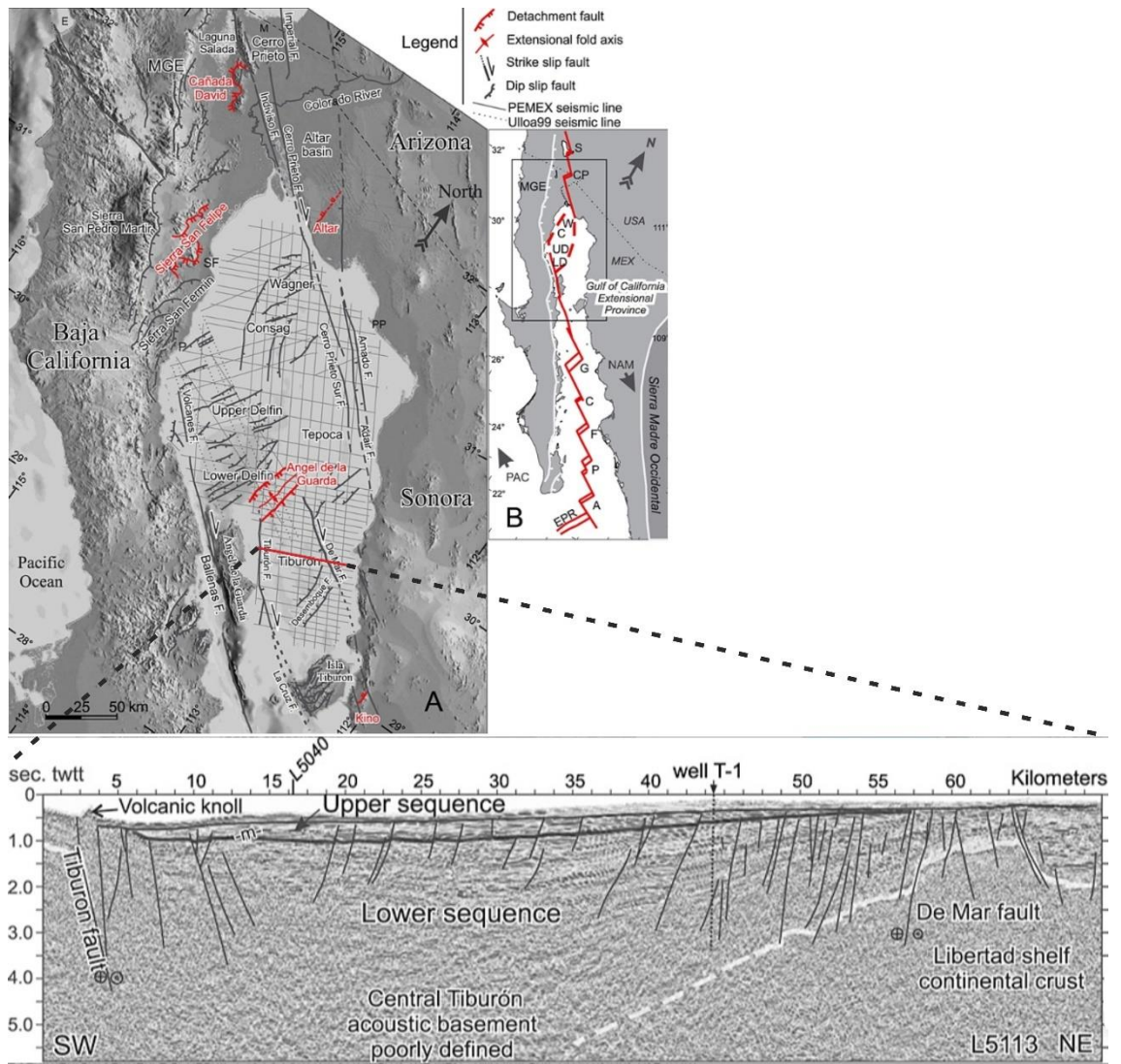


Figure 5.10: Structural framework of the Gulf of California and seismic profile in Tiburon basin bounded by strike-slip and oblique slip faults (after Martín-Barajas et al., 2013 and references therein).

5.6.5 Bohai, China

The Bohai Basin in Northern China is identified as a pull-apart basin, bound by major NE-SW and minor E-W and NNE-SSW trending structures (Figure 5.11), sharing a similar structural template with the Atlas system (Figure 2.1).

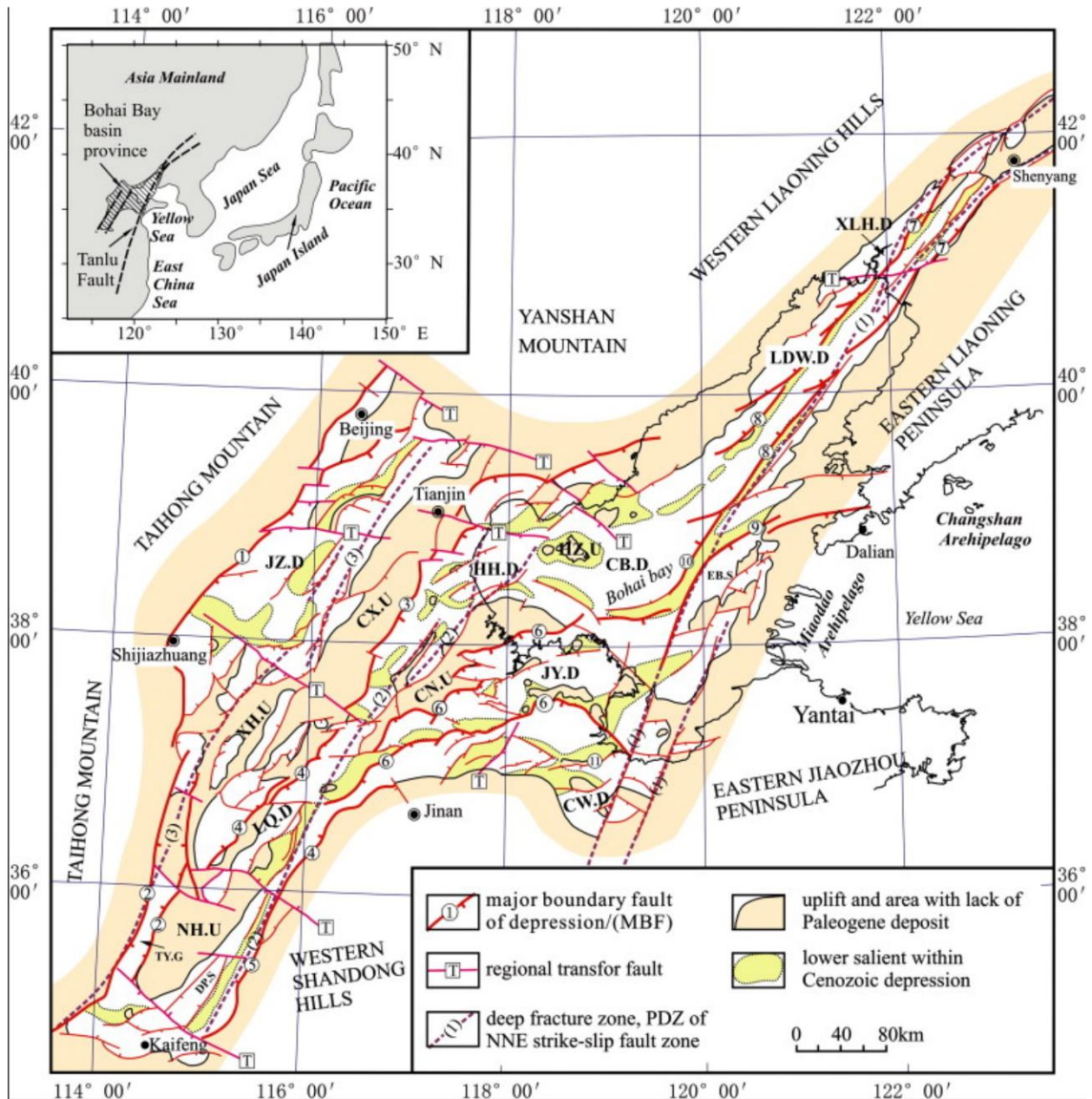


Figure 5.11: Structural map of the Bohai basin in China illustrating the master dextral strike-slip fault with NE-SW orientation (Qi & Yang, 2010).

The stress field induced by plate movement in the Bohai Basin led to the reactivation of lithospheric scale pre-existing structures (Allen et al., 1997; Klimetz, 1983), resulting in the formation of depressions and uplifts (Qi & Yang, 2010). The variety of fault types within the basin implies a stress field including normal, oblique extension, and strike-slip (Allen et al., 1997; Farangitakis et al., 2020; Qi & Yang, 2010). Local uplift and compression along strike-slip faults in

the Bohai Basin may be attributed to either a subsequent compressional event (Qi & Yang, 2010) or ongoing strike-slip activity (Farangitakis et al., 2020). Additionally, the lithospheric-scale strike-slip faults in the Bohai Basin may accommodate magmatic material due to mantle upwelling (Qi & Yang, 2010).

While these characteristics align with observations in the Atlas system (Figure 2.11), some distinctions exist. In the Bohai Basin, the stress field alternates between orthogonal and strike-slip, and the syn-rift sediments display typical growth strata, occasionally exhibiting discontinuities near the strike-slip faults (Allen et al., 1998; Qi & Yang, 2010). In contrast, the Atlas system exhibits additional contractional deformation, with growth strata corresponding to the stress regime (Figures 2.6 and 2.8d).

5.7 Suggested future research

5.7.1 Magmatism in oblique rifts

Further investigation of the addition of magmatism effects in the oblique system is required. In this study, this was limited by available research time and well data. In the High Atlas, samples could have been collected to do some ^{40}Ar - ^{39}Ar geochronology, however, due to limited time, this was not feasible. Dating the magmatic material identified in the fracture zones in the Central High Atlas (Chapter 2) would give further insights into the magma influence in the oblique extensional setting. Similarly, in Ghana, Chapter 4, published well data were used, which mostly focus on the proximal domain, and do not indicate specific timing on the magma supply. Well data in the Romanche Fracture Zone and the continental-oceanic boundary would give more information about the magma supply during rifting. Lastly, the analysis of magmatism in oblique rifts would indicate the effect on the rheology of the oblique rift systems, and how this could control the asymmetry during their evolution.

5.7.2 Data availability

In this study, I used field and 2D seismic reflection data to identify the structural configuration, crustal characteristics, and paleostress variations within different rift systems influenced by strike-slip tectonics. However, for a more comprehensive investigation and analysis of strike-slip tectonics, it is imperative to incorporate data and modelling that capture lateral variations.

The utilization of 3D seismic reflection data or densely sampled 2D seismic reflection data would provide a more detailed and precise image of the structural configuration. While the data density for the Ghanaian margin, as demonstrated in Chapter 4, is sufficient, additional data are required for the Atlas system. This would not only further support the fieldwork observations, but also contribute valuable insights to the evolutionary processes. Similarly, the Florida margin requires additional 2D or even 3D seismic reflection data to effectively identify and characterise any potential strike-slip tectonics in the region.

5.7.3 Modelling

Apart from the additional data, the incorporation of a series of models can enhance the analysis of strike-slip tectonics, providing valuable insights for each

of the individual case study areas (Chapters 2-4) as well as contributing to the development of the current strike-slip tectonics model (Figure 5.5). These modelling approaches include (1) numerical, (2) analogue modelling, and (3) plate reconstruction models.

- Numerical and analogue modelling for strike-slip tectonics: Numerical and analogue modelling would be the best approach for strike-slip tectonics. These would capture stress variation and the evolution of the faults along the transform margin of Ghana and the failed Atlas rift system. This approach will offer insights into the fault evolution in different segments of Ghana and a more accurate understanding of stress variation over time in both regions. Regional scale 4D models can be constructed based on the current seismic reflection data, field data, numerical, and analogue modelling, allowing for comparisons with current models in oblique rifting and transform margins (Agostini et al., 2009; Brune, 2014; de Souza Rodrigues et al., 2023; Farangitakis et al., 2019, 2020; Wu et al., 2009; Zwaan et al., 2016).
- Gulf of Mexico: The aforementioned models would aid in identifying potential strike-slip activity in the Gulf of Mexico during the early stages of rifting, as further discussed in Chapter 3. Plate reconstruction would further contribute to existing plate models (Filina & Beutel, 2022; Kneller & Johnson, 2011; Lundin & Doré, 2017; Minguez et al., 2020; Pindell et al., 2021).
- Atlas system: Various models would assist in identifying the exact timing and degree of obliquity in the Atlas system. Testing different models would provide insights into the initiation and cessation of the transtensional phase, adding more information to previous plate reconstructions (Ellouz et al., 2003; Escosa et al., 2021; Fernandez, 2019; Schettino & Turco, 2011). According to the field data presented in Chapter 2, the cessation of the transtensional phase is ambiguous due to the multiple erosional phases.
- Ghana: In the Equatorial Atlantic, understanding crustal limits, sedimentation age, and stress regime along the margin can minimize the uncertainty in the plate boundaries prior to the Pangaea breakup (Heine et al., 2013; Moulin et al., 2010; Pindell et al., 2021; Pindell, 1985; Ye et al.,

2017). This information can identify changes in plate motion and precisely pinpoint active structures in time.

The examination and modelling of these aspects would contribute to the identification and prediction of hazards and resource potential in such systems, with variations based on the degree of obliquity within these systems.

5.8 Conclusions

This thesis investigates strike-slip tectonics in extensional systems, focusing on three distinct case study areas: the Florida margin in the Gulf of Mexico, the High Atlas in Morocco, and the Ghanaian margin in the Equatorial Atlantic. Seismic reflection data and field data were used for the margins and the onshore Atlas system, respectively. The analysis in the first two study areas started with an initial lack of clarity regarding the presence of strike-slip and transtensional movement, which was inferred from plate reconstruction models. Therefore, the identification of strike-slip extension remained unknown until the completion of the areas' analysis. Specifically, in the Gulf of Mexico, there is no discernible evidence of strike-slip movement during the rifting and therefore, it cannot be distinguished as a transform margin. In contrast, the Atlas system and the Ghanaian margin indicate the presence of strike-slip movement and the study involved the examination of tectono-stratigraphy, paleostress analysis, the influence of inherited structures, and crustal architecture.

It is worth emphasising the interplay among pre-existing structures, tectono-stratigraphy and the stress regime in the examined regions. Based on the Atlas system, the Ghanaian margin, and analogous extensional strike-slip systems in comparison with the thesis areas, it becomes evident that the pre-existing structures are initially reactivated under the influence of a strike-slip stress regime, followed by the formation of newly developed structures in the later stages. The stress regime displays variability based on the geometries of faults, rift systems, and margins, while sedimentation patterns can provide indications of the system's obliquity. In cases of orthogonal extension, sediments tend to form typical growth strata geometries, whereas the higher the obliquity in the system, the more sub-horizontal sediment geometries are developed.

At the crustal scale, major strike-slip faults play a role in accommodating intrusions due to mantle upwelling. These intrusions may be situated in the centre of the rifted system, as observed in the Atlas system, and at the main transform fault, as observed in Ghana. In the latter case, the intrusions and the juxtaposition of the oceanic crust against the continental crust, along with thermal conductivity, can transform the continental crust into a hybrid continental-magmatic crust. This transformation typically occurs at the outer corner of the margin, establishing a continental-oceanic boundary. Lastly, continental stretching is generally limited in

oblique systems and it is concentrated within the segments of the margin influenced by orthogonal extension. Whereas, continental thickening may occur at the transform fault zone.

The studied areas were then compared to distinguish the differences between the transform and rifted margins. Lastly, their individual kinematic analyses were integrated into understanding the evolution of Pangaea's break-up from the Late Triassic to Late Cretaceous, focusing on the Atlantic region.

References

- Abd-Allah, A. M. A., Abdel Aal, M. H., El-Said, M. M., & Abd El-Naby, A. (2014). Structural evolution of the southern transfer zone of the Gulf of Suez rift, Egypt. *Journal of African Earth Sciences*, *96*, 21–38. <https://doi.org/10.1016/j.jafrearsci.2014.03.008>
- Abebe, B., Acocella, V., Korme, T., & Ayalew, D. (2007). Quaternary faulting and volcanism in the Main Ethiopian Rift. *Journal of African Earth Sciences*, *48*(2–3), 115–124. <https://doi.org/10.1016/j.jafrearsci.2006.10.005>
- Abebe, T., Manetti, P., Bonini, M., Corti, G., Innocenti, F., Mazzarini, F., & Pecskey, Z. (2005). Geological map (scale 1: 200,000) of the northern Main Ethiopian Rift and its implication for the volcano-tectonic evolution of the rift. *Geol. Soc. Am. Map Chart Ser., MCH094*.
- Adda, G., W. ., Atta-Peters, D. ., & Ben-Awuah, J. (2015). Burial History, Thermal Maturity and Petroleum Generation History of the Lower Paleozoic Petroleum System in the Saltpond Basin, Offshore Ghana*. *Search and Discovery*.
- Affaton, P., Sougy, J., & Trompette, R. (1980). The tectono-stratigraphic relationships between the upper Precambrian and lower Paleozoic Volta Basin and the Pan-African Dahomeyide orogenic belt (West Africa). *American Journal of Science*, *280*(3), 224–248. <https://doi.org/10.2475/AJS.280.3.224>
- Agostini, A., Corti, G., Zeoli, A., & Mulugeta, G. (2009). Evolution, pattern, and partitioning of deformation during oblique continental rifting: Inferences from lithospheric-scale centrifuge models. *Geochemistry, Geophysics, Geosystems*, *10*(11). <https://doi.org/10.1029/2009GC002676>
- Ait Brahim, L., Chotin, P., Hinaj, S., Abdelouafi, A., El Adraoui, A., Nakcha, C., Dhont, D., Charroud, M., Sossey Alaoui, F., Amrhar, M., Bouaza, A., Tabyaoui, H., & Chaouni, A. (2002). Paleostress evolution in the Moroccan African margin from Triassic to Present. *Tectonophysics*, *357*(1–4), 187–205. [https://doi.org/10.1016/S0040-1951\(02\)00368-2](https://doi.org/10.1016/S0040-1951(02)00368-2)
- Akpaki, B. N. (1978). Geologic structure and evolution of the Keta basin, Ghana, West Africa. *Geological Society of America Bulletin*, *89*(1), 124. [https://doi.org/10.1130/0016-7606\(1978\)89<124:GSAEOT>2.0.CO;2](https://doi.org/10.1130/0016-7606(1978)89<124:GSAEOT>2.0.CO;2)
- Alger, R. P., & Crain, E. R. (1966). Defining evaporite deposits with electrical well logs. *In: Second Symposium on Salt. The Northern Ohio Geological Society*, *2*, 116–130.
- Allen, M.B., Macdonald, D. I. M., Xun, Z., Vincent, S. J., & Brouet-Menzies, C. (1997). Early Cenozoic two-phase extension and late Cenozoic thermal subsidence and inversion of the Bohai Basin, northern China. *Marine and Petroleum Geology*, *14*(7–8), 951–972. [https://doi.org/10.1016/S0264-8172\(97\)00027-5](https://doi.org/10.1016/S0264-8172(97)00027-5)
- Allen, Mark B., Macdonald, D. I. M., Xun, Z., Vincent, S. J., & Brouet-Menzies, C. (1998). Transtensional deformation in the evolution of the Bohai Basin, northern China. *Geological Society, London, Special Publications*, *135*(1), 215–229. <https://doi.org/10.1144/GSL.SP.1998.135.01.14>
- Allouban, M., Karaoui, B., Mahmoudi, A., Baïdder, L., Hafid, A., Goodenough, K., & Eddebbi, A. (2021). Petrographic and geochemical study of Jurassic-Cretaceous intrusive massifs (Gabbros-syenites) of the Eastern High Atlas, Morocco (Rich-Talsint axis). *Journal of African Earth Sciences*, *184*, 104280. <https://doi.org/10.1016/j.jafrearsci.2021.104280>

- Andrade, J. F. P., Gomes, M. P., Bezerra, F. H. R., de Castro, D. L., & Vital, H. (2018). Morphotectonic development of the Ceará Terrace: a marginal ridge on the western side of the Romanche Fracture Zone in the Brazilian Equatorial Margin. *Geo-Marine Letters*, 38(4), 371–384. <https://doi.org/10.1007/S00367-018-0541-Y>
- Angelier, J. (1984). Tectonic Analysis of Fault Slip Data Sets . *Journal of Geophysical Research*, 89(B7), 5835–5848. <https://doi.org/10.1029/JB089iB07p05835>
- Antobreh, A. A., Faleide, J. I., Tsikalas, F., & Planke, S. (2009). Rift–shear architecture and tectonic development of the Ghana margin deduced from multichannel seismic reflection and potential field data. *Marine and Petroleum Geology*, 26(3), 345–368. <https://doi.org/10.1016/j.marpetgeo.2008.04.005>
- Aragón-Arreola, M., & Martín-Barajas, A. (2007). Westward migration of extension in the northern Gulf of California, Mexico. *Geology*, 35(6), 571. <https://doi.org/10.1130/G23360A.1>
- Armando, G. (1999). Intracontinental alkaline magmatism: Geology, petrography, mineralogy and geochemistry of the gabbro-syenitic Jebel Hayim Massif (Central High Atlas, Morocco). *Mémoires de Géologie de l'Université de Lausanne*, 31, 1–106.
- Arthaud, F., & Matte, P. (1977). Late Paleozoic strike-slip faulting in southern Europe and northern Africa: Result of a right-lateral shear zone between the Appalachians and the Urals. *Bulletin of the Geological Society of America*, 88(9), 1305–1320. [https://doi.org/10.1130/0016-7606\(1977\)88<1305:LPSFIS>2.0.CO;2](https://doi.org/10.1130/0016-7606(1977)88<1305:LPSFIS>2.0.CO;2)
- Attoh, K., & Brown, L. (2008). Deep structure of the southeastern margin of the West African craton from seismic reflection data, offshore Ghana. *Geological Society, London, Special Publications*, 297(1), 499–508. <https://doi.org/10.1144/SP297.24>
- Attoh, K., Brown, L., Guo, J., & Heanlein, J. (2004). Seismic stratigraphic record of transpression and uplift on the Romanche transform margin, offshore Ghana. *Tectonophysics*, 378(1–2), 1–16. <https://doi.org/10.1016/j.tecto.2003.09.026>
- Attoh, K., Dallmeyer, R. D., & Affaton, P. (1997). Chronology of nappe assembly in the Pan-African Dahomeyide orogen, West Africa: evidence from ⁴⁰Ar/³⁹Ar mineral ages. *Precambrian Research*, 82(1–2), 153–171. [https://doi.org/10.1016/S0301-9268\(96\)00031-9](https://doi.org/10.1016/S0301-9268(96)00031-9)
- Axen, G. J., & Fletcher, J. M. (1998). Late Miocene-Pleistocene Extensional Faulting, Northern Gulf of California, Mexico and Salton Trough, California. *International Geology Review*, 40(3), 217–244. <https://doi.org/10.1080/00206819809465207>
- Aydin, A., & Page, B. M. (1984). Diverse Pliocene-Quaternary tectonics in a transform environment, San Francisco Bay region, California. *Geological Society of America Bulletin*, 95(11), 1303. [https://doi.org/10.1130/0016-7606\(1984\)95<1303:DPTIAT>2.0.CO;2](https://doi.org/10.1130/0016-7606(1984)95<1303:DPTIAT>2.0.CO;2)
- Aydin, A., Schultz, R., & Campagna, D. (1990). *Fault-normal dilation in pull-apart basins: implications for the relationship between strike-slip faults and volcanic activity*.
- Aydin, Atilla, & Nur, A. (1982). Evolution of pull-apart basins and their scale independence. *Tectonics*, 1(1), 91–105. <https://doi.org/10.1029/TC001i001p00091>
- Babcock, C. V. (1970). *Significance of probable age of basement rock in the Mobil, No. 1 FSL 224-A well, Offshore Franklin County* . Florida Department of Environmental Protection.
- Baidder, L., Karim, M., El Arabi, E. H., Soulaïmani, A., Amhoud, H., Kaoukaya, A., Mahmoudi, A., Boudad, L., Ouanaimi, H., Eddebbi, A., Hilalil, M., et Badra, L., &

- Allouban, A. (2018). Carte géologique du Maroc (1/50 000), feuille ayt khojmane. *Notes et Mémoires Serv. Géol. Maroc N°592 (2018)*.
- Barnett, J. A. M., Mortimer, J., Rippon, J. H., Walsh, J. J., & Watterson, J. (1987). Displacement geometry in the volume containing a single normal fault. *American Association of Petroleum Geologists Bulletin*, 71, 925–937.
- Basile, C., Mascle, J., Popoff, M., Bouillin, J. P., & Mascle, G. (1993). The Ivory Coast-Ghana transform margin: A marginal ridge structure deduced from seismic data. *Tectonophysics*, 222(1), 1–19. [https://doi.org/10.1016/0040-1951\(93\)90186-N](https://doi.org/10.1016/0040-1951(93)90186-N)
- Basile, Christophe. (2015). Transform continental margins — part 1: Concepts and models. *Tectonophysics*, 661, 1–10. <https://doi.org/10.1016/j.tecto.2015.08.034>
- Basile, Christophe, & Allemand, P. (2002). Erosion and flexural uplift along transform faults. *Geophysical Journal International*, 151(2), 646–653. <https://doi.org/10.1046/j.1365-246X.2002.01805.x>
- Basile, Christophe, Girault, I., Paquette, J. L., Agranier, A., Loncke, L., Heuret, A., & Poetisi, E. (2020). The Jurassic magmatism of the Demerara Plateau (offshore French Guiana) as a remnant of the Sierra Leone hotspot during the Atlantic rifting. *Scientific Reports*, 10(7486), 1–12. <https://doi.org/10.1038/s41598-020-64333-5>
- Basile, Christophe, Mascle, J., Benkheilil, J., & Bouillin, J.-P. (1998). Geodynamic Evolution of the Cote d'Ivoire-Ghana Transform margin: An overview of LEG 159 Results. *Scientific Results*, 159, 101–110.
- Basile, Christophe, Mascle, J., & Guiraud, R. (2005). Phanerozoic geological evolution of the Equatorial Atlantic domain. *Journal of African Earth Sciences*, 43(1–3), 275–282. <https://doi.org/10.1016/j.jafrearsci.2005.07.011>
- Basilone, L., Roberts, G. G., Maia de Almeida, N., Fernandes, V. M., de Souza, A. C. B., Alves, D. P. V., & Jovane, L. (2023). Cretaceous to Recent tectono-sedimentary history and subsidence of the Barreirinhas, Ceará and Potiguar Basins, Brazilian Equatorial Margin. *Basin Research*, 1–24. <https://doi.org/10.1111/bre.12810>
- Bassetto, M., Alkmim, F. F., Szatmari, P., & Mohriak, W. U. (2000). The oceanic segment of the Southern Brazilian margin: Morpho-structural domains and their tectonic significance. In *Geophysical Monograph Series* (Vol. 115, pp. 235–299). Blackwell Publishing Ltd. <https://doi.org/10.1029/GM115p0235>
- Bastow, I. D., & Keir, D. (2011). The protracted development of the continent–ocean transition in Afar. *Nature Geoscience*, 4(4), 248–250. <https://doi.org/10.1038/ngeo1095>
- Beauchamp, J. (1988). Triassic sedimentation and rifting in the High Atlas (Morocco). *Developments in Geotectonics*, 22(C), 477–497. <https://doi.org/10.1016/B978-0-444-42903-2.50025-7>
- Bécel, A., Davis, J. K., Shuck, B. D., Van Avendonk, H. J. A., & Gibson, J. C. (2020). Evidence for a Prolonged Continental Breakup Resulting From Slow Extension Rates at the Eastern North American Volcanic Rifted Margin. *Journal of Geophysical Research: Solid Earth*, 125(9), e2020JB020093. <https://doi.org/10.1029/2020JB020093>
- Bellahsen, N., Leroy, S., Autin, J., Razin, P., D'Acremont, E., Sloan, H., Pik, R., Ahmed, A., & Khanbari, K. (2013). Pre-existing oblique transfer zones and transfer/transform relationships in continental margins: New insights from the southeastern Gulf of Aden, Socotra Island, Yemen. *Tectonophysics*, 607, 32–50.

<https://doi.org/10.1016/j.tecto.2013.07.036>

- Bellier, O., & Sébrier, M. (1994). Relationship between tectonism and volcanism along the Great Sumatran Fault Zone deduced by spot image analyses. *Tectonophysics*, 233(3–4), 215–231. [https://doi.org/10.1016/0040-1951\(94\)90242-9](https://doi.org/10.1016/0040-1951(94)90242-9)
- Ben-Avraham, Z., Hartnady, C. J. H., & Malan, J. A. (1993). Early tectonic extension between the Agulhas Bank and the Falkland Plateau due to the rotation of the Lafonia microplate. *Earth and Planetary Science Letters*, 117(1–2), 43–58. [https://doi.org/10.1016/0012-821X\(93\)90116-Q](https://doi.org/10.1016/0012-821X(93)90116-Q)
- Benkhelil, J., Mascle, J., & Tricart, P. (1995). The Guinea continental margin: an example of a structurally complex transform margin. *Tectonophysics*, 248(1–2), 117–137. [https://doi.org/10.1016/0040-1951\(94\)00246-6](https://doi.org/10.1016/0040-1951(94)00246-6)
- Bennett, S. E. K., Oskin, M. E., & Iriondo, A. (2013). Transtensional rifting in the proto-Gulf of California near Bahia Kino, Sonora, Mexico. *Geological Society of America Bulletin*, 125(11–12), 1752–1782. <https://doi.org/10.1130/B30676.1>
- Bennett, S.E.K. (2013). *The Role of Rift Obliquity in Formation of the Gulf of California*. University of California, Davis.
- Bennett, Scott E.K., & Oskin, M. E. (2014). Oblique rifting ruptures continents: Example from the Gulf of California shear zone. *Geology*, 42(3), 215–218. <https://doi.org/10.1130/G34904.1>
- Bensalah, M. K., Youbi, N., Mata, J., Madeira, J., Martins, L., El Hachimi, H., Bertrand, H., Marzoli, A., Bellieni, G., Doblas, M., Font, E., Medina, F., Mahmoudi, A., Beraâouz, E. H., Miranda, R., Verati, C., De Min, A., Ben Abbou, M., & Zayane, R. (2013). The Jurassic–Cretaceous basaltic magmatism of the Oued El-Abid syncline (High Atlas, Morocco): Physical volcanology, geochemistry and geodynamic implications. *Journal of African Earth Sciences*, 81, 60–81. <https://doi.org/10.1016/J.JAFREARSCI.2013.01.004>
- Berndt, C., Mjelde, R., Planke, S., Shimamura, H., & Faleide, J. I. (2001). Controls on the tectono-magmatic evolution of a volcanic transform margin: the Vøring Transform Margin, NE Atlantic. *Marine Geophysical Researches*, 22, 133–152.
- Berndt, C., Planke, S., Alvestad, E., Tsikalas, F., & Rasmussen, T. (2001). Seismic volcanostratigraphy of the Norwegian Margin: Constraints on tectonomagmatic break-up processes. *Journal of the Geological Society*, 158(3), 413–426. <https://doi.org/10.1144/jgs.158.3.413>
- Beydoun, Z. . (1970). A discussion on the structure and evolution of the Red Sea and the nature of the Red Sea, Gulf of Aden and Ethiopia rift junction - Southern Arabia and northern Somalia: Comparative geology. *Philosophical Transactions of the Royal Society of London. Series A, Mathematical and Physical Sciences*, 267(1181), 267–292. <https://doi.org/10.1098/RSTA.1970.0036>
- Biari, Y., Klingelhoefer, F., Franke, D., Funck, T., Loncke, L., Sibuet, J. C., Basile, C., Austin, J. A., Rigoti, C. A., Sahabi, M., Benabdellouahed, M., & Roest, W. R. (2021). Structure and evolution of the Atlantic passive margins: A review of existing rifting models from wide-angle seismic data and kinematic reconstruction. *Marine and Petroleum Geology*, 126, 104898. <https://doi.org/10.1016/J.MARPETGEO.2021.104898>
- Biddle, K. T., & Christie-Blick, N. (1985). *GLOSSARY STRIKE SLIP DEFORMATION BASIN FORMATION AND SEDIMENTATION*. <https://doi.org/10.7916/D8PK0RDK>
- Bigot-Cormier, F., Basile, C., Poupeau, G., Bouillin, J. P., & Labrin, E. (2005). Denudation of the Côte d'Ivoire-Ghana transform continental margin from apatite

- fission tracks. *Terra Nova*, 17(2), 189–195. <https://doi.org/10.1111/J.1365-3121.2005.00605.X>
- Bird, D. E., Burke, K., Hall, S. A., & Casey, J. F. (2005). Gulf of Mexico tectonic history: Hotspot tracks, crustal boundaries, and early salt distribution. *AAPG Bulletin*, 89(3), 311–328. <https://doi.org/10.1306/10280404026>
- Blarez, E., & Mascle, J. (1988). Shallow structures and evolution of the Ivory Coast and Ghana transform margin. *Marine and Petroleum Geology*, 5(1), 54–64. [https://doi.org/10.1016/0264-8172\(88\)90039-6](https://doi.org/10.1016/0264-8172(88)90039-6)
- Bonatti, E., Brunelli, D., Buck, W., Cipriani, A., Fabretti, P., Ferrante, V., Gasperini, L., & Ligi, M. (2005). Flexural uplift of a lithospheric slab near the Vema transform (Central Atlantic): Timing and mechanisms. *Earth and Planetary Science Letters*, 240(3–4), 642–655. <https://doi.org/10.1016/j.epsl.2005.10.010>
- Bosworth, W., & Morley, C. K. (1994). Structural and stratigraphic evolution of the Anza rift, Kenya. *Tectonophysics*, 236(1–4), 93–115. [https://doi.org/10.1016/0040-1951\(94\)90171-6](https://doi.org/10.1016/0040-1951(94)90171-6)
- Bouchouata, A., Canerot, J., Souhel, A., & Almeras, Y. (1995). Jurassic sequence stratigraphy and geodynamic evolution in the Talmest-Tazoult area, central high Atlas, Morocco. *Comptes Rendus - Academie Des Sciences, Serie II: Sciences de La Terre et Des Planetes*, 320(8), 749–756.
- Bouillin, J.-P., Poupeau, G., Basile, C., Labrin, E., & Mascle, J. (1998). Thermal Constrains on the Côte d'Ivoire-Ghana transform margin: evidence from apatite fission tracks. In: Mascle, J., Lohmann, G. P. & Moullade, M. (Eds) *Proceedings of the Ocean Drilling Program, Scientific Results. Ocean Drilling Program, College Station, TX*, 159, 43–48.
- Brevik, A. J., Mjelde, R., Faleide, J. I., & Murai, Y. (2006). Rates of continental breakup magmatism and seafloor spreading in the Norway Basin–Iceland plume interaction. *Journal of Geophysical Research: Solid Earth*, 111(B7). <https://doi.org/10.1029/2005JB004004>
- Brevik, A. J., Verhoef, J., & Faleide, J. I. (1999). Effect of thermal contrasts on gravity modeling at passive margins: Results from the western Barents Sea. *Journal of Geophysical Research: Solid Earth*, 104(B7), 15293–15311. <https://doi.org/10.1029/1998JB900022>
- Brune, S. (2014). Evolution of stress and fault patterns in oblique rift systems: 3-D numerical lithospheric-scale experiments from rift to breakup. *Geochemistry, Geophysics, Geosystems*, 15(8), 3392–3415. <https://doi.org/10.1002/2014GC005446>
- Brune, S. (2016). A Review of Geodynamic Processes and Natural Hazards. In *Rifts and Rifted Margins* (pp. 11–37). <https://doi.org/10.1002/9781119054146.ch2>
- Brune, S., Heine, C., Clift, P. D., & Pérez-Gussinyé, M. (2017). Rifted margin architecture and crustal rheology: Reviewing Iberia-Newfoundland, Central South Atlantic, and South China Sea. *Marine and Petroleum Geology*, 79, 257–281. <https://doi.org/10.1016/J.MARPETGEO.2016.10.018>
- Brune, S., Williams, S. E., & Dietmar Müller, R. (2018). Oblique rifting: The rule, not the exception. *Solid Earth*, 9(5), 1187–1206. <https://doi.org/10.5194/se-9-1187-2018>
- Buffler, R.T., Schlager, W., & Pisciotto, K. A. (1984). Introduction and explanatory notes. *Initial Reports DSDP, Leg 77, Ft. Lauderdale to San Juan*, 5–22. <https://doi.org/10.2973/DSDP.PROC.77.101.1984>
- Buffler, R., Schlager, W., Bowdler, J., Cotillon, P. H., Halley, R. B., Kinoshita, H.,

- Magoon III, L. B., McNulty, C. L., Patton, J. W., Pisciotto, K. A., Premoli Silva, I., Avello Suarez, O., Testarmata, M. M., Tyson, R. V., & Watkins, D. K. (1984). Site 537. In *Initial Reports of the Deep Sea Drilling Project*, 77 (Vol. 77, pp. 279–336). U.S. Government Printing Office. <https://doi.org/10.2973/dsdp.proc.77.104.1984>
- Buffler, R. T., & Sawyer, D. S. (1985). Distribution of Crust and Early History, Gulf of Mexico Basin. *Gulf Coast Association of Geological Societies Transactions*, 35, 333–344.
- Burchfiel, B. C., & Stewart, J. H. (1966). “Pull-apart” Origin of the Central Segment of Death Valley, California. *Geological Society of America Bulletin*, 77, 439–442. [https://doi.org/https://doi.org/10.1130/0016-7606\(1966\)77\[439:POOTCS\]2.0.CO;2](https://doi.org/https://doi.org/10.1130/0016-7606(1966)77[439:POOTCS]2.0.CO;2)
- Burke, K., & Torsvik, T. H. (2004). Derivation of Large Igneous Provinces of the past 200 million years from long-term heterogeneities in the deep mantle. *Earth and Planetary Science Letters*, 227(3–4), 531–538. <https://doi.org/10.1016/J.EPSL.2004.09.015>
- Busby, C. J., Putirka, K., Melosh, B., Renne, P. R., Hagan, J. C., Gambs, M., & Wesoloski, C. (2018). A tale of two Walker Lane pull-apart basins in the ancestral Cascades arc, central Sierra Nevada, California. *Geosphere*, 14(5), 2068–2117. <https://doi.org/10.1130/GES01398.1>
- Calvín, P., Casas-Sainz, A. M., Villalaín, J. J., & Moussaid, B. (2018). Extensional vs. compressional deformation in the Central High Atlas salt province: A paleomagnetic approach. *Tectonophysics*, 734–735, 130–147. <https://doi.org/10.1016/J.TECTO.2018.04.007>
- Calvín, P., Ruiz-Martínez, V. C., Villalaín, J. J., Casas-Sainz, A. M., & Moussaid, B. (2017). Emplacement and Deformation of Mesozoic Gabbros of the High Atlas (Morocco): Paleomagnetism and Magnetic Fabrics. *Tectonics*, 36(12), 3012–3037. <https://doi.org/10.1002/2017TC004578>
- Campan, A. (1995). Analyse cinématique de l’Atlantique équatorial: implications sur l’évolution de l’Atlantique Sud et sur la frontière de plaques Amérique du Nord/Amérique du Sud. *Ph.D. Thesis, Université Pierre et Marie Curie, Paris*, 352.
- Charriere, A. (1996). Contexte paléogéographique et paléotectonique de la formation des bassins crétacés du Moyen-Atlas (Maroc) à la lumière des données stratigraphiques. *Bulletin de La Société Géologique de France*, 167(5), 617–626.
- Charrière, A., Haddoumi, H., & Mojon, P. O. (2005). Découverte de Jurassique supérieur et d’un niveau marin du Barrémien dans les « couches rouges » continentales du Haut Atlas central marocain : implications paléogéographiques et structurales. *Comptes Rendus Palevol*, 4(5), 385–394. <https://doi.org/10.1016/J.CRPV.2005.04.009>
- Charrière, A., Ibouh, H., & Haddoumi, H. (2011). Le Haut Atlas Central de Beni Mellal à Imilchil. In: Michard, A., Saddiqi, O., Chalouan, A., Rjimati, E.C., Mouttaqi, A. (Eds.). *Notes et Mémoires Du Service Géologique Du Maroc*, 109–164.
- Chen, Y. (1988). Thermal model of oceanic transform faults. *Journal of Geophysical Research: Solid Earth*, 93(B8), 8839–8851. <https://doi.org/10.1029/JB093iB08p08839>
- Chorowicz, J. (1989). Transfer and transform fault zones in continental rifts: examples in the Afro-Arabian Rift System. Implications of crust breaking. *Journal of African Earth Sciences (and the Middle East)*, 8(2–4), 203–214. [https://doi.org/10.1016/S0899-5362\(89\)80025-9](https://doi.org/10.1016/S0899-5362(89)80025-9)
- Chorowicz, J., & Mukonki, M. (1979). Linéaments anciens, zones transformantes

récentes et géotectonique des fossés de l'Est africain, d'après la télédétection et la microtectonique. *Musée Royal d'Afrique Centrale, Tervuren (Belgique), Département Des Géologie et Des Mines, Rapport Annuel*, 143–167.

- Chorowicz, Jean. (2005). The East African rift system. *Journal of African Earth Sciences*, 43(1–3), 379–410. <https://doi.org/10.1016/j.jafrearsci.2005.07.019>
- Chorowicz, Jean, Collet, B., Bonavia, F. F., & Korme, T. (1994). Northwest to north-northwest extension direction in the Ethiopian rift deduced from the orientation of extension structures and fault-slip analysis. *Geological Society of America Bulletin*, 106(12), 1560–1570. [https://doi.org/10.1130/0016-7606\(1994\)105<1560:NTNED>2.3.CO;2](https://doi.org/10.1130/0016-7606(1994)105<1560:NTNED>2.3.CO;2)
- Christensen, N. I., & Mooney, W. D. (1995). Seismic velocity structure and composition of the continental crust: A global view. *Journal of Geophysical Research: Solid Earth*, 100(B6), 9761–9788. <https://doi.org/10.1029/95JB00259>
- Christeson, G. L., Van Avendonk, H. J. A., Norton, I. O., Snedden, J. W., Eddy, D. R., Karner, G. D., & Johnson, C. A. (2014). Deep crustal structure in the eastern Gulf of Mexico. *Journal of Geophysical Research: Solid Earth*, 119(9), 6782–6801. <https://doi.org/10.1002/2014JB011045>
- Christie-Blick, N., & Biddle, K. T. (1985). Deformation and Basin Formation along Strike-slip Faults. In *Strike-Slip Deformation, Basin Formation, and Sedimentation* (pp. 1–34). SEPM (Society for Sedimentary Geology). <https://doi.org/10.2110/pec.85.37.0001>
- Clarke, D. B., & Beutel, E. K. (2020). Davis Strait Paleocene picrites: Products of a plume or plates? *Earth-Science Reviews*, 206, 102770. <https://doi.org/10.1016/j.earscirev.2019.01.012>
- Clift, P. D., Lorenzo, J., Carter, A., & Hurford, A. J. (1997). Transform tectonics and thermal rejuvenation on the Côte d'Ivoire-Ghana margin, west Africa. *Journal of the Geological Society*, 154(3), 483–489. <https://doi.org/10.1144/gsjgs.154.3.0483>
- Clift, Peter D., & Lorenzo, J. M. (1999). Flexural unloading and uplift along the Côte d'Ivoire-Ghana Transform Margin, equatorial Atlantic. *Journal of Geophysical Research: Solid Earth*, 104(B11), 25257–25274. <https://doi.org/10.1029/1999JB900247>
- Clift, Peter D, Carter, A., & Hurford, A. J. (1998). Apatite Fission Track Analysis of Sites 959 and 960 on the Transform Continental Margin of Ghana,, West Africa. In *In: Mascle, J., Lohmann, G. P. & Moullade, M. (eds) Proceedings of the Ocean Drilling Program, Scientific Results, Volume 159. Ocean Drilling Program, College Station, TX* (pp. 35–41).
- Corti, G. (2008). Control of rift obliquity on the evolution and segmentation of the main Ethiopian rift. *Nature Geoscience* 2008 1:4, 1(4), 258–262. <https://doi.org/10.1038/ngeo160>
- Corti, G. (2009). Continental rift evolution: From rift initiation to incipient break-up in the Main Ethiopian Rift, East Africa. *Earth-Science Reviews*, 96(1–2), 1–53. <https://doi.org/10.1016/j.earscirev.2009.06.005>
- Corti, G., & Dooley, T. P. (2015). Lithospheric-scale centrifuge models of pull-apart basins. *Tectonophysics*, 664, 154–163. <https://doi.org/10.1016/j.tecto.2015.09.004>
- Corti, G., Nencini, R., & Skyttä, P. (2020). Modelling the influence of pre-existing brittle fabrics on the development and architecture pull-apart basins. *Journal of Structural Geology*, 131, 103937. <https://doi.org/10.1016/J.JSG.2019.103937>
- Costa, I. G. da, Beltrami, Carlos, V., & Alves, L. E. (1990). Ceara Basin: tectono-

sedimentary evolution and oil habitat; A evolucao tectono-sedimentar eo habitat do oleo da Bacia do Ceara. *Boletim de Geociências Da Petrobras*, 4.

- Crowell, J.C. (1974). Sedimentation Along the San Andreas Fault California. *The Society of Economic Paleontologists and Mineralogists (SEPM) Modern and Ancient Geosynclinal Sedimentation*, 19, 292–303.
- Crowell, John C. (1974). Origin of Late Cenozoic Basins in Southern California. *Special Publication of the Society of Economic Paleontologists and Mineralogists*, 22, 190–204.
- Curry, M. A. E., Peel, F. J., Hudec, M. R., & Norton, I. O. (2018). Extensional models for the development of passive-margin salt basins, with application to the Gulf of Mexico. *Basin Research*, 30(6), 1180–1199. <https://doi.org/10.1111/bre.12299>
- Daggett, P. H., Morgan, P., Boulos, F. K., Hennin, S. F., El-Sherif, A. A., El-Sayed, A. A., Basta, N. Z., & Melek, Y. S. (1986). Seismicity and active tectonics of the Egyptian Red Sea margin and the northern Red Sea. *Tectonophysics*, 125(4), 313–324. [https://doi.org/10.1016/0040-1951\(86\)90168-X](https://doi.org/10.1016/0040-1951(86)90168-X)
- Dailly, P., Henderson, T., Kanschat, K., Lowry, P., & Sills, S. (2017). The Jubilee Field, Ghana: Opening the Late Cretaceous Play in the West African Transform Margin. In *Giant Fields of the Decade 2000–2010*. The American Association of Petroleum Geologists. <https://doi.org/10.1306/13572010M1132997>
- Dale, A. J. (2013). Crustal type, Tectonic origin, and Petroleum Potential of the Bahamas Carbonate Platform . *MSc Thesis, University of Houston, Houston, TX*. <https://uh-ir.tdl.org/handle/10657/1058>
- Daly, M. C., Chorowicz, J., & Fairhead, J. D. (1989). Rift basin evolution in Africa: the influence of reactivated steep basement shear zones. *Geological Society, London, Special Publications*, 44(1), 309–334. <https://doi.org/10.1144/GSL.SP.1989.044.01.17>
- Dalziel, I. W. D. (1991). Pacific margins of Laurentia and East Antarctica-Australia as a conjugate rift pair: Evidence and implications for an Eocambrian supercontinent. *Geology*, 19, 598–601.
- Davison, I., Faull, T., Greenhalgh, J., O Beirne, E., & Steel, I. (2016). Transpressional structures and hydrocarbon potential along the Romanche Fracture Zone: a review. *Geological Society, London, Special Publications*, 431(1), 235–248. <https://doi.org/10.1144/SP431.2>
- de Castro, D. L., Oliveira, D. C., Herrera, D. R. H., Bezerra, F. H. R., Romeiro, M. A. T., & Araújo, M. N. C. (2022). Crustal evolution of divergent and transform segments of the Brazilian Equatorial Margin derived from integrated geophysical data: Insights from basement grain heritage. *Earth-Science Reviews*, 232, 104132. <https://doi.org/10.1016/j.earscirev.2022.104132>
- de Matos, R. M. D. (1992). The Northeast Brazilian Rift System. *Tectonics*, 11(4), 766–791. <https://doi.org/10.1029/91TC03092>
- De Paola, N., Holdsworth, R. E., McCaffrey, K. J. W., & Barchi, M. R. (2005). Partitioned transtension: an alternative to basin inversion models. *Journal of Structural Geology*, 27(4), 607–625. <https://doi.org/10.1016/j.jsg.2005.01.006>
- de Souza Rodrigues, R., Alves da Silva, F. C., & Venâncio, M. B. (2023). Oblique rifting along transfer zones: The structural evolution model revealed by physical modeling. *Journal of South American Earth Sciences*, 121, 104153. <https://doi.org/10.1016/j.jsames.2022.104153>
- Deighton, I. C., Winter, F., & Chisari, D. (2017). Recent High Resolution Seismic,

Magnetic and Gravity Data Throws New Light on the Early Development of the Gulf of Mexico. *AAPG 2017 Annual Convention and Exhibition*.

- Delvaux, D. (2001). Tectonic and palaeostress evolution of the Tanganyika-Rukwa-Malawi rift segment, East African rift System. *Peri-Tethys Memoir*, 6, 545–567.
- Delvaux, D., & Sperner, B. (2003). New aspects of tectonic stress inversion with reference to the TENSOR program. *Geological Society, London, Special Publications*, 212(1), 75–100. <https://doi.org/10.1144/GSL.SP.2003.212.01.06>
- Destro, N., Szatmari, P., & Ladeira, E. A. (1994). Post-Devonian transpressional reactivation of a Proterozoic ductile shear zone in Ceará, NE Brazil. *Journal of Structural Geology*, 16(1), 35–45. [https://doi.org/10.1016/0191-8141\(94\)90016-7](https://doi.org/10.1016/0191-8141(94)90016-7)
- Dewey, J. F., Hempton, M. R., Kidd, W. S. F., Saroglu, F., & Şengör, A. M. C. (1986). Shortening of continental lithosphere: the neotectonics of Eastern Anatolia — a young collision zone. *Geological Society, London, Special Publications*, 19(1), 1–36. <https://doi.org/10.1144/GSL.SP.1986.019.01.01>
- Diabat, A. A., Atallah, M., & Salih, M. R. (2004). Paleostress analysis of the Cretaceous rocks in the eastern margin of the Dead Sea transform, Jordan. *Journal of African Earth Sciences*, 38(5), 449–460. <https://doi.org/10.1016/j.jafrearsci.2004.04.002>
- Díaz-Azpiroz, M., Brune, S., Leever, K. A., Fernández, C., & Czeck, D. M. (2016). Tectonics of oblique plate boundary systems. *Tectonophysics*, 693, 165–170. <https://doi.org/10.1016/j.tecto.2016.07.028>
- Ding, W., Sun, Z., Dadd, K., Fang, Y., & Li, J. (2018). Structures within the oceanic crust of the central South China Sea basin and their implications for oceanic accretionary processes. *Earth and Planetary Science Letters*, 488, 115–125. <https://doi.org/10.1016/j.epsl.2018.02.011>
- Direen, N. G., Borissova, I., Stagg, H. M. J., Colwell, J. B., & Symonds, P. A. (2007). Nature of the continent–ocean transition zone along the southern Australian continental margin: a comparison of the Naturaliste Plateau, SW Australia, and the central Great Australian Bight sectors. *Geological Society, London, Special Publications*, 282(1), 239–263. <https://doi.org/10.1144/SP282.12>
- Dix, C. H. (1955). Seismic Velocities From Surface Measurements. *Geophysics*, 20(1), 68–86. <https://doi.org/10.1190/1.1438126>
- Dobson, L. M., & Buffler, R. T. (1997). Seismic stratigraphy and geologic history of Jurassic rocks, Northeastern Gulf of Mexico. *AAPG Bulletin*, 81(1), 100–120. <https://doi.org/10.1306/522b42a3-1727-11d7-8645000102c1865d>
- Donnadieu, Y., Pucéat, E., Moiroud, M., Guillocheau, F., & Deconinck, J.-F. (2016). A better-ventilated ocean triggered by Late Cretaceous changes in continental configuration. *Nature Communications*, 7(1), 10316. <https://doi.org/10.1038/ncomms10316>
- Doré, T., & Lundin, E. (2015). RESEARCH FOCUS: Hyperextended continental margins—Knowns and unknowns. *Geology*, 43(1), 95–96. <https://doi.org/10.1130/focus012015.1>
- Du Dresnay, R., Agard, J., Schmitt, M., Lebedeff, V., & Dubar, G. (1997). Carte géologique du Haut-Atlas d'Anoual-Bou Anane (Haut Atlas Oriental) au 1/200.000. *Not. Mem. Serv. Géol*, 46.
- Eagles, G. (2007). New angles on South Atlantic opening. *Geophysical Journal International*, 168(1), 353–361. <https://doi.org/10.1111/j.1365-246X.2006.03206.x>
- Ebinger, C. (2005). Continental break-up: The East African perspective. *Astronomy and*

- Geophysics*, 46(2), 2.16-2.21. <https://doi.org/10.1111/j.1468-4004.2005.46216.x>
- Ebinger, C. J. (1989). Tectonic development of the western branch of the East African rift system. *Geological Society of America Bulletin*, 101(7), 885–903. [https://doi.org/10.1130/0016-7606\(1989\)101<0885:TDOTWB>2.3.CO;2](https://doi.org/10.1130/0016-7606(1989)101<0885:TDOTWB>2.3.CO;2)
- Ebinger, C. J., & Casey, M. (2001). Continental breakup in magmatic provinces: An Ethiopian example. *Geology*, 29(6), 527. [https://doi.org/10.1130/0091-7613\(2001\)029<0527:CBIMPA>2.0.CO;2](https://doi.org/10.1130/0091-7613(2001)029<0527:CBIMPA>2.0.CO;2)
- Eddy, D. R., Van Avendonk, H. J. A., Christeson, G. L., & Norton, I. O. (2018). Structure and origin of the rifted margin of the northern Gulf of Mexico. *Geosphere*, 14(4), 1804–1817. <https://doi.org/10.1130/GES01662.1>
- Eddy, D. R., Van Avendonk, H. J. A., Christeson, G. L., Norton, I. O., Karner, G. D., Johnson, C. A., & Snedden, J. W. (2014). Deep crustal structure of the northeastern Gulf of Mexico: Implications for rift evolution and seafloor spreading. *Journal of Geophysical Research: Solid Earth*, 119(9), 6802–6822. <https://doi.org/10.1002/2014JB011311>
- Edwards, R. A., Whitmarsh, R. B., & Scrutton, R. A. (1997). Synthesis of the crustal structure of the transform continental margin off Ghana, northern Gulf of Guinea. *Geo-Marine Letters*, 17(1), 12–20. <https://doi.org/10.1007/PL00007202>
- Edwards, Rosemary A., Whitmarsh, R. B., & Scrutton, R. A. (1997). The crustal structure across the transform continental margin off Ghana, eastern equatorial Atlantic. *Journal of Geophysical Research: Solid Earth*, 102(B1), 747–772. <https://doi.org/10.1029/96JB02098>
- El-Sawy, E.-S. K., & Masrouhi, A. (2019). Structural style and kinematic evolution of Al Ji'lani area, Ad Dawadimi terrane, Saudi Arabia. *Journal of African Earth Sciences*, 150, 451–465. <https://doi.org/10.1016/j.jafrearsci.2018.08.021>
- El Kochri, A., & Chorowicz, J. (1996). Oblique extension in the Jurassic trough of the central and eastern High Atlas (Morocco). *Canadian Journal of Earth Sciences*, 33(1), 84–92. <https://doi.org/10.1139/E96-009>
- Eldholm, O. (1989). Evolution of the Voring volcanic margin. *Proc. ODP, Sci. Results*, 104, 1033–1065.
- Eldholm, O., Tsikalas, F., & Faleide, J. I. (2002). Continental margin off Norway 62–75°N: Palaeogene tectono-magmatic segmentation and sedimentation. *Geological Society, London, Special Publications*, 197(1), 39–68. <https://doi.org/10.1144/GSL.SP.2002.197.01.03>
- Eldholm, Olav, Faleide, J. I., & Myhre, A. M. (1987). Continent-ocean transition at the western Barents Sea/Svalbard continental margin. *Geology*, 15(12), 1118. [https://doi.org/10.1130/0091-7613\(1987\)15<1118:CTATWB>2.0.CO;2](https://doi.org/10.1130/0091-7613(1987)15<1118:CTATWB>2.0.CO;2)
- Ellero, A., Malusà, M. G., Ottria, G., Ouanaimi, H., & Froitzheim, N. (2020). Transpressional structuring of the High Atlas belt, Morocco. *Journal of Structural Geology*, 135, 104021. <https://doi.org/10.1016/j.jsg.2020.104021>
- Ellero, A., Ottria, G., G., M., & Ouanaimi, H. (2012). Structural Geological Analysis of the High Atlas (Morocco): Evidences of a Transpressional Fold-Thrust Belt. In *Tectonics - Recent Advances*. InTech. <https://doi.org/10.5772/50071>
- Elliott, D. (1976). A Discussion on natural strain and geological structure - The energy balance and deformation mechanisms of thrust sheets. *Philosophical Transactions of the Royal Society of London. Series A, Mathematical and Physical Sciences*, 283(1312), 289–312. <https://doi.org/10.1098/rsta.1976.0086>

- Ellouz, N., Patriat, M., Gaulier, J. M., Bouatmani, R., & Sabounji, S. (2003). From rifting to Alpine inversion: Mesozoic and Cenozoic subsidence history of some Moroccan basins. *Sedimentary Geology*, 156(1–4), 185–212. [https://doi.org/10.1016/S0037-0738\(02\)00288-9](https://doi.org/10.1016/S0037-0738(02)00288-9)
- Erlich, R. N., & Pindell, J. (2020). Crustal origin of the West Florida Terrane, and detrital zircon provenance and development of accommodation during initial rifting of the southeastern Gulf of Mexico and western Bahamas. *Geological Society, London, Special Publications*, 504, SP504-2020–14. <https://doi.org/10.1144/sp504-2020-14>
- Escosa, F. O., Leprêtre, R., Spina, V., Gimeno-Vives, O., Kergaravat, C., Mohn, G., & Frizon de Lamotte, D. (2021). Polyphased mesozoic rifting from the Atlas to the north-west Africa paleomargin. *Earth-Science Reviews*, 220, 103732. <https://doi.org/10.1016/J.EARSCIREV.2021.103732>
- Essaifi, A., & Zayane, R. (2018). Petrogenesis and origin of the Upper Jurassic-Lower Cretaceous magmatism in Central High Atlas (Morocco): Major, trace element and isotopic (Sr-Nd) constraints. *Journal of African Earth Sciences*, 137, 229–245. <https://doi.org/10.1016/J.JAFREARSCI.2017.10.002>
- Etris, E. L., Crabtree, N. J., Dewar, J., & Pickford, S. (2001). True depth conversion: more than a pretty picture. *CSEG Recorder*, 26(9), 11–22.
- Ettaki, M., Ibouh, H., Chellai, E. H., & Milhi, A. (2007). Les structures "diapiriques" liasiques du Haut-Atlas central, Maroc: exemple de la ride d'Ikerzi. *Afr. Geosci. Rev.*, 14, 79–93.
- Evans, I., Kendall, S. C. C. G., & Warme, J. E. (1974). Jurassic Sedimentation in the High Atlas Mountains of Morocco during Early Rifting of Africa and North America. *Geology*, 2(6), 295. [https://doi.org/10.1130/0091-7613\(1974\)2<295:JSITHA>2.0.CO;2](https://doi.org/10.1130/0091-7613(1974)2<295:JSITHA>2.0.CO;2)
- Exxon World Mapping Project. (1985). Tectonic map of the World. *Exxon Production Research Company, Houston, USA*.
- Fadile, A. (2003). Carte géologique du Maroc au 1/100 000, feuille d'Imilchil. *Notes et Mémoires Du Service Géologique Du Maroc*, 397.
- Faleide, J. I., Myhre, A. M., & Eldholm, O. (1988). Early Tertiary volcanism at the western Barents Sea margin. *Geological Society, London, Special Publications*, 39(1), 135–146. <https://doi.org/10.1144/GSL.SP.1988.039.01.13>
- Faleide, Jan Inge, Tsikalas, F., Breivik, A. J., Mjelde, R., Ritzmann, O., Engen, Ø., Wilson, J., & Eldholm, O. (2008). Structure and evolution of the continental margin off Norway and the Barents Sea. *Episodes*, 31(1), 82–91. <https://doi.org/10.18814/epiiugs/2008/v31i1/012>
- Farangitakis, G. P., McCaffrey, K. J. W., Willingshofer, E., Allen, M. B., Kalnins, L. M., van Hunen, J., Persaud, P., & Sokoutis, D. (2020). The structural evolution of pull-apart basins in response to changes in plate motion. *Basin Research*, 33(2), 1603–1625. <https://doi.org/10.1111/BRE.12528>
- Farangitakis, G. P., Sokoutis, D., McCaffrey, K. J. W., Willingshofer, E., Kalnins, L. M., Phethean, J. J. J., Hunen, J., & Steen, V. (2019). Analogue Modeling of Plate Rotation Effects in Transform Margins and Rift-Transform Intersections. *Tectonics*, 38(3), 823–841. <https://doi.org/10.1029/2018TC005261>
- Fedan, B. (1989). Evolution géodynamique d'un bassin intraplaque sur décrochements: le Moyen Atlas (Maroc) durant le Méso-Cénozoïque. *Inst. Scientifique Service Des Publ.*

- Fekkak, A., Ouanaimi, H., Michard, A., Soulaïmani, A., Ettachfini, E. M., Berrada, I., El Arabi, H., Lagnaoui, A., & Saddiqi, O. (2018). Thick-skinned tectonics in a Late Cretaceous-Neogene intracontinental belt (High Atlas Mountains, Morocco): The flat-ramp fault control on basement shortening and cover folding. *Journal of African Earth Sciences*, *140*, 169–188. <https://doi.org/10.1016/j.jafrearsci.2018.01.008>
- Fernandez, O. (2019). The Jurassic evolution of the Africa-Iberia conjugate margin and its implications on the evolution of the Atlantic-Tethys triple junction. *Tectonophysics*, *750*, 379–393. <https://doi.org/10.1016/j.tecto.2018.12.006>
- Filatova, N. I. (2008). Specifics of magmatism in marginal continental and marginal-sea pull-apart basins: Western periphery of the Pacific Ocean. *Petrology*, *16*(5), 448–467.
- Filina, I., Austin, J., Doré, T., Johnson, E., Minguez, D., Norton, I., Snedden, J., & Stern, R. J. (2022). Opening of the Gulf of Mexico: What we know, what questions remain, and how we might answer them. *Tectonophysics*, *822*, 229150. <https://doi.org/10.1016/j.tecto.2021.229150>
- Filina, I., & Beutel, E. (2022). Geological and Geophysical Constraints Guide New Tectonic Reconstruction of the Gulf of Mexico. *Authorea Preprints*. <https://doi.org/10.1002/ESSOAR.10511463.1>
- Filina, I., & Hartford, L. (2021). Subsurface structures along western Yucatan from integrated geophysical analysis. *Marine and Petroleum Geology*, *127*, 104964. <https://doi.org/10.1016/j.marpetgeo.2021.104964>
- Filina, I., Liu, M., & Beutel, E. (2020). Evidence of ridge propagation in the eastern Gulf of Mexico from integrated analysis of potential fields and seismic data. *Tectonophysics*, *775*, 228307. <https://doi.org/10.1016/j.tecto.2019.228307>
- Fletcher, J. M., & Spelz, R. M. (2009). Patterns of Quaternary deformation and rupture propagation associated with an active low-angle normal fault, Laguna Salada, Mexico: Evidence of a rolling hinge? *Geosphere*, *5*(4), 385–407. <https://doi.org/10.1130/GES00206.1>
- Fodor, L. I. (2007). Segment linkage and the state of stress in transtensional transfer zones: field examples from the Pannonian Basin. *Geological Society, London, Special Publications*, *290*(1), 417–431. <https://doi.org/10.1144/SP290.16>
- Fossen, H., Teyssier, C., & Whitney, D. L. (2013). Transtensional folding. *Journal of Structural Geology*, *56*, 89–102. <https://doi.org/10.1016/J.JSG.2013.09.004>
- Franke, D. (2013). Rifting, lithosphere breakup and volcanism: Comparison of magma-poor and volcanic rifted margins. In *Marine and Petroleum Geology* (Vol. 43, pp. 63–87). Elsevier. <https://doi.org/10.1016/j.marpetgeo.2012.11.003>
- Frizon de Lamotte, D., Zizi, M., Missenard, Y., Hafid, M., El Azzouzi, M., Maury, R. C., Charrière, A., Taki, Z., Benammi, M., & Michard, A. (2008). The Atlas system. *Lecture Notes in Earth Sciences*, *116*, 133–202. https://doi.org/10.1007/978-3-540-77076-3_4
- Frizon de Lamotte, Dominique, Bezar, B. Saint, Bracène, R., & Mercier, E. (2000). The two main steps of the atlas building and geodynamics of the Western Mediterranean. *Tectonics*, *19*(4), 740–761. <https://doi.org/10.1029/2000TC900003>
- Frizon de Lamotte, Dominique, Fourdan, B., Leleu, S., Leparmentier, F., & De Clarens, P. (2015). Style of rifting and the stages of Pangea breakup. *Tectonics*, *34*(5), 1009–1029. <https://doi.org/10.1002/2014TC003760>
- Frizon de Lamotte, Dominique, Leturmy, P., Missenard, Y., Khomsi, S., Ruiz, G.,

- Saddiqi, O., Guillocheau, F., & Michard, A. (2009). Mesozoic and Cenozoic vertical movements in the Atlas system (Algeria, Morocco, Tunisia): An overview. *Tectonophysics*, *475*(1), 9–28. <https://doi.org/10.1016/J.TECTO.2008.10.024>
- Frizon de Lamotte, Dominique, Raulin, C., Mouchot, N., Wrobel-Daveau, J.-C., Blanpied, C., & Ringenbach, J.-C. (2011). The southernmost margin of the Tethys realm during the Mesozoic and Cenozoic: Initial geometry and timing of the inversion processes. *Tectonics*, *30*(3), n/a-n/a. <https://doi.org/10.1029/2010TC002691>
- Fu, L., Wei, J., Kusky, T. M., Chen, H., Tan, J., Li, Y., Shi, W., Chen, C., & Zhao, S. (2012). The Cretaceous Duimianguo adakite-like intrusion from the Chifeng region, northern North China Craton: Crustal contamination of basaltic magma in an intracontinental extensional environment. *Lithos*, *134–135*, 273–288. <https://doi.org/10.1016/j.lithos.2012.01.007>
- Gardner, G. H. F., Gardner, L. W., & Gregory, A. R. (1974). Formation Velocity and Density - The Diagnostic Basics for Stratigraphic Traps. *Geophysics*, *39*(6), 770–780. <https://doi.org/10.1190/1.1440465>
- Gasperini, L., Bernoulli, D., Bonatti, E., Borsetti, A., Ligi, M., Negri, A., Sartori, R., & von Salis, K. (2001). Lower Cretaceous to Eocene sedimentary transverse ridge at the Romanche Fracture Zone and the opening of the equatorial Atlantic. *Marine Geology*, *176*(1–4), 101–119. [https://doi.org/10.1016/S0025-3227\(01\)00146-3](https://doi.org/10.1016/S0025-3227(01)00146-3)
- Gastil, R. G., & Krummenacher, D. (1977). Reconnaissance geology of coastal Sonora between Puerto Lobos and Bahia Kino. *Geological Society of America Bulletin*, *88*(2), 189. [https://doi.org/10.1130/0016-7606\(1977\)88<189:RGOC>2.0.CO;2](https://doi.org/10.1130/0016-7606(1977)88<189:RGOC>2.0.CO;2)
- Ghorbal, B., Bertotti, G., & Andriessen, P. (2007). New insights into the tectono-morphic evolution of the Western Meseta (Morocco), NW Africa) based on low-temperature thermochronology, Meeting Europ. *Union Geosci. Geophys. Res. Abstr*, *09820*.
- Gillard, M., Autin, J., & Manatschal, G. (2016). Fault systems at hyper-extended rifted margins and embryonic oceanic crust: Structural style, evolution and relation to magma. *Marine and Petroleum Geology*, *76*, 51–67. <https://doi.org/10.1016/j.marpetgeo.2016.05.013>
- Gillard, M., Autin, J., Manatschal, G., Sauter, D., Munsch, M., & Schaming, M. (2015). Tectonomagmatic evolution of the final stages of rifting along the deep conjugate Australian-Antarctic magma-poor rifted margins: Constraints from seismic observations. *Tectonics*, *34*(4), 753–783. <https://doi.org/10.1002/2015TC003850>
- Gillard, M., Sauter, D., Tugend, J., Tomasi, S., Epin, M. E., & Manatschal, G. (2017). Birth of an oceanic spreading center at a magma-poor rift system. *Scientific Reports* *2017* *7*:1, *7*(1), 1–6. <https://doi.org/10.1038/s41598-017-15522-2>
- Girard, G., & van Wyk de Vries, B. (2005). The Managua Graben and Las Sierras-Masaya volcanic complex (Nicaragua); pull-apart localization by an intrusive complex: results from analogue modeling. *Journal of Volcanology and Geothermal Research*, *144*(1–4), 37–57. <https://doi.org/10.1016/j.jvolgeores.2004.11.016>
- Gouiza, M., Bertotti, G., Hafid, M., & Cloetingh, S. (2010). Kinematic and thermal evolution of the Moroccan rifted continental margin: Doukkala-High Atlas transect. *Tectonics*, *5008*. <https://doi.org/10.1029/2009TC002464>
- Granot, R., & Dymant, J. (2015). The Cretaceous opening of the South Atlantic Ocean. *Earth and Planetary Science Letters*, *414*, 156–163. <https://doi.org/10.1016/j.epsl.2015.01.015>

- Guezal, J., El Baghdadi, M., & Barakat, A. (2014). The Jurassic–Cretaceous volcanism of the Atlas of Beni-Mellal (Central High Atlas, Morocco): evidence from clinopyroxene composition. *Arabian Journal of Geosciences* 2014 8:2, 8(2), 977–986. <https://doi.org/10.1007/S12517-013-1256-Z>
- Guiraud, M., Benkhelil, J., Mascle, J., Basile, C., Mascle, G., Bouillin, J. P., & Cousin, M. (1997). Synrift to syntransform deformation along the Côte d'Ivoire-Ghana transform margin: Evidence from deep-sea dives. *Geo-Marine Letters*, 17(1), 70–78. <https://doi.org/10.1007/s003670050010>
- Haddoumi, H., Charrière, A., & Mojon, P. O. (2010). Stratigraphie et sédimentologie des « Couches rouges » continentales du Jurassique-Crétacé du Haut Atlas central (Maroc) : implications paléogéographiques et géodynamiques. *Geobios*, 43(4), 433–451. <https://doi.org/10.1016/J.GEOBIOS.2010.01.001>
- Hafid, M., Zizi, M., Bally, A. W., & Ait Salem, A. (2006). Structural styles of the western onshore and offshore termination of the High Atlas, Morocco. *Comptes Rendus Geoscience*, 338(1–2), 50–64. <https://doi.org/10.1016/j.crte.2005.10.007>
- Hailwood, E. A., & Mitchell, J. G. (1971). Palaeomagnetic and Radiometric Dating Results from Jurassic Intrusions in South Morocco. *Geophysical Journal International*, 24(4), 351–364. <https://doi.org/10.1111/J.1365-246X.1971.TB02183.X>
- Hall, D. J. (1990). Gulf Coast-East Coast magnetic anomaly 1: root of the main crustal decollement for the Appalachian-Ouachita orogen. *Geology*, 18(9), 862–865. [https://doi.org/10.1130/0091-7613\(1990\)018<0862:GCECMA>2.3.CO;2](https://doi.org/10.1130/0091-7613(1990)018<0862:GCECMA>2.3.CO;2)
- Harding, T. . (1990). Identification of Wrench Faults Using Subsurface Structural Data: Criteria and Pitfalls (1). *AAPG Bulletin*, 74. <https://doi.org/10.1306/0C9B2533-1710-11D7-8645000102C1865D>
- Harding, T. P. (1974). Petroleum Traps Associated with Wrench Faults. *AAPG Bulletin*, 58(7), 1290–1304. <https://doi.org/10.1306/83D91669-16C7-11D7-8645000102C1865D>
- Harding, T. P. ., Vierbuchen, R. C. ., & Christie-Blick, N. (1985). Structural Styles, Plate-Tectonic Settings, And Hydrocarbon Traps of Divergent (Transtensional) Wrench Faults. *The Society of Economic Paleontologists and Mineralogists. SEMP Spec. Pub.*
- Harry, D. L., & Sawyer, D. S. (1992). A dynamic model of extension in the Baltimore Canyon Trough Region. *Tectonics*, 11(2), 420–436. <https://doi.org/10.1029/91TC03012>
- He, B., Xu, Y. G., & Paterson, S. (2009). Magmatic diapirism of the Fangshan pluton, southwest of Beijing, China. *Journal of Structural Geology*, 31(6), 615–626. <https://doi.org/10.1016/J.JSG.2009.04.007>
- He, H., Pan, Y., Tauxe, L., Qin, H., & Zhu, R. (2008). Toward age determination of the M0r (Barremian–Aptian boundary) of the Early Cretaceous. *Physics of the Earth and Planetary Interiors*, 169(1–4), 41–48. <https://doi.org/10.1016/j.pepi.2008.07.014>
- Heatherington, A. L., & Mueller, P. A. (1991). Geochemical evidence for Triassic rifting in southwestern Florida. *Tectonophysics*, 188(3–4), 291–302. [https://doi.org/10.1016/0040-1951\(91\)90460-A](https://doi.org/10.1016/0040-1951(91)90460-A)
- Heatherington, A. L., & Mueller, P. A. (1999). Lithospheric sources of North Florida, USA tholeiites and implications for the origin of the Suwannee terrane. *Lithos*, 46(2), 215–233. [https://doi.org/10.1016/S0024-4937\(98\)00063-2](https://doi.org/10.1016/S0024-4937(98)00063-2)

- Heatherington, A. L., & Mueller, P. A. (2003). Mesozoic igneous activity in the Suwannee terrane, Southeastern USA: Petrogenesis and Gondwanan affinities. *Gondwana Research*, 6(2), 296–311. [https://doi.org/10.1016/S1342-937X\(05\)70979-5](https://doi.org/10.1016/S1342-937X(05)70979-5)
- Heezen, B. C. (1960). The rift in the ocean floor. *Scientific American*, 203(4), 98–114.
- Heezen, B. C., Bunce, E. T., Hersey, J. B., & Tharp, M. (1964). Chain and romanche fracture zones. *Deep Sea Research and Oceanographic Abstracts*, 11(1), 11–33. [https://doi.org/10.1016/0011-7471\(64\)91079-4](https://doi.org/10.1016/0011-7471(64)91079-4)
- Heezen, B. C., Gerard, R. D., & Tharp, M. (1964). The Vema fracture zone in the equatorial Atlantic. *Journal of Geophysical Research*, 69(4), 733–739. <https://doi.org/10.1029/JZ069i004p00733>
- Heezen, B. C., & Tharp, M. (1965). Tectonic fabric of the Atlantic and Indian oceans and continental drift. *Philosophical Transactions of the Royal Society of London. Series A, Mathematical and Physical Sciences*, 258(1088), 90–106. <https://doi.org/10.1098/rsta.1965.0024>
- Heine, C., Zoethout, J., & Müller, R. D. (2013). Kinematics of the South Atlantic rift. *Solid Earth*, 4(2), 215–253. <https://doi.org/10.5194/se-4-215-2013>
- Hoggard, M. J., Winterbourne, J., Czarnota, K., & White, N. (2017). Oceanic residual depth measurements, the plate cooling model, and global dynamic topography. *Journal of Geophysical Research: Solid Earth*, 122(3), 2328–2372. <https://doi.org/10.1002/2016JB013457>
- Holbrook, W. S., & Kelemen, P. B. (1993). Large igneous province on the US Atlantic margin and implications for magmatism during continental breakup. *Nature*, 364, 433–436.
- Holbrook, W. S., Purdy, G. M., Sheridan, R. E., Glover III, L., Talwani, M., Ewing, J., & Hutchinson, D. (1994). Seismic structure of the US Mid-Atlantic continental margin. *Journal of Geophysical Research*, 99(B9), 17871–17891. <https://doi.org/10.1029/94jb00729>
- Holmes, M. A. (1998). Thermal diagenesis of cretaceous sediment recovered at the Cote D'Ivoire-Ghana Transform Margin. *Proceedings of the Ocean Drilling Program: Scientific Results*, 159, 53–70. <https://doi.org/10.2973/odp.proc.sr.159.001.1998>
- Hudec, M. R., Jackson, M. P. A., & Peel, F. J. (2013). Influence of deep Louann structure on the evolution of the northern Gulf of Mexico. *AAPG Bulletin*, 97(10), 1711–1735. <https://doi.org/10.1306/04011312074>
- Hudec, M. R., & Norton, I. O. (2019). Upper Jurassic structure and evolution of the Yucatán and Campeche subbasins, southern Gulf of Mexico. *AAPG Bulletin*, 103(5), 1133–1151. <https://doi.org/10.1306/11151817405>
- Hudec, M. R., Norton, I. O., Jackson, M. P. A., & Peel, F. J. (2013). Jurassic evolution of the Gulf of Mexico salt basin. *AAPG Bulletin*, 97(10), 1683–1710. <https://doi.org/10.1306/04011312073>
- Huguen, C., Guiraud, M., Benkhelil, J., & Mascle, J. (2001). Synlithification deformation processes of the Cretaceous sediments of the Ivory Coast-Ghana transform margin: A way to detail the margin history. *Tectonics*, 20(6), 959–975. <https://doi.org/10.1029/2001TC900015>
- Huon, S. ., Cornee, J. J. ., Pique, A. ., Rais, N. ., Clauer, N. ., Liewig, N. ., & Zayane R. (1993). Mise en évidence au Maroc d'événements thermiques d'âge triasico-liasique liés à l'ouverture de l'Atlantique . *Bulletin de La Société Géologique de*

France, 164(2), 165–176.

- IHS. (2010). *Saltpond Basin Ghana*. IHS Energy Group, in Basin Monitor, IHS Inc.
- Illsley-Kemp, F., Bull, J. M., Keir, D., Gerya, T. V., Pagli, C., Gernon, T., Ayele, A., Goitom, B., Hammond, J., & Kendall, J. M. (2018). Initiation of a Proto-Transform Fault Prior to Seafloor Spreading. *Geochemistry, Geophysics, Geosystems*, 19, 4744–4756. <https://doi.org/10.1029/2018GC007947>
- Imbert, P. (2005). The Mesozoic Opening of the Gulf of Mexico: Part 1, Evidence for Oceanic Accretion During and After Salt Deposition. In *Petroleum Systems of Divergent Continental Margin Basins: 25th Annual* (pp. 1119–1150). SOCIETY OF ECONOMIC PALEONTOLOGISTS AND MINERALOGISTS. <https://doi.org/10.5724/gcs.05.25.1119>
- Imbert, P., & Philippe, Y. (2005). The Mesozoic Opening of the Gulf of Mexico: Part 2, Integrating Seismic and Magnetic Data into a General Opening Model. In *Petroleum Systems of Divergent Continental Margin Basins: 25th Annual* (pp. 1151–1190). Society of Economic Paleontologists and Mineralogists. <https://doi.org/10.5724/gcs.05.25.1151>
- Izquierdo-Llavall, E., Ringenbach, J. C., Sapin, F., Rives, T., & Callot, J. P. (2022). Crustal structure and lateral variations in the Gulf of Mexico conjugate margins: From rifting to break-up. *Marine and Petroleum Geology*, 136, 105484. <https://doi.org/10.1016/J.MARPETGEO.2021.105484>
- Jackson, J., & McKenzie, D. (1983). The geometrical evolution of normal fault systems. *Journal of Structural Geology*, 5(5), 471–482. [https://doi.org/10.1016/0191-8141\(83\)90053-6](https://doi.org/10.1016/0191-8141(83)90053-6)
- Jeannot, L., & Buiter, S. J. H. (2018). A quantitative analysis of transtensional margin width. *Earth and Planetary Science Letters*, 491, 95–108. <https://doi.org/10.1016/j.epsl.2018.03.003>
- Jebsen, C., & Faleide, J. I. (1998). Tertiary rifting and magmatism at the western Barents Sea margin (Vestbakken volcanic province). *III International Conference on Arctic Margins, ICAM III; Abstracts; Plenary Lectures, Talks and Posters*, 92.
- Jenny, J. (1988). Mémoire explicatif de la carte géologique du Maroc au 1/100.000 (feuille d'Azilal, Haut-Atlas central). *Notes et Mem. Serv. Géol. Rabat*, 339. <https://pascal-francis.inist.fr/vibad/index.php?action=getRecordDetail&idt=PASCALGEODEBRGM73224800>
- Jossen, J.-A., Couvreur, G., Benshili, K., Du Dresnay, R., Elmi, S., & Septfontaine, M. (1990). Zawayat Ahancal - Carte Géologique Du Maroc. *Notes et Memoires*, 355.
- Jossen, J.-A., Couvreur, G., Benshili, K., Du Dresnay, R., Taquet, P., Septfontaine, M., & Wernli, R. (1985). Beni Mellal - Carte Géologique Du Maroc, AU 1/100 000. *Notes et Memoires*, 341.
- Jossen, J. A. (1988). Carte géologique de Zawayat Ahancal. 1/100.000. *Notes et Mémoires Du Service Géologique Du Maroc*.
- Judd, A. G., Hovland, M., Dimitrov, L. I., García Gil, S., & Jukes, V. (2002). The geological methane budget at Continental Margins and its influence on climate change. *Geofluids*, 2(2), 109–126. <https://doi.org/10.1046/j.1468-8123.2002.00027.x>
- Kaspereit, D., Mann, M., Sanyal, S. R., Ickard, B., & Hulen, J. (2016). Updated conceptual model and reserve estimate for the Salton Sea geothermal field, Imperial Valley, California. *Geothermal Research Transactions*, 40, 57–66.

- Kazmin, V. (1980). Transform faults in the East African Rift System. Geodynamic evolution of the Afro-Arabic Rift System. *Roma Accademia Nazionale Dei Lincei. Atti Dei Convegna Lincei*, 47, 65–73.
- Kilembe, E. A., & Rosendahl, B. R. (1992). Structure and stratigraphy of the Rukwa rift. *Tectonophysics*, 209(1–4), 143–158. [https://doi.org/10.1016/0040-1951\(92\)90016-Y](https://doi.org/10.1016/0040-1951(92)90016-Y)
- Klimetz, M. P. (1983). Speculations on the Mesozoic Plate tectonic evolution of eastern China. *Tectonics*, 2(2), 139–166. <https://doi.org/10.1029/TC002i002p00139>
- Klitgord, K. D., Popenoe, P., & Schouten, H. (1984). Florida: A Jurassic transform plate boundary. *Journal of Geophysical Research: Solid Earth*, 89(B9), 7753–7772. <https://doi.org/10.1029/JB089iB09p07753>
- Klitgord, K. D., & Schouten, H. (1986). Plate kinematics of the central Atlantic. *The Western North Atlantic Region*, 351–378. <https://doi.org/10.1130/DNAG-GNA-M.351>
- Kneller, E. A., & Johnson, C. A. (2011). Plate Kinematics of the Gulf of Mexico Based on Integrated Observations from the Central and South Atlantic. *Gulf Coast Association of Geological Societies Transactions*, 61, 283–299.
- Kristensen, T. B., Rotevatn, A., Marvik, M., Henstra, G. A., Gawthorpe, R. L., & Ravnås, R. (2018). Structural evolution of sheared margin basins: the role of strain partitioning. Sørvestsnaget Basin, Norwegian Barents Sea. *Basin Research*, 30(2), 279–301. <https://doi.org/10.1111/BRE.12253>
- Kroner, U., & Romer, R. L. (2013). Two plates - Many subduction zones: The Variscan orogeny reconsidered. In *Gondwana Research* (Vol. 24, Issue 1, pp. 298–329). Elsevier. <https://doi.org/10.1016/j.gr.2013.03.001>
- Kusznir, N. J., Roberts, A. M., & Alvey, A. D. (2020). Crustal structure of the conjugate Equatorial Atlantic Margins, derived by gravity anomaly inversion. *Geological Society, London, Special Publications*, 476(1), 83–107. <https://doi.org/10.1144/SP476.5>
- Labails, C., Olivet, J.-L., Aslanian, D., & Roest, W. R. (2010). An alternative early opening scenario for the Central Atlantic Ocean. *Earth and Planetary Science Letters*, 297(3–4), 355–368. <https://doi.org/10.1016/j.epsl.2010.06.024>
- Lachkar, N., Guiraud, M., Harfi, A. El, Dommergues, J.-L., Dera, G., & Durllet, C. (2009). Early Jurassic normal faulting in a carbonate extensional basin: characterization of tectonically driven platform drowning (High Atlas rift, Morocco). *Journal of the Geological Society*, 166(3), 413–430. <https://doi.org/10.1144/0016-76492008-084>
- Land, L. S., Kupecz, J. A., & Mack, L. E. (1988). Louann salt geochemistry (Gulf of Mexico sedimentary basin, U.S.A.): A preliminary synthesis. *Chemical Geology*, 74(1–2), 25–35. [https://doi.org/10.1016/0009-2541\(88\)90144-1](https://doi.org/10.1016/0009-2541(88)90144-1)
- LASE Study Group. (1986). Deep structure of the US East Coast passive margin from large aperture seismic experiments (LASE). *Marine and Petroleum Geology*, 3(3), 234–242. [https://doi.org/10.1016/0264-8172\(86\)90047-4](https://doi.org/10.1016/0264-8172(86)90047-4)
- Laville, E., & Harmand, C. (1982). Évolution magmatique et tectonique du bassin intracontinental mésozoïque du Haut Atlas (Maroc): un modèle de mise en place synsédimentaire de massifs “anorogéniques” liés à des décrochements. *Bulletin de La Société Géologique de France*, S7-XXIV(2), 213–227. <https://doi.org/10.2113/GSSGFBULL.S7-XXIV.2.213>
- Laville, E., Zayane, E., Honnorez, J., & Piqué, A. (1994). Le métamorphisme jurassique

du Haut Atlas central (Maroc); épisodes synschisteux et hydrothermaux. *Comptes Rendus de l'Académie Des Sciences. Série 2. Sciences de La Terre et Des Planètes*, 318(10), 1349–1356.

- Laville, E. (1985). *Evolution sédimentaire, tectonique et magmatique du bassin jurassique du Haut Atlas(Maroc): modèle en relais multiples de décrochements (Doctoral dissertation)*.
- Laville, E., & Piqué, A. (1991). La Distension crustale atlantique et atlasique au Maroc au debut du Mesozoique; le rejeu des structures hercyniennes. *Bulletin de La Société Géologique de France*, 162(6), 1161–1171.
- Laville, Edgard. (1988). A multiple releasing and restraining stepover model for the Jurassic strike-slip basin of the Central High Atlas (Morocco). *Developments in Geotectonics*, 22(C), 499–523. <https://doi.org/10.1016/B978-0-444-42903-2.50026-9>
- Laville, Edgard, & Petit, J.-P. (1984). Role of synsedimentary strike-slip faults in the formation of Moroccan Triassic basins. *Geology*, 12(7), 424. [https://doi.org/10.1130/0091-7613\(1984\)12<424:ROSSFI>2.0.CO;2](https://doi.org/10.1130/0091-7613(1984)12<424:ROSSFI>2.0.CO;2)
- Laville, Edgard, & Piqué, A. (1992). Jurassic penetrative deformation and Cenozoic uplift in the Central High Atlas (Morocco): A tectonic model. structural and orogenic inversions. *Geologische Rundschau*, 81(1), 157–170. <https://doi.org/10.1007/BF01764546>
- Laville, Edgard, Pique, A., Amrhar, M., & Charroud, M. (2004). A restatement of the Mesozoic Atlasic Rifting (Morocco). *Journal of African Earth Sciences*, 38(2), 145–153. <https://doi.org/10.1016/j.jafrearsci.2003.12.003>
- Le Pichon, X., & Fox, P. J. (1971). Marginal offsets, fracture zones, and the early opening of the North Atlantic. *Journal of Geophysical Research*, 76(26), 6294–6308. <https://doi.org/10.1029/JB076i026p06294>
- Leprêtre, R., Missenard, Y., Barbarand, J., Gautheron, C., Jovie, I., & Saddiqi, O. (2018). Polyphased Inversions of an Intracontinental Rift: Case Study of the Marrakech High Atlas, Morocco. *Tectonics*, 37(3), 818–841. <https://doi.org/10.1002/2017TC004693>
- Leprêtre, Rémi, Missenard, Y., Saint-Bezar, B., Barbarand, J., Delpéch, G., Yans, J., Dekoninck, A., & Saddiqi, O. (2015). The three main steps of the Marrakech High Atlas building in Morocco: Structural evidences from the southern foreland, Imini area. *Journal of African Earth Sciences*, 109, 177–194. <https://doi.org/10.1016/j.jafrearsci.2015.05.013>
- Lewis, C. J., & Stock, J. M. (1998). Paleomagnetic evidence of localized vertical axis rotation during Neogene extension, Sierra San Fermín, northeastern Baja California, Mexico. *Journal of Geophysical Research: Solid Earth*, 103(B2), 2455–2470. <https://doi.org/10.1029/97JB02673>
- Libak, A., Mjelde, R., Keers, H., Faleide, J. I., & Murai, Y. (2012). An integrated geophysical study of Vestbakken Volcanic Province, western Barents Sea continental margin, and adjacent oceanic crust. *Marine Geophysical Research*, 33(2), 185–207. <https://doi.org/10.1007/s11001-012-9155-3>
- Lin, P., Bird, D. E., & Mann, P. (2019). Crustal structure of an extinct, late Jurassic-to-earliest Cretaceous spreading center and its adjacent oceanic crust in the eastern Gulf of Mexico. *Marine Geophysical Research*, 40(3), 395–418. <https://doi.org/10.1007/s11001-019-09379-5>
- Lister, G. S., Etheridge, M. A., & Symonds, P. A. (1991). Detachment models for the

- formation of passive continental margins. *Tectonics*, 10(5), 1038–1064. <https://doi.org/10.1029/90TC01007>
- Liu, M., Filina, I., & Mann, P. (2019). Crustal structure of Mesozoic rifting in the northeastern Gulf of Mexico from integration of seismic and potential fields data. *Interpretation*, 7(4), T857–T867. <https://doi.org/10.1190/INT-2018-0259.1>
- Lizarralde, D., Axen, G. J., Brown, H. E., Fletcher, J. M., González-Fernández, A., Harding, A. J., Holbrook, W. S., Kent, G. M., Paramo, P., Sutherland, F., & Umhoefer, P. J. (2007). Variation in styles of rifting in the Gulf of California. *Nature*, 448(7152), 466–469. <https://doi.org/10.1038/nature06035>
- Loncke, L., Roest, W. R., Klingelhoefer, F., Basile, C., Graindorge, D., Heuret, A., Marcaillou, B., Museur, T., Fanget, A. S., & Mercier de Lépinay, M. (2020). Transform Marginal Plateaus. *Earth-Science Reviews*, 203(102940), 102940. <https://doi.org/10.1016/j.earscirev.2019.102940>
- Lorenzo, J. M. (1997). Sheared continent–ocean margins: an overview. *Geo-Marine Letters*, 17(1), 1–3. <https://doi.org/10.1007/PL00007201>
- Lorenzo, Juan M., Mutter, J. C., & Larson, R. L. (1991). Development of the continent–ocean transform boundary of the southern Exmouth Plateau. *Geology*, 19(8), 843–846. [https://doi.org/10.1130/0091-7613\(1991\)019<0843:DOTCOT>2.3.CO;2](https://doi.org/10.1130/0091-7613(1991)019<0843:DOTCOT>2.3.CO;2)
- Lundin, E. R., & Doré, A. G. (2017). The Gulf of Mexico and Canada Basin: Genetic siblings on either side of North America. *GSA Today*, 27(1), 4–11. <https://doi.org/10.1130/GSATG274A.1>
- Lundin, E. R., Doré, A. G., Naliboff, J., & Van Wijk, J. (2022). Utilization of continental transforms in break-up: observations, models, and a potential link to magmatism. *Geological Society, London, Special Publications*, 524(1), 121–145. <https://doi.org/10.1144/SP524-2021-119>
- MacGregor, D. S., Robinson, J., & Spear, G. (2003). Play fairways of the Gulf of Guinea transform margin. *Geological Society, London, Special Publications*, 207(1), 131–150. <https://doi.org/10.1144/GSL.SP.2003.207.7>
- MacRae, G., & Watkins, J. (1996). Desoto Canyon Salt Basin: Tectonic evolution and salts structural styles. *Gulf Coast Association of Geological Societies Transactions*, v. 46, 53–61.
- Maia de Almeida, N., Alves, T. M., Filho, F. N., Freire, G. S. S., de Souza, A. C. B., Leopoldino Oliveira, K. M., Normando, M. N., & Barbosa, T. H. S. (2020). A three-dimensional (3D) structural model for an oil-producing basin of the Brazilian equatorial margin. *Marine and Petroleum Geology*, 122, 104599. <https://doi.org/10.1016/j.marpetgeo.2020.104599>
- Maia de Almeida, N., Alves, T. M., Filho, F. N., Freire, G. S. S., de Souza, A. C. B., Normando, M. N., Oliveira, K. M. L., & da Silva Barbosa, T. H. (2020). Tectono-sedimentary evolution and petroleum systems of the Mundaú subbasin: A new deep-water exploration frontier in equatorial Brazil. *AAPG Bulletin*, 104(4), 795–824. <https://doi.org/10.1306/07151917381>
- Malinverno, A., Hildebrandt, J., Tominaga, M., & Channell, J. E. T. (2012). M-sequence geomagnetic polarity time scale (MHTC12) that steadies global spreading rates and incorporates astrochronology constraints. *Journal of Geophysical Research: Solid Earth*, 117(B6). <https://doi.org/10.1029/2012JB009260>
- Mann, P., Hempton, M. R., Bradley, D. C., & Burke, K. (1983). Development of pull-apart basins. *The Journal of Geology*, 91(5), 529–554.
- Mann, Paul. (2007). Global catalogue, classification and tectonic origins of restraining-

- and releasing bends on active and ancient strike-slip fault systems. *Geological Society Special Publication*, 290(1), 13–142. <https://doi.org/10.1144/SP290.2>
- Mao, J., Liu, P., Goldfarb, R. J., Goryachev, N. A., Pirajno, F., Zheng, W., Zhou, M., Zhao, C., Xie, G., Yuan, S., & Liu, M. (2021). Cretaceous large-scale metal accumulation triggered by post-subductional large-scale extension, East Asia. *Ore Geology Reviews*, 136, 104270. <https://doi.org/10.1016/j.oregeorev.2021.104270>
- Marks, K. M., & Tikku, A. A. (2001). Cretaceous reconstructions of East Antarctica, Africa and Madagascar. *Earth and Planetary Science Letters*, 186(3–4), 479–495. [https://doi.org/10.1016/S0012-821X\(01\)00262-X](https://doi.org/10.1016/S0012-821X(01)00262-X)
- Markwick, P. J., Paton, D. A., & Mortimer, E. J. (2022). Mapping the complexity of transform margins. *Geological Society, London, Special Publications*, 524(1), 245–277. <https://doi.org/10.1144/SP524-2021-82>
- Martín-Barajas, A., Stock, J. M., Layer, P., Hausback, B., Renne, P., & López-Martínez, M. (1995). Arc-rift transition volcanism in the Puertecitos Volcanic Province, northeastern Baja California, Mexico. *Geological Society of America Bulletin*, 107(4), 407–0424. [https://doi.org/10.1130/0016-7606\(1995\)107<0407:ARTVIT>2.3.CO;2](https://doi.org/10.1130/0016-7606(1995)107<0407:ARTVIT>2.3.CO;2)
- Martín-Martín, J. D., Vergés, J., Saura, E., Moragas, M., Messenger, G., Baqués, V., Razin, P., Grélaud, C., Malaval, M., Joussiaume, R., Casciello, E., Cruz-Orosa, I., & Hunt, D. W. (2017). Diapiric growth within an Early Jurassic rift basin: The Tazoult salt wall (central High Atlas, Morocco). *Tectonics*, 36(1), 2–32. <https://doi.org/10.1002/2016TC004300>
- Martín-Barajas, A., González-Escobar, M., Fletcher, J. M., Pacheco, M., Oskin, M., & Dorsey, R. (2013). Thick deltaic sedimentation and detachment faulting delay the onset of continental rapture in the Northern Gulf of California: Analysis of seismic reflection profiles. *Tectonics*, 32(5), 1294–1311. <https://doi.org/10.1002/tect.20063>
- Marton, G., & Buffler, R. T. (1994). Jurassic Reconstruction of the Gulf of Mexico Basin. *International Geology Review*, 36(6), 545–586. <https://doi.org/10.1080/00206819409465475>
- Marton, G.L., & Buffler, R. . (2016). Jurassic-Cretaceous Tectonic Evolution of the Southeastern Gulf of Mexico, Constrains on the Style and Timing of Gulf of Mexico Rift-Drift Development. *AAPG Research and Discovery Article #41945*. <https://doi.org/10.1111/bre.12059>
- Marton, Gyorgy L., & Buffler, R. T. (1999). Chapter 3 Jurassic—early cretaceous tectono-paleogeographic evolution of the southeastern gulf of Mexico basin. In *Sedimentary Basins of the World* (Vol. 4, Issue C, pp. 63–91). Elsevier. [https://doi.org/10.1016/S1874-5997\(99\)80037-9](https://doi.org/10.1016/S1874-5997(99)80037-9)
- Marzoli, A., Bertrand, H., Youbi, N., Callegaro, S., Merle, R., Reisberg, L., Chiaradia, M., Brownlee, S. I., Jourdan, F., Zanetti, A., Davies, J. H. F. L., Cuppone, T., Mahmoudi, A., Medina, F., Renne, P. R., Bellieni, G., Crivellari, S., El Hachimi, H., Bensalah, M. K., ... Tegner, C. (2019). The Central Atlantic Magmatic Province (CAMP) in Morocco. *Journal of Petrology*, 60(5), 945–996. <https://doi.org/10.1093/PETROLOGY/EGZ021>
- Marzoli, A., Renne, P. R., Piccirillo, E. M., Ernesto, M., Bellieni, G., & Min, A. De. (1999). Extensive 200-Million-Year-Old Continental Flood Basalts of the Central Atlantic Magmatic Province. *Science*, 284(5414), 616–618. <https://doi.org/10.1126/science.284.5414.616>
- Masclé, J., Lohmann, G. P. ., & Clift, P. D. (1996). PRINCIPAL RESULTS ODP Leg 159, Ghana Margin . *Proceedings of the Ocean Drilling Program Initial Reports*,

159, 297–314.

https://www.academia.edu/2600859/PRINCIPAL_RESULTS_ODP_Leg_159_Ghana_Margin

- Mascle, J. (1976). Atlantic-type continental margins – distinction of two basic structural types. *Anais Da Academia Brasileira de Ciencias*, 48, 191–197.
- Mascle, Jean, & Blarez, E. (1987). Evidence for transform margin evolution from the Ivory Coast–Ghana continental margin. *Nature*, 326(6111), 378–381. <https://doi.org/10.1038/326378a0>
- Mascle, Jean, Blarez, E., & Marinho, M. (1988). The shallow structures of the Guinea and Ivory Coast-Ghana transform margins: Their bearing on the Equatorial Atlantic Mesozoic evolution. *Tectonophysics*, 155(1–4), 193–209. [https://doi.org/10.1016/0040-1951\(88\)90266-1](https://doi.org/10.1016/0040-1951(88)90266-1)
- Mattauer, M., Tapponnier, P., & Proust, F. (1977). Sur les mecanismes de formation des chaines intracontinentales; l'exemple des chaines atlasiques du Maroc. *Bulletin de La Société Géologique de France*, S7-XIX(3), 521–526. <https://doi.org/10.2113/gssgfbull.s7-xix.3.521>
- Matthews, K. J., Müller, R. D., Wessel, P., & Whittaker, J. M. (2011). The tectonic fabric of the ocean basins. *Journal of Geophysical Research*, 116(B12), 1–28. <https://doi.org/10.1029/2011JB008413>
- McBride, J. H. (1991). Constraints on the structure and tectonic development of the Early Mesozoic South Georgia Rift, southeastern United States; Seismic reflection data processing and interpretation. *Tectonics*, 10(5), 1065–1083. <https://doi.org/10.1029/90TC02682>
- McClay, K., & Massimo, B. (2001). Analog models of restraining stepovers in strike-slip fault systems. *AAPG Bulletin*, 85(2), 233–260.
- McDermott, C., Collier, J. S., Lonergan, L., Fruehn, J., & Bellingham, P. (2019). Seismic velocity structure of seaward-dipping reflectors on the South American continental margin. *Earth and Planetary Science Letters*, 521, 14–24. <https://doi.org/10.1016/j.epsl.2019.05.049>
- McDermott, C., Lonergan, L., Collier, J. S., McDermott, K. G., & Bellingham, P. (2018). Characterization of Seaward-Dipping Reflectors Along the South American Atlantic Margin and Implications for Continental Breakup. *Tectonics*, 37(9), 3303–3327. <https://doi.org/10.1029/2017TC004923>
- McKenzie, D. (1978). Some remarks on the development of sedimentary basins. *Earth and Planetary Science Letters*, 40(1), 25–32. [https://doi.org/10.1016/0012-821X\(78\)90071-7](https://doi.org/10.1016/0012-821X(78)90071-7)
- Meert, J. G., & Lieberman, B. S. (2008). The Neoproterozoic assembly of Gondwana and its relationship to the Ediacaran–Cambrian radiation. *Gondwana Research*, 14(1–2), 5–21. <https://doi.org/10.1016/j.gr.2007.06.007>
- Menzies, M. A., Klemperer, S. L., Ebinger, C. J., & Baker, J. (2002). Characteristics of volcanic rifted margins. *Geological Society of America Special Paper Boulder, Colorado*, 1–14.
- Mercier de Lépinay, M., Loncke, L., Basile, C., Roest, W. R., Patriat, M., Maillard, A., & De Clarens, P. (2016). Transform continental margins – Part 2: A worldwide review. *Tectonophysics*, 693(Part A), 96–115. <https://doi.org/10.1016/j.tecto.2016.05.038>
- Meyer, B., Saltus, R., & Chulliat, A. (2017). EMAG2: Earth Magnetic Anomaly Grid (2-arc-minute resolution) Version 3. National Centers for Environmental Information,

NOAA. Model. *National Centers for Environmental Information*, NOAA, 5194.
<https://doi.org/10.7289/V5H70CVX>

- Michard, A., Soulaïmani, A., Hoepffner, C., Ouanaimi, H., Baidder, L., Rjimati, E. C., & Saddiqi, O. (2010). The South-Western Branch of the Variscan Belt: Evidence from Morocco. *Tectonophysics*, 492(1–4), 1–24.
<https://doi.org/10.1016/J.TECTO.2010.05.021>
- Michard, André, Saddiqi, O., Chalouan, A., & Frizon de Lamotte, D. (2008). *Continental Evolution: The Geology of Morocco* (André Michard, O. Saddiqi, A. Chalouan, & D. F. de Lamotte (eds.); Vol. 116). Springer Berlin Heidelberg.
<https://doi.org/10.1007/978-3-540-77076-3>
- Mickus, K., Stern, R. J., Keller, G. R., & Anthony, E. Y. (2009). Potential field evidence for a volcanic rifted margin along the Texas Gulf Coast. *Geology*, 37(5), 387–390.
<https://doi.org/10.1130/G25465A.1>
- Milhi, A. (1997). Carte géologique du Maroc au 1/100.000. Feuille de Tinerhir (Haut-Atlas central). *Notes et Mem. Serv. Géol. Rabat*. 337.
- Milhi, A., Ettaki, M., Chellai, E. H., & Hadri, M. (2002). The lithostratigraphic formations of moroccan jurassic central High-Atlas: Interrelationships and paleogeographic reconstitution. *Revue de Paleobiologie*, 21, 241–256.
- Minguez, D., Gerald Hensel, E., & Johnson, E. A. E. (2020). A fresh look at Gulf of Mexico Tectonics: Testing rotations and breakup mechanisms from the perspective of seismically constrained potential fields modelling and plate kinematics. *Interpretation*, 8(4), SS31–SS45. <https://doi.org/10.1190/int-2019-0256.1>
- Minshull, T. A. (2002). The break-up of continents and the formation of new ocean basins. *Philosophical Transactions of the Royal Society of London. Series A: Mathematical, Physical and Engineering Sciences*, 360(1801), 2839–2852.
<https://doi.org/10.1098/rsta.2002.1059>
- Minshull, T. A., Muller, M. R., Robinson, C. J., White, R. S., & Bickle, M. J. (1998). Is the oceanic Moho a serpentinization front? *Geological Society, London, Special Publications*, 148(1), 71–80.
- Mizusaki, A. M. P., & Saracchini, F. E. (1991). *Catálogo geral de dados geocronológicos da Petrobras. Internal Report*. 4.
- Mizusaki, A. M. P., Thomaz-Filho, A., Milani, E. J., & de Césero, P. (2002). Mesozoic and Cenozoic igneous activity and its tectonic control in northeastern Brazil. *Journal of South American Earth Sciences*, 15(2), 183–198.
[https://doi.org/10.1016/S0895-9811\(02\)00014-7](https://doi.org/10.1016/S0895-9811(02)00014-7)
- Mjelde, R., Raum, T., Breivik, A., Shimamura, H., Murai, Y., Takanami, T., & Faleide, J. I. (2005). Crustal structure of the Vøring Margin, NE Atlantic: a review of geological implications based on recent OBS data. *Geological Society, London, Petroleum Geology Conference Series*, 6(1), 803–813.
<https://doi.org/10.1144/0060803>
- Mjelde, R., Raum, T., Myhren, B., Shimamura, H., Murai, Y., Takanami, T., Karpuz, R., & Næss, U. (2005). Continent-ocean transition on the Vøring Plateau, NE Atlantic, derived from densely sampled ocean bottom seismometer data. *Journal of Geophysical Research: Solid Earth*, 110(B5), 1–19.
<https://doi.org/10.1029/2004JB003026>
- Mjelde, R., Sellevoll, M. A., Shimamura, H., Iwasaki, T., & Kanazawa, T. (1993). Crustal Structure Beneath Lofoten, N. Norway, From Vertical Incidence and Wide-

Angle Seismic Data. *Geophysical Journal International*, 114(1), 116–126.
<https://doi.org/10.1111/j.1365-246X.1993.tb01471.x>

- Mjelde, R., Shimamura, H., Kanazawa, T., Kodaira, S., Raum, T., & Shiobara, H. (2003). Crustal lineaments, distribution of lower crustal intrusives and structural evolution of the Vøring Margin, NE Atlantic; new insight from wide-angle seismic models. *Tectonophysics*, 369(3–4), 199–218. [https://doi.org/10.1016/S0040-1951\(03\)00199-9](https://doi.org/10.1016/S0040-1951(03)00199-9)
- Monbaron, M. (1985). Carte géologique du Maroc: feuille de Béni-Mellal à 1/100.000. *Notes et Mémoires Du Service Géologique Du Maroc, Rabat*, 341.
- Montenegro, C. G. L., Gomes, M. P., de Castro, D. L., Perez, Y. A., & Oliveira, D. C. (2021). The Barreirinhas Basin internal architecture and the evidence of transform movements along the Romanche Fracture Zone, Brazilian Equatorial Margin. *Journal of South American Earth Sciences*, 107, 103049. <https://doi.org/10.1016/j.jsames.2020.103049>
- Moragas, M., Vergés, J., Saura, E., Martín-Martín, J.-D., Messenger, G., Merino-Tomé, O., Suárez-Ruiz, I., Razin, P., Grélaud, C., Malaval, M., Jousiaume, R., & Hunt, D. W. (2018). Jurassic rifting to post-rift subsidence analysis in the Central High Atlas and its relation to salt diapirism. *Basin Research*, 30, 336–362. <https://doi.org/10.1111/BRE.12223>
- Morais Neto, J. M., Pessoa Neto, O. C., Lana, C. C., & Zalán, P. V. (2003). Bacias sedimentares brasileiras: bacia do Ceará. *Phoenix*, 57, 1–6.
- Moratti, G., Benvenuti, M., Santo, A. P., Laurenzi, M. A., Braschi, E., & Tommasini, S. (2018). New ⁴⁰Ar–³⁹Ar dating of Lower Cretaceous basalts at the southern front of the Central High Atlas, Morocco: insights on late Mesozoic tectonics, sedimentation and magmatism. *International Journal of Earth Sciences*, 107(7), 2491–2515. <https://doi.org/10.1007/S00531-018-1609-7>
- Moulin, M., Aslanian, D., & Unternehr, P. (2010). A new starting point for the South and Equatorial Atlantic Ocean. *Earth-Science Reviews*, 98(1–2), 1–37. <https://doi.org/10.1016/j.earscirev.2009.08.001>
- Müller, R. D., Sdrolias, M., Gaina, C., & Roest, W. R. (2008). Age, spreading rates, and spreading asymmetry of the world's ocean crust. *Geochemistry, Geophysics, Geosystems*, 9(4). <https://doi.org/10.1029/2007GC001743>
- Müller, R. D., Zahirovic, S., Williams, S. E., Cannon, J., Seton, M., Bower, D. J., Tetley, M. G., Heine, C., Le Breton, E., Liu, S., Russell, S. H. J., Yang, T., Leonard, J., & Gurnis, M. (2019). A Global Plate Model Including Lithospheric Deformation Along Major Rifts and Orogens Since the Triassic. *Tectonics*, 38(6), 1884–1907. <https://doi.org/10.1029/2018TC005462>
- Mutter, J. C., Buck, W. R., & Zehnder, C. M. (1988). Convective partial melting: 1. A model for the formation of thick basaltic sequences during the initiation of spreading. *Journal of Geophysical Research: Solid Earth*, 93(B2), 1031–1048. <https://doi.org/10.1029/JB093iB02p01031>
- Mutter, J. C., & Larson, R. L. (1989). Extension of the Exmouth Plateau, offshore northwestern Australia: Deep seismic reflection/refraction evidence for simple and pure shear mechanisms. *Geology*, 17(1), 15–18. [https://doi.org/10.1130/0091-7613\(1989\)017<0015:EOTEPO>2.3.CO;2](https://doi.org/10.1130/0091-7613(1989)017<0015:EOTEPO>2.3.CO;2)
- Muttoni, G., Kent, D. V., Garzanti, E., Brack, P., Abrahamsen, N., & Gaetani, M. (2003). Early Permian Pangea “B” to Late Permian Pangea “A.” *Earth and Planetary Science Letters*, 215(3–4), 379–394. [https://doi.org/10.1016/S0012-821X\(03\)00452-7](https://doi.org/10.1016/S0012-821X(03)00452-7)

- Naliboff, J. B., Buitter, S. J. H., Péron-Pinvidic, G., Osmundsen, P. T., & Tetreault, J. (2017). Complex fault interaction controls continental rifting. *Nature Communications*, 8(1), 1–9. <https://doi.org/10.1038/s41467-017-00904-x>
- Nemčok, M., Doran, H., Doré, A. G., Ledvényiová, L., Rybár, S., Staniaszek, S., & Gontar, T. (2023). Tectonic development, thermal regimes and hydrocarbon habitat of transform margins, and their differences from rifted margins – an introduction. *Geological Society, London, Special Publications*, 524(1), 1–38. <https://doi.org/10.1144/SP524-2022-242>
- Nemčok, M., Henk, A., Allen, R., Sikora, P. J., & Stuart, C. (2013). Continental break-up along strike-slip fault zones; observations from the Equatorial Atlantic. *Geological Society, London, Special Publications*, 369(1), 537–556. <https://doi.org/10.1144/SP369.8>
- Nemčok, M., Henk, A., & Molčan, M. (2016). The role of pre-break-up heat flow on the thermal history of a transform margin. *Geological Society, London, Special Publications*, 431(1), 249–271. <https://doi.org/10.1144/SP431.4>
- Nemčok, M., Rybár, S., Sinha, S. T., Hermeston, S. A., & Ledvényiová, L. (2016). Transform margins: development, controls and petroleum systems – an introduction. *Geological Society, London, Special Publications*, 431(1), 1–38. <https://doi.org/10.1144/SP431.15>
- Nemčok, M., Sinha, S. T., Stuart, C. J., Welker, C., Choudhuri, M., Sharma, S. P., Misra, A. A., Sinha, N., & Venkatraman, S. (2013). East Indian margin evolution and crustal architecture: Integration of deep reflection seismic interpretation and gravity modelling. *Geological Society Special Publication*, 369(1), 477–496. <https://doi.org/10.1144/SP369.6>
- Nemčok, Michal, Ledvényiová, L., Henk, A., Rybár, S., Sinha, S. T., Pospíšil, L., Mikuška, J., Jánošík, M., Csibri, T., Staniaszek, S., Baranowski, A., & Gontar, T. (2022). Early post-breakup kinematic adjustments of continental–oceanic transform fault zones: Cape Range, Coromandal and Romanche transform margin case study. *Geological Society, London, Special Publications*, 524, SP524-2021–2110. <https://doi.org/10.1144/SP524-2021-110>
- Ngako, V., Affaton, P., Nnange, J. M., & Njanko, T. (2003). Pan-African tectonic evolution in central and southern Cameroon: transpression and transtension during sinistral shear movements. *Journal of African Earth Sciences*, 36(3), 207–214. [https://doi.org/10.1016/S0899-5362\(03\)00023-X](https://doi.org/10.1016/S0899-5362(03)00023-X)
- Nguyen, L. C., & Mann, P. (2016). Gravity and magnetic constraints on the Jurassic opening of the oceanic Gulf of Mexico and the location and tectonic history of the Western Main transform fault along the eastern continental margin of Mexico. *Interpretation*, 4(1), SC23–SC33. <https://doi.org/10.1190/INT-2015-0110.1>
- Nirrengarten, M., Mohn, G., Kuszniir, N. J., Sapin, F., Despinois, F., Pubellier, M., Chang, S. P., Larsen, H. C., & Ringenbach, J. C. (2020). Extension modes and breakup processes of the southeast China-Northwest Palawan conjugate rifted margins. *Marine and Petroleum Geology*, 113, 104123. <https://doi.org/10.1016/j.marpetgeo.2019.104123>
- Noda, A. (2013). Strike-Slip Basin – Its Configuration and Sedimentary Facies. In *Mechanism of Sedimentary Basin Formation - Multidisciplinary Approach on Active Plate Margins* (pp. 27–57). InTech. <https://doi.org/10.5772/56593>
- Norcliffe, J. R., Paton, D. A., Mortimer, E. J., McCaig, A. M., Nicholls, H., Rodriguez, K., Hodgson, N., & Van Der Spuy, D. (2018). Laterally Confined Volcanic Successions (LCVS); recording rift-jumps during the formation of magma-rich margins. *Earth and Planetary Science Letters*, 504, 53–63.

<https://doi.org/10.1016/j.epsl.2018.09.033>

- Nürnberg, D., & Müller, R. D. (1991). The tectonic evolution of the South Atlantic from Late Jurassic to present. *Tectonophysics*, 191(1–2), 27–53. [https://doi.org/10.1016/0040-1951\(91\)90231-G](https://doi.org/10.1016/0040-1951(91)90231-G)
- Olesen, O., Lundin, E., Nordgulen, Ø., Osmundsen, P. T., Skilbrei, J. R., Smethurst, M. A., Solli, A., Bugge, T., & Fichler, C. (2002). Bridging the gap between the onshore and offshore geology in Nordland, northern Norway. *Norwegian Journal of Geology/Norsk Geologisk Forening*, 82(4).
- Oskin, M. (2002). *Part I. Tectonic evolution of the northern Gulf of California, Mexico, deduced from conjugate rifted margins of the Upper Delfin Basin. Part II. Active folding and seismic hazard in central Los Angeles, California.*
- Paton, D.A., Pindell, J., McDermott, K., Bellingham, P., & Horn, B. (2017). Evolution of seaward-dipping reflectors at the onset of oceanic crust formation at volcanic passive margins: Insights from the South Atlantic. *Geology*, 45(5), 439–442. <https://doi.org/10.1130/G38706.1>
- Paton, Douglas A., Mortimer, E. J., Markwick, P. J., Khan, J., Davids, A., Tshikovhi, R., & Van der Spuy, D. (2023). Coeval development of extensional and contractional features along transform margins: insights from the Diaz Marginal Ridge. *Geological Society, London, Special Publications*, 524(1), 307–325. <https://doi.org/10.1144/SP524-2021-88>
- Peacock, D. C. P., & Sanderson, D. J. (1995). Strike-slip relay ramps. *Journal of Structural Geology*, 17(10), 1351–1360. [https://doi.org/10.1016/0191-8141\(95\)97303-W](https://doi.org/10.1016/0191-8141(95)97303-W)
- Pérez-Díaz, L., & Eagles, G. (2014). Constraining South Atlantic growth with seafloor spreading data. *Tectonics*, 33(9), 1848–1873. <https://doi.org/10.1002/2014TC003644>
- Peron-Pinvidic, G., Manatschal, P., & Osmundsen, P. (2013) Structural comparison of archetypal Atlantic rifted margins: A review of observations and concepts, 43 *Marine and Petroleum Geology* 21. <https://doi.org/10.1016/j.marpetgeo.2013.02.002>
- Persaud, P., Stock, J. M., Steckler, M. S., Martín-Barajas, A., Diebold, J. B., González-Fernández, A., & Mountain, G. S. (2003). Active deformation and shallow structure of the Wagner, Consag, and Delfín Basins, northern Gulf of California, Mexico. *Journal of Geophysical Research: Solid Earth*, 108(B7). <https://doi.org/10.1029/2002JB001937>
- Philippon, M., & Corti, G. (2016). Obliquity along plate boundaries. *Tectonophysics*, 693, 171–182. <https://doi.org/10.1016/J.TECTO.2016.05.033>
- Pierre, A., Durllet, C., Razin, P., & Chellai, E. H. (2010). Spatial and temporal distribution of ooids along a Jurassic carbonate ramp: Amellago outcrop transect, High-Atlas, Morocco. *Geological Society, London, Special Publications*, 329(1), 65–88. <https://doi.org/10.1144/SP329.4>
- Pindell, J., Graham, R., & Horn, B. (2014). Rapid outer marginal collapse at the rift to drift transition of passive margin evolution, with a Gulf of Mexico case study. *Basin Research*, 26(6), 701–725. <https://doi.org/10.1111/bre.12059>
- Pindell, J. L. (1985). Alleghenian reconstruction and subsequent evolution of the Gulf of Mexico, Bahamas, and Proto-Caribbean. *Tectonics*, 4(1), 1–39. <https://doi.org/10.1029/TC004i001p00001>
- Pindell, J. L., & Kennan, L. (2009). Tectonic evolution of the Gulf of Mexico, Caribbean

- and northern South America in the mantle reference frame: an update. *Geological Society, London, Special Publications*, 328(1), 1–55.
<https://doi.org/10.1144/SP328.1>
- Pindell, J., Weber, B., Elrich, W.-H., Cossey, S., Bitter, M., Molina, R., Graham, R., & Elrich, R. (2019, May). *Strontium Isotope Dating of Evaporites and the Breakup of the Gulf of Mexico and Proto-Caribbean Seaway*.
<http://www.searchanddiscovery.com/abstracts/html/2019/ace2019/abstracts/1635.html>
- Pindell, James;, Radovich, B., & Horn, B. W. (2011). Western Florida: A New Exploration Frontier in the US Gulf of Mexico. *GeoExPro*, 8, 37–40.
- Pindell, James, & Dewey, J. F. (1982). Permo-Triassic reconstruction of western Pangea and the evolution of the Gulf of Mexico/Caribbean region. *Tectonics*, 1(2), 179–211. <https://doi.org/10.1029/TC001i002p00179>
- Pindell, James, & Heyn, T. (2022). Dynamo-thermal subsidence and sag–salt section deposition as magma-rich rifted margins move off plume centres along incipient lines of break-up. *Journal of the Geological Society*, 179(5), jgs2021-095.
<https://doi.org/10.1144/JGS2021-095>
- Pindell, James, & Kennan, L. (2001). Kinematic Evolution of the Gulf of Mexico and Caribbean. *GCSSEPM Foundation 21st Annual Research Conference Transactions, Petroleum Systems of Deep-Water Basins*, 193–220.
- Pindell, James, Miranda, E. C., Cerón, A., & Hernandez, L. (2016). Aeromagnetic Map Constrains Jurassic–Early Cretaceous Synrift, Break Up, and Rotational Seafloor Spreading History in the Gulf of Mexico. In *Mesozoic of the Gulf Rim and Beyond: New Progress in Science and Exploration of the Gulf of Mexico Basin* (pp. 123–153). Gulf Coast Section SEPM. <https://doi.org/10.5724/gcs.15.35.0123>
- Pindell, James, Villagómez, D., Molina-Garza, R., Graham, R., & Weber, B. (2021). A revised synthesis of the rift and drift history of the Gulf of Mexico and surrounding regions in the light of improved age dating of the Middle Jurassic salt. *Geological Society, London, Special Publications*, 504(1), 29–76.
<https://doi.org/10.1144/SP504-2020-43>
- Pinéo, T. R. G., Palheta, E. S. M., Costa, F. G., Vasconcelos, A. M., Gomes, I. P., Gomes, F. E. M., Bessa, M. D. M. R., Lima, A. F., Holanda, J. L. R., & Freire, D. P. C. (2020). Projeto Geologia e Recursos Minerais do Estado do Ceará. Escala 1:500.000. *CPRM, Fortaleza*.
- Piqué, A., Tricart, P., Guiraud, R., Laville, E., Bouaziz, S., Amrhar, M., & Ouali, R. A. (2002). The mesozoic-cenozoic atlas belt (north africa): An overview. *Geodinamica Acta*, 15(3), 185–208.
<https://doi.org/10.1080/09853111.2002.10510752>
- Pirajno, F. (2000). Ore Deposits and Mantle Plumes. *Ore Deposits and Mantle Plumes*.
<https://doi.org/10.1007/978-94-017-2502-6>
- Planke, S., Alvestad, E., & Eldholm, O. (1999). Seismic characteristics of basaltic extrusive and intrusive rocks. *The Leading Edge*, 18(3), 342–348.
<https://doi.org/10.1190/1.1438289>
- Planke, S., & Eldholm, O. (1994). Seismic response and construction of seaward dipping wedges of flood basalts: Vøring volcanic margin. *Journal of Geophysical Research: Solid Earth*, 99(B5), 9263–9278. <https://doi.org/10.1029/94JB00468>
- Planke, S., Symonds, P. A., Alvestad, E., & Skogseid, J. (2000). Seismic volcanostratigraphy of large-volume basaltic extrusive complexes on rifted

- margins. *Journal of Geophysical Research: Solid Earth*, 105(B8), 19335–19351. <https://doi.org/10.1029/1999jb900005>
- Polteau, S., Planke, S., Zastrozhnov, D., Abdelmalak, M. M., Lebedeva-Ivanova, N., Planke, E. E., Svensen, H. H., Mazzini, A., Gernigon, L., Myklebust, R., Kjølhamar, B. E., Pedersen, R. B., Sandstå, N. R., & Bünz, S. (2020). Upper Cretaceous-Paleogene stratigraphy and development of the Mimir High, Vøring Transform Margin, Norwegian Sea. *Marine and Petroleum Geology*, 122, 104717. <https://doi.org/10.1016/J.MARPETGEO.2020.104717>
- Pontes, F. ., & Asmus, H. E. (1976). The Brazilian marginal basins: current state of knowledge. *Proc. Internat. Symposium on Continental Margins of Atlantic Type, Sao Paulo, Brazil, Oct 13–17, 1975: Anais Da Academia Brasileira de Ciências*, 48, 215–329.
- Posey, H. H., Richard Kyle, J., Jackson, T. J., Hurst, S. D., & Price, P. E. (1987). Multiple fluid components of salt diapirs and salt dome cap rocks, Gulf Coast, U.S.A. *Applied Geochemistry*, 2(5–6), 523–534. [https://doi.org/10.1016/0883-2927\(87\)90006-0](https://doi.org/10.1016/0883-2927(87)90006-0)
- Pouliquen, G., Connard, G., Kearns, H., Gouiza, M., & Paton, D. (2017). Public domain satellite gravity inversion offshore Somalia combining layered-Earth and voxel based modelling. *First Break*, 35(9), 73–79.
- Prol-Ledesma, R. M., Arango-Galván, C., & Torres-Vera, M.-A. (2016). Rigorous Analysis of Available Data from Cerro Prieto and Las Tres Virgenes Geothermal Fields with Calculations for Expanded Electricity Generation. *Natural Resources Research*, 25(4), 445–458. <https://doi.org/10.1007/s11053-016-9295-2>
- Pucci, S., Pantosti, D., Barchi, M., & Palyvos, N. (2007). A complex seismogenic shear zone: The Düzce segment of North Anatolian Fault (Turkey). *Earth and Planetary Science Letters*, 262(1–2), 185–203. <https://doi.org/10.1016/j.epsl.2007.07.038>
- Pulham, A. J., Peel, F. J., Rives, T., Delph, B., Salel, J.-F., Wu, J., & Requejo, R. (2019). *The age of the Louann Salt; insights from historic isotopic analyses in salt stocks from the onshore interior salt basins of the Northern Gulf of Mexico. In: GCSSEPM Foundation 37th Annual Perkins-Rosen Research Conference.*
- Qi, J., & Yang, Q. (2010). Cenozoic structural deformation and dynamic processes of the Bohai Bay basin province, China. *Marine and Petroleum Geology*, 27(4), 757–771. <https://doi.org/10.1016/j.marpetgeo.2009.08.012>
- Rabinowitz, P. D., & Labrecque, J. (1979). The Mesozoic South Atlantic Ocean and evolution of its continental margins. *Journal of Geophysical Research: Solid Earth*, 84(B11), 5973–6002. <https://doi.org/10.1029/JB084IB11P05973>
- Ranero, C. R., & Pérez-Gussinyé, M. (2010). Sequential faulting explains the asymmetry and extension discrepancy of conjugate margins. *Nature* , 468(7321), 294–299. <https://doi.org/10.1038/nature09520>
- Rao, G., Lin, A., Yan, B., Jia, D., Wu, X., & Ren, Z. (2011). Co-seismic Riedel shear structures produced by the 2010 Mw 6.9 Yushu earthquake, central Tibetan Plateau, China. *Tectonophysics*, 507(1–4), 86–94. <https://doi.org/10.1016/j.tecto.2011.05.011>
- Reeve, M. T., Magee, C., Bastow, I. D., McDermott, C., Jackson, C. A.-L., Bell, R. E., & Prytulak, J. (2021). Nature of the Cuvier Abyssal Plain crust, offshore NW Australia. *Journal of the Geological Society*, 178(5). <https://doi.org/10.1144/jgs2020-172>
- Reid, H. F., Davis, W. M., Lawson, A. C., & Ransome, F. L. (1913). Report of the

- Committee on the Nomenclature of Faults. *Geological Society of America Bulletin*, 24(1), 163–186. <https://doi.org/10.1130/GSAB-24-163>
- Rey, S. S., Planke, S., Symonds, P. A., & Faleide, J. I. (2008). Seismic volcanostratigraphy of the Gascoyne margin, Western Australia. *Journal of Volcanology and Geothermal Research*, 172(1–2), 112–131. <https://doi.org/10.1016/j.jvolgeores.2006.11.013>
- Richard, P., & Krantz, R. W. (1991). Experiments on fault reactivation in strike-slip mode. *Tectonophysics*, 188(1–2), 117–131. [https://doi.org/10.1016/0040-1951\(91\)90318-M](https://doi.org/10.1016/0040-1951(91)90318-M)
- Riedel, W. (1929). Zur Mechanik Geologischer Brucherscheinungen. Zentralblatt für Mineralogie. *Geologie Und Paleontologie B*, 354–368.
- Ritzmann, O. (2003). Architecture and geodynamic evolution of the Svalbard Archipelago, the Yermak Plateau and the Fram Strait oceanic Province from deep seismic experiments= Aufbau und geodynamische Entwicklungsgeschichte des Svalbard-Archipels, des Yermak Plateaus und der o. *Berichte Zur Polar-Und Meeresforschung (Reports on Polar and Marine Research)*, 439.
- Ritzmann, O., Jokat, W., Czuba, W., Guterch, A., Mjelde, R., & Nishimura, Y. (2004). A deep seismic transect from Hovgård Ridge to northwestern Svalbard across the continental-ocean transition: A sheared margin study. *Geophysical Journal International*, 157(2), 683–702. <https://doi.org/10.1111/j.1365-246X.2004.02204.x>
- Roche, V., Ringenbach, J.-C., Sapin, F., & Leroy, S. (2023). South and East African fracture zones: a long lifespan since the breakup of Gondwana. *Geological Society, London, Special Publications*, 524(1), 279–305. <https://doi.org/10.1144/SP524-2022-25>
- Rolley, J. P., & Etienne, H. (1978). Carte géologique du Maroc au 1: 100.000: notice explicative. Feuille Afourer (Haut Atlas central). *Éditions Du Service Géologique Du Maroc*.
- Rooney, T., Furman, T., Bastow, I., Ayalew, D., & Yirgu, G. (2007). Lithospheric modification during crustal extension in the Main Ethiopian Rift. *Journal of Geophysical Research: Solid Earth*, 112(B10). <https://doi.org/10.1029/2006JB004916>
- Rosendahl, B. R., Kilembe, E., & Kaczmarick, K. (1992). Comparison of the Tanganyika, Malawi, Rukwa and Turkana Rift zones from analyses of seismic reflection data. *Tectonophysics*, 213(1–2), 235–256. [https://doi.org/10.1016/0040-1951\(92\)90261-4](https://doi.org/10.1016/0040-1951(92)90261-4)
- Rosenthal, M., Ben-Avraham, Z., & Schattner, U. (2019). Almost a sharp cut – A case study of the cross point between a continental transform and a rift, based on 3D gravity modeling. *Tectonophysics*, 761, 46–64. <https://doi.org/10.1016/j.tecto.2019.04.012>
- Rotevatn, A., & Peacock, D. C. P. (2018). Strike-slip reactivation of segmented normal faults: Implications for basin structure and fluid flow. *Basin Research*, 30(6), 1264–1279. <https://doi.org/10.1111/BRE.12303>
- Rowan, M. G. (2014). Passive-margin salt basins: hyperextension, evaporite deposition, and salt tectonics. *Basin Research*, 26(1), 154–182. <https://doi.org/10.1111/bre.12043>
- Rowan, M.G., Sumner, H. S., Huston, H., Venkatraman, S., & Dunbar, D. (2012). Constraining Interpretations of the Crustal Architecture of the Northern Gulf of Mexico. *The Gulf Coast Association of Geological Societies*, 62, 605–608.

- Rowan, M. G. (2018). The South Atlantic and Gulf of Mexico salt basins: crustal thinning, subsidence and accommodation for salt and presalt strata. *Geological Society, London, Special Publications*, 476(1), 333–363. <https://doi.org/10.1144/sp476.6>
- Rüpke, L. H., Schmid, D. W., Hartz, E. H., & Martinsen, B. (2010). Basin modelling of a transform margin setting: structural, thermal and hydrocarbon evolution of the Tano Basin, Ghana. *Petroleum Geoscience*, 16(3), 283–298. <https://doi.org/10.1144/1354-079309-905>
- Sage, F., Basile, C., Mascle, J., Pontoise, B., & Whitmarsh, R. B. (2000). Crustal structure of the continent-ocean transition off the Cote d'Ivoire-Ghana transform margin: Implications for thermal exchanges across the palaeotransform boundary. *Geophysical Journal International*, 143(3), 662–678. <https://doi.org/10.1046/j.1365-246X.2000.00276.x>
- Sage, F., Pontoise, B., Mascle, J., Basile, C., & Arnould, L. (1997). Crustal structure and ocean-continent transition at marginal ridge: The Côte d'Ivoire-Ghana marginal ridge. *Geo-Marine Letters*, 17(1), 40–48. <https://doi.org/10.1007/PL00007206/METRICS>
- Sagong, H., Kwon, S. T., Cheong, C. S., & Choi, S. H. (2001). Geochemical and isotopic studies of the Cretaceous igneous rocks in the Yeongdong Basin, Korea: implications for the origin of magmatism in pull-apart basin. *Geosciences Journal*, 5(191–201).
- Salvador, A. (1987). Late Triassic- Jurassic paleogeography and origin of Gulf of Mexico basin. *American Association of Petroleum Geologists Bulletin*, 71(4), 419–451. <https://doi.org/10.1306/94886ec5-1704-11d7-8645000102c1865d>
- Salvador, A. (1991). *Triassic–Jurassic*, in A. Salvador, ed., *The Gulf of Mexico Basin: Geological Society of America, The Geology of North America. J*, 131–180.
- Sanchez-Zamora, O., Doguin, P., Couch, R. W., & Ness, G. E. (1991). Magnetic anomalies of the northern Gulf of California: Structural and thermal interpretations: Chapter 22: Part III. Regional Geophysics and Geology. In *The Gulf and Peninsular Province of the Californias*. (pp. 377–402).
- Sanderson, D. J., & Marchini, W. R. D. (1984). Transpression. *Journal of Structural Geology*, 6(5), 449–458. [https://doi.org/10.1016/0191-8141\(84\)90058-0](https://doi.org/10.1016/0191-8141(84)90058-0)
- Sandwell, D., & Schubert, G. (1982). Lithospheric flexure at fracture zones. *Journal of Geophysical Research*, 87(B6), 4657–4667.
- Sandwell, D. T., Müller, R. D., Smith, W. H. F., Garcia, E., & Francis, R. (2014). New global marine gravity model from CryoSat-2 and Jason-1 reveals buried tectonic structure. *Science*, 346(6205), 65–67. <https://doi.org/10.1126/science.1258213>
- Sandwell, D. T., & Smith, W. H. F. (1997). Marine gravity anomaly from Geosat and ERS 1 satellite altimetry. *Journal of Geophysical Research: Solid Earth*, 102(B5), 10039–10054. <https://doi.org/10.1029/96JB03223>
- Saura, E., Vergés, J., Martín-Martín, J. D., Messenger, G., Moragas, M., Razin, P., Grélaud, C., Joussiaume, R., Malaval, M., Homke, S., & Hunt, D. W. (2014). Syn- to post-rift diapirism and minibasins of the Central High Atlas (Morocco): the changing face of a mountain belt. *Journal of the Geological Society*, 171(1), 97–105. <https://doi.org/10.1144/jgs2013-079>
- Scarselli, N., Duval, G., Martin, J., McClay, K., & Toothill, S. (2020). Insights into the Early Evolution of the Côte d'Ivoire Margin (West Africa). *Geological Society, London, Special Publications*, 476(1), 109–133. <https://doi.org/10.1144/SP476.8>

- Schaer, J., & Rodgers, J. (1987). *Evolution and structure of the High Atlas of Morocco*.
- Schettino, A., & Turco, E. (2009). Breakup of Pangaea and plate kinematics of the central Atlantic and Atlas regions. *Geophysical Journal International*, 178(2), 1078–1097. <https://doi.org/10.1111/j.1365-246X.2009.04186.x>
- Schettino, A., & Turco, E. (2011). Tectonic history of the Western Tethys since the Late Triassic. *Bulletin of the Geological Society of America*, 123(1–2), 89–105. <https://doi.org/10.1130/B30064.1>
- Schlager, W. . B. R. T. . A. D. . P. R. (1984). Geologic History of the Southeastern Gulf of Mexico. *Initial Reports of the Deep Sea Drilling Project*, 77, 715–738.
- Schultz, P. (1999). The Seismic Velocity Model as an Interpretation Asset. *SEG - Distinguished Instructor Short Course*.
- Schwarz, G., & Wigger, P. J. (1988). Geophysical studies of the earth's crust and upper mantle in the Atlas system of Morocco. In: Jacobshagen V.H. (eds) *The Atlas System of Morocco*. In *The Atlas System of Morocco* (15th ed., pp. 339–357). Springer-Verlag. <https://doi.org/10.1007/bfb0011600>
- Scotese, C. R. (2016). Tutorial: PALEOMAP paleoAtlas for GPlates and the paleoData plotter program. PALEOMAP Project. *Technical Report*, 56.
- Scrutton, R. A. (1979). On Sheared Passive Continental Margins. *Developments in Geotectonics*, 15, 293–305. <https://doi.org/10.1016/B978-0-444-41851-7.50020-0>
- Seiler, C., Fletcher, J. M., Quigley, M. C., Gleadow, A. J. W., & Kohn, B. P. (2010). Neogene structural evolution of the Sierra San Felipe, Baja California: Evidence for proto-gulf transtension in the Gulf Extensional Province? *Tectonophysics*, 488(1–4), 87–109. <https://doi.org/10.1016/j.tecto.2009.09.026>
- Skogly, O. (1998). Seismic characterization and emplacement of intrusives in the Vøring Basin. *Cand Scient Thesis, Department of Geology, University of Oslo*.
- Skogseid, J., Pedersen, T., Eldholm, O., & Larsen, B. T. (1992). Tectonism and magmatism during NE Atlantic continental break-up: the Vøring Margin. *Geological Society, London, Special Publications*, 68(1), 305–320. <https://doi.org/10.1144/GSL.SP.1992.068.01.19>
- Skogseid, J., Planke, S., Faleide, J. I., Pedersen, T., Eldholm, O., & Neverdal, F. (2000). NE Atlantic continental rifting and volcanic margin formation. *Geological Society, London, Special Publications*, 167(1), 295–326. <https://doi.org/10.1144/GSL.SP.2000.167.01.12>
- Smith, M., & Mosley, P. (1993). Crustal heterogeneity and basement influence on the development of the Kenya Rift, East Africa. *Tectonics*, 12(2), 591–606. <https://doi.org/10.1029/92TC01710>
- Smith, W. H. F., & Sandwell, D. T. (1997). Global sea floor topography from satellite altimetry and ship depth soundings. *Science*, 277(5334), 1956–1962. <https://doi.org/10.1126/SCIENCE.277.5334.1956/ASSET/FBFA5CB2-0680-4A97-B98D-A5648B80563E/ASSETS/GRAPHIC/SE3875739005.JPEG>
- Snedden, J. W. ., & Galloway, W. E. (2019). *The Gulf of Mexico sedimentary basin : depositional evolution and petroleum applications*. Cambridge University Press.
- Snedden, J. W., Norton, I. O., Christeson, G. L., & Sanford, J. C. (2014). Interaction of Deepwater Deposition and a Mid-Ocean Spreading Center, Eastern Gulf of Mexico Basin, USA. *GCAGS*, 64, 371–383.
- Soares Júnior, A. V., Costa, J. B. S., & Hasui, Y. (2008). Evolução da margem atlântica equatorial do Brasil: Três fases distensivas. *Geociencias*, 27(4), 427–437.

- Specht, T. D., & Rosendahl, B. R. (1989). Architecture of the Lake Malawi Rift, East Africa. *Journal of African Earth Sciences (and the Middle East)*, 8(2–4), 355–382. [https://doi.org/10.1016/S0899-5362\(89\)80032-6](https://doi.org/10.1016/S0899-5362(89)80032-6)
- Stanca, R. M., McCarthy, D. J., Paton, D. A., Hodgson, D. M., & Mortimer, E. J. (2022). The tectono-stratigraphic architecture of the Falkland Plateau basin; implications for the evolution of the Falkland Islands Microplate. *Gondwana Research*, 105, 320–342. <https://doi.org/10.1016/j.gr.2021.09.014>
- Steier, A., & Mann, P. (2019). Late Mesozoic gravity sliding and Oxfordian hydrocarbon reservoir potential of the northern Yucatan margin. *Marine and Petroleum Geology*, 103, 681–701. <https://doi.org/10.1016/J.MARPETGEO.2019.03.001>
- Steltenpohl, M. G., Hames, W. E., & Andresen, A. (2004). The Silurian to Permian history of a metamorphic core complex in Lofoten, northern Scandinavian Caledonides. *Tectonics*, 23(1). <https://doi.org/10.1029/2003TC001522>
- Strand, K. (1988). Sedimentary Facies and Sediment Composition Changes in Response to tectonics of the Côte d'Ivoire-Ghana Transform Margin. In: Proceedings of the Ocean Drilling Program. *Scientific Results*, 159, 113–123.
- Suckro, S. K., Gohl, K., Funck, T., Heyde, I., Schreckenberger, B., Gerlings, J., & Damm, V. (2013). The Davis Strait crust—a transform margin between two oceanic basins. *Geophysical Journal International*, 193(1), 78–97. <https://doi.org/10.1093/gji/ggs126>
- Suo, Y. H., Li, S. Z., Zhao, S. J., Somerville, I. D., Yu, S., Dai, L. M., Xu, L. Q., Cao, X. Z., & Wang, P. C. (2015). Continental margin basins in East Asia: tectonic implications of the Meso-Cenozoic East China Sea pull-apart basins. *Geological Journal*, 50(2), 139–156. <https://doi.org/10.1002/gj.2535>
- Sutra, E., & Manatschal, G. (2012). How does the continental crust thin in a hyperextended rifted margin? Insights from the Iberia margin. *Geology*, 40(2), 139–142. <https://doi.org/10.1130/G32786.1>
- Sylvester, A. G. (1988). Strike-slip faults. *Geological Society of America Bulletin*, 100, 1666–1703.
- Tari, G. (2006). Traditional and New Play Types of the Offshore Tano Basin of Côte d'Ivoire and Ghana, West Africa. *Houston Geological Society Bulletin*, 48(5), 27–30.
- Tatar, O., Yurtmen, S., Temiz, H., Guersoy, H., Kocbulut, F., Mesci, B. L., & Guezou, J. C. (2007). Intracontinental quaternary volcanism in the Niksar pull-apart basin, North Anatolian Fault Zone, Turkey. *Turkish Journal of Earth Sciences*, 16(4), 417–440.
- Tavares, A. C., de Castro, D. L., Bezerra, F. H. R., Oliveira, D. C., Vannucchi, P., Iacopini, D., Jovane, L., & Vital, H. (2020). The Romanche fracture zone influences the segmentation of the equatorial margin of Brazil. *Journal of South American Earth Sciences*, 103, 102738. <https://doi.org/10.1016/j.jsames.2020.102738>
- Tavares, A. C., de Castro, D. L., Clausen, O. R., Bezerra, F. H. R., Sousa, M. O. L., Gomes, M. P., Vital, H., & de Oliveira, D. C. (2022). Continental-scale structural heritage from rift extension to postrift inversion: Implications for the central Brazilian Equatorial Margin evolution. *Tectonophysics*, 837, 229446. <https://doi.org/10.1016/j.tecto.2022.229446>
- Teixell, A., Arboleya, M. L., Julivert, M., & Charroud, M. (2003). Tectonic shortening and topography in the central High Atlas (Morocco). *Tectonics*, 22(5).

<https://doi.org/10.1029/2002TC001460>

- Teixell, A., Barnolas, A., Rosales, I., & Arboleya, M.-L. (2017). Structural and facies architecture of a diapir-related carbonate minibasin (lower and middle Jurassic, High Atlas, Morocco). *Marine and Petroleum Geology*, *81*, 334–360. <https://doi.org/10.1016/j.marpetgeo.2017.01.003>
- Tetteh, J. T. (2016). The Cretaceous Play of Tano Basin, Ghana. *Int. J. Appl. Sci. Technol.*, *6*(1), 1–10.
- Thomaz Filho, A., Cordani, U. G., & Marino, O. (1974). Idades K/Ar de rochas basálticas da Bacia Amazônica e sua significação tectônica regional. *Anais*, *6*(273–278).
- Thybo, H., & Artemieva, I. M. (2013). Moho and magmatic underplating in continental lithosphere. In *Tectonophysics* (Vol. 609, pp. 605–619). Elsevier. <https://doi.org/10.1016/j.tecto.2013.05.032>
- Tidjani, M. E.-H., Affaton, P., Louis, P., & Socohou, A. (1997). Gravity characteristics of the Pan-African Orogen in Ghana, Togo and Benin (west Africa). *Journal of African Earth Sciences*, *24*(3), 241–258. [https://doi.org/10.1016/S0899-5362\(97\)00041-9](https://doi.org/10.1016/S0899-5362(97)00041-9)
- Tiercelin, J. J., Chorowicz, J., Bellon, H., Richert, J. P., Mwanbene, J. T., & Walgenwitz, F. (1988). East African rift system: offset, age and tectonic significance of the Tanganyika-Rukwa-Malawi intracontinental transcurrent fault zone. *Tectonophysics*, *148*(3–4), 241–252. [https://doi.org/10.1016/0040-1951\(88\)90133-3](https://doi.org/10.1016/0040-1951(88)90133-3)
- Todd, B. J., & Keen, C. E. (1989). Temperature effects and their geological consequences at transform margins. *Canadian Journal of Earth Sciences*, *26*(12), 2591–2603. <https://doi.org/10.1139/e89-221>
- Toft, P. B., Arkani-Hamed, J., & Haggerty, S. E. (1990). The effects of serpentinization on density and magnetic susceptibility: a petrophysical model. *Physics of the Earth and Planetary Interiors*, *65*(1–2), 137–157. [https://doi.org/10.1016/0031-9201\(90\)90082-9](https://doi.org/10.1016/0031-9201(90)90082-9)
- Torres-López, S., Casas, A. M., Villalaín, J. J., El Ouardi, H., & Moussaid, B. (2016). Pre-Cenomanian vs. Cenozoic folding in the High Atlas revealed by palaeomagnetic data. *Terra Nova*, *28*(2), 110–119. <https://doi.org/10.1111/TER.12197>
- Trompette, R. (1994). Geology of Western Gondwana, Pan-African/Brasiliano Aggregation of South America and Africa. *AA Balkema, Rotterdam, Brookfield*, *350*, 165–193.
- Trosdorf, I., Zalán, P. V., Figueiredo, J. J. P., & Soares, E. F. (2007). Bacia de Barreirinhas. *Boletim de Geociências Da Petrobras*, *15*(2), 331–339.
- Tsikalas, F., Eldholm, O., & Faleide, J. I. (2005). Crustal structure of the Lofoten–Vesterålen continental margin, off Norway. *Tectonophysics*, *404*(3–4), 151–174. <https://doi.org/10.1016/j.tecto.2005.04.002>
- Tugend, J., Gillard, M., Manatschal, G., Nirrengarten, M., Harkin, C., Epin, M. E., Sauter, D., Autin, J., Kuszniir, N., & McDermott, K. (2018). Reappraisal of the magma-rich versus magma-poor rifted margin archetypes. *Geological Society, London, Special Publication*, *476*(1), 23–47. <https://doi.org/10.1144/SP476.9>
- Uenzelmann-Neben, G., & Gohl, K. (2004). The Agulhas Ridge, South Atlantic: The Peculiar Structure of a Fracture Zone. *Marine Geophysical Researches*, *25*(3–4), 305–319. <https://doi.org/10.1007/s11001-005-1338-8>

- van Avendonk, H. J. A., Christeson, G. L., Norton, I. O., & Eddy, D. R. (2015). Continental rifting and sediment infill in the northwestern Gulf of Mexico. *Geology*, 43(7), 631–634. <https://doi.org/10.1130/G36798.1>
- Vasconcelos, A. M., Veiga Júnior, J., Colares, J. Q. S., Ribeiro, J. A. P., Gomes, I. P., Medeiros, M. F., & Forgiarini, L. L. (2004). Folha SA.23-São Luís. *Carta Geológica Do Brasil Ao Milionésimo, Sistema de Informações Geográficas. Programa Geologia Do Brasil [CD-ROM]. Brasília, DF: CPRM.*
- Venkat-Ramani, M., & Tikoff, B. (2002). Physical models of transtensional folding. *Geology*, 30(6), 526.
- Vergés, J., Moragas, M., Martín-Martín, J. D., Saura, E., Casciello, E., Razin, P., Grelaud, C., Malaval, M., Jousiame, R., Messenger, G., Sharp, I., & Hunt, D. W. (2017). Salt Tectonics in the Atlas Mountains of Morocco. In *Permo-Triassic Salt Provinces of Europe, North Africa and the Atlantic Margins* (pp. 563–579). Elsevier. <https://doi.org/10.1016/b978-0-12-809417-4.00027-6>
- Viola, G., Odonne, F., & Mancktelow, N. . (2004). Analogue modelling of reverse fault reactivation in strike–slip and transpressive regimes: application to the Giudicarie fault system, Italian Eastern Alps. *Journal of Structural Geology*, 26(3), 401–418. <https://doi.org/10.1016/j.jsg.2003.08.014>
- Walker, J. D. ., Geissman, J. W., Bowring, S. A., & Babcock, L. E. (2018). *GSA Geologic Time Scale v. 5.0*. Geological Society of America.
- Walsh, J. J., & Watterson, J. (1991). Geometric and kinematic coherence and scale effects in normal fault systems. *Geological Society, London, Special Publications*, 56(1), 193–203. <https://doi.org/10.1144/GSL.SP.1991.056.01.13>
- Warne, J. E. (1988). Jurassic carbonate facies of the central and eastern High Atlas rift, Morocco. In *The Atlas System of Morocco: Studies on its Geodynamic Evolution* (pp. 169–199).
- Watterson, J. (1986). Fault dimensions, displacements and growth. *Pure and Applied Geophysics PAGEOPH*, 124(1–2), 365–373. <https://doi.org/10.1007/BF00875732>
- Wegener, A. (1912). Die entstehung der kontinente. *Geologische Rundschau*, 3(4), 276–292.
- Wheeler, W. H., & Karson, J. A. (1994). Extension and subsidence adjacent to a “weak” continental transform: An example from the Rukwa rift, East Africa. *Geology*, 22(7), 625. [https://doi.org/10.1130/0091-7613\(1994\)022<0625:EASATA>2.3.CO;2](https://doi.org/10.1130/0091-7613(1994)022<0625:EASATA>2.3.CO;2)
- White, N. (1993). Recovery of strain rate variation from inversion of subsidence data. *Nature*, 366(6454), 449–452. <https://doi.org/10.1038/366449a0>
- White, R., & McKenzie, D. (1989). Magmatism at rift zones: The generation of volcanic continental margins and flood basalts. *Journal of Geophysical Research*, 94(B6), 7729. <https://doi.org/10.1029/JB094iB06p07685>
- White, R. S., Smith, L. K., Roberts, A. W., Christie, P. A. F., Kusznir, N. J., Roberts, A. M., Healy, D., Spitzer, R., Chappell, A., Eccles, J. D., Fletcher, R., Hurst, N., Lunnun, Z., Parkin, C. J., & Tymms, V. J. (2008). Lower-crustal intrusion on the North Atlantic continental margin. *Nature*, 452(7186), 460–464. <https://doi.org/10.1038/nature06687>
- White, R. S., Spence, G. D., Fowler, S. R., McKenzie, D. P., Westbrook, G. K., & Bowen, A. N. (1987). Magmatism at rifted continental margins. *Nature*, 330, 439–444.

- Whitmarsh, R. B., Manatschal, G., & Minshull, T. A. (2001). Evolution of magma-poor continental margins from rifting to seafloor spreading. *Nature*, *413*(6852), 150–154. <https://doi.org/10.1038/35093085>
- Wilson, J. T. (1965). A new class of faults and their bearing on continental drift. *Nature*, *207*(4995), 343–347.
- Wolfenden, E., Ebinger, C., Yirgu, G., Deino, A., & Ayalew, D. (2004). Evolution of the northern Main Ethiopian rift: birth of a triple junction. *Earth and Planetary Science Letters*, *224*(1–2), 213–228. <https://doi.org/10.1016/j.epsl.2004.04.022>
- Woodcock, N. H. (1986). The role of strike-slip fault systems at plate boundaries. *Philosophical Transactions - Royal Society of London, Series A*, *317*(1539), 13–29. <https://doi.org/10.1098/rsta.1986.0021>
- Woodcock, Nigel H., & Fischer, M. (1986). Strike-slip duplexes. *Journal of Structural Geology*, *8*(7), 725–735. [https://doi.org/10.1016/0191-8141\(86\)90021-0](https://doi.org/10.1016/0191-8141(86)90021-0)
- Wu, J. E., McClay, K., Whitehouse, P., & Dooley, T. (2009). 4D analogue modelling of transtensional pull-apart basins. *Marine and Petroleum Geology*, *26*(8), 1608–1623. <https://doi.org/10.1016/J.MARPETGEO.2008.06.007>
- Yassin, M. A., Hariri, M. M., Abdullatif, O. M., Korvin, G., & Makkawi, M. (2017). Evolution history of transtensional pull-apart, oblique rift basin and its implication on hydrocarbon exploration: A case study from Sufyan Sub-basin, Muglad Basin, Sudan. *Marine and Petroleum Geology*, *79*, 282–299. <https://doi.org/10.1016/j.marpetgeo.2016.10.016>
- Ye, J., Chardon, D., Rouby, D., Guillocheau, F., Dall'asta, M., Ferry, J. N., & Broucke, O. (2017). Paleogeographic and structural evolution of northwestern Africa and its Atlantic margins since the early Mesozoic. *Geosphere*, *13*(4), 1254–1284. <https://doi.org/10.1130/GES01426.1>
- Ye, J., Rouby, D., Chardon, D., Dall'asta, M., Guillocheau, F., Robin, C., & Ferry, J. N. (2019). Post-rift stratigraphic architectures along the African margin of the Equatorial Atlantic: Part I the influence of extension obliquity. *Tectonophysics*, *753*, 49–62. <https://doi.org/10.1016/j.tecto.2019.01.003>
- Zalán, P. V. (2004). Evolução fanerozóica das bacias sedimentares brasileiras. *Geologia Do Continente Sul-Americano: Evolução Da Obra de Fernando Flávio Marques de Almeida*. São Paulo, Beca, 595–613.
- Zalan, P. V., Nelson, E. P., Warme, J. E., & Davis, T. L. (1985). The Piauí Basin: Rifting and Wrenching in an Equatorial Atlantic Transform Basin. *Strike-Slip Deformation, Basin Formation, and Sedimentation. The Society of Economic Paleontologists and Mineralogists. Special Publication 37*.
- Zwaan, F., Schreurs, G., Naliboff, J., & Buiters, S. J. H. (2016). Insights into the effects of oblique extension on continental rift interaction from 3D analogue and numerical models. *Tectonophysics*, *693*, 239–260. <https://doi.org/10.1016/j.tecto.2016.02.036>

Appendix

A. Appendix for Chapter 2 – High Atlas, Morocco



Figure 0.1: Sub-horizontal normal faults in vertical beds in the southern NE-SW regional scale fault of Ouaouizaght.

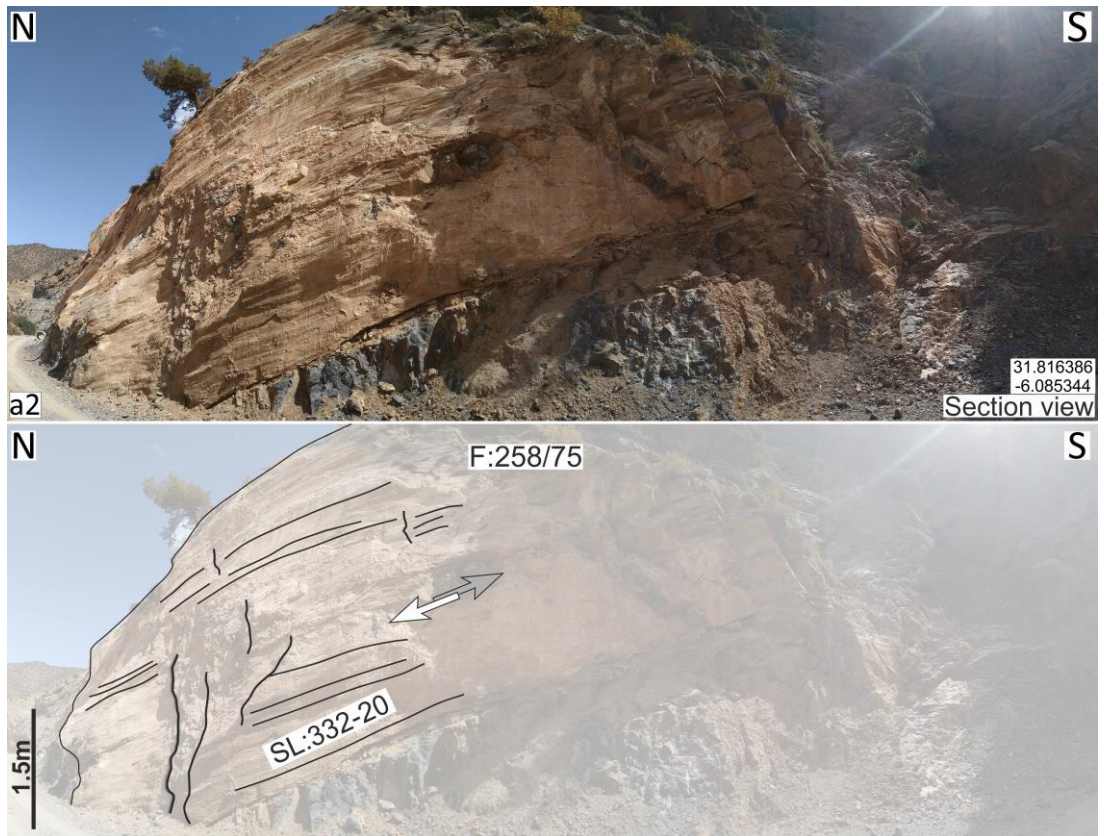


Figure 0.2: NW-SE trending fault in the Zawayat-Ahancal region.

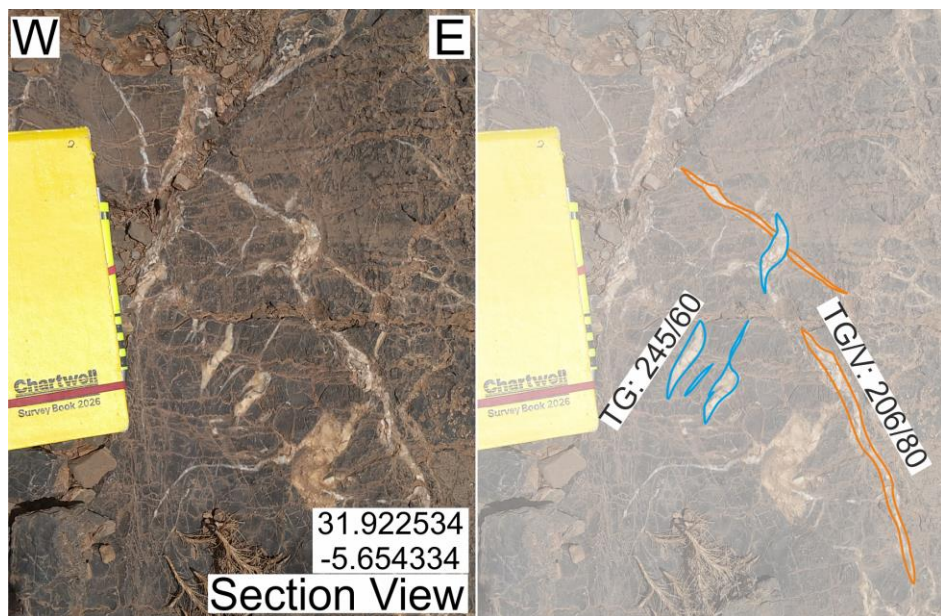


Figure 0.3: Post-Middle Jurassic (blue) and syn-Middle Jurassic (orange) tensional fractures in the Early Jurassic carbonates.

Table A-1: Field data from the Ait Attab region, locality (a). The shear interpretation corresponds to the overall kinematic and not individually each Riedel structure.

Type	Lat (Y)	Long (X)	Elev	Measurement (azimuth/dip)	Notes
Fracture	32.126760	-6.877156	685.616821	135/66	P - sinistral shear
Fracture	32.126760	-6.877156	685.616821	308/50	P - sinistral shear
Fracture	32.126744	-6.877053	683.810547	259/72	P - sinistral shear
Fracture	32.126744	-6.877053	683.810547	155/76	P' - sinistral shear
Fracture	32.126744	-6.877053	683.810547	321/54	P - sinistral shear
Fracture	32.126744	-6.877053	683.810547	078/63	M - sinistral shear
Fracture	32.126744	-6.877053	683.810547	166/61	P' - sinistral shear
Fracture	32.126744	-6.877053	683.810547	067/52	R - sinistral shear
Fracture	32.126744	-6.877053	683.810547	155/76	P' - sinistral shear
Fracture	32.126744	-6.877053	683.810547	299/66	P - sinistral shear
Fracture	32.126642	-6.877097	690.611084	308/57	P - sinistral shear
Fracture	32.126642	-6.877097	690.611084	159/48	P' - sinistral shear
Fracture	32.126642	-6.877097	690.611084	202/76	M - sinistral shear
Fracture	32.126642	-6.877097	690.611084	025/70	P' - sinistral shear
Fracture	32.126642	-6.877097	690.611084	155/52	P - sinistral shear

Table A-2: Field data from the Ait Attab region, locality (b). The shear interpretation corresponds to the overall kinematic and not individually each Riedel structure.

Type	Lat (Y)	Long (X)	Elev	Measurement (azimuth/dip)	Notes
Fracture	32.125411	-6.870504	641.534302	026/66	R - sinistral
Fracture	32.125411	-6.870504	641.534302	051/58	P-sinistral
Fracture	32.125411	-6.870504	641.534302	045/40	P-sinistral
Fracture	32.125411	-6.870504	641.534302	025/40	R - sinistral
Fracture	32.125411	-6.870504	641.534302	067/64	P-sinistral
Fracture	32.097087	-6.901789	529.116150	247/50	P' - dextral shear
Fracture	32.097087	-6.901789	529.116150	302/35	M - dextral shear
Fracture	32.097087	-6.901789	529.116150	297/35	P - dextral shear
Fracture	32.097087	-6.901789	529.116150	132/55	R - dextral shear
Fracture	32.097087	-6.901789	529.116150	156/62	R' - dextral shear
Fracture	32.097087	-6.901789	529.116150	041/63	R' - dextral shear
Fracture	32.097087	-6.901789	529.116150	250/36	P - dextral shear
Fracture	32.097087	-6.901789	529.116150	311/35	M - dextral shear

Fracture	32.097087	-6.901789	529.116150	332/31	R - dextral shear
Fracture	32.097087	-6.901789	529.116150	298/30	M - dextral shear
Fracture	32.125348	-6.870535	641.590637	142/67	M - sinistral shear
Fracture	32.125348	-6.870535	641.590637	140/56	M - sinistral shear
Fracture	32.125348	-6.870535	641.590637	042/56	P' - sinistral shear
Fracture	32.125348	-6.870535	641.590637	029/45	P' - sinistral shear
Fracture	32.125348	-6.870535	641.590637	146/67	R - sinistral shear
Fracture	32.125348	-6.870535	641.590637	146/68	R - sinistral shear
Fracture	32.125411	-6.870504	641.534302	026/66	R - sinistral
Fracture	32.125411	-6.870504	641.534302	051/58	P - sinistral
Fracture	32.125411	-6.870504	641.534302	039/64	M - sinistral
Fracture	32.125411	-6.870504	641.534302	045/40	P - sinistral
Fracture	32.125411	-6.870504	641.534302	148/51	R' - sinistral
Fracture	32.125411	-6.870504	641.534302	149/52	R' - sinistral
Fracture	32.125411	-6.870504	641.534302	031/50	R - sinistral
Fracture	32.125411	-6.870504	641.534302	010/40	R' - sinistral
Fracture	32.125411	-6.870504	641.534302	067/64	R' - sinistral
Fracture	32.125411	-6.870504	641.534302	002/55	M - sinistral
Fracture	32.125566	-6.870734	653.074219	140/71	R - sinistral shear
Fracture	32.125566	-6.870734	653.074219	064/68	R' - sinistral shear
Fracture	32.125566	-6.870734	653.074219	027/67	P' - sinistral shear
Fracture	32.125566	-6.870734	653.074219	282/56	R - sinistral shear
Fracture	32.125566	-6.870734	653.074219	338/30	P - sinistral shear
Fracture	32.125566	-6.870734	653.074219	156/56	P - sinistral shear
Fracture	32.147533	-6.758764	889.526062	263/50	R - sinistral shear
Fracture	32.147533	-6.758764	889.526062	262/44	M - sinistral shear
Fracture	32.147533	-6.758764	889.526062	277/62	M - sinistral shear
Fracture	32.147533	-6.758764	889.526062	009/45	P - sinistral shear
Fracture	32.147533	-6.758764	889.526062	268/54	R' - sinistral shear
Fracture	32.147533	-6.758764	889.526062	247/49	P' - sinistral shear
Fracture	32.147533	-6.758764	889.526062	034/52	M - sinistral shear

Table A-3: Field data from the Ait Attab region, localities (c-d). The shear interpretation corresponds to the overall kinematic and not individually each Riedel structure.

Type	Lat (Y)	Long (X)	Elev	Measurement (azimuth/dip)	Notes
------	---------	----------	------	---------------------------	-------

Fracture	32.121029	-6.551535	761.050171	078/58	P - sinistral shear
Fracture	32.121029	-6.551535	761.050171	201/56	P - sinistral shear
Fracture	32.121029	-6.551535	761.050171	355/70	R' - sinistral shear
Fracture	32.121029	-6.551535	761.050171	031/76	M - sinistral shear
Fracture	32.121029	-6.551535	761.050171	047/56	M - sinistral shear
Fracture	32.121029	-6.551535	761.050171	002/77	R' - sinistral shear
Fracture	32.121029	-6.551535	761.050171	173/64	R' - sinistral shear
Fracture	32.121029	-6.551535	761.050171	243/76	P - sinistral shear
Fracture	32.121029	-6.551535	761.050171	357/66	R' - sinistral shear
Fracture	32.121029	-6.551535	761.050171	355/53	R' - sinistral shear
Fracture	32.121029	-6.551535	761.050171	037/66	M - sinistral shear
Fault	32.127326	-6.523720	1033.532959	016/73	fault
Fault	32.127326	-6.523720	1033.532959	238/47	fault
Fault	32.127326	-6.523720	1033.532959	052/40	fault
Stylolite	32.120971	-6.551620	748.706482	214-60	Stylolites
Stylolite	32.120971	-6.551620	748.706482	225-78	Stylolites
Fracture	32.120971	-6.551620	748.706482	067/64	M - sinistral
Fracture	32.120971	-6.551620	748.706482	081/47	M - sinistral
Fracture	32.120971	-6.551620	748.706482	080/52	P- sinistral
Fracture	32.120971	-6.551620	748.706482	137/83	P' - sinistral shear
Fracture	32.120971	-6.551620	748.706482	068/72	P - sinistral shear
Fracture	32.120971	-6.551620	748.706482	059/71	R - sinistral shear

Table A-4: Field data from the Ait Attab region, localities (e-f). The shear interpretation corresponds to the overall kinematic and not individually each Riedel structure.

Type	Lat (Y)	Long (X)	Elev	Measurement (azimuth/dip)	Notes
Fault	32.021134	-6.703638	904.355591	258/88	fault
Fault	32.021134	-6.703638	904.355591	143/86	fault
Fault	32.020817	-6.704231	905.000000	321/48	fault
Fault	32.020817	-6.704231	905.000000	075/38	fault
Fault	32.020780	-6.704350	905.000000	113/52	fault
Fault	32.020780	-6.704350	905.000000	108/66	fault

Table A-5: Field data from the Ouauizaght region, locality (a).

Type	Lat (Y)	Long (X)	Elev	Measurement (azimuth/dip)	Notes
Fault	32.276165	-6.283639	1398.4448240	072/83	-
Fault	32.276197	-6.284021	1403.2412110	261/55	-
Fault	32.276433	-6.284541	1413.9626460	308/88	-
Fault	32.276165	-6.283639	1398.4448240	072/83	-
Fault	32.276165	-6.283639	1398.4448240	331/57	-
Fault	32.276165	-6.283639	1398.4448240	331/57	-
Fault	32.276288	-6.284195	1403.6231690	316/69	-
Fault	32.276376	-6.284370	1410.0346680	241/66	-
Fault	32.276376	-6.284370	1410.0346680	286/54	-
Fault	32.276433	-6.284541	1413.9626460	308/88	-
Fault	32.276375	-6.284860	1404.7929690	259/74	-

Table A-6: Field data from the Ouauizaght region, localities (b-c). The shear interpretation corresponds to the overall kinematic and not individually each Riedel structure.

Type	Lat (Y)	Long (X)	Elev	Measurement (azimuth/dip)	Notes
Fault	32.270822	-6.259378	1750.851929	079/87	-
Slickenside	32.270822	-6.259378	1750.851929	173-03	Sinistral movement
Fracture	32.270847	-6.259417	1747.282837	283/68	M - sinistral
Fracture	32.270847	-6.259417	1747.282837	285/67	P - sinistral
Fracture	32.270847	-6.259417	1747.282837	049/82	T - sinistral tension gashes
Fracture	32.270847	-6.259417	1747.282837	309/75	P- sinistral
Fracture	32.270847	-6.259417	1747.282837	038/82	T - sinistral tension gashes
Fracture	32.270847	-6.259417	1747.282837	120/67	P- sinistral
Fracture	32.270847	-6.259417	1747.282837	171/67	T - sinistral tension gashes
Fracture	32.270847	-6.259417	1747.282837	086/84	M - sinistral
Fracture	32.270847	-6.259417	1747.282837	330/87	T - sinistral tension gashes
Fracture	32.270847	-6.259417	1747.282837	233/76	R' - sinistral
Stylolites	32.270847	-6.259417	1747.282837	298-64	Stylolites
Stylolites	32.270847	-6.259417	1747.282837	290-52	Stylolites
Fault	32.270994	-6.259281	1759.067749	266/80	F
Fault	32.270994	-6.259281	1759.067749	268/78	F - sinistral
Fracture	32.270994	-6.259281	1759.067749	208/80	TG
Fracture	32.270994	-6.259281	1759.067749	210/78	TG
Fracture	32.270994	-6.259281	1759.067749	063/86	TG
Fracture	32.270994	-6.259281	1759.067749	215/85	TG
Fracture	32.270994	-6.259281	1759.067749	236/85	TG
Fracture	32.270994	-6.259281	1759.067749	234/86	TG
Fracture	32.270994	-6.259281	1759.067749	028/84	TG
Fault	32.270994	-6.259281	1759.067749	272/65	F - dextral
Fracture	32.271244	-6.259271	1758.255005	054/83	TG

Fracture	32.271244	-6.259271	1758.255005	238/83	TG
Fracture	32.271244	-6.259271	1758.255005	052/85	TG
Fracture	32.271244	-6.259271	1758.255005	240/88	TG
Fault	32.271244	-6.259271	1758.255005	295/79	F - sinistral
Fault	32.271335	-6.259215	1765.532593	265/83	F - sinistral
Fracture	32.271335	-6.259215	1765.532593	252/87	TG
Fracture	32.271335	-6.259215	1765.532593	090/84	TG

Table A-7: Field data from the Ouauizaght region, localities (d-e).

Type	Lat (Y)	Long (X)	Elev	Measurement (azimuth/dip)	Notes
Fault	32.206558	-6.306614	1547.998291	250/75	
Slickenslide	32.206558	-6.306614	1547.998291	189-53	Dextral movement with calcites
Slickenslide	32.206558	-6.306614	1547.998291	192-32	
Fault	32.206149	-6.306238	1532.387085	154/80	-
Fault	32.205731	-6.307954	1525.888672	196/65	-

Table A-8: Field data from the Ouauizaght region, locality (B.1).

Type	Lat (Y)	Long (X)	Elev	Measurement (azimuth/dip)	Notes
Fault	32.090297	-6.306874	1532.4552000	139/29	vertical beds
Fault	32.090164	-6.306718	1531.3909910	113/25	vertical beds
Fault	32.090022	-6.306422	1532.4190670	127/34	vertical beds
Fault	32.090022	-6.306422	1532.4190670	119/19	vertical beds
Fault	32.090022	-6.306422	1532.4190670	115/04	vertical beds
Fault	32.089804	-6.305942	1535.3471680	292/09	vertical beds
Fault	32.089804	-6.305942	1535.3471680	305/11	vertical beds
Fault	32.089742	-6.305836	1531.6142580	103/20	vertical beds
Fault	32.089742	-6.305836	1531.6142580	295/05	vertical beds

Table A-9: Field data from the Zawyat-Ahancal region.

Type	Lat (Y)	Long (X)	Elev	Measurement (azimuth/dip)	Notes
Bedding	31.827699	-6.131276	1725.259033	006/24	-
Bedding	31.827634	-6.131515	1730.653931	001/24	-
Bedding	31.826575	-6.127829	1792.275024	339/24	-
Bedding	31.826685	-6.127802	1793.039185	337/25	-
Bedding	31.826591	-6.127504	1789.207764	340/35	-
Bedding	31.826595	-6.127503	1789.206421	356/23	-
Bedding	31.826699	-6.127172	1789.781738	357/44	-
Bedding	31.826618	-6.127219	1796.309937	336/40	-
Bedding	31.826494	-6.126679	1786.168945	352/30	-
Bedding	31.826501	-6.126682	1789.035400	343/32	-
Bedding	31.826530	-6.126265	1791.340454	332/47	-
Bedding	31.826524	-6.126230	1795.178955	338/44	-
Bedding	31.826366	-6.126380	1779.962891	330/40	-
Bedding	31.826356	-6.126335	1780.003784	342/38	-
Bedding	31.826366	-6.126151	1783.516602	334/32	-
Bedding	31.826402	-6.126168	1783.016846	331/46	-
Bedding	31.827832	-6.124795	1751.374023	336/36	-
Bedding	31.827901	-6.124821	1755.986450	337/43	-
Bedding	31.827838	-6.124749	1745.305908	344/48	-
Bedding	31.827968	-6.124504	1744.695312	330/53	-
Bedding	31.827993	-6.124501	1746.756958	333/47	-
Bedding	31.828059	-6.124587	1744.285400	338/46	-
Bedding	31.829950	-6.123254	1724.169434	346/30	-
Bedding	31.829960	-6.123258	1728.339722	338/35	-
Bedding	31.830038	-6.122994	1726.656250	344/35	-
Bedding	31.830012	-6.122953	1721.903442	348/31	-
Bedding	31.832228	-6.118909	1691.838257	004/30	-
Bedding	31.832138	-6.118850	1692.355957	336/38	-
Bedding	31.832195	-6.118698	1686.032593	348/37	-
Bedding	31.832125	-6.118556	1689.403931	340/36	-
Bedding	31.832220	-6.118479	1694.213257	344/38	-
Bedding	31.832166	-6.118463	1686.403687	342/30	-
Bedding	31.832060	-6.118213	1680.714355	350/35	-
Bedding	31.832019	-6.118132	1679.573242	342/36	-
Bedding	31.832079	-6.118059	1678.552490	011/35	-
Bedding	31.832184	-6.117859	1679.085205	353/32	-
Bedding	31.832389	-6.117360	1680.180664	341/20	-
Bedding	31.832457	-6.117353	1679.819092	344/32	-
Bedding	31.832415	-6.116894	1714.648804	354/32	-
Bedding	31.832487	-6.116843	1699.225220	350/37	-
Bedding	31.833152	-6.115042	1676.867920	000/34	-
Bedding	31.833114	-6.115096	1694.669678	001/34	-
Bedding	31.833097	-6.115012	1681.482910	010/30	-
Bedding	31.833242	-6.114794	1682.886841	019/36	-
Bedding	31.833265	-6.114838	1677.173584	011/25	-
Bedding	31.833615	-6.115131	1695.118286	006/19	-
Bedding	31.833623	-6.114926	1692.632568	012/25	-
Bedding	31.833638	-6.115098	1702.190308	014/32	-
Bedding	31.833644	-6.115055	1696.741333	032/36	-

Bedding	31.833522	-6.114941	1685.767334	358/28	-
Bedding	31.833512	-6.114978	1692.753296	332/25	-
Bedding	31.833448	-6.114842	1683.624878	002/26	-
Bedding	31.833365	-6.114912	1681.504395	001/30	-
Bedding	31.833085	-6.114793	1670.571777	356/36	-
Bedding	31.833165	-6.114532	1663.893555	004/29	-
Bedding	31.833094	-6.114684	1657.581177	010/35	-
Bedding	31.833118	-6.114581	1662.105469	003/32	-
Bedding	31.833894	-6.111918	1641.613770	350/32	-
Bedding	31.833940	-6.111798	1641.834839	002/22	-
Fracture	31.816386	-6.085344	1706.734741	080/60	-
Fracture	31.814654	-6.086429	1737.335327	212/53	T - dextral
Fracture	31.814654	-6.086429	1737.335327	355/24	T - dextral
Fracture	31.814654	-6.086429	1737.335327	247/24	T - dextral
Fracture	31.814654	-6.086429	1737.335327	296/56	vein
Fracture	31.814157	-6.086586	1774.725952	347/06	T -dextral shear
Fracture	31.814157	-6.086586	1774.725952	052/82	T - sinistral shear
Fracture	31.814157	-6.086586	1774.725952	230/02	T - dextral
Fault	31.830731	-6.170004	2401.547119	337/84	-
Fault	31.830731	-6.170004	2401.547119	354/88	-
Fault	31.830731	-6.170004	2401.547119	339/87	-
Fault	31.830731	-6.170004	2401.547119	084/87	-
Fault	31.814157	-6.086586	1774.725952	012/79	-
Fault	31.814157	-6.086586	1774.725952	052/57	-
Fault	31.823860	-6.088327	1652.261475	258/45	-
Fault	31.823860	-6.088327	1652.261475	271/71	-
Fault	31.823998	-6.087817	1669.733398	292/80	-
Fault	31.823998	-6.087817	1669.733398	280/70	-
Fault	31.823998	-6.087817	1669.733398	297/88	-
Fault	31.823998	-6.087817	1669.733398	152/43	-
Slickenside	31.823971	-6.087398	1674.571411	280-80	dextral
Fault	31.823971	-6.087398	1674.571411	290/79	-
Fault	31.823971	-6.087398	1674.571411	170/73	-
Fault	31.823971	-6.087398	1674.571411	280/87	-
Fault	31.816386	-6.085344	1706.734741	014	-
Slcikenside	31.816386	-6.085344	1706.734741	014	Dextral
Fracture	31.816386	-6.085344	1706.734741	014	T - sinistral shear
Fracture	31.816386	-6.085344	1706.734741	014	Vein - sinistral

Table A-10: Field data from the Agoudal region, locality (a).

Type	Lat (Y)	Long (X)	Elev	Measurement (azimuth/dip)	Notes
TG	31.92226	-5.65443	2816.520508	258/56	Post-MJ
TG	31.92226	-5.65443	2816.520508	255/57	Post-MJ
TG	31.92226	-5.65443	2816.520508	052/54	Post-MJ
TG	31.92226	-5.65443	2816.520508	310/33	Post-MJ
TG	31.92226	-5.65443	2816.520508	001/54	Post-MJ
TG	31.92226	-5.65443	2816.520508	336/34	Post-MJ
TG	31.92226	-5.65443	2816.520508	347/26	Post-MJ
TG	31.92226	-5.65443	2816.520508	217/80	Syn-MJ
TG	31.92226	-5.65443	2816.520508	230/77	Syn-MJ
TG	31.92226	-5.65443	2816.520508	040/84	Syn-MJ
Vein	31.92226	-5.65443	2816.520508	028/87	Syn-MJ
TG	31.92226	-5.65443	2816.520508	034/62	Syn-MJ
TG	31.92226	-5.65443	2816.520508	050/65	Syn-MJ
TG	31.92226	-5.65443	2816.520508	048/59	Syn-MJ
TG	31.92226	-5.65443	2816.520508	217/73	Syn-MJ
Vein	31.92237	-5.65422	2822.236572	224/77	Syn-MJ
TG	31.92237	-5.65422	2822.236572	055/86	Syn-MJ
TG	31.92237	-5.65422	2822.236572	240/75	Syn-MJ
Vein	31.92319	-5.65219	2800.523193	250/70	Syn-MJ
Vein	31.92319	-5.65219	2800.523193	053/74	Syn-MJ
TG/V	31.92226	-5.65443	2816.520508	013/85	Syn-EJ
Vein	31.92226	-5.65443	2816.520508	010/86	Syn-EJ
Vein	31.92226	-5.65443	2816.520508	008/87	Syn-EJ
Vein	31.92226	-5.65443	2816.520508	256/86	Syn-EJ
Vein	31.92237	-5.65422	2822.236572	264/80	Syn-EJ
TG	31.92253	-5.65433	2805.829346	084/86	Syn-EJ
TG	31.92253	-5.65433	2805.829346	010/82	Syn-EJ
TG	31.92253	-5.65433	2805.829346	280/80	Syn-EJ
TG	31.92253	-5.65433	2805.829346	275/80	Syn-EJ
Vein	31.92253	-5.65433	2805.829346	286/82	Syn-EJ

Table A-11: Field data from the Agoudal region, localities (b-d).

Type	Lat (Y)	Long (X)	Elev	Measurement (azimuth/dip)
Vein	31.91908	-5.64883	2674.01318	210/84
Vein	31.91908	-5.64883	2674.01318	045/80
Vein	31.91908	-5.64883	2674.01318	042/80
Vein	31.91908	-5.64883	2674.01318	056/85
Vein	31.91908	-5.64883	2674.01318	262/87
Vein	31.91908	-5.64883	2674.01318	050/80
Vein	31.91908	-5.64883	2674.01318	304/45
Vein	31.91908	-5.64883	2674.01318	272/66
Vein	31.91818	-5.64782	2658.94043	310/70

Vein	31.91818	-5.64782	2658.94043	238/74
Vein	31.91817	-5.64769	2666.57129	235/78
Vein	31.91817	-5.64769	2666.57129	242/89
Vein	31.91817	-5.64769	2666.57129	244/88
Vein	31.91817	-5.64769	2666.57129	068/86
Vein	31.91817	-5.64769	2666.57129	060/80
Vein	31.91817	-5.64769	2666.57129	090/52
Vein	31.91689	-5.64578	2638.77612	210/70
Vein	31.91824	-5.64774	2655.08106	236/86
Vein	31.91824	-5.64774	2655.08106	195/84
Vein	31.91843	-5.64832	2670.98975	255/78
Vein	31.91843	-5.64832	2670.98975	222/77
Vein	31.91843	-5.64832	2670.98975	075/75
Vein	31.91863	-5.64851	2669.81152	224/87
Vein	31.91863	-5.64851	2669.81152	248/72
Vein	31.91863	-5.64851	2669.81152	232/89
Vein	31.91863	-5.64851	2669.81152	242/74
Vein	31.91863	-5.64851	2669.81152	308/73
Fault	31.91908	-5.64883	2674.01318	030/62
Fault	31.91908	-5.64883	2674.01318	036/70
Fault	31.91903	-5.64848	2674.56177	228/87
Fault	31.91903	-5.64848	2674.56177	225/84
Fault	31.91689	-5.64578	2638.77612	240/85
Fault	31.91689	-5.64578	2638.77612	240/85
Fault	31.91689	-5.64578	2638.77612	240/85
Fault	31.91689	-5.64578	2638.77612	240/85
Fault	31.91689	-5.64578	2638.77612	212/83
Fault	31.91689	-5.64578	2638.77612	212/83
Fault	31.91843	-5.64832	2670.98975	300/60
Joint	31.91735	-5.64585	2662.6023	234/75
Joint	31.91735	-5.64585	2662.6023	230/78
Joint	31.91735	-5.64585	2662.6023	235/79
TG	31.91908	-5.64883	2674.01318	305/55
TG	31.91908	-5.64883	2674.01318	065/68
TG	31.91903	-5.64848	2674.56177	032/85
TG	31.91903	-5.64848	2674.56177	256/76
TG	31.91903	-5.64848	2674.56177	220/60
TG	31.91861	-5.64832	2661.64233	244/68
TG	31.91818	-5.64782	2658.94043	110/80
TG	31.91818	-5.64782	2658.94043	306/66
TG	31.91817	-5.64769	2666.57129	055/83
TG	31.91735	-5.64585	2662.6023	250/76
TG	31.91735	-5.64585	2662.6023	246/72
TG	31.91735	-5.64585	2662.6023	242/82
TG	31.91735	-5.64585	2662.6023	245/75
TG	31.91689	-5.64578	2638.77612	010/86
TG	31.91689	-5.64578	2638.77612	010/80
TG	31.91689	-5.64578	2638.77612	010/82
TG	31.91689	-5.64578	2638.77612	020/85
TG	31.91843	-5.64832	2670.98975	350/71
Bedding	31.9195	-5.64925	2602.487061	120/53
Bedding	31.91942	-5.64913	2588.431152	124/56
Bedding	31.91913	-5.64891	2669.377197	138/55
Bedding	31.91908	-5.64883	2674.013184	138/66

Bedding	31.91897	-5.64863	2687.154541	122/45
Bedding	31.91903	-5.64848	2674.561768	130/48
Bedding	31.91861	-5.64832	2661.642334	110/60
Bedding	31.91854	-5.64823	2670.180908	130/40
Bedding	31.91851	-5.64813	2655.992920	130/35
Bedding	31.91843	-5.64809	2663.977539	132/40
Bedding	31.91833	-5.64793	2663.718262	136/36
Bedding	31.91818	-5.64782	2658.940430	147/36
Bedding	31.91817	-5.64769	2666.571289	156/32
Bedding	31.91793	-5.64731	2655.049805	128/35
Bedding	31.91757	-5.6467	2656.978516	122/25
Bedding	31.91748	-5.64638	2650.489502	124/30
Bedding	31.91735	-5.64585	2662.602295	135/25
Bedding	31.9172	-5.64558	2651.806396	130/20
Bedding	31.9173	-5.64645	2656.462646	130/30
Bedding	31.91711	-5.64627	2653.776611	115/25
Bedding	31.91675	-5.64622	2657.084717	112/35
Bedding	31.91614	-5.64614	2668.530273	176/30
Bedding	31.91689	-5.64578	2638.776123	144/12
Bedding	31.91824	-5.64774	2655.081055	125/37
Bedding	31.91816	-5.64792	2659.690430	138/36
Bedding	31.91828	-5.64801	2666.784668	130/36
Bedding	31.91843	-5.64832	2670.989746	140/42
Bedding	31.91858	-5.64844	2669.922852	125/53
Bedding	31.91863	-5.64851	2669.811523	120/46
Bedding	31.91895	-5.64889	2677.548096	136/50
Bedding	31.91902	-5.64904	2675.150879	136/57
Bedding	31.91912	-5.64926	2675.492920	145/67
Bedding	31.91964	-5.64926	2696.803955	156/65

Table A-12: Field data from the Agoudal region, locality (e).

Type	Lat (Y)	Long (X)	Elev	Measurement (azimuth/dip)
Bedding	31.98411	-5.55265	2483.352051	295/70
Bedding	31.98411	-5.55257	2479.312988	300/85
Bedding	31.98411	-5.55257	2479.312988	310/85
Bedding	31.9842	-5.55223	2478.602295	305/85
Bedding	31.98423	-5.55211	2482.604980	302/80
Bedding	31.98416	-5.55186	2475.522461	115/75
Bedding	31.98415	-5.55171	2469.791992	110/60
Bedding	31.9841	-5.55154	2465.346436	110/60
Bedding	31.98409	-5.55138	2464.264893	105/57
Bedding	31.98413	-5.5513	2463.025146	114/50
Bedding	31.98392	-5.55068	2482.238281	088/50
Bedding	31.98384	-5.55047	2471.599609	110/50
Bedding	31.98393	-5.55038	2493.564941	108/20
Bedding	31.98403	-5.54989	2505.330078	014/15
Bedding	31.98309	-5.55315	2462.552490	292/83
Bedding	31.98309	-5.55307	2468.221436	110/85
Bedding	31.9832	-5.55239	2461.172119	112/74

Bedding	31.98318	-5.55222	2451.183350	110/60
Bedding	31.98332	-5.55204	2441.037354	104/57
Bedding	31.98342	-5.5518	2431.766846	108/38
Bedding	31.98349	-5.55165	2447.099365	094/48
Bedding	31.98358	-5.5515	2449.788086	110/55
Bedding	31.98366	-5.55135	2449.740234	109/52
Bedding	31.98183	-5.5534	2445.065918	115/85
Bedding	31.98192	-5.55318	2453.632324	102/60
Bedding	31.98195	-5.55306	2450.089355	115/75
Bedding	31.98219	-5.55237	2444.756836	102/53
Bedding	31.98233	-5.55198	2445.749512	090/36
Bedding	31.98239	-5.55187	2444.584229	114/37
Bedding	31.98252	-5.55175	2446.981689	102/43
Bedding	31.98267	-5.5516	2455.115723	094/38
Bedding	31.98292	-5.55137	2438.997559	096/35
Bedding	31.9828	-5.55112	2443.343262	105/34
Bedding	31.98152	-5.55096	2437.370850	332/15
Bedding	31.98103	-5.55091	2435.180176	095/20
Bedding	31.98094	-5.55068	2436.144287	098/16

Table A-13: Field data from the Er-Rich region, localities (a-c).

Type	Lat (Y)	Long (X)	Elev	Measurement (azimuth/dip)	Notes
Fault	32.36761	-4.467864	1507.160278	270/75	Post-MJ - sinistral
Fault	32.36761	-4.467864	1507.160278	230/80	Post-MJ - dextral
Fault	32.36761	-4.467864	1507.160278	238/84	Post-MJ - dextral
Fault	32.36764	-4.467999	1499.460449	247/87	post-MJ
Fault	32.36764	-4.467999	1499.460449	072/87	post-MJ
Fault	32.36764	-4.467999	1499.460449	208/74	Post-MJ - sinistral
Fault	32.35669	-4.45683	1473.957153	238/60	post-MJ
Fault	32.36767	-4.467826	1507.293823	263/76	post-MJ
Fault	32.36767	-4.467826	1507.293823	263/76	post-MJ
Fault	32.36765	-4.467887	1514.354492	053/72	Post-MJ - dextral
Fault	32.36765	-4.467887	1514.354492	073/69	Post-MJ - sinistral
Fault	32.36754	-4.467863	1479.599487	241/87	Post-MJ - sinistral
Fault	32.36754	-4.467863	1479.599487	241/87	Post-MJ - sinistral
Fault	32.36724	-4.468123	1507.197266	267/83	post-MJ
Fault	32.36724	-4.468123	1507.197266	247/80	post-MJ
Fault	32.36642	-4.465394	1499.109009	074/72	post-MJ
Fault	32.36642	-4.465394	1499.109009	278/84	post-MJ
Fault	32.36642	-4.465394	1499.109009	278/84	post-MJ
Fault	32.36641	-4.465233	1502.345703	262/83	post-MJ
Fault	32.36641	-4.465233	1502.345703	262/83	post-MJ
Fault	32.36641	-4.465196	1502.115601	265/76	post-MJ
Fault	32.36641	-4.465196	1502.115601	262/80	post-MJ
Fault	32.36641	-4.465196	1502.115601	262/80	post-MJ
Fault	32.35692	-4.456972	1476.298584	040/86	post-MJ
Fault	32.35692	-4.456972	1476.298584	060/73	post-MJ
Fault	32.35692	-4.456972	1476.298584	057/78	Post-MJ - sinistral
Fault	32.35668	-4.456811	1481.968018	269/56	Post-MJ - sinistral
Fault	32.35668	-4.456811	1481.968018	248/72	Post-MJ - sinistral
Fault	32.35668	-4.456811	1481.968018	210/80	Post-MJ - dextral
Fault	32.35667	-4.456678	1470.792236	229/65	Post-MJ - sinistral
Fault	32.35667	-4.456678	1470.792236	229/65	post-MJ
Fault	32.35667	-4.456678	1470.792236	016/65	Post-MJ - dextral
Fault	32.35667	-4.456678	1470.792236	016/65	Post-MJ - dextral
Fault	32.35667	-4.456678	1470.792236	039/60	Post-MJ - sinistral
Fault	32.35668	-4.456606	1473.751709	212/85	post-MJ
Fault	32.35668	-4.456606	1473.751709	212/85	post-MJ
Fault	32.35668	-4.456606	1473.751709	014/87	post-MJ
Fault	32.35668	-4.456606	1473.751709	200/86	post-MJ
Fault	32.33554	-4.457971	1451.141724	220/84	post-MJ
Fault	32.33554	-4.457971	1451.141724	088/87	Post-MJ - sinistral

Fault	32.33552	-4.457882	1451.129883	286/75	post-MJ
Fault	32.35649	-4.45672	1467.980103	032/74	post-MJ
Fault	32.35649	-4.45672	1467.980103	032/74	post-MJ
Fault	32.35682	-4.456671	1482.045532	230/77	Post-MJ - sinistral
Fault	32.35682	-4.456671	1482.045532	230/82	Post-MJ - sinistral
Fault	32.35698	-4.456514	1486.043945	046/75	post-MJ
Fault	32.3564	-4.457114	1470.970215	025/86	post-MJ
Fault	32.3564	-4.457114	1470.970215	024/85	post-MJ
Fault	32.36636	-4.46552	1507.448975	079/73	dextral
Fault	32.36636	-4.46552	1507.448975	096/67	post-MJ
Fault	32.36636	-4.46552	1507.448975	096/67	post-MJ
TG	32.36761	-4.467864	1507.160278	038/78	post-MJ
TG	32.36764	-4.467999	1499.460449	192/82	post-MJ
TG	32.36764	-4.467999	1499.460449	277/83	post-MJ
TG	32.36754	-4.467863	1479.599487	240/74	post-MJ
TG	32.36754	-4.467863	1479.599487	250/86	post-MJ
TG	32.36754	-4.467863	1479.599487	195/85	post-MJ
TG	32.36754	-4.467863	1479.599487	216/87	post-MJ
TG	32.36762	-4.467994	1509.372192	211/87	post-MJ
TG	32.36641	-4.465233	1502.345703	217/80	post-MJ
TG	32.36641	-4.465233	1502.345703	243/82	post-MJ
TG	32.36641	-4.465196	1502.115601	258/87	post-MJ
TG	32.36641	-4.465196	1502.115601	251/82	post-MJ
TG	32.36641	-4.465196	1502.115601	253/86	post-MJ
TG	32.36641	-4.465196	1502.115601	223/67	post-MJ
TG	32.35692	-4.456972	1476.298584	065/85	post-MJ
TG	32.35692	-4.456972	1476.298584	253/84	post-MJ
TG	32.35692	-4.456972	1476.298584	102/77	post-MJ
TG	32.35678	-4.456911	1490.127930	040/89	post-MJ
TG	32.35678	-4.456911	1490.127930	071/65	post-MJ
TG	32.35678	-4.456911	1490.127930	033/73	post-MJ
TG	32.35668	-4.456811	1481.968018	208/81	post-MJ
TG	32.35668	-4.456811	1481.968018	014/84	post-MJ
TG	32.35668	-4.456811	1481.968018	196/81	post-MJ
TG	32.35667	-4.456678	1470.792236	242/78	post-MJ
TG	32.35667	-4.456678	1470.792236	202/85	post-MJ
TG	32.35668	-4.456606	1473.751709	025/88	post-MJ
TG	32.35668	-4.456606	1473.751709	205/86	post-MJ
TG	32.35698	-4.456514	1486.043945	014/73	post-MJ
TG	32.35713	-4.456357	1490.042358	080/83	post-MJ
TG	32.35729	-4.4562	1494.040771	084/76	post-MJ
TG	32.35745	-4.456043	1498.039184	080/83	post-MJ
TG	32.35761	-4.455886	1502.037597	090/82	post-MJ
TG	32.3564	-4.457114	1470.970215	072/83	post-MJ
TG	32.3564	-4.457114	1470.970215	087/86	post-MJ
TG	32.3564	-4.457114	1470.970215	074/82	post-MJ
TG	32.3564	-4.457114	1470.970215	273/85	post-MJ
Fault	32.35697	-4.457019	1477.968506	148/70	syn-MJ FZ
Fault	32.36642	-4.465394	1499.109009	278/84	syn-MJ
Fault	32.35678	-4.456911	1490.127930	225/86	syn-MJ sinistral
Fault	32.35678	-4.456911	1490.127930	225/86	syn-MJ sinistral

Fault	32.35667	-4.456678	1470.792236	356/77	syn-MJ sinistral
Fault	32.33552	-4.457882	1451.129883	346/84	syn-MJ
Fault	32.3564	-4.457114	1470.970215	002/80	syn-MJ
Fault	32.36636	-4.46552	1507.448975	079/73	syn-MJ dextral
TG	32.36764	-4.467999	1499.460449	298/68	syn-MJ
TG	32.3567	-4.456887	1471.583130	165/76	syn-MJ
TG	32.35669	-4.456878	1476.111938	358/86	syn-MJ
TG	32.35697	-4.457019	1477.968506	345/47	syn-MJ
TG	32.35697	-4.457019	1477.968506	314/66	syn-MJ
TG	32.36754	-4.467863	1479.599487	169/89	syn-MJ
TG	32.35692	-4.456972	1476.298584	350/75	syn-MJ
TG	32.35692	-4.456972	1476.298584	099/78	syn-MJ
TG	32.35692	-4.456972	1476.298584	020/87	syn-MJ
TG	32.35668	-4.456811	1481.968018	352/86	syn-MJ
TG	32.33554	-4.457971	1451.141724	195/88	syn-MJ
TG	32.33554	-4.457971	1451.141724	004/65	syn-MJ
TG	32.33552	-4.457882	1451.129883	302/86	syn-MJ
TG	32.33552	-4.457882	1451.129883	352/55	syn-MJ
TG	32.33552	-4.457882	1451.129883	332/66	syn-MJ
TG	32.33552	-4.457882	1451.129883	340/64	syn-MJ
TG	32.35649	-4.45672	1467.980103	290/75	syn-MJ
TG	32.35649	-4.45672	1467.980103	180/75	syn-MJ
TG	32.35649	-4.45672	1467.980103	164/80	syn-MJ
TG	32.35649	-4.45672	1467.980103	352/87	syn-MJ
TG	32.35649	-4.45672	1467.980103	176/82	syn-MJ
TG	32.35682	-4.456671	1482.045532	145/87	syn-MJ
TG	32.35776	-4.455729	1506.036010	106/84	syn-MJ
Joints/Cleavage	32.33821	-4.457823	1438.724976	314/80	-
Joints/Cleavage	32.33865	-4.454204	1430.053101	200/75	-
Joints/Cleavage	32.33863	-4.450288	1441.310425	310/50	-
Joints/Cleavage	32.35593	-4.456367	1468.628174	320/45	-
Joints/Cleavage	32.35593	-4.456367	1468.628174	042/40	-
Joints/Cleavage	32.35593	-4.456367	1468.628174	312/40	-
bedding	32.34136	-4.461701	1471.181274	310/60	-
bedding	32.34136	-4.461701	1471.181274	313/30	-
bedding	32.33983	-4.461206	1459.442749	297/55	-
bedding	32.33987	-4.461014	1459.706055	314/54	-
bedding	32.33971	-4.459564	1456.661499	306/70	-
bedding	32.33945	-4.459315	1453.506836	307/70	-
bedding	32.33928	-4.458839	1451.262939	311/46	-
bedding	32.33836	-4.458541	1445.327393	307/46	-
bedding	32.33821	-4.457823	1438.724976	310/50	-
bedding	32.33808	-4.457371	1443.967285	312/60	-
bedding	32.33854	-4.455177	1431.282837	315/43	-
bedding	32.33865	-4.454204	1430.053101	312/40	-
bedding	32.3385	-4.454025	1432.501465	315/43	-
bedding	32.33823	-4.453126	1420.682251	326/35	-
bedding	32.33831	-4.452701	1434.133301	305/33	-
bedding	32.33827	-4.452298	1435.784180	328/40	-
bedding	32.33866	-4.451652	1439.214600	298/43	-
bedding	32.33863	-4.450288	1441.310425	320/45	-
bedding	32.33849	-4.450433	1437.341064	290/35	-

Table A-14: Field data from the Er-Rich region, localities (d).

Type	Lat (Y)	Long (X)	Elev	Measurement (azimuth/dip)
Joints/Cleavage	32.33275	-4.426792	1493.795288	064/84
Joints/Cleavage	32.33275	-4.426792	1493.795288	352/60
Vein	32.33212	-4.428285	1497.491455	358/80
Vein	32.33212	-4.428285	1497.491455	169/76
Vein	32.33212	-4.428285	1497.491455	334/60
Vein	32.33239	-4.429347	1499.767090	357/87
Vein	32.33196	-4.429535	1504.425415	357/83
bedding	32.33302	-4.426752	1514.930664	336/14
bedding	32.33301	-4.426762	1500.758301	357/34
bedding	32.33291	-4.426822	1496.918091	352/45
bedding	32.33286	-4.42683	1495.584961	354/46
bedding	32.33279	-4.426787	1494.107544	353/46
bedding	32.33275	-4.426792	1493.795288	350/46
bedding	32.33271	-4.42667	1495.813965	350/44
bedding	32.33301	-4.427315	1498.296021	340/27
bedding	32.33267	-4.427229	1491.882080	328/27
bedding	32.33266	-4.427187	1491.315063	327/33
bedding	32.33249	-4.427052	1482.343140	345/34
bedding	32.33252	-4.427788	1489.569336	340/31
bedding	32.3325	-4.427774	1497.449585	344/25
bedding	32.33218	-4.428009	1504.298218	285/14
bedding	32.3322	-4.428121	1500.342529	282/10
bedding	32.33212	-4.428285	1497.491455	236/02
bedding	32.33218	-4.428065	1495.945801	280/10
bedding	32.33225	-4.427995	1494.396973	294/15
bedding	32.33184	-4.429168	1499.737915	356/16
bedding	32.33186	-4.429036	1498.092407	208/12
bedding	32.33171	-4.429022	1496.473999	344/08
bedding	32.3316	-4.428998	1487.596191	340/25

Table A-15: Field data from the Bou Annane region.

Type	Lat (Y)	Long (X)	Elev	Measurement (azimuth/dip)
bedding	32.33597	-3.30026	1228.609497	152/20
bedding	32.33582	-3.30014	1229.839111	168/15
bedding	32.3356	-3.30009	1239.622803	158/15
bedding	32.33536	-3.29986	1229.157593	178/20
bedding	32.3351	-3.29963	1235.874756	176/12
bedding	32.33469	-3.29954	1240.824219	158/10
bedding	32.33441	-3.29945	1246.923218	181/06
bedding	32.33415	-3.29941	1254.390015	198/04
bedding	32.3534	-3.30151	1158.993042	000/40
TG	32.3534	-3.30151	1158.993042	300/68
TG	32.3534	-3.30151	1158.993042	345/64
TG	32.35996	-3.29777	1155.778687	021/86
TG	32.35996	-3.29777	1155.778687	284/54
TG	32.36037	-3.29782	1157.477295	078/85
bedding	32.36262	-3.29838	1149.558838	180/05

B. Appendix for Chapter 3 – Florida, Eastern Gulf of Mexico

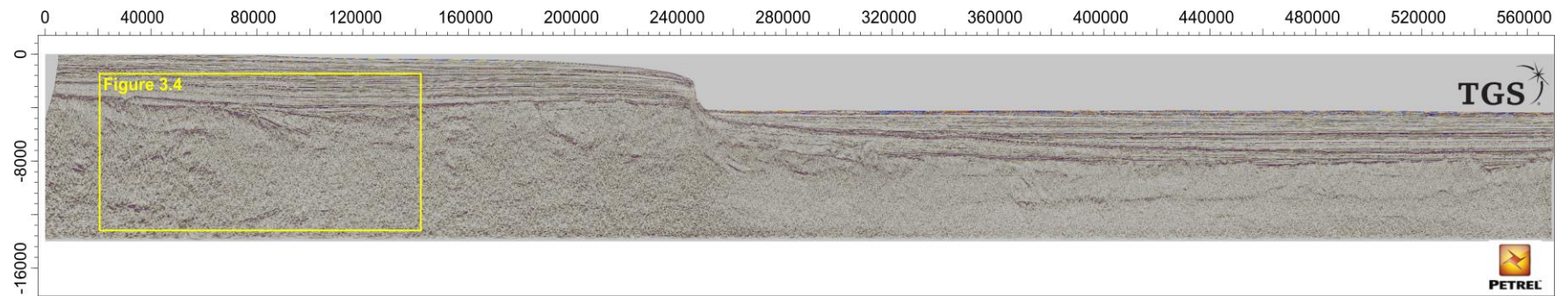


Figure 0.4: Seismic line B of the Eastern Gulf of Mexico. Seismic data courtesy of TGS.

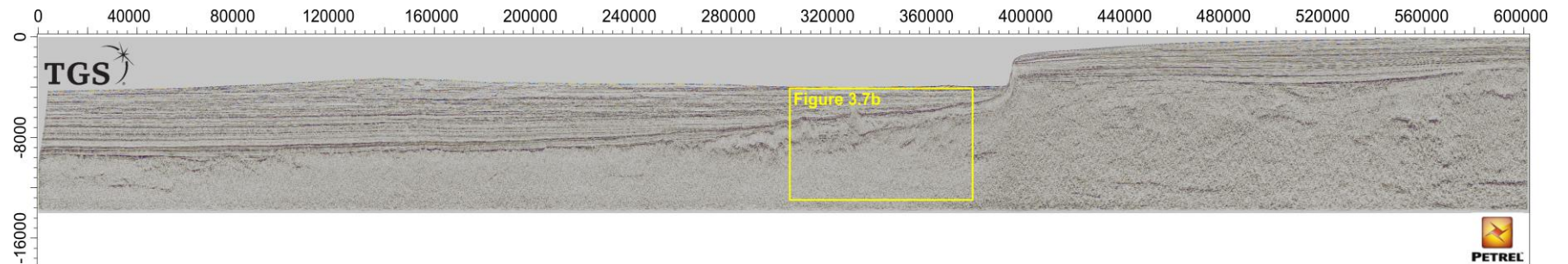


Figure 0.5: Seismic line C of the Eastern Gulf of Mexico. Seismic data courtesy of TGS.

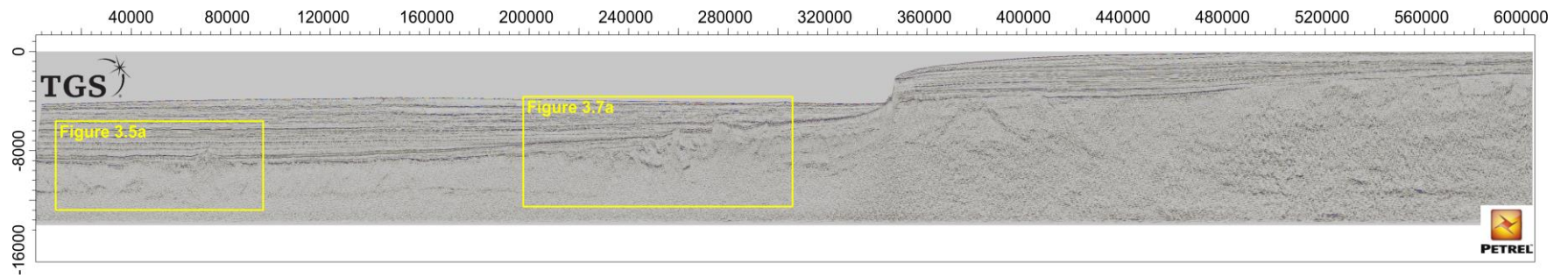


Figure 0.6: Seismic line D of the Eastern Gulf of Mexico. Seismic data courtesy of TGS.

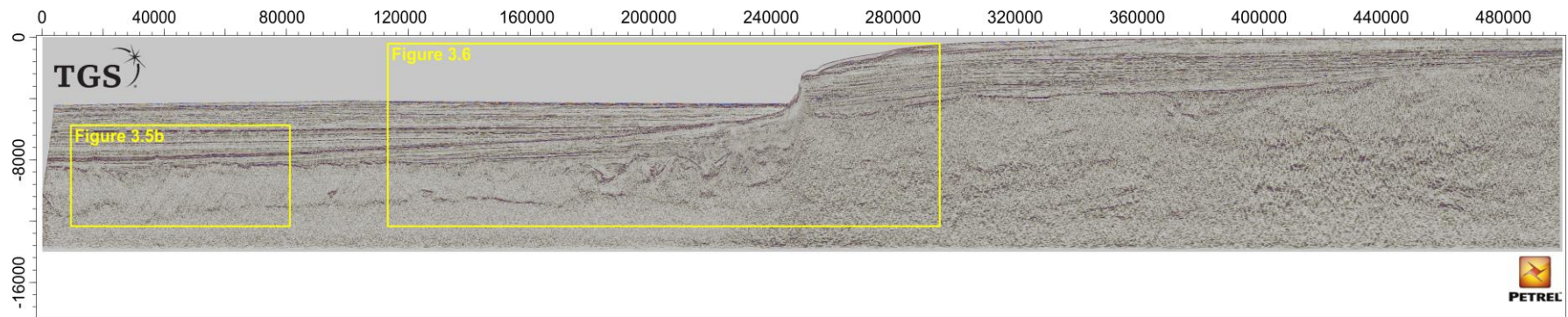


Figure 0.7: Seismic line E of the Eastern Gulf of Mexico. Seismic data courtesy of TGS.

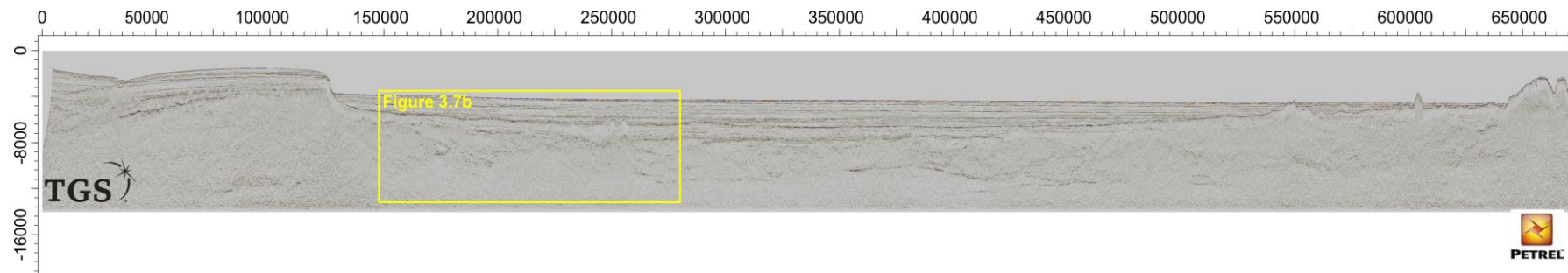


Figure 0.8: Seismic line H of the Eastern Gulf of Mexico. Seismic data courtesy of TGS.

C. Appendix for Chapter 4 – Ghana, Equatorial Atlantic

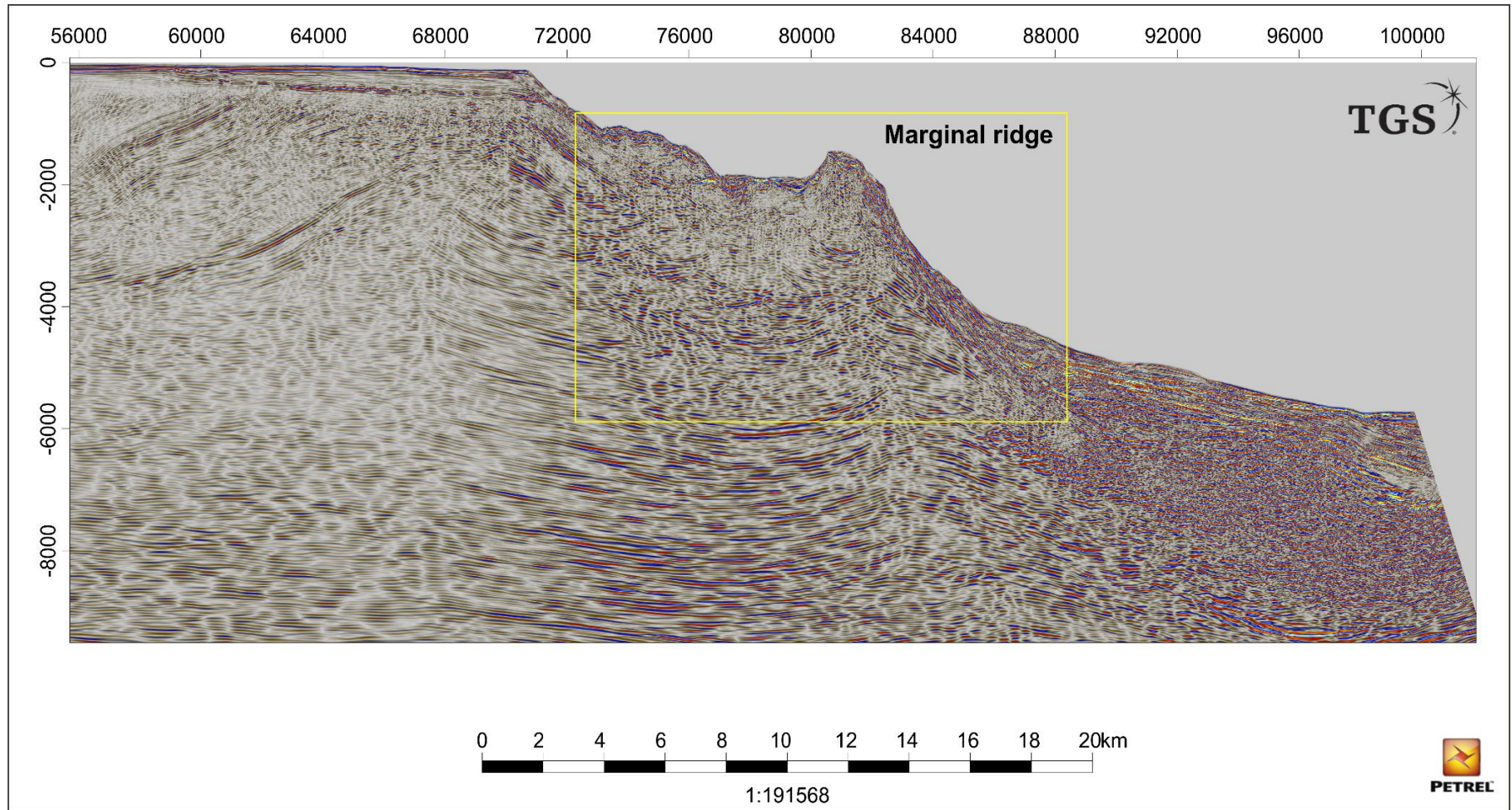


Figure 0.9: Indicative marginal ridge of the Ghanaian margin. Seismic data courtesy of TGS.

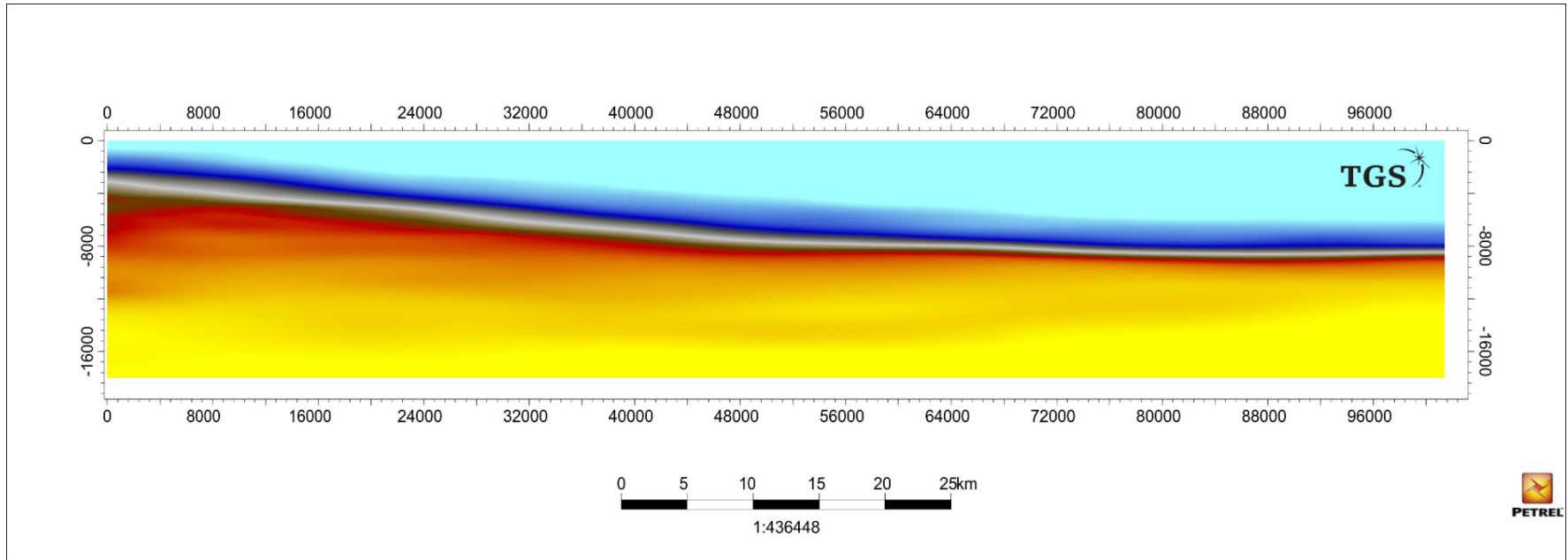


Figure 0.10: Indicative migration velocity line. Seismic data courtesy of TGS.

Athanasia Vasileiou

Characterisation of strike-slip tectonics in rifts and rifted margins